

**Analysis of the Response of Modal
Parameters to Damage in CFRP Laminates
using a Novel Modal Identification Method**

© Daerefa-a Mitsheal Amafabia

**A thesis Submitted to the University of Hertfordshire in partial fulfilment
of the requirements for the degree of
Doctor of Philosophy**

**School of Engineering and Computer Science, University of
Hertfordshire**

April, 2019

Abstract

Nowadays, composite materials are widely used in several industries, e.g. the aeronautical, automotive, and marine, due to their excellent properties, such as stiffness and strength to weight ratios and high resistance to corrosion. However, they are prone to develop Barely Visible Impact Damage (BVID) from low to medium energy impacts (i.e. 1 – 10 m/s and 11 – 30 m/s respectively) that are reported to occur during both service and maintenance, such as bird strike; hailstones and tool drops. Therefore, Structural Health Monitoring (SHM) techniques have been developed to allow identifying damage at an early stage, in an attempt to avoid catastrophic consequences.

Vibration measurement was conducted on healthy and damaged Carbon Fibre Reinforced Polymers (CFRPs) specimens. Damage is introduced to the specimen through a static indentation and the work done by the hemispherical indenter measured. This test was mainly for the purpose of damage introduction in the test samples. In this work, the effects of damage on the individual mode were studied to understand the response pattern of the modal parameters. It is intended that the current study will inform the development of a new damage identification method based on the variations between healthy and damaged specimen's dynamic results.

A new modal identification method (“Elliptical Plane”) that uses an alternative plot of the receptance has been developed in this work. The Elliptical Plane method used the energy dissipated per cycle of vibration as a starting point, to identify modal constants from Frequency Response Functions (FRFs). In comparison with the method of inverse, this new method produces accurate results, for systems that are lightly damped with its modes well-spaced. The sine of the phase of the receptance is plotted against the amplitude of the receptance, through which damping was calculated from the slope of a linear fit to the resulting plot. The results show that, there are other relevant properties of the plot that were not yet delve into by researchers. The shape of the plot is elliptical, near the resonant frequencies, whereby both parts of the modal constants (real and imaginary) can be determined from numerical curve-fitting. The method offers a new perspective on the way the receptance may be represented, in the Elliptical Plane, which may bring valuable insights for other researchers in the field. The novel method is

discussed through both numerical and experimental examples. It is a simple method and easy to use.

Interestingly, as the energy level increases, the percentage changes in both the modal frequency and damping increases. The linear equations reveal that there is a correlation between the increase in energy and the percentage variation in modal frequency and damping, especially from a threshold energy level determined to be between 15J and 20J for the analysed cases.

Finally, modal identification is conducted on the healthy and damaged specimens, and the results were analysed with BETAlab software and the Elliptical Modal identification method. It was observed that the Elliptical Modal identification method provides some interesting results. For instance, a comparison between the modal damping from the ellipse and BETAlab methods revealed that, the level of reduction in the modal damping from the ellipse method is higher than that of the BETAlab. This behaviour offers a promising future in the area of damage identification in structures.

Acknowledgement

I would like to sincerely acknowledge my supervisors: Dr Opukuro David-West, Dr Diogo Montalvão and Prof. George Haritos for their guidance and continuous support during the research.

Special thanks to Mr David Bell and Dr Anatolii Babutskyi who gave me access to test facilities in the various laboratories. The author gratefully appreciates the Niger Delta Development Commission (NDDC) for the funding of this research work through grant number NDDC/DEHSS/2015PGFS/RVS/025.

My appreciation to my grandmother Madam Lily A. LongJohn, my mother Mrs Patricia I. Asemebo and my aunt Madam Soibi A. Iboroma, whose unending love and encouragement during my studies and always, were inestimable. Special thanks to my siblings Frank Alex, Fortune I. Asemebo, Augustina I. Asemebo and Helen I. Asemebo, who made all efforts in making my struggle easier. I am very thankful to my cousins and their wives Mr and Mrs Ibietela Kanikwu, Mr and Mrs Isobeye Roberts and my niece Susan I. Whyse for being there for me always. I am grateful to my family and friends who have been a pillar of love and indispensably, support to me all these years. I sincerely appreciate Engr. and Mrs Lawrence Martyns Yellow, Dr and Mrs Christian Uruaka, Pst. and Deaconess Ibaranyanakaye, Mrs Patricia Lawson, Mrs Sonye Allannah, Chief O.K Anabaraba, Chief Sara-Igbe, Chief Bekinbo Soberekon, Mr and Mrs Adokiye Charles, Engr. and Mrs Richard Ibaranyanakaye, Mr Otelemate Horsefall, Mr Lucky Wobodo Alerechi, Mr and Mrs Vincent Daka, Mr Clement Dumbiri Aghaulor, Mrs Elsy Braide, Engr. Dr. and Mrs Saturday Ebigenibo Genuine, Prof. Victor Omuaru, Engr and Mrs Mann Dokubo, Pa Morowei Blessing, Mr and Mrs Tamuno-olobo Ibama, Mr and Mrs Ibikunoma George, Mr Kingsley Sogules, Mr Fubara Somoni, Mr Benebo Gogo-Abite, Mr and Mrs Fayama Horatio Yellowe and a host of others, for all their support and encouragement during these years. Thank you to the woman that came along and gave my life a new meaning – my wife Engr. (Mrs) Ibiye Daerefa-a Amafabia.

Finally, I am forever grateful to my creator for bringing me this far. All thanks to the great and mighty God.

Table of Contents

ABSTRACT.....	I
ACKNOWLEDGEMENT	III
TABLE OF CONTENTS.....	IV
LIST OF TABLES.....	VII
LIST OF FIGURES.....	VIII
DEDICATION.....	XV
NOMENCLATURE	XVI
PUBLICATIONS.....	XVIII
1 INTRODUCTION	1
1.1 AIM.....	2
1.2 OBJECTIVES	2
1.3 CONTRIBUTION TO KNOWLEDGE	2
1.4 RESEARCH OUTLINE	2
2 REVIEW OF LITERATURE.....	5
2.1 INTRODUCTION	5
2.2 DAMAGE IDENTIFICATION PROCEDURES.....	5
2.3 THE PROCESS OF SHM.....	6
2.3.1 <i>Operational Evaluation</i>	6
2.3.2 <i>Acquisition of Data, Fusion and Cleansing</i>	7
2.3.3 <i>Extraction of Feature and Condensation of Information</i>	7
2.3.4 <i>Statistical Model Development</i>	7
2.4 AN OVERVIEW OF DAMAGE IDENTIFICATION IN COMPOSITE MATERIALS.....	8
2.4.1 <i>Vibration-based</i>	8
2.4.1.1 Modal Strain Energy.....	12
2.4.1.2 Frequency Method.....	12
2.4.1.3 Transmissibility	14
2.4.1.4 Damping	19
2.4.1.5 Lamb Waves	21
2.4.2 <i>Acoustic-based</i>	27
2.4.2.1 Acoustic Emission (AE).....	27
2.4.2.2 Ultrasonic.....	31
2.4.2.3 Acousto-Ultrasonic.....	32
2.4.2.4 Vibro-Acoustic.....	34
2.4.3 <i>Instrumentation-based</i>	35
2.4.3.1 Sensor Networks	35
2.4.3.2 Eddy Currents.....	39
2.4.3.3 Electrical Resistance.....	41
2.4.3.4 Infrared Thermography.....	43
2.4.3.5 Nonlinear Elastic Wave Spectroscopy	45
2.4.4 <i>Artificial Neural Networks</i>	46
2.5 PROGNOSIS	55
2.6 CONCLUDING REMARKS	56
3 THE FAILURE MECHANISMS OF COMPOSITE MATERIALS	59
3.1 INTRODUCTION	59
3.2 TYPES OF FAILURE MECHANISMS.....	59
3.2.1 <i>Matrix Cracking</i>	59
3.2.2 <i>Fibre Fracture</i>	60
3.2.3 <i>Debonding</i>	61
3.2.4 <i>Delamination</i>	62
3.2.5 <i>Fibre Pullout</i>	62
3.2.6 <i>Micro-buckling</i>	63

Analysis of the Response of Modal Parameters to Damage in CFRP Laminates using a Novel Modal Identification Method

3.2.7	<i>Kink Bands</i>	63
3.3	CONCLUDING REMARKS	65
4	REPRESENTATION OF THE RECEPTANCE IN THE ELLIPTICAL PLANE	68
4.1	RELEVANCE OF THE REPRESENTATION OF THE RECEPTANCE IN THE ELLIPTICAL PLANE	68
4.2	INTRODUCTION	68
4.3	THEORETICAL DEVELOPMENT	70
4.3.1	<i>Definitions</i>	70
4.3.2	<i>Determination of the Hysteretic Damping</i>	71
4.3.3	<i>Determination of the Real and Imaginary Parts of the Modal Constant</i>	73
4.4	PROPERTIES OF THE RECEPTANCE IN THE ‘ELLIPTICAL PLANE’	75
4.5	NUMERICAL VALIDATION OF THE “ELLIPTICAL PLANE” MODAL IDENTIFICATION METHOD	78
4.6	EXPERIMENTAL VALIDATION OF THE “ELLIPTICAL PLANE” MODAL IDENTIFICATION METHOD.....	83
4.6.1	<i>Experimentation Setup</i>	83
4.6.2	<i>Results</i>	84
4.6.3	<i>Validation of Experimental Results</i>	89
4.7	THE REDUCTION OF UNCERTAINTY ON THE ELLIPTICAL PLANE MODAL IDENTIFICATION METHOD	91
4.7.1	<i>Numerical Curve-Fitting Methods</i>	91
4.7.2	<i>Numerical Example</i>	93
4.8	CONCLUDING REMARKS	96
5	EXPERIMENTAL MEASUREMENTS	99
5.1	DESIGN AND MANUFACTURING OF TEST BASE AND HEMISPHERICAL INDENTER	99
5.2	MANUFACTURING OF CFRP COMPOSITE LAMINATES	99
5.2.1	<i>Stacking Sequence</i>	99
5.2.2	<i>Manufacturing Process</i>	100
5.2.3	<i>The Curing Process</i>	101
5.3	GENERALITIES ON THE EXPERIMENTAL SETUP.....	103
5.4	EXPERIMENTAL RESULTS FROM BETALAB	106
5.4.1	<i>Introduction of Damage into Test Specimens</i>	106
5.4.2	<i>Deviation of Frequency and Damping with Damage Progression</i>	111
6.	Plate B3 90/0/±45S	119
7.	Plates C1 90/02S.....	120
8.	Plate C2 90/02S.....	121
9.	Plate C3 90/02S.....	123
10.	Plate C4 90/02S	124
11.	Plate D1 902/03S	125
12.	Plate D2 902/03S	127
13.	Plate E1903/03S.....	128
14.	Plate E2 903/03S	129
15.	Plate F1 0/±45/90S	131
16.	Plate G1 903/03/903.....	132
5.4.3	<i>Preliminary Observations on the Effect of Damage on different Stacking Configurations</i>	133
5.4.4	<i>The Behavioural Pattern of Modal Parameters due to Increased Energy Level</i>	136
1.	Plates A1 – 2 90/±45/0S.....	136
2.	Plates B1 – 2 90/0/±45S.....	139
3.	Plates C1 – 2 C1 90/02S	141
4.	Plates D1 902/03S and E1903/03S.....	143
5.4.5	<i>The Correlation between the Energy Increase and Modal Parameters</i>	144
5.5	EXPERIMENTAL RESULTS FROM THE ELLIPTICAL METHOD	148
5.5.1	<i>Plates A1 – 3, B1 – 2, C1 – 3, D1 – 2 and E1</i>	148
5.5.2	<i>F1 and G1</i>	152
5.6	A COMPARISON OF THE MODAL DAMPING BETWEEN ELLIPSE METHOD AND BETALAB	153
5.7	CONCLUDING REMARKS	159
6	CONCLUSION AND FUTURE WORK	161
6.1	CONCLUSIONS	161
6.2	FUTURE WORK	162
	REFERENCES	164
	APPENDIX A: DEVIATION IN THE ELLIPTICAL AREAS	186

Analysis of the Response of Modal Parameters to Damage in CFRP Laminates using a Novel Modal Identification Method

APPENDIX B: VARIATION IN THE MODAL PARAMETERS (BETALAB).....	188
APPENDIX C: ACHIEVEMENT	194

List of Tables

Table 2.1 Summary of the damage techniques.	49
Table 4.1 Numerical models' modal simulated properties.	81
Table 4.2 Results from the modal identification (numerical examples).	81
Table 4.3 Difference between the theoretical values and the numerical results (all values are expressed in %).	82
Table 4.4 Results from the Modal identification using the Elliptical Plane technique (experimental examples).	88
Table 4.5 Results from the Modal identification using the software BETAlab (experimental examples).	89
Table 4.6 Difference between the results obtained with the Elliptical Plane technique and the software BETAlab (all values are expressed in %).	89
Table 4.7 Results from the modal identification using BETAlab (numerical examples).	90
Table 4.8 Difference between the theoretical values and the numerical results from BETAlab (all values are expressed in %).	90
Table 4.9 Averaged numerical results from the modal identification in the 15–25Hz and 45–55Hz ranges (values between brackets are the percent error committed).	95
Table 4.10 Numerical results from the modal identification using the software presented in section 4 in the 15–25 Hz and 45–55 Hz ranges (values between brackets are the percent error committed).	95
Table 5.1 Types of specimens and designations.	100
Table 5.2 Energy absorbed by test specimens.	111

List of Figures

Figure 2.1 Dynamic models interrelation (hysteretic damping case) [25].....	11
Figure 2.2 Stress waves due to the presence of crack in a material under stress [12].	28
Figure 3.1 Matrix cracks in the GFRP in the reinforced direction [188].....	59
Figure 3.2 Fibre matrix debonding [200].....	61
Figure 3.3 Fibre micro-buckling [215].	63
Figure 3.4 Kink band [222].....	64
Figure 4.1 Mass-Spring-damper system.	70
Figure 4.2 The representation of the receptance in the Argand plane.	74
Figure 4.3 Numerical example of the amplitude and phase of a SDOF receptance in the frequency domain.	76
Figure 4.4 Numerical example of the same SDOF receptance represented in figure 4.3 in the ‘elliptical plane’.....	77
Figure 4.5 Amplitude of the MDOF receptance for numerical case 7 in the frequency domain.	79
Figure 4.6 MDOF receptance for numerical case 7 (Ffigure 4.5) represented in the ‘Elliptical Plane’ with two ellipses fitting the data at the vicinity of the mode shapes (the plot was mirrored for better convenience. Only half of the ellipse is actually visible with the discussed method).....	79
Figure 4.7 Amplitude and phase of the receptance in the frequency domain near the 1st resonance of simulated case 7.	79
Figure 4.8 Receptance near the 1st resonance of simulated case 7 (represented in the ‘Elliptical Plane’) with the modal identification fitting ellipse (the plot was mirrored for better convenience).	80
Figure 4.9 Amplitude and phase of the receptance in the frequency domain near the 2nd resonance of simulated case 7.	80
Figure 4.10 Receptance near the 2nd resonance of simulated case 7 (represented in the ‘Elliptical Plane’) with the modal identification fitting ellipse (the plot was mirrored for better convenience).	80
Figure 4.11 Schematic of the undamaged specimen experimental setup.	84
Figure 4.12 Test plate with force excitation point and response measurement locations.	84

Figure 4.13 Receptance curve in the 0 to 200 Hz frequency range – experimental curve and regenerated identified curves through the Elliptical Plane technique and the software BETAlab.85

Figure 4.14 Amplitude and phase of the receptance in the frequency domain near the 1st experimental resonance.....85

Figure 4.15 Receptance near the 1st experimental resonance (represented in the ‘Elliptical Plane’) with the modal identification fitting ellipse (the plot was mirrored for better convenience).86

Figure 4.16 Amplitude and phase of the receptance in the frequency domain near the 2nd experimental resonance.....86

Figure 4.17 Receptance near the 2nd experimental resonance (represented in the ‘Elliptical Plane’) with the modal identification fitting ellipse (the plot was mirrored for better convenience).86

Figure 4.18 Amplitude and phase of the receptance in the frequency domain near the 3rd experimental resonance.87

Figure 4.19 Receptance near the 3rd experimental resonance (represented in the ‘Elliptical Plane’) with the modal identification fitting ellipse (the plot was mirrored for better convenience).87

Figure 4.20 Amplitude and phase of the receptance in the frequency domain near the 4th experimental resonance.87

Figure 4.21 Receptance near the 4th experimental resonance (represented in the ‘Elliptical Plane’) with the modal identification fitting ellipse (the plot was mirrored for better convenience).88

Figure 4.22 Best-fitting ellipses using the LSF method in Equation (49) and the iterative method in Equation (52): (a) data set 1, and (b) data set 2.....94

Figure 4.23 Best-fitting ellipses using the LSF method in Equation (49) and the iterative method in Equation (52), after enforcing the limit to be between ± 1 : (a) data set 1, and (b) data set 2.....94

Figure 5.1 (a) Impactor; (b) Test support base.99

Figure 5.2 Left: Prepreg cutting process; Right: Pressuring process..... 101

Figure 5.3 Vacuum bagging..... 102

Figure 5.4 Autoclave: (a) when open; (b) when closed. 102

Figure 5.5 Curing cycle..... 102

Figure 5.6 Manufactured samples.....	103
Figure 5.7 The undamaged specimen experimental setup.	104
Figure 5.8 Receptance curve and phase plot of an undamaged quasi-isotropic composite laminate as seen in LabVIEW.	105
Figure 5.9 Static testing.	106
Figure 5.10 Work done by the impactor obtained from the static tests of specimen A.	107
Figure 5.11 Work done by the impactor obtained from the static tests of specimen B.	108
Figure 5.12 Work done by the impactor obtained from the static tests of specimen C.	108
Figure 5.13 Work done by the impactor obtained from the static tests of specimen D.	109
Figure 5.14 Work done by the impactor obtained from the static tests of specimen E.....	109
Figure 5.15 Work done by the impactor obtained from the static tests of specimen F and G.	110
Figure 5.16 A microscopic photograph: (a) impact surface, (b) damaged surface...	111
Figure 5.17 Changes in the modal frequency for plate A1.....	112
Figure 5.18 Changes in the modal damping for plate A1.....	113
Figure 5.19 Changes in the modal frequency for plate A2.....	114
Figure 5.20 Changes in the modal damping for plate A2.....	114
Figure 5.21 Changes in the modal frequency for plate A3.....	115
Figure 5.22 Changes in the modal damping for plate A3.....	115
Figure 5.23 Changes in the modal frequency for plate B1.	116
Figure 5.24 Changes in the modal damping for plate B1.	117
Figure 5.25 Changes in the modal frequency for plate B2.	118
Figure 5.26 Changes in the modal damping for plate B2.	118
Figure 5.27 Changes in the modal frequency for plate B3.	119
Figure 5.28 Changes in the modal damping for plate B3.	119
Figure 5.29 Changes in the modal frequency for plate C1.	120
Figure 5.30 Changes in the modal damping for plate C1.	121
Figure 5.31 Changes in the modal frequency for plate C2.	122

Figure 5.32 Changes in the modal damping for plate C2.	122
Figure 5.33 Changes in the modal frequency for plate C3.	123
Figure 5.34 Changes in the modal damping for plate C3.	123
Figure 5.35 Changes in the modal frequency for plate C4.	124
Figure 5.36 Changes in the modal damping for plate C4.	125
Figure 5.37 Changes in the modal frequency for plate D1.	126
Figure 5.38 Changes in the modal damping for plate D1.	126
Figure 5.39 Changes in the modal frequency for plate D2.	127
Figure 5.40 Changes in the modal damping for plate D2.	128
Figure 5.41 Changes in the modal frequency for plate E1.	129
Figure 5.42 Changes in the modal damping for plate E1.	129
Figure 5.43 Changes in the modal frequency for plate E2.	130
Figure 5.44 Changes in the modal damping for plate E2.	130
Figure 5.45 Changes in the Modal frequency for plate F1.	131
Figure 5.46 Changes in the Modal damping for plate F1.	131
Figure 5.47 Changes in the Modal frequency for plate G1.	132
Figure 5.48 Changes in the Modal damping for plate G1.	133
Figure 5.49 Modal parameters response to damage based on stacking configuration (1st test).	134
Figure 5.50 Modal parameters response to damage based on stacking configuration (2 nd test).	134
Figure 5.51 Modal parameters response to damage based on stacking sequence (3 rd test).	134
Figure 5.52 Modal parameters response to increased energy level in plate A1: (a) Modal frequency (b) Modal damping.	137
Figure 5.53 Modal parameters response to increased energy level in plate A2: (a) Modal frequency (b) Modal damping.	138
Figure 5.54 Modal parameters response to increased energy level in plate B1: (a) Modal frequency (b) Modal damping.	139
Figure 5.55 Modal parameters response to increased energy level in plate B2: (a) Modal frequency (b) Modal damping.	140
Figure 5.56 Modal parameters response to increased energy level in plate C1: (a) Modal frequency (b) Modal damping.	141

Figure 5.57 Modal parameters response to increased energy level in plate C2: (a) Modal frequency (b) Modal damping.	142
Figure 5.58 Modal parameters response to increased energy level in plate D1: (a) Modal frequency (b) Modal damping.	143
Figure 5.59 Modal parameters response to increased energy level in plate E1: (a) Modal frequency (b) Modal damping.	144
Figure 5.60 Linear trend for identifying the correlation between energy increase and modal parameters from Plate A1: (LHS) modal frequency (RHS) modal damping.	145
Figure 5.61 Linear trend for identifying the correlation between energy increase and modal parameters from plate A2: (LHS) modal frequency (RHS) modal damping.	145
Figure 5.62 Linear trend for identifying the correlation between energy increase and modal parameters from plate B1: (LHS) modal frequency (RHS) modal damping.	145
Figure 5.63 Linear trend for identifying the correlation between energy increase and modal parameters from plate B2: (LHS) modal frequency (RHS) modal damping.	146
Figure 5.64 Linear trend for identifying the correlation between energy increase and modal parameters from plate C1: (LHS) modal frequency (RHS) modal damping.	146
Figure 5.65 Linear trend for identifying the correlation between energy increase and modal parameters from plate C2: (LHS) modal frequency (RHS) modal damping.	146
Figure 5.66 Linear trend for identifying the correlation between energy increase and modal parameters from plate D1: (LHS) modal frequency (RHS) modal damping.	147
Figure 5.67 Linear trend for identifying the correlation between energy increase and modal parameters from plate E1: (LHS) modal frequency (RHS) modal damping.	147
Figure 5.68 Healthy Receptance amplitude and phase for plate A1 at 55Hz.	148
Figure 5.69 Damaged Receptance amplitude and phase for plate A1 at 55Hz.	148
Figure 5.70 Healthy ellipse for plate A1 at 55Hz.	148

Figure 5.71 Damaged ellipse for plate A1 at 55Hz.	149
Figure 5.72 Healthy Receptance amplitude and phase for plate B1 at 55Hz.	149
Figure 5.73 Damaged Receptance amplitude and phase for plate B1 at 55Hz.....	149
Figure 5.74 Healthy ellipse for plate B1 at 55Hz.	149
Figure 5.75 Damage ellipse for plate B1 at 55Hz.....	150
Figure 5.76 Variation in the area of the ellipse for Plates A1, A2 and A3.	150
Figure 5.77 Variation in the area of ellipse for Plate B1 and B2.....	151
Figure 5.78 Variation in the area of ellipse for Plate C1, C2 and C3.	151
Figure 5.79 Variation in the area of ellipse for Plate D1 and D2.	151
Figure 5.80 Variation in the area of ellipse for Plate E1.	152
Figure 5.81 Variation in the area of ellipse for plate F1.....	152
Figure 5.82 Variation in the area of ellipse for Plate G1	153
Figure 5.83 Comparison of Plate A1 modal damping from: (a) BETAlab; (b) Ellipse Method.....	154
Figure 5.84 Comparison of Plate A2 modal damping from: (a) BETAlab; (b) Ellipse Method.....	154
Figure 5.85 Comparison of Plate A3 modal damping from: (a) BETAlab; (b) Ellipse Method.....	154
Figure 5.86 Comparison of Plate B1 modal damping from: (a) BETAlab; (b) Ellipse Method.....	155
Figure 5.87 Comparison of Plate B2 modal damping from: (a) BETAlab; (b) Ellipse Method.....	155
Figure 5.88 Comparison of Plate C1 modal damping from: (a) BETAlab; (b) Ellipse Method.....	156
Figure 5.89 Comparison of Plate C2 modal damping from: (a) BETAlab; (b) Ellipse Method.....	156
Figure 5.90 Comparison of Plate D1 modal damping from: (a) BETAlab; (b) Ellipse Method.....	157
Figure 5.91 Comparison of Plate D2 modal damping from: (a) BETAlab; (b) Ellipse Method.....	157
Figure 5.92 Comparison of Plate E1 modal damping from: (a) BETAlab; (b) Ellipse Method.....	157

Figure 5.93 Comparison of Plate F1 modal damping from: (a) BETAlab; (b) Ellipse Method.....	158
Figure 5.94 Comparison of Plate G1 modal damping from: (a) BETAlab; (b) Ellipse Method.....	158

Dedication

I dedicate this thesis to the memory of my late grandfather, Alozie James LongJohn, who taught me how to be diligent in all my endeavours. To my grandmother, Madam Lily A. LongJohn, whose undiluted love and care solidified my zeal to excel.

*In loving memory of my cousin,
Late Prophetess Dodoba Marcus Iboroma, who passed away few weeks
to my final Viva.*

Nomenclature

2D	Two dimensions.
3D	Three dimensions.
ADSM	Absolute Difference of Strain Mode shapes.
AE	Acoustic Emission.
ANN	Artificial Neural Network.
AU	Acoustic-Ultrasonic.
BVID	Barely Visible Impact Damage.
CF	Composite Fibre.
CFRP	Carbon Fibre Reinforced Polymer.
CNT	Carbon Nanotubes.
CRF	Characteristic Response Function.
CWT	Continuous Wavelet Transform.
DaDI	Damping Damage Indicator.
DAQ	Data Acquisition Card
DFB	Distributed Feedback.
DLF	Damage Location Factor.
DOF	Degree-of-Freedom.
DRQ	Detection and Relative Damage Quantification.
DSCF	Damage Severity Correction Factor.
EMA	Experimental Modal Analysis.
EP	Epoxy.
FBG	Fibre Bragg Grating.
FE	Finite Element.
FML	Fibre Metal Laminate.
FRF	Frequency Response Function.
GFRP	Glass Fibre Reinforced Plastic.
GLARE	Glass Laminate Aluminium Reinforced Epoxy.
GMR	Giant Magneto-Resistive.
GNP	Graphite Nanoplatelets.
HHT	Hilbert-Huang Transform.
HTS-SQUID	High-Temperature Superconducting Quantum Interference Device

Analysis of the Response of Modal Parameters to Damage in CFRP Laminates using a Novel Modal Identification Method

IHAET	Induction Heating Assisted Eddy-current Testing
LDV	Laser Doppler Vibrometer
MDOF	Multiple Degrees of Freedom.
MFC	Macro Fibre Composite.
MNN	Modular Neural Network.
MSC	Mode Shape Curvature.
MuDI	Multi-parameter Damage Indicator.
NDE	Non-Destructive Evaluation
NDT	Non-Destructive Testing.
NEWS	Nonlinear Elastic Wave Spectroscopy.
NOFRF	Nonlinear Output Frequency Response Function.
ODS	Operational Deflection Shape.
OMA	Operational Modal Analysis.
PCA	Principal Component Analysis.
PSD	Power Spectral Density.
PZT	Piezoelectric Transducer / Piezoelectric lead-Zirconate-Titanate.
RC	Reinforced Concrete.
RVAC	Response Vector Assurance Criterion.
SDOF	Single Degree of Freedom.
SHM	Structural Health Monitoring.
SLV	Scanning Laser Vibrometry
SSP	Split Spectrum Processing
SQUID	Superconducting Quantum Interference Device.
SVM	Support Vector Machines.
TF	Transmissibility Function.
TNEWS	Transient Nonlinear Elastic Wave Spectroscope.
TRC	Textile Reinforced Cement.
QST	Quasi-Static Testing

Publications

The following publications were produced from this research work.

Journal Papers

1. Amafabia, D. M., Montalvão, D., David-West, O. and Haritos, G., 2019. Elliptical Method for Damage Identification in Carbon Fibre Reinforced Polymer Laminates. Submitted to *Advances in Materials Science and Engineering*; **2019, Article ID 5237129**.
2. Montalvão, D. and Amafabia, D. M., 2018. An alternative representation of the receptance: the 'elliptical plane' and its modal properties. *Mechanical Systems and Signal processing*; **103, 236-249**.
3. Amafabia, D. M., Montalvão, D., David-West, O. and Haritos, G., 2017. A Review of Structural Health Monitoring Techniques as Applied to Composite Structures. *Structural Durability & Health Monitoring*; **11(2), 91-147**.

International Conferences

1. Montalvão, D., Dupac, M., Amafabia, D. M., David-West O. and Haritos, G., 2018. On reducing uncertainty on the Elliptical Plane modal identification method. *In: VETOMAC'18 - 14th International Conference on Vibration Engineering and Technology of Machinery, 10th – 13th September 2018, Superior Technical Institute, Lisbon, Portugal*.
2. Amafabia, D. M., David-West, O., Montalvão, D. and Haritos, G., 2017. Damage detection in CFRP Composite Plates based on evolving Modal Parameters. *In BSSM'17 12th International Conference on Advances in Experimental Mechanics 29th – 31st August 2017 University of Sheffield, Sheffield, UK*.
3. Montalvão, D., Amafabia, D. M. and Silva, J.M.M., 2017. And yet another method for the identification of modal constants in experimental modal analysis. *In: IOMAC'17 – 7th International Operational Modal Analysis Conference, 10th – 12th May 2017, Ingolstadt, Germany*.

National Conference with Poster Presentation

1. Amafabia, D. M., David-West, O., Montalvão, D. and Haritos, G., 2019. Modal Parameters Response to Increased Energy Absorption in CFRP Laminates. *In: ECS'19 1st Engineering and Computer Science Research Conference, 17th April 2019, University of Hertfordshire, UK*.

Papers submitted to Peer-Reviewed Journals (currently under review)

1. Amafabia, D. M., Montalvão, D., David-West, O. and Haritos, G., 2019. Variations in the Modal Parameters due an Increased Impact Damage in Carbon Fibre Reinforced Polymer Rectangular Laminates. Submitted to ***Composite Structures*** [Under Review].

“The time will come when diligent research over long periods will bring to light things which now lie hidden. A single lifetime, even though entirely devoted to the sky, would not be enough for the investigation of so vast a subject... And so, this knowledge will be unfolded only through long successive ages. There will come a time when our descendants will be amazed that we did not know things that are so plain to them... Many discoveries are reserved for ages still to come, when memory of us will have been effaced.”

— Seneca, Natural Questions

1 Introduction

Structural Health Monitoring (SHM) is the process of detecting, locating and quantifying damage in structures for maintenance management to increase the life cycle of the structure [1,2]. Most processes are based on the identification of deviations from a “normal” or “healthy” condition. Ideally, deviations should be determined at an early stage of damage initiation and corrected by conducting suitable maintenance activities to avoid unexpected failure, thereby improving structural integrity, reliability and availability [3]. Composite materials have gained wide application in several industries with the aim of reducing the total weight of structures while increasing its mechanical properties such as strength and stiffness. Hence, the need to use SHM to detect damage at its incipient stage of initiation in composite materials is of high importance.

Composite materials have gained wide acceptance in industries such as aerospace, marine, automotive, civil infrastructures and sports equipment, due to their unique mechanical properties, namely strength and stiffness-to-weight ratios [3–7]. Composites result from the combination of two or more distinct materials to form a single material that has enhanced mechanical properties when compared to the individual properties of the constituent elements. In the particular case of composite laminates, these are composed of two or more layers that are laid up together [8], reinforced with aligned fibres [9] and a matrix, such as an epoxy resin, acting as a bonding medium.

However, during maintenance, assembling, or in use, a composite material is often subjected to low-velocity impacts which result in Barely Visible Impact Damage (BVID) [5,10]. This is due to the deficiency in the through-thickness properties of the composite laminate [11]. The impact on the surface would not show many visible marks, but a noticeable mark on the opposite side of the material which is usually not accessible through visual inspection. That could compromise the integrity of the composite material and reduce its life cycle. In fact, with the presence of BVID, the material would no longer be safe for use as its mechanical properties may have been compromised.

1.1 Aim

The overall aim of this research is to provide an understanding of how modal parameters relate to damage in Carbon Fibre Reinforced Polymers (CFRP) laminates.

1.2 Objectives

In summary, the objectives of this research are:

- Design and manufacture test specimens.
- Conduct static loading tests to introduce damage.
- Carry out vibration measurements of undamaged and damaged specimens.
- Analyse the results from both undamaged and damaged specimens.
- Develop an alternative method to represent the receptance (A new modal identification method) that can be used for SHM.
- Proposal of a damage identification method.

1.3 Contribution to Knowledge

- A novel method for the identification of the modal constants from FRFs, based on the dissipated energy per vibration cycle. It is mostly suitable for lightly damped system.
- It also offers a new perspective on the way the receptance may be represented, in a so-called ‘elliptical plane’, which may bring valuable insights for other researchers in the field.
- Other researchers focused on the effects of damage from a global perspective; this work studied the effects on the individual mode. The benefit of considering the local mode is that it offers a better representation of the damage location and its severity in a structure.

1.4 Research Outline

This thesis is divided into six chapters as follows:

Chapter 1 states the aim, objectives and the contribution to knowledge. This chapter provides the gateway to the research work.

Chapter 2 covers the damage identification procedures, SHM processes, and the literature review of the failure mechanisms and some of the up-to-date damage

identification techniques for composite structures. This chapter has been published in *Structural Durability & Health Monitoring* journal [12].

Chapter 3 highlights the manufacturing process of the test specimen for the research work, the basics of mechanics of composite materials and its failure mechanisms. An integral part of this chapter was published in *Structural Durability & Health Monitoring* journal [12].

Chapter 4 presented an alternative method to represent the receptance. It presents a novel method (Elliptical Plane) for the identification of modal parameters. It also explores ways to minimise the uncertainty on the Elliptical Plane modal identification method. This chapter was published in *Mechanical Systems and Signal processing* journal and presented at *the IOMAC'17, Ingolstadt, Germany and VECTOMAC'18, Lisbon, Portugal* [13–15].

Chapter 5 shows the experimental measurements and result from the analysis. In this chapter, both BETAlab software and the Elliptical Method, for modal identification was used to analyse the test data. This chapter has been presented at the *BSSM'17, University of Sheffield, United Kingdom; ECS'19, University of Hertfordshire, United Kingdom* [16,17], and some part of the work has been published in *Advances in Materials Science and Engineering* and submitted to *Composite Structures* journals for publication.

Chapter 6 summarises the findings in the research work and present suggestions for future works to be conducted.

“Engineering problems are under-defined, there are many solutions, good, bad and indifferent. The art is to arrive at a good solution. This is a creative activity, involving imagination, intuition and deliberate choice.”

— Ove Arup

2 Review of Literature

2.1 Introduction

The outstanding importance of composite laminates cannot be overemphasised. It has taken a noticeable place in the technological applications, due to its stiffness-to-weight ratio and strength, when compared to metals. Industries such as aviation, automobile, construction, petroleum, marine and nuclear energy, has increasingly used it.

However, despite the numerous advantages of composite laminates, it still has several limitations. The limitations are its failure mechanisms such as matrix cracking, fibre fracture, debonding, delamination, fibre pull-out, micro-buckling, and kink band.

Failures do not take place without a trigger that may be a chain of unattended critical events. Different types of failures occur in CFRPs due to impact loads. Although high, medium and low energy impact affects composite materials, it is more susceptible to low and medium velocity impact [5]. To design a better SHM technique, it is necessary to investigate the root causes of the failure mode.

Several non-destructive techniques such as ultrasound, X-ray, visual inspection, acoustic emission, and eddy-current have been used for SHM [18]. However, none of these techniques has a perfect solution for SHM of composite structures; they all have their peculiar advantages and limitations. Over the years, SHM has evolved and prompted the development of an online method for monitoring. These methods are primarily based on information from smart materials, mechanical properties, image processing, statistical pattern recognition, and optical fibres [18].

This chapter presents a review of the literature on some of the existing techniques for damage detection in composite materials, with their advantages and limitations. A summary of the damage identification techniques in CFRPs are presented in a tabulated format for easy reference.

2.2 Damage Identification Procedures

According to Rytter [19], there are four steps of damage identification procedures:

- i. Determine the presence of damage in the structure.

- ii. Determine the damage location in the structure.
- iii. Determine the severity of the damage in the structure.
- iv. Predict the remaining useful life of the structure.

Damage identification and localisation in structures require the prior knowledge of the state of the undamaged structure [20], in order to detect any deviations in the chosen damage indicators from the experimental results. The presence of damage and its location in a structure is determined by global and local diagnosis respectively.

2.3 The Process of SHM

Sohn *et al.*[21] investigated the issue associated with the detection of damage in the context of statistical pattern recognition paradigm [22]. The paradigm was expressed as four processes, namely:

- i. Operational evaluation.
- ii. Acquisition of data, fusion, and cleansing.
- iii. Extraction of features and condensation of information.
- iv. Statistical model development for feature discrimination.

Section 2.3.1 to 2.3.4 focused on the review by Sohn *et al.*[21] and the work presented by Farrar *et al.*[22]; a flow chart for conducting SHM process can be found in [22].

2.3.1 Operational Evaluation

An operational evaluation process in SHM provides answers to damage detection process, such as failure mode for the monitored system, the operational and environmental conditions at which the monitored system functions, the limitations on data acquisition from the system in operation and the economic related concerns [22]. Recently, Tjirkallis and Kyprianou [23] used the correlation between maxima decay lines of the continuous wavelet transform (CWT) of the stress waves from the monitored system under varying operational and environmental conditions. Although the proposed method was effective in identifying damage in a system, further work is required to apply the method continuously for days to a healthy system with an initially induced crack growth.

2.3.2 Acquisition of Data, Fusion and Cleansing

Data acquisition process focused on choosing a suitable sensor(s) to actuate/acquire stress in a structure, appropriate position to mount sensors, required number of sensors, and hardware for data acquisition, storage, and analysis. These decisions are usually influenced by the economic situation and vary from one application to another. Another consideration is data acquisition intervals. Depending on the criticality of the system and the nature of the damage being monitored; data could be collected at periodic intervals or continuously at specified short intervals to get a piece of broad information about the damage.

Data fusion is the process of harmonising data acquired from the system with the different sensors damage detection process. To get the global information about a structure, multiple sensors are sometimes mounted at several locations on the structure to acquire stress waves. The data collected from the different sensors are integrated to ease measurement. It is, therefore, necessary to be able to filter the data from the stream of data acquired and collect the useful data/reject the unwanted data in the feature selection process. This process is known as data cleansing.

2.3.3 Extraction of Feature and Condensation of Information

Feature extraction enables the differentiation of undamaged and damaged structure based on the damage sensitive properties acquired from structure monitored [21,22]. It is necessary to compress the information acquired as the quantity of data becomes very large. Data condensation becomes necessary when several sets of data over the lifecycle of a structure are to be compared. This process increases the level of accuracy of the estimates of the feature's statistical distribution.

2.3.4 Statistical Model Development

When statistical model development algorithm uses the data acquired from both the undamaged and damaged structures to determine the health of the structure, it is referred to as supervised learning [20–22].

Algorithms that are applied to data that are not consisting of examples from the defective structure is referred to as unsupervised learning [21]. According to Sohn *et al.*[21], some of the supervised learning methods are neural networks, linear discriminants, surface analysis and genetic algorithms. On the other hand, examples of unsupervised methods are control chart analysis and novelty detection methods [21]. In addition, one necessary issue in statistical model development is to create the sensitivity of the model features to the presence of defect to eliminate false damage recognition. In this case, misleading results such as false positives (i.e. detected undamaged sample identified as damaged), or false negatives (i.e. undetected damaged samples identified as healthy).

2.4 An Overview of Damage Identification in Composite Materials

Many techniques have been developed over the years to detect damage at an early stage in composite materials. However, it is not possible to have a single technique that can be effective for all loading conditions, material constitution and failure mode. All techniques have their own advantages and limitations. The application of a technique can be based on the criticality of the equipment, available resources, and skilled personnel to apply it.

The aim is to increase the reliability and availability of equipment with the available damage detection technique at the lowest cost without compromising standards. This research work, is based on vibration technique and as such more attention will be given to vibration-based methods. Because, unlike other techniques, vibration-based techniques offer a clearer and precise information about the state of a structure based on the dynamic properties of the structure. In this section, a critical review of some of the damage identification techniques is presented.

2.4.1 Vibration-based

Most vibration-based methods are based on the relationship between the change in the state of the structure and the change in its vibration response. That is, the change in the dynamic properties of the structure may be related to the presence of damage. For instance, the presence of damage in a structure may alter properties such as the stiffness and strength. Since dynamic models may be described from structural properties of

mass, stiffness, and damping, then it is plausible to presume that the vibration responses of the structure at an undamaged state will differ from the damaged state. Hence, it is often necessary to have a prior knowledge of the vibration responses of the undamaged structure to use as a set standard. Vibration-based SHM for damage detection is time-saving and relatively cost-effective. It can also be applied in real-time monitoring of structures.

According to Maia and Silva [24], the dynamics of a system with N -degree of freedom (DOF) can be illustrated with either spatial, modal or response model – that can be linked to each other by either forward or inverse paths [25].

The dynamic characteristics of a structure, are couched in a spatial distribution of mass, stiffness, and damping properties represented in terms of matrices of mass $[M]$, stiffness $[K]$, and damping $[C]$ (for a viscously damped model) or $[D]$ (for an hysteretically damped model) [25]. Let each DOF be expressed by a coordinate $x_i(t)$ with an applied force $f_i(t)$ where $i = 1, 2, 3, \dots, N$ DOFs, then the model can be illustrated using the Newton's second law of motion for hysteretically damped system as:

$$[M]\{\ddot{x}(t)\} + [K]\{x(t)\} + i[D]\{x(t)\} = \{f(t)\} \quad (1)$$

For a viscously damped system, it is modelled as:

$$[M]\{\ddot{x}(t)\} + [C]\{\dot{x}(t)\} + [K]\{x(t)\} = \{f(t)\} \quad (2)$$

It is quite difficult to deal with the viscously damped model illustrated in Equation (2), when damping is non-proportional [24]. It is worthy to note that, in real cases viscous or hysteretic damping is non-proportional. However, to solve the Equations, it is often useful to consider the approximation that it is proportional, as it eliminates coupling and we get a diagonal matrix. Hence, proportional damping can be assumed as a special case of damping and it suggests that the damping matrix is a linear combination of the mass and stiffness matrices. In the case of the hysteretic damping, this is:

$$D = a[M] + b[K] \quad (3)$$

where a and b are real scalars. This kind of damping model is also known as classical damping or Rayleigh damping. The dynamic behaviour of structures that are subjected to varying loading is usually illustrated with constant hysterical damping model. Hence, the Equation of motion will be based on the hysteretic damping. Supposing there is a general solution of the form:

$$\{x(t)\} = \{\bar{X}\}e^{i\lambda t} \quad (4)$$

where $\{\bar{X}\}$ is an $N \times 1$ vector of time-dependent response amplitudes, and replacing it into Equation (1), we will have:

$$[[K] - \lambda^2[M] + i[D]]\{\bar{X}\} = \{0\} \quad (5)$$

which is a complex eigenvalue problem, when solved results in the solution described by N complex eigenvalues λ_r^2 and N real eigenvectors Φ . The λ_r^2 have information on the natural frequencies of the system and Φ contains information on the mode shapes. The complex eigenvalue λ_r^2 can be defined as:

$$\lambda_r^2 = \omega_r^2(1 + i\eta_r) \quad (6)$$

where η_r and ω_r are the damping loss factor and natural frequency, respectively, for mode r . It is possible to link the spatial model with the modal model by orthogonality conditions of the modal matrix:

$$[\Phi]^T[M][\Phi] = [I] \quad (7)$$

$$[\Phi]^T[K] + i[D][\Phi] = [\lambda_r^2] \quad (8)$$

where $[I]$ represents the identity matrix, $[\Phi]$ is the mass-normalised mode shape matrix. This implies that the mode shape matrix is a non-singular invertible matrix [25]. Hence, a spatial description of the model can be obtained from the modal model and conversely.

However, instead of that, a response model described by Frequency Response Functions (FRFs) is obtained. Considering the frequency domain in a steady state, the FRF $H(\omega)$ can be determined for each frequency ω :

$$H(\omega) = \frac{X(\omega)}{F(\omega)} \quad (9)$$

where $X(\omega)$ and $F(\omega)$ represents the complex response and the complex force respectively. Also, the FRF can be referred to as receptance, mobility, or accelerance, based on the complex response being prescribed as displacement, velocity, or acceleration, respectively. These quantities can be linked with each other by differentiation and integration. According to Maia and Silva [24], for the case of receptance, the relationship between the response model and the modal model is:

$$[\alpha(\omega)] = [\Phi][\lambda_r^2 - \omega^2]^{-1}[\Phi]^T \quad (10)$$

where $[\alpha(\omega)]$ is the receptance matrix. Hence, starting with a spatial model a response model was obtained after going through an intermediate modal model. This sequence is normally executed when theoretical analysis is the starting point. Nonetheless, if the complexity of systems is such that it is difficult to model it analytically, the inverse method should be followed where the starting point is the response model with the experimental evaluation of the system FRFs. There are several methods that allow the extraction of the modal characteristics of a system from the experimentally obtained response model [24]. The procedure is known as modal identification. Figure 2.1 shows the relation between spatial, modal and response models.

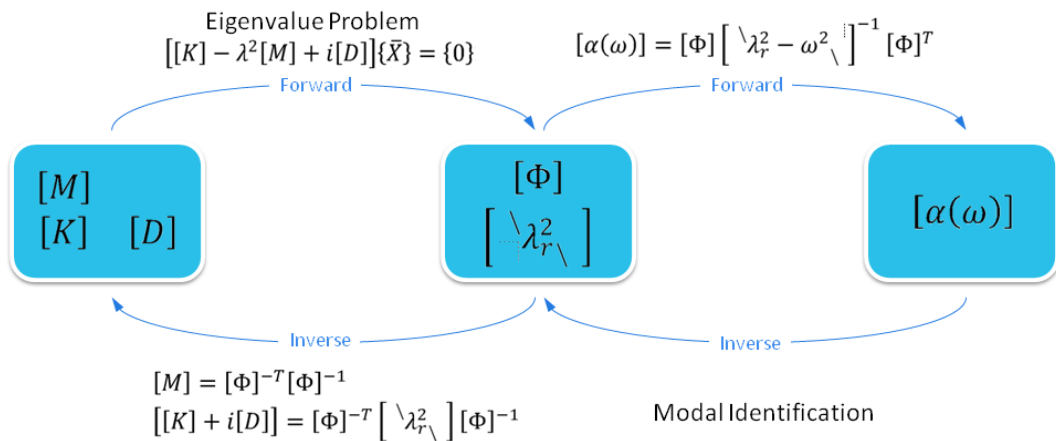


Figure 2.1 Dynamic models interrelation (hysteretic damping case) [25].

Each term of the receptance matrix in Equation (10) would be of the form:

$$\alpha_{jk}(\omega) = \frac{\bar{X}_j}{F_k} = \sum_{r=1}^N \frac{r\bar{A}_{jk}}{\omega_r^2 - \omega^2 + i\eta_r\omega_r^2} \quad (11)$$

where \bar{X}_j is the complex response amplitude in the j coordinate and F_k is the amplitude of the applied force in the k coordinate.

2.4.1.1 Modal Strain Energy

Ooijevaar *et al.*[26] investigated a vibration-based damage identification method known as the modal strain energy damage index algorithm. The method was applied to composite T-beams that are vibrating under bending and torsional mode, to detect and localise delamination. A Laser Doppler Vibrometer (LDV) was used to determine the FRFs between the point of excitation and the measurement points along the test specimen. The authors obtained the modal parameters (modal damping factors, natural frequencies and mode shapes) from the FRF measurements using Experimental Modal Analysis (EMA). The results show that the measurement of changes in natural frequencies of the bending mode can be used to detect damage in the specimen. However, the sensitivity of the damage index depends on the distance between the delamination and the measuring points. They affirm that as the number of measurement points reduces, the sensitivity of the damage index to detect damage at some distance from the measurement points is affected.

2.4.1.2 Frequency Method

Although the frequency response measurement method can be used to detect relatively small damage in a simple structure, it cannot be generally used on its own to provide information about the type, size, location, and orientation of damage [27].

Kim [28] identified damage in both laminated composites and sandwich composite beams using the reconstructed residual FRF-based damage identification method. The method is based on the differences between the FRFs of damaged and undamaged test structures. It was found that the changes in the natural frequencies and modal damping ratios of a composite structure can be used to identify debonding or delamination because the FRFs are noticeably affected by the global changes in stiffness and

damping due to the delamination in the composite structure [28]. However, the damage indicator based on the measured FRF-curve area is not consistent. The FRF-curve area is the potential energy density of the structures based on the assumption of unit inertial energy density [28].

Manoach *et al.*[29] investigated nonlinear vibration models to study the impact of damage on the vibration response of structures with varied temperatures. The damage detection method was based on Poincaré maps of responses, which is a standard tool used for dynamic systems inspection [29]. The authors confirmed from their results that damage can affect the time domain response of a beam and that a change in temperature leads to a nonlinear change in the dynamic response of the beam. A useful aspect of this method is that the prior knowledge of a reference healthy state of the structure is not required.

Herman *et al.*[30] used wavelets [31] to detect damage in composite T-stiffened panels, which are often used in the aviation industry and other light structures. A scanning LDV was used to measure the displacements and mode shapes induced by elastic stress waves at different frequencies [30]. They followed a typical approach whereby any deviation in the modal properties between the undamaged and damaged states is used to detect and localise damage. They conducted both numerical and experimental analysis and found correlations between the modal parameters and the presence of damage, either in the form of cracks or porosity.

Pérez *et al.*[32] studied the possibility of using vibration-based techniques to detect low impact damage in composite laminates. The authors assessed and compared four modal-based damage indicators (frequency shift, mode shape change, curvature mode shape change and residual load-bearing capacity) by comparing results from undamaged and damaged states. Additionally, their study investigated the effectiveness of the damage indicators in detecting damage, its location, and the damage progression in the test specimen. They found that relative changes in the natural frequencies are smaller than those observed for mode shapes. However, they also noted that the sensitivity of the damage indicators depends on the number of measured coordinates (DOFs) and the number of mode within the measurement frequency range.

Wang *et al.*[33] conducted numerical analysis on anisotropic composite laminate plates and examined the impact damage had on the vibration characteristics. Damage was modelled as a local reduction of the stiffness. The severity of damage, damage anisotropy (the ratio of the reduction of stiffness in each direction to the reduction of stiffness in the longitudinal direction) and damage location, were the damage features used to describe different damage scenarios in the composite structure [33]. The dynamic governing Equation was established based on classical theory and the perturbation method was used to obtain analytical solutions. An FEA was conducted to verify the effectiveness of their proposed method. The results show that the impact on the vibration characteristics of the three damage features is not similar.

Unlike the modal curvature and strain energy, the natural frequencies and modal displacements are less sensitive to damage. The numerical results indicate that:

- Damage in the longitudinal direction has the highest impact on the vibration response when compared to other directions
- Damage has more impact on the vibration characteristics when it is away from nodal lines
- An increase in the severity and size of damage results in a reduction in the natural frequencies and modal strain energy.

Wang *et al.*[33] suggested that the perturbation-based vibration analysis developed can be used to assess the impact of damage on the vibration characteristics of anisotropic plates and also detect damage in laminated plates.

Many other vibration-based methods use aspects of the vibration response. Since these are very vast, it was decided to further discuss them in different independent sections, as is the case of transmissibility-based methods.

2.4.1.3 Transmissibility

Transmissibility analysis has gained a lot of attention in the past decade due to its simplicity of implementation, as it uses conventional vibration transducers and does not require that the loading conditions are known. In simple terms, the ratio between two measured outputs (responses at different coordinates) is known as the transmissibility

function (TF) [34,35]. Among other types of frequency domain system identification methods, some authors argue that the transmissibility response methods are more sensitive to local variations in the structure: it is suitable for output-only data from the structure and it is sensitive to local structural changes [35,36]. In other words, transmissibility does not consider the excitation force (input data); rather it uses only responses (output data). Therefore, since it does not require the loads to be known, it can be considered as a case of the broader area of operational modal analysis (OMA), tackling at least one issue from EMA. Among the first to explore the concept of Transmissibility in Multiple Degree of Freedom (MDOF) systems is Ribeiro *et al.*[37–39].

In order to reduce or eliminate human error and cost during data collection from structures, Yi *et al.*[40] developed mobile sensors to detect damage in civil structure and transmit it to a computer for processing. They used TF analysis to process the data extracted from the structure by the mobile sensors, to detect damage in the structure. The proposed technique showed to can locate damage under certain circumstances. Furthermore, not many sensors are needed, and it does not require extensive human effort to operate. However, the authors agreed that more study is required to enable the mobile sensors to detect a wider range of other potential damages in the structure.

Lang *et al.*[41] developed a nonlinear output FRF (NOFRF) transmissibility-based technique to detect and locate linear and nonlinear damage in MDOF structures. The concept of NOFRF was proposed to analyse nonlinear systems in the frequency domain [42]. Lang *et al.*[41] defined the concept of transmissibility of the NOFRF as the ratio of the maximum order NOFRF linked with two varying output responses of concern in a nonlinear system. They conducted both experimental and numerical studies to validate the technique. Results show that the technique is effective, and it can be used for both detection and localisation of damage in real structures. The technique depends only on the linear characteristics of the system; hence does not change with the system's inputs.

According to Devriendt and Guillaume [43], it was not always feasible to use transmissibility measurements to identify modal parameters. However, since the transmissibility changes with the location of the input forces, it can be used to determine

the system's poles [43]. The authors could identify the modal parameters of a structure by combining transmissibility measurements under various loading conditions. The loading conditions were achieved by a change in ambient forces or by using an impact hammer to apply forces at different locations on the test specimens [43]. Unlike the classical output-only techniques, the transmissibility-based method does not require the operational forces to be white noise; it can be a swept sine, coloured noise, impact, etc [43,44].

Similarly, Devriendt *et al.*[34] detected and located damage frequency domain TFs. They suggested the use of small frequency bands only that are close to the resonance frequencies of the structure to determine damage. In addition, the required frequency band should be selected to improve the reliability of the method. Both numerical and experimental results were presented to validate the technique of damage detection.

Sampaio *et al.*[45] summarised the concept of transmissibility and used it to detect and localise damage in structures. In their work, the special case of the transmissibility matrix for an MDOF. They assumed that forces are applied at a given subset A only, of all the coordinates measured, M. Hence, the response at coordinate i can be determined from:

$$X_i = \{H_{iA}\}^T \{F_A\} \quad (12)$$

The remaining M-I responses will be attained from:

$$X_{M-i} = [H_{M-i,A}] \{F_A\} \quad (13)$$

Adding *Equations (12) and (13)*, we obtain:

$$X_i = \{H_{iA}\}^T [H_{M-i,A}]^{-1} \{X_{M-i}\} \quad (14)$$

According to Equation (14), each response X_i is given by a linear combination of the remaining response $\{X_{M-i}\}$. Such relationship represents a transmissibility [45]:

$$\{T_{M-i}\}^T = \{H_{iA}\}^T [H_{M-i,A}]^{-1} \quad (15)$$

The number of remaining coordinates M-I must be greater or equal to the number of coordinates A. For example, if there are three response coordinates (M=3) and two force coordinates (A=2). For each coordinate, Equation (14) results to:

$$\begin{aligned} X_1 &= T_{12}X_2 + T_{13}X_3 \\ X_2 &= T_{21}X_1 + T_{23}X_3 \\ X_3 &= T_{31}X_1 + T_{32}X_2 \end{aligned} \quad (16)$$

If zero is added to each transmissibility vector at each i^{th} column, we obtain:

$$\begin{Bmatrix} X_1 \\ X_2 \\ X_3 \end{Bmatrix} = \begin{bmatrix} 0 & T_{12} & T_{13} \\ T_{21} & 0 & T_{23} \\ T_{31} & T_{32} & 0 \end{bmatrix} \quad (17)$$

where $[T]$ is the transmissibility matrix as a function of the frequency that relates itself with all the set of measured responses contained in the response vector $\{X\}$. It is like *auto-transmissibility* [45]. The presence of damage in the structure would indicate variation in $[T]$, and it will become T^d . The ‘ d ’ stands for damage. Their work was focused on damage detection and localisation. The authors presented a graphical display of the undamaged $[T]$ and damaged T^d for each frequency to make it feasible to visually detect any deviation in the transmissibility coefficients that revealed the presence of damage in the structure.

According to Sampaio *et al.* [45], the global matrices for the healthy and damaged cases can also be obtained by summing up all the frequency range. They assert that, although the damage location can be revealed by summing up the changes between the transmissibility maps for all the frequencies, the wide difference that can ensue near the resonances and anti-resonances will affect the process. From their results, it is shown that the method they presented has the potential for both damage detection and localisation. However, the limitation was prevented by counting how many times the differences in the maximum transmissibility occur in each structural element.

Maia *et al.* [18] proposed the use of the transmissibility response function to detect and quantify the severity of damage. They conducted numerical simulations and compared the results with those obtained from FRFs. The authors also validated the proposed

method with experimental testing. It was confirmed that the transmissibility is sensitive for the detection and quantification of the damage extension.

Devriendt and Guillaume [44] conducted a numerical experiment on a cantilever beam and compared the results from input-output modal analysis based on FRFs and output-only responses based on transmissibility measurements. It was observed that the correct system poles can be identified starting from only the transmissibility measurements.

Maia *et al.*[46] proposed the use of transmissibility with detection and relative damage quantification indicator (DRQ) to detect damage in structures. A DRQ value of 1 or 0 means no damage or damage exist respectively. To conduct the experiments, the responses were measured with seven accelerometers mounted on a beam at different locations. Two shakers were used to excite the beam and two force transducers were used at the excitation coordinates to measure the applied forces. The level of force applied on the beam was changed through various rounds of tests. The effectiveness of the DRQ depends on the Response Vector Assurance Criterion (RVAC) between the damaged and undamaged response vectors. Since the load applied to a structure determines the response generated, a correlation that does not depend on load is required. Transmissibility was used to generate curves that are not dependent on the applied loads when there was no damage in the beam. As damage increases, the DRQ value reduces below 1 sharply.

Maia *et al.*[18] compared the results of the DRQ and the transmissibility damage indicator (TDI) from numerical and experimental results. The two indicators are based on the RVAC correlation factor. It was observed that the TDI detects and quantify damage better than the DRQ. In addition, the more the measurement coordinates for each applied force, the better the results achieved with TDI.

More recently, Li *et al.*[47] developed a technique that is based on transmissibility response measurements to detect and identify the changes in structural damping and stiffness. They investigated the effects of the local variation in stiffness and damping on the TFs and observed that there is a considerable difference between the input force and the variation in stiffness and damping. The authors developed a new damage indicator that is based on the differences between TFs before and after the variations in

stiffness and damping. Several simulations were conducted to validate the damage detection indicator. In addition, factors such as the position of the applied force, frequency bandwidth and boundary conditions were determined to influence the performance of TFs [47]. The proposed damage indicator was shown to be effective in the detection of variations in both damping and stiffness.

Zhou *et al.* [36] proposed the use of power spectral density (PSD) transmissibility by conducting a numerical simulation with a cantilever beam. The mechanical stiffness was reduced in certain elements to simulate damage. The authors excited the damaged and undamaged beams at a centre node using a simulated impulse force spectrum. In their study, the results show that the proposed method can detect minor damages in the beam. It is also suggested that it can possibly be applied to real structures undergoing random excitation.

To solve the problems associated with the use of multiple sensors in condition monitoring, as is the case of wind turbines, Zhang *et al.*[48] proposed the use of the TF. This is to circumvent the conventional practice of using multiple sensors to determine the conditions at varying positions, which can be a quite tedious procedure. Nevertheless, the authors used transmissibility response measurements to generate a single damage indicator (correlation-based TDI). Both numerical simulations and experimental data were analysed to verify the capability of the proposed method.

2.4.1.4 Damping

According to Keye *et al.*[49], the modal damping factors may be a more sensitive parameter to damage in delaminated composite structures than the natural frequencies. For example, in order to grasp the correlation between modal parameters and the level of damage in composite materials, Shahdin *et al.*[50] conducted an impact test on Carbon Fibre (CF) entangled sandwich materials to understand the correlation between the damage level density and modal parameters. They conducted vibration tests on damaged and undamaged specimens, monitored the changes in the modal damping factors before, and after the damage was initiated. Heavy and light entangled sandwich materials were used. The heavy specimens have 2.5 times more resin than the light specimens do. The results indicated that due to the better damping characteristics, the light materials are more sensitive to damage compared to the heavy materials. It was

concluded that damping shows more sensitivity to damage than changes in stiffness. Therefore, it is suggested the use of damping as a damage indicator for SHM purposes in composite materials [50].

Montalvão *et al.*[51] proposed the use of the Damping Damage Indicator (DaDI) based on changes in the modal damping factors between undamaged and impact damaged CFRP laminates for the localisation of damage. The authors claim that this is a cost-effective approach since only two transducers are needed. However, more transducers may be necessary to improve the reliability of the modal identification process. Since this is an EMA based method, a force transducer is required to measure the force at the excitation coordinate. A Laser Doppler Velocimetry (LDV) was used to measure the responses at four different coordinates. However, the uncertainty involved in the modal identification process of the modal damping factors still constitutes a hindrance to its application.

In order to circumvent the problem with the identification of the modal damping factors in lightly damped structures, Montalvão *et al.*[5] proposed a Multi-parameter Damage Indicator (MuDI) that makes use of a weighted combination of both the modal damping factor and natural frequency changes. They introduced damage in two different sets of CFRP laminate plates with different layups (quasi-isotropic and orthotropic). Damage was introduced following a quasi-static approach [11,52–56] and was measured based on the quantity of energy released during the procedure. The results from numerical simulations and experimental tests show that there is a good agreement between the MuDI and damage in the composite laminates. In another work, it was also found that as the damage progressively increases, the modal damping factors increases too [6]. However, the authors observed that despite the approximately direct proportionality relationship between structural damping and damage, the changes of the individual modal damping factors are not easy to determine.

In an attempt to enhance the precision of the assessment of the modal damping factors, Montalvão and Silva [57] have recently proposed a novel method that is based on the amount of energy released per cycle of vibration of a material. To determine the effectiveness of the method, both numerical and experimental studies were conducted. The results of their study show that the proposed method is appropriate for lightly

damped systems having well-spaced mode[57]. Despite that, it has not yet been shown if this improves or not the accuracy of the location of the damage in CFRPs when using either the DaDI or the MuDI.

Gonilha *et al.*[58] presented modal identification experimental tests on a GFRP-concrete hybrid footbridge prototype that is made of a thin fibre reinforced deck and two GFRP girders. First, they excited the deck with an impact hammer and measured the FRFs. Next, they determined the mode shapes, vibration mode frequencies, and damping ratios using input-output modal identification based on the method of rational fraction polynomial, and output-only response data. Finally, they compared the experimental data with both analytical and numerical simulations to determine the effectiveness of the simulation tools for GFRP-concrete structures. They confirmed that the comparison of experimental data with both analytical and numerical simulations indicates that these models are suitable for the earlier stage of design to detect possible damages on time.

Kiral *et al.*[59] studied the effect of impact failure on the damping ratio and natural frequency of woven-epoxy beams. In their work, different sizes of damage at different locations on the beam were introduced by impact tests. A non-contact vibration measurement system was used to record the free vibration responses, and the damping ratios were determined using the exponent of the free vibration envelope and logarithmic decrement. Their results show that the damping ratio increases as the damage level increases and the natural frequencies are less sensitive to damage.

2.4.1.5 Lamb Waves

Lamb waves for damage detection have been used for decades and have received much attention from researchers. The application of Lamb waves for damage detection in composite materials commenced between the late 1980s and early 1990s [3]. For example, Su *et al.*[60] reviewed Lamb wave based damage detection methods for composite materials. They also discussed the propagation mechanisms of Lamb waves in composite materials, modelling and simulation, selection of the relevant mode, data collection and signal processing.

Lamb waves can be described as elastic disturbances that travel through thick solid plates without a significant decay in intensity [61]. The two types of Lamb wave mode are symmetric (S_o) and antisymmetric mode (A_o). Kessler *et al.*[3] used Lamb waves for the detection of matrix cracks, delamination, and through-thickness holes in graphite/epoxy composite test specimens. The strength of penetration of Lamb waves through a material is easily determined by their dispersion curves. The curves show the plot of phase velocity versus excitation frequency and the group velocity versus the excitation frequency. The curves are generated from the antisymmetric Lamb waves solution [3]:

$$\frac{\tan(\bar{d}\sqrt{1+\zeta^2})}{\tan(\bar{d}\sqrt{\xi^2+\zeta^2})} + \frac{(2\zeta^2-1)^2}{4\zeta^2\sqrt{1-\zeta^2}\sqrt{\xi^2-\zeta^2}} = 0 \quad (18)$$

where ξ , ζ , and \bar{d} are the non-dimensional parameters used to describe Lamb wave propagation in isotropic materials. The non-dimensional parameters are stated as:

$$\xi^2 = \frac{C_t^2}{C_l^2}; \zeta^2 = \frac{C_t^2}{C_{phase}^2}; \bar{d} = \frac{k_t t}{2} \quad (19)$$

where c_t , c_l , c_{phase} , k_t and t are transverse (shear) wave velocity, longitudinal (pressure) wave velocity, phase velocity, wave number, and time, respectively. These velocities depend on the material properties and can be defined by Lamé's constants [62]:

$$\mu = \frac{E}{2(1+\nu)}; \lambda = \frac{E\nu}{(1-2\nu)(1+\nu)} \quad (20)$$

$$c_t^2 = \frac{\mu}{\rho}; c_l^2 = \frac{(\lambda+2\mu)}{\rho}; k_t = \frac{\omega}{c_t} \quad (21)$$

where ν is the Poisson's ratio, ρ is the density, ω is the angular frequency, E is Young's modulus and μ and λ are the Lamé's constants. These Equations are important because they show that the Lamb waves propagation mechanisms ultimately depend on the constituent material properties, the reason why they have been proposed by some authors to be used as SHM sensitive features. The results obtained from Kessler *et al.*[3]

experiments indicate that Lamb waves are more sensitive to the local impact of damage in composites when compared to the use of FRFs, as they can provide more information on the characteristics of incipient damages. Lamb wave based damage detection methods provides better information at low frequencies than at high frequencies, typically in the range of 1 to 10MHz [63]. Despite their capability to detect damage, they have some limitations. An active driving system is required to propagate the waves through the structure and the data is relatively complex to interpret [3]. However, they are suitable for the *in situ* detection and location of damage in composite materials, and can possibly locate damage due to the nature of their local response [3]. Cawley and Alleyne [64] discussed how to excites and receives suitable Lamb mode(s) for better data representation.

Diamanti *et al.*[65] inspected a monolithic and sandwich composite beam. The authors generated A_o mode at 15 kHz and 20 kHz using piezoelectric transducers (PZT) and further applied to the identification of delaminations, matrix cracking, and broken fibres. The results indicated that damage in the sandwich composite beam and CFRP beam were detected and located effectively. However, they suggested the combination of Lamb waves and ultrasonic C-scan techniques to quantify the damage.

Yang *et al.*[66] adopted finite element models with explicit dynamic analysis to investigate excitation, data collection methods and transport phenomenon of Lamb waves through composite materials. They used various models of piezoelectric actuator/sensors to measure effective shear forces, effective displacements and effective bending moment excitation mode. The numerical simulations show that the adopted models for both S_o and A_o mode produce consistent results. Nonetheless, even if the sensor model was not suitable for the shear horizontal mode, it was able to determine the symmetric and antisymmetric Lamb wave mode.

Ng and Veidt [67] proposed the use of an *in situ* method based on Lamb waves technique to monitor and locate damage in fibre reinforced composite laminates. The exact location was detected through a graphical representation. They scanned damaged and undamaged specimens using networks of transducers. The cross-correlation between the excitation pulse and the envelope of the scattered signal was analysed to reconstruct a damage localisation image. The obtained results indicated that the

proposed technique could effectively detect and locate damages that are within the area of the network of sensors in the composite laminates

With the intent of increasing the effectiveness and accuracy of Lamb waves for the identification of delamination in composite laminates, Hu *et al.*[68] examined the impact of the Lamb waves excitation frequency on the strength of the signals reflected due to delamination in CFRP laminates. In their research, the authors chose the A_0 mode to enable them to detect minor damages. Since within a low-frequency band the wavelength of the A_0 mode is smaller than the wavelength of the S_0 mode, A_0 mode is more sensitive to minor damages such as transverse cracks and delamination in the composite laminates [3,68,69]. Hence, Hu *et al.*[68] investigated the generation and relationship of the A_0 wave mode with the delamination at various frequencies. It was confirmed that there was at least one optimal excitation frequency that produces the reflected signals with the highest intensity from the delamination. The results revealed that the optimal excitation frequencies are all within the range of the natural frequencies of the local delaminated areas like the pure flexural vibration mode – the deformation pattern of the A_0 mode.

Okabe *et al.*[70] evaluated the characteristics of the broadband of Lamb waves generation using a system that incorporates macro fibre composite (MFC) actuators and fibre Bragg grating (FBG) sensors. The MFC generates the Lamb waves into the composite laminates and the FBG is used to collect the emitted signals for analysis. They separated the Lamb waves in the composite laminate into S_0 and A_0 mode by using MFCs that are localised together to excite the Lamb waves and using two FBGs installed on the laminate as receivers. Both experimental and numerical analysis were conducted to confirm the proposed technique. The results indicated that the method could be used in detecting the size of delamination in a CFRP quasi-isotropic plate.

Manson *et al.*[71] decided to publish the studies they conducted between 1998 and 2001 on damage assessment in smart composite structures because of the applicability of their findings. Their studies were phased in two stages: (i) the evaluation of the suitability of Lamb waves for damage inspection in composite plates and (ii) the assessment of the application of novelty detection based on Lamb wave scattering for detecting minor damages in composite plates. The novelty detection is based on the

difference between the normal condition of the structure and the measured data [71]. Damage was introduced on a square CFRP plate with a $0^\circ - 90^\circ$ weave of fibres, by drilling several holes. At the final stage, they introduced BVID, characterised by internal delamination, through a controlled impact on the composite laminate. A 5 – cycle tone bursts at 280 kHz and 115 kHz was used to excite the S_o and A_o mode respectively. The Lamb waves were generated from a piezoelectric disc. The results obtained indicated that Lamb waves are effective in detecting considerably small damages in composite laminates. However, changes in the environment of the structure, operating conditions, like temperature and moisture [23] or variation in the instrumentation, have a strong impact on the accuracy of the damage detection method.

The effectiveness of the A_o mode in detecting small damages within low frequencies in composite materials has increased its application in SHM. Mustapha *et al.*[72] used A_o mode to estimate debonding in the sandwich (with a core) carbon fibre/epoxy plastic (CF/EP) composite structures. Sandwich structures usually are lightweight, possess high bending stiffness and have excellent dynamic properties [72]. These properties have increased their applicability in the construction, aerospace and manufacturing industries. Unfortunately, impact loads tend to initiate debonding between the core at the centre and the two faces that sandwich it, thereby reducing the component's mechanical properties. No matter how small the defects at the skin-stiffener connection are, they can influence the performance of the structure [73]. The primary limitation of a sandwich structure is that it hides defects, which makes it difficult to detect damage through visual inspection and many other NDT methods. Mustapha *et al.*[72] investigated the impact of the size of debonding on the delay in time of flight (ToF) and energy of the reflected signals of the A_o mode of low-frequency in the sandwich of CP/EP composite beams. In their study, they initiated debonding in the beams at varying locations. They used an active signal generation to activate the signal and a data acquisition system was used to collect Lamb wave signals for analysis. A 5 – cycle sinusoidal toneburst was generated and the Lamb waves were collected with a PZT sensor. In their work, they could locate debonding using the ToF of the waves reflected by the damage. The results show that A_o mode can be used to determine debonding in sandwich composite beams in the low-frequency ranges of 0 to 30 kHz.

However, the correlation between the level of debonding and the ToF of the waves reflected by damage (debonding) was not unique.

Zhao *et al.*[74] assessed the health of structures by observing the deviation of Lamb waves during propagation through the structure. The areas where the deviations occurred were mapped out based on ultrasonic Lamb waves tomography imaging. The result indicates that tomographic imaging enables the Lamb waves to visually represent and monitor damage in structures.

Ben *et al.*[75] suggested the use of ultrasonic-based Lamb waves propagation to locate and assess damage in composite materials. The presence of damage in a structure would cause the Lamb waves to deviate from its path of propagation, which is normally in a straight path, affecting its intensity too. This means that the magnitude of Lamb waves excited into a damaged structure is reduced when extracted from the receiving end for analysis. This was the idea behind Ben *et al.*[75] research work. Their results show the effectiveness of ultrasonic-based Lamb waves method for damage detection in composite structures, as confirmed by several other researchers [76–78].

Keulen *et al.*[79] proposed a sparse network that can identify damage over a wide range of composite material. They utilised an algorithm that considers the damage progression history in composite materials for better damage identification in structures. The method used a hexagonal arrangement of 12 PZTs, against the dense network of transducers that is usually necessary to monitor larger areas. The Lamb waves were actuated with one of the transducers through the test specimen and other transducers were used to receive and collect the data. The results indicated that the inclusion of damage progression history increased the efficiency of identifying possible damage within a range of 12 mm of the confirmed damage in the material.

Carboni *et al.*[78] studied how Lamb waves travel through materials in order to design a single mode of propagation method for damage identification. This method would ease the interpretation of Lamb waves. A CFRP laminate was used for the experiment. They characterised the elastic properties and the scattering behaviour of Lamb waves propagation through the composite laminate. A statistical approach was used to determine primary factors affecting the sensitivity response against artificial and

natural delamination in a composite laminate. One of the results obtained suggested that the analysis of the elastic signal waves received by PZT sensors could be simplified by actuating the Lamb waves within the frequency range of 0 - 50 Hz.

More recently, Mustapha *et al.* [80] used guided ultrasonic wave signals based on a pitch and catch configuration of PZT actuator and sensors to determine the size of BVID in CF/EP sandwich beams and panels introduced by a step-wise quasi-static indentation. They used the deviations in the characteristics of A_0 and S_0 mode and correlated them with the damage size. Three PZTs were installed on the test specimen: one was used as the actuator and the remaining two as sensors. A toneburst of 60 Volt confined in a Hanning window serves as the input signal for the actuator. It was observed from the results that residual deformations on the skin were about the same with the extent of the dent and the damaged location within the honeycomb core. Again, the modes of Lamb waves were sensitive to even a 0.2 mm size of a dent on the composite laminate.

2.4.2 Acoustic-based

2.4.2.1 Acoustic Emission (AE)

According to Mba and Rao [81], Acoustic Emission (AE) was originally developed as a technique for non-destructive testing (NDT) to monitor and sense cracks in structures and materials. Sensors are used to pick up and analyse the attributes of transient elastic waves (stress waves) generated by crack growth and propagation [82,83]. When loads are exerted on a structure that has a crack, the crack may generate stress waves, which are picked up by the AE sensor mounted on the surface of the structure, as illustrated in the schematic example in figure 2.2

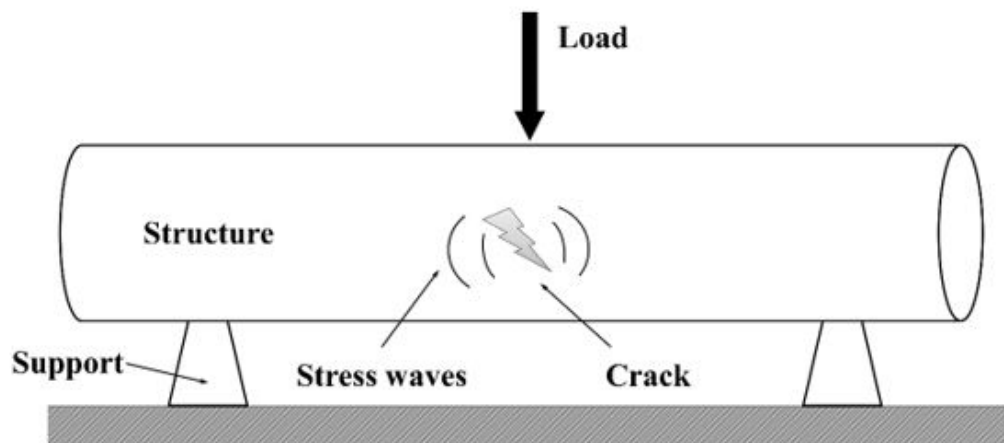


Figure 2.2 Stress waves due to the presence of crack in a material under stress [12].

AE is highly sensitive to the development of damage in composite structures. However, to explore the full potential of AE in SHM applied to composite materials, the velocity and attenuation of sound wave propagation in composite materials should be known. AE techniques can be used to study the damage propagation and characterise its failure mechanisms in composite structures [84]. Mechraoui *et al.*[85] analysed the propagation and evolution of velocity of acoustic waves in glass/epoxy composite materials. In their study, after conducting a static bending test, they analysed the damage mechanisms based on amplitude correction. They measured the real velocity based on the difference between the arrival times of each signal and the location of sensors to localise the different mechanisms of damage on the specimen such as delamination, crack, and the fibre break. The measured velocity was compared with the value of the theoretical velocity determined with theoretical model analysis. The AE could localise the introduced damages on the composite plate. However, based on the attenuation curve, amplitude correction can be used to enhance the localisation of damage in the test specimen. With this method, the amplitudes of the signal can be obtained without attenuations. See more information in [85].

Liu *et al.*[86] studied the damage growth and the failure mechanisms in carbon fibre/epoxy composite laminates having different layup patterns with holes at their centres using AE techniques. They extracted representative features such as counting, energy, and amplitude with the load history to investigate failure mechanisms of

composites. Their work was not comprehensive, as they only tried to establish the true mapping between the AE responses and properties of failure of composites.

Yun *et al.*[82] investigated the suitability of the AE approach to monitoring the damage progression in reinforced concrete (RC) beams strengthened in flexure with CFRP sheets. Their aim was to develop a health monitoring method based on AE techniques for RC structures that are strengthened with CFRP sheets. They considered the effectiveness of the strengthening based on the numbers of layers of CFRP sheets and the imperfections of the construction. To simulate imperfection in the construction, the CFRP was bonded without adhesive inside 10% and 20% area of the bonding area of the CFRP sheets. The AE signals were extracted and studied for all test specimens. The results of their analysis show that, depending on the active mechanism of damage, the characteristics of the signal – event, amplitude versus duration and amplitude versus frequency - have differences in the various stages of loading.

Also, Noorsuhada [87] conducted an extensive review of the use of AE techniques for the assessment of fatigue damage in RC structures. From the review, it was identified that fatigue damage test of RC structures based on increasing fatigue load is limited, and AE analyses such as intensity analysis, AE parameter analysis is limited. Aggelis *et al.*[88] studied the fracture behaviour of composite cross-ply laminates using both ultrasonic and acoustic techniques. In their study, they use tension-tension fatigue and incremental loading until the specimen failed. The results show that AE activity is highly related to the accumulation of damage in incremental tensile step loading. The results from the numerical simulation indicate that damage isolates the distinct layers due to the specific geometry of laminates. Huang *et al.*[89] suggested an approach for the localisation of AE in a marble stone using distributed feedback (DFB) fibre lasers, with the objective of identifying damage in civil structures.

In order to increase the effectiveness of the AE technique for SHM in textile reinforced cement (TRC), Blom *et al.*[90] related acoustic emission parameters to the mechanisms of fracture that contributed the most to the failure of the composite laminate. The primary parameters of AE signals are the activity, the total number of events, and energy [91]. Hamdi *et al.*[92] extracted suitable damage descriptors using the Hilbert-Huang transform (HHT) for the understanding of AE patterns. This approach

contributed to the understanding of damage evolution in structures. It provided relevant results for the extraction of non-stationary acoustic emission waves. Again, Blom *et al.*[93] monitored the flexibility of TRC laminates using the AE technique. They observed that AE could monitor the failure mechanisms and also identify the stress field. Bravo *et al.*[94] used the AE technique to examine the process of damage evolution in bio and green composites. Recently, Fotouhi *et al.*[95] investigated the relationship between the corresponding damage mechanism in thin-ply unidirectional carbon/glass hybrid laminates undergoing tensile loading and AE events. In their work, they established a criterion that is based on the values of energy and amplitude to identify the fragmentation failure mode. The evolution of damage in the test specimen was monitored with the cumulative numbers of the AE signals. It was concluded that the method can be used to characterise the mechanisms of failure in hybrid laminates and can detect damage initiation and propagation.

Akil *et al.*[96] compare the notch and flexibility of pultruded jute/glass and kenaf/glass hybrid polyester composites by monitoring them with acoustic emission technique. Pultrusion is a technique used for the fabrication of composite materials with a better reinforcement, tensile strength, and consistent quality [97–99]. Aymerich and Staszewski [100] established the use of the nonlinear acoustic technique for detection of impact damage in composite laminates. They introduced a high-frequency acoustic wave to a piezoelectric sensor at a location on the composite and receive it with another sensor. An electromagnetic shaker was used to excite a low-frequency flexural mode to induce damage. A pattern of sidebands close to the acoustic harmonic in the power spectrum indicates the damage caused by the impact on the specimen. It was confirmed that there is a linear relationship between the magnitude of the sidebands and the severity of damage in the specimen. However, they observed that the responses to different boundary conditions for the healthy and damaged specimens were not uniform. Further studies were required to identify and characterise the non-damage related nonlinearities.

2.4.2.2 Ultrasonic

Ultrasonic inspection methods are capable of detecting defects (delamination, porosity, crack, etc.) and providing mechanical properties (e.g., anisotropic elastic constants) on composite materials after the damage has been introduced [101].

The multi-layered arrangement of composite laminates makes it quite complex to detect damage when compared to metals. This is due to the anisotropic properties of the constituent materials and sensitivity to echoes [102]. During the damage detection procedure, echoes from the particles from the composite materials disturb the elastic waves from the damage, hence polluting the original signal from the damage. Hence, it is required to filter the unwanted echoes to detect any incipient damage in the composite structure.

Matrix cracking in composite laminates has been a source of concern in the engineering industry because it usually is the first flaw to occur. As such, several techniques have been developed to detect and locate them during the initiation stage [103]. Aymerich and Meili [104] analysed matrix cracking and delamination in composite laminates through ultrasonic inspection. In their work, they scanned test specimens with ultrasonic oblique and normal incidence in a pulse-echo (or one-sided) mode using a focused broadband transducer. The results indicated that the technique was effective in detecting matrix cracking in the composite. However, the oblique incidence ultrasonic method is more sensitive to matrix cracking, while the normal incidence ultrasonic method is more effective for delamination.

Kinra *et al.*[105] established an ultrasonic backscattering method to detect matrix cracks in ply-by-ply graphite/epoxy composite laminates. The ultrasonic backscattering method uses an oblique incident beam. A SONIX FlexSCAN ultrasonic scanning system was used for the data collection. Results show that the identification of matrix crack in the mid-ply does not depend on the damage in the intermediate plies. In other words, damage in the intermediate plies does not suggest that the middle plies would have damage too. Also, Hosur *et al.*[106] used ultrasonic C-scan to detect and map delamination in CFRP laminates. They developed software called IMPCTDAM to analyse the raw images from the C-scan and quantify the level of damage. A C-scan

enables the determination of the thickness of the material, damage location and possibly the severity of the damage in it [107]. In their work, they made some general assumptions based on their results: the impact damage increases as the depth increase until it attains maximum size; the behaviour of the composite laminate undergoing compression and buckling due to impact loading can be studied using data from the maximum delamination and its position, etc.

Ng *et al.*[102] applied the ultrasonic technique to investigate delamination in multi-layered glass reinforced plastics. The defect in the glass fibre reinforced laminate was detected and located with a single transducer based on pulse-echo mode, and the signal-to-noise ratio was enhanced with the use of a split spectrum processing (SSP) method to achieve a clear representation of the signal from the damage in the laminates. The SSP conditioners filter the interfering echoes from the particles of the constituent laminates. The technique is based on the analysis of the frequency of the signal spectrum.

In another application, Sharma *et al.*[108] reaffirmed the effectiveness of ultrasonic inspection technique in damage detection, by using it to monitor the initiation and evolution of corrosion in concrete reinforcing bars in concrete after been repaired with glass and CF sheets. The results obtained show the effectiveness of the ultrasonic guided waves to monitor the evolution of corrosion in the test structure. Although their study was conducted at a laboratory scale, it is claimed that it can be extended to a full-scale structure by scaling up the ultrasonic pulse energy.

2.4.2.3 Acousto-Ultrasonic

Acoustic-ultrasonic (AU) based methods use two ultrasonic sensors, each located at different points on the test specimen. AU methods are non-destructive evaluation (NDE) techniques developed around the late 1970s to determine the mechanical properties of composite structures [109,110]. One of the sensors serves as an actuator used to initiate the ultrasonic wave through the test material, whereas the other is the receiver of the reflected AU transient stress wave used for analysis. A pulsing PZT initiates broadband ultrasonic stress waves in the test specimen [111,112]. This technique measures the relative efficiency of AU signals propagation across the test material [113]. The presence of damage in a material reduces the strength of the AU

signal that is transmitted through it. Gyekenyesi *et al.*[111] used the AU technique to investigate the presence of damage and stress levels in two ceramic composites under loading, unloading, and reloading tensile tests. Their aim was to show the possibility of using AU as an *in situ* NDE technique for damage monitoring for two types of silicon carbide fibre/silicon carbide matrix (SiC/SiC) composite systems and stress dependence of the AU method. They loaded the test samples mechanically in the load/unload/reload runs to determine the impact of stress levels on the AU waves. The results indicated that the enhanced matrix composite labelled HN-C-ENH has a higher transverse crack density than the standard matrix composite, HN-C-STD. From the analysis of AU parameters, the mean square value of the PSD was able to monitor the accumulated damage more consistently [111]. In addition, the AU measurements related to the HN-C-ENH composites did not indicate stress dependence, whereas the AU measurements related to the HN-C-STD version did [111].

Loutas and Kostopoulos, [112] monitored the evolution of damage in carbon/carbon reinforced composite laminates that are subjected to loading, unloading, and reloading, using AU based methods. The comprehensive details of the experimental method and material characterisation can be found in [114]. A pulse generator and a transducer were used to introduce the AU stress waves into the test specimen. A similar transducer was used to collect the reflected AU stress due to the applied load. It was confirmed that the AU technique is suitable for monitoring the damage evolution in composite materials, including delamination [115].

Loutas *et al.*[116] investigated the efficiency of AU measurements in the development of damage in CFRP laminates during fatigue tensile loading. Damaged and undamaged composite laminates were used for the experiment, to compare the deviations in the measured parameters. They Carbon Nanotubes (CNTs) to modify the epoxy-matrix of quasi-isotropic CF reinforced laminates. The aim was to monitor the accumulation of damage in the test specimens during fatigue. In their work, they also tested four composite specimens with the measurement of AU signals at 80% stress level of the maximum tensile stress. The idea was to confirm if the AU wave parameters separated from the emitted signals change in a monotonic manner, which could be a pointer to the evolution or accumulation of damage in the laminate. The authors could monitor the initiation, evolution, and accumulation of damage during the fatigue tests.

Torres-Arredondo *et al.*[117] applied AU for the detection and classification of damage in CFRP sandwich structures. They mounted four transducers separated at equal distances on the surface of the test specimen and introduced varying types of damage on the test specimen. The authors used an excitation signal of 12 Hanning windowed cosine train signal with 5-cycles and a 50 kHz carrier frequency in order to boost the propagation efficiency of the AU signals through the material. In their study, a method that is based on the hierarchical nonlinear principal component analysis (PCA), square prediction measurements, and self-organising maps, was applied to detect and locate damage. The technique was also able to characterise fatigue damage in aluminium plates [118].

2.4.2.4 Vibro-Acoustic

Vibro-acoustic modulation techniques are highly sensitive to the presence of nonlinearities [119]. In the vibro-acoustic modulation technique, the structure is excited with a pumping signal while it is simultaneously interrogated with a more sensitive probing signal [119]. According to Aymerich and Staszewski, [120] vibro-acoustic techniques are sensitive to cracks in structures [119]. Hence, several researchers have used this technique to detect fatigue cracks in metallic structures effectively [121–123], but application in composite structures still is limited [124]. Aymerich and Staszewski, [120] monitored low impact damage in a rectangular laminated composite plate. They excited the composite plate with a constant amplitude probing signal and slow amplitude-modulated vibration pumping signal simultaneously. The pumping signal was introduced to the specimen with an electromagnetic shaker. Experimental results indicated the amplitude of the sidebands is related to the amount of damage in the plate.

Klepka *et al.*[125] used a nonlinear vibro-acoustic modulation to detect damage in composite chiral sandwich panels. The authors used low-profile PZTs to actuate the ultrasonic wave in the test specimen, and a scanning laser vibrometry (SLV) to acquire the vibro-acoustic waves. The results show the effectiveness of this technique in detecting debonding between the composite surface and the chiral core, which was verified by a classical vibrothermographic analysis [125] and is in agreement with the results presented in [120]. In addition, Sarigül and Karagözlü [126] examined the impact of the type of composite material, the number of layers and orientation of ply

on the coupled vibro-acoustic properties of plates i.e, their natural frequencies by conducting regression analysis.

Klepka *et al.*[124] also studied the effect of low and high-frequency excitations in nonlinear vibro-acoustic. The authors observed the nonlinear modulations in ultrasonic waves due to damage in composite chiral sandwich panels using high-frequency ultrasonic and low-frequency modal excitations. The spectra of the signal response indicated only the frequency components related to the propagating ultrasonic wave and the low-frequency excitation when the specimen is undamaged. In the presence of damage, there are additional sidebands around the two main ultrasonic components [119,120,124,125]. The level of damage in the structure relates to a number of sidebands and the amplitude of the sidebands depends on the intensity of modulation.

Likewise, Pieczonka *et al.*[127] detected BVID in light composite sandwich panels using nonlinear vibro-acoustic modulation method. The authors considered different levels of damage in two damaged and undamaged panels. Vibrothermographic inspection of the specimens was used to validate the results from the vibro-acoustic analysis.

2.4.3 Instrumentation-based

2.4.3.1 Sensor Networks

Due to the continuous technological advancement in SHM, composite laminates can be embedded with sensors in order to enhance effective monitoring and detection of damage initiation and progression. However, this must be done during the manufacturing process and it often compromises the stiffness and strength of the composites. Masmoudi *et al.*[128] investigated the effects of embedded piezoelectric sensors on the bending fatigue strength of composite laminates. They examined and compared the results from composite laminates with and without embedded sensors using AE to capture and monitor the generated transient elastic waves. A classification *k-means* method was used to evaluate the acoustic signature to determine the evolution and various failure mode in composites with and without embedded sensors. They observed that the mechanical behaviour of both types of composites indicates no difference in form, but the composite with embedded sensors was more sensitive to

damage than the one where the sensor was mounted to the surface of the structure. Although methods based on embedded sensors are usually cost-effective to implement [129], care must be taken to avoid excessive weight and reduced mechanical properties of the composite materials, since the embedded network of sensors will be part of the structural component.

Ghezzi *et al.*[130] investigated the effect of integrated sensors on the integrity and mechanical response in fibreglass epoxy laminates. In their work, monotonic tensile tests on fibreglass epoxy laminates were conducted to monitor initiation of damage and detect damage. From the results, it was shown that the initiation of debonding starts at the bond between the implanted sensor and the composite resin. Due to the high-stress levels, cracks occur around the specimen. They concluded that, although integrating a sensor network in composites is feasible and effective for damage identification, care must be taken in the design of the sensor, the method of integration, data collection, signal processing and analysis, and the estimation of the changes in the mechanical performance due to the presence of embedded sensors [130].

Alexopoulos *et al.*[129] integrated conductive CNT fibres to nonconductive GFRP test specimens in order to determine the behaviour of the material under different loading conditions by measuring the variations in the electrical resistance on the CNT fibre. They correlated the response of the GFRP to mechanical load and the electrical resistance measurements of the embedded CNT fibres to monitor and detect damage. The correlation between the two parameters depends on the loading history of the material. According to the authors, the advantage of using CNT fibres is that they are easy to insert and do not reduce the mechanical properties of the material. Based on their results, it was concluded that the CNT fibres have better sensing and damage monitoring capability of nonconductive composites than embedded CFs and modified (doped) conductive matrices.

Ksouri *et al.*[131] installed an accelerometer sensor network on a composite laminate to examine the response of the composite structure to an impact load. In their work, they introduced shock propagation waves through the network of accelerometer sensors. The idea was to compare the responses received from the accelerometers before and after the initiation of damage. The results indicate that the method was

suitable for the detection of damage in the composite structure. However, the method was unable to localise damage in the system.

Giurgiutiu and Santoni-Bottai [132] examined the advantages of the use of embedded piezoelectric wafer active sensors to impart and receive elastic waves for damage detection and localisation in unidirectional and quasi-isotropic composite plates. While some conventional ultrasonic transducers function through the application of vibration pressure on the test surface, the piezoelectric wafer active sensors function through surface pinching and are strain coupled with the surface of the structure [132]. The authors claim that this improves the performance over ultrasonic transducers in the transmission and reception of elastic stress waves. In addition, piezoelectric wafer active sensors are less expensive, lightweight and can be used for SHM in large structures.

Nauman *et al.*[133] conducted three-point bending tests on multilayer composite laminate specimens with two embedded sensors at different locations in order to determine the behaviour of the material during bending. The sensors are positioned in such a way that they can monitor compression and traction deformations in the material and can also detect matrix fracture initiation and propagation [133]. The embedded sensors could generate the stress-strain history of the test specimens. The results from the three-point bending test provide information on the health of the specimen and data related to propagation of the crack, delamination, and fracture inside the material under quasi-static loading. However, there needs to be an improvement of the sensor's sensitivity and bandwidth and compatibility between the embedded sensors and with carbon or other multifilament tows that are used as fibre reinforcements.

Dziendzikowski *et al.*[134] conducted an impact test on a CFRP laminate with an embedded network of PZT sensors. The aim was to determine the effectiveness of the embedded network of sensors in detecting BVIDs. Three impacts with different energies were applied to the test specimen and the emitted elastic stress waves were received with the PZT network for analysis. The health of the test specimen was determined from the selected signal characteristics known as damage indices. However, apart from damages, other factors such as weather can have an effect on the signal acquired, which can result in false positive or false negative indications [134]. To avoid

that, the authors suggested that there should be a balance between the level of sensitivity of the damage indices to damages and the stability of the damage indices under different working conditions of the PZTs.

Luo and Liu [135], integrated graphite nanoplatelets (GNPs) into an epoxy/fibreglass composite laminate. The GNP thin fibre sensor enabled to determine the state of the local resin curing in the composite material during the manufacturing process [135]. In addition, it could map out the state of stress and strain in the material when under load. The embedded GNPs in the composite laminate make the structure smart, in such a way that it enables the structure to act as a sensor that is capable to self-monitor its damaged condition. According to the authors, the GNP fibre sensor is currently only suitable for non-conducting composite materials. Hence, it is yet to be applied to conductive composites such as CFRPs.

Cenek *et al.*[136] conducted a series of tests to detect and locate low energy impact damages in carbon composite materials by embedding piezoelectric sensors in three different layouts at different depths. The sensors were installed on a lean flexible printed circuit before integrating them into the composite laminates. The results from the experiments show that all the layouts could detect the impact energies applied to the test specimens, but the sensors that are close to the surface of the specimen are more sensitive. However, even if the authors could detect and locate damage, the method was not sufficient to determine its type and severity.

As mentioned earlier, one limitation of embedding sensors in composite structures is that this may impact on their host's mechanical properties [137], for example through the addition of weight. This challenge has engaged several researchers in the attempt to devise means to reduce the weight contribution from the sensors, while at the same time the reliability and durability are not compromised. Through miniaturisation of the embedded sensors, the impact may be noticeably reduced, thereby maintaining the original properties of the composite structure almost unchanged. To this end, Salas *et al.*[138] designed a miniature wireless sensor network that works through an inductively coupled coil. The authors confirmed the possibility of generating power using inductive coils for a piezoelectric wafer active sensor system in CFRP composites

for SHM. However, CFRPs are found to introduce limitations in power transmission due to the conductive nature of carbon fibres.

Lu *et al.*[139] used FBG sensors to detect structural dynamic response signals from CFRP structures and extracted the damage characteristic through Fourier transform and PCA methods. The dynamic response signal was generated by an active actuation method. From the damage characteristics acquired, they could detect damage with one-class support vector machines technique and the localisation and severity of damage were achieved with multi-class C-support vector classification techniques. In their study, the accuracy of the damage detection was claimed to be above 90%. However, there are challenges associated with the use of FBGs in composite structures. For example, Kinet *et al.*[140] reviewed some challenges due to the use of FBGs in composite materials. In their study, they analysed the problems linked to the demodulation of the amplitude spectrum during and after the curing process, the distinction between the effect of temperature and strain, and the relation between the integrated optical fibres and the surroundings.

The presence of micro-cracks in the composite structure tampers with its contour by increasing the surface roughness. Such changes on the surface can be used to monitor the health of structures and detect damage by measuring the surface roughness [141]. Zuluaga-Ramírez *et al.*[142] measured the surface roughness of CFRP test specimens with a confocal microscope in order to assess the development of surface roughness due to fatigue loads applied to the structure. In their study, loads were applied based on the standard load sequence for fighter aircraft. The authors thoroughly scanned the test samples vertically in order not to miss any point. They ensured that every point on the surface of the test material passes through a pinhole to the focus plane. Results indicated that fatigue loads are the prime culprits that cause surface roughness, affecting the topography of the composite structure surface.

2.4.3.2 Eddy Currents

Eddy-current based techniques work on the basis of electromagnetism, whereby the conductivity of a material can be detected without having contact with it [143]. Khandetskii and Martynovich [144] applied an eddy-current technique to detect damage near the edges of composite laminates. They used a finite difference method to

study a two-dimensional model of carbon reinforced composite material that was made up of alternating layers of the reinforcing fabric and binding material with delamination on a boundary between layers [144]. The authors mounted a rectangular eddy-current transducer on the edge of the specimen to generate a vector potential field. The results obtained from the calculations at different widths of the delamination suggest that the modulation pulse width due to damage is almost a linear function of the width of the delamination.

Bonavolontà *et al.*[145] recommended the use of an eddy-current method based on a high-temperature superconducting quantum interference device (HTS-SQUID) to assess a glass laminate aluminium reinforced epoxy (GLARE) structure. The HTS-SQUID sensor is sensitive to any deviation in the magnetic field due to incipient damage in the composite material even at a low excitation frequency [145]. The authors used a steel impactor to introduce different flaws on the GLARE specimen by changing the level of impact between the range of 5J and 36J. Results showed the effectiveness of the eddy-current method based on the HTS-SQUID magnetometer to analyse the various damage stages in GLARE composites. Additionally, experimental results showed that the mechanical properties of the fibre/metal laminate under stress could be determined using the eddy-current method based on the HTS-SQUID magnetometer.

Additionally, Bonavolontà *et al.*[146] expanded the application of eddy currents to the identification of damage in GLARE composite laminates by using HTS-SQUID and giant magneto-resistive (GMR) sensors. Their aim was to correlate the performance and effectiveness of HTS-SQUID and GMR sensors to detect damage in fibre/metal laminate composite materials. According to the authors, the limitation of the typical eddy currents is related to the decreasing sensitivity of the search coil with the increasing lift-off and tilting of the probe. The choice of the two different sensors was to overcome the primary limitation of the eddy-current technique in damage detection. In their study, a Teflon and wet cotton were used to introduce defects and porosity respectively in the test specimens. The results show that the HTS-SQUID sensor has a higher sensitivity to the porosity inside the test specimen than the GMR sensor, due to its larger magnetic field. Additionally, the eddy-current method using HTS-SQUID first order gradiometer and the GMR second order gradiometer could detect internal flaws in multilayers metallic alloys.

Yin *et al.*[143] designed three multifrequency eddy-current sensors to measure the bulk conductivity, characterise directionality, detection of fault and imaging of unidirectional, cross-ply, and impact damaged CFRP specimens. The authors simulated the sensor responses with both analytical and finite element models. From the results achieved, Yin *et al.*[143] claimed that the characterisation of CFRP specimens with an instrument that is based on eddy-current principles is feasible.

Mizukami *et al.*[147] presented the induction heating assisted eddy-current testing (IHAET) for the detection of delamination in thermoplastic CFRPs' welded areas. Delamination may develop in CFRPS during welding due to several reasons, for instance: expansion of entrapped air, an insufficient squeeze of air in the bond line due to insufficient pressure and thermal stresses [147]. To detect delamination in the specimen, an induction heating was initiated to increase the temperature of the specimen. The damaged area was identified based on the gradients of temperature across the specimen. Since delamination increases the temperature of a composite laminate, the spots with higher temperature indicate the defective locations [147]. The induction heating improved the effectiveness of the eddy-current testing for the detection of delamination in the laminate. According to the authors, the IHAET can detect delamination faster than ultrasonic testing because it does not require scanning time and a coupling medium. Mizukami *et al.*[147] used a statistical diagnosis method [148] known as system identification-F test method (SI-F method) and IHAET sensors to detect a 2mm deep delamination with an area of 450 mm² in a 4mm thick specimen. However, the method could not detect delamination as large as 300 mm².

2.4.3.3 Electrical Resistance

Among other features, CFs have high electrical conductivity. With this property, carbon fibres can conduct electricity in CFRPs. The presence of damage in the CFRPs may alter the electrical conductivity of the carbon fibres, due to, for example, the discontinuity of the fibres. Hence, the fibres in the CFRPs may act as embedded sensors [149–151] that can be used for SHM [152].

In 1999, Abry *et al.*[153] conducted a two-stage study on CFRPs: the inspection of the route of electrical conduction in an unloaded test specimen based on the change of electrode location, and the implementation of monotonic (tension and compression) and

cyclic testing of CFRPs of different fibre fractions. The authors observed that the path of electrical conductivity across the CFRPs occurred in the longitudinal direction of the fibre and in the transverse direction of the plies. The presence of damage in the composite laminate reduced the level of electrical conductivity. The advantage of this method is that it can be used to detect very small damage in terms of fibre breakage. However, the accuracy of this method depends on how large the through-thickness resistivity of the fibres is. This implies that the volume of the fibres and location of electrodes will determine the level of sensitivity of this method to the presence of damage.

Wang *et al.*[154] monitored the impact damage on continuous CF epoxy-matrix composite laminates by measuring the electrical resistance. Their work was aimed at verifying the possibility of detecting impact damage on CF epoxy-matrix composite laminates, examining the capability of the oblique and surface resistances for damage detection in the test composites, and the comparison between the effectiveness of ultrasonic and electrical resistance measurement techniques. From the results, it was noticed that the surface resistance is sensitive to fibre breakage and the oblique resistance is more sensitive to delamination of the fibre. This technique is claimed to be more sensitive to damage in CF composites than ultrasonic techniques are [154].

Viets *et al.*[155] used electrical resistance measurements for the identification of BVIDs in GFRPs that are altered with nanoparticles. They studied the effect of diverse nanoparticles and filler contents. The determination of the local electrical resistance changes due to the presence of impact damage introduced on the specimen with an impact of 7.65J was aided with silver ink electrodes on the test specimen. It was stated that this technique is suitable for both on-site and off-site SHM of fibre reinforced plastic (FRP) structures.

Kwon *et al.*[156] examined the level of sensitivity of CNT paste to damage in composites using electrical resistance measurements. The dispersion of the CNT in the epoxy matrices was inspected using electrical resistance measurements and its load-sensing ability during tensile testing was observed by four-point electrical resistance measurements. Artificial cracks were introduced into the test specimens and the cracks

were filled with CNT paste [156]. The variation in the electrical resistance of the test specimen was used to detect crack progression.

2.4.3.4 Infrared Thermography

Infrared thermography is highly suitable for the monitoring and detection of porosity in composite laminates. The pore morphology of composite materials is of great concern in the aerospace industry [157] since the porosity of the material reduces the mechanical properties of the composite laminates. This could compromise the safety of the structure. Due to the increasing application of CFRPs in the manufacturing of critical parts of aeronautical structures, it is important to continuously monitor and detect any inherent fault in it promptly.

The porosity in the composite normally occurs during the curing procedure due to loss of pressure in the autoclave [157]. Therefore, effective quality control and inspection methods should be put in place during production to detect possible voids at the earliest stage. Mayr *et al.* [157] assessed the porosity in CFRPs using active thermography. In their work, X-ray computed tomography was used to determine the level of porosity and the microstructure of the pores. From the results obtained, it was observed that the shape and size of the pores in the composite affects the measured thermal diffusivity. In addition, the experimental result on active thermography correlates with the results obtained with an ultrasonic method with respect to the influence of the shapes of pores.

Meola and Toscano [158] explored the use of flash thermography to determine the quantity and distribution of pores in composite laminates. They presented relevant literature with respect to the use of flash thermography to assess the percentage of porosity in fibre reinforced composite materials. In their experiment, new data was obtained from some specimens, which has a different level of porosity, two different stacking sequences, and insertion of slags in the specimen in order to simulate local delamination. It was confirmed that the measure of thermal diffusivity using flash thermography as a porosity evaluation parameter, is a substitute for the ultrasonic attenuation estimation. The use of flash thermography requires no coupling media, surface finishing does not affect its use, it can detect defects and assess the level of porosity within one test [158].

Meola and Carlomagno [159] used infrared thermography to study the effect of low-velocity impact on GFRPs. Their work has two objectives: the mapping of the temperature of the surface of the specimen when impacted and NDE before and after impact on the specimen. Optical lock-in thermography was used to inspect the test specimen for possible manufacturing defects. The different energy level was impacted on the specimen and the material behaviour was monitored with an infrared camera. The results obtained indicate that during impact there were variations in temperature within a short time and only high-frequency imaging device could capture it. The initiation of damage can be determined from the temperature-time maps. In fact, the increase in temperature corresponds to the onset of the impact damage on the specimen.

Defects in the bond due to delamination, the wrong installation of CFRP to concrete, and cracking can impact on the integrity of the composite CFRP system [160]. Infrared thermography testing method has been reliable in detecting and monitoring of bond defects in composite materials [160]. Tashan and Al-Mahaidi [160] used active pulse thermography and lock-in thermography to investigate bond defects between layers of CFRP laminates in concrete and CFRP fabric in steel. The active pulse thermography works based on exposing the surface of the test material to short temperature stimulation and recording the temperature pattern of the heated test material as thermal images, while the lock-in thermography generates heat externally same way as the pulse procedure but covers a broader range of different thermal frequencies [160]. The results from their experiment indicate that the maximum thermal magnitude has a linear relationship with the input heat flux. In addition, the number of CFRP layers determines how accurate infrared thermography can detect the sizes and shapes of possible defects. The smaller the layers the more accurate the detection. The capability of this technique also depends on the heating method, positioning, and inspection intervals.

Montanini and Freni [161] simulated subsurface defects in GFRP laminates used for the manufacturing of yachts. They used optically excited lock-in thermography to quantitatively assessed defects in it. The authors assessed the influence of defect aspect ratio, detectability of defects simulating delamination, and the influence of damages over the gel-coat finish layer. The results show that lock-in infrared thermography is very efficient for the detection of defects in GFRP structures. However, some limitations were evident when used to inspect thick GFRP marine structures, due to

inhomogeneity, high thermal transmittance, and a low emissivity of the gel-coated surface. This makes it difficult to measure radiation and flaw sizing. In addition, Maier *et al.* [162] study the capacity of infrared thermography to detect low impact damages in composite plates. The aim of their work was to detect the impact of damaged locations and provide information on its location for more damage analysis. They charged the test specimens with specified impact loads to simulate the effect of stone chips and analysed the specimens with thermography. From the results, it was shown that impact events were elastic for lower impact energies that are up to 3J. In addition, at impact energies up to 4J, it was possible to detect the damage by visual inspection. While impact energies up to 5J and beyond will result in catastrophic damage, making it very easy to detect visually.

2.4.3.5 Nonlinear Elastic Wave Spectroscopy

The nonlinear elastic wave characteristics are able to indicate early signs of degradation on a material [163]. Among other researchers, Meo and Zumpano, [164] studied the suitability of nonlinear elastic wave spectroscopy (NEWS) in the detection of impact damage in a sandwich panel. This technique detects damages from the presence of harmonics and sidebands on the spectrum of the acquired signal. These are generated by the high and low-frequency harmonic signals interaction [165]. In their study, they generated a high-frequency signal and a low-frequency signal with two distinct PZTs. Three acoustic sensors were used to collect the response signals for analysis. The experiment was conducted on damaged and undamaged specimens for comparison. From the analysis, the nonlinearity of the damaged specimen showed sidebands and harmonics of the excited frequencies. However, the NEWS technique cannot indicate the location of damage but its presence alone.

Zumpano and Meo [166] presented a transient NEWS (TNEWS) to detect and localise damage in a composite panel. The TNEWS measures the variations in the transient dynamic responses of a structure based on its nonlinear behaviour caused by damage. The TNEWS detects damage in a three-stage process: acquisition of the structural responses, detection of damage, and localisation of damage [166]. The authors were able to detect and localise damage in the test specimen with this technique.

2.4.4 Artificial Neural Networks

Artificial neural networks (ANN) SHM based methods appeared as a result of the possible presence of multi-variant damages in a particular structure [20]. ANN is an approach that is capable of learning when trained and this characteristic has made it useful in SHM and other engineering applications. The training procedure ends when the mean-squared-error between the observed data and the ANN results for the entire element has reached a specified target or after the completion of a specified learning period [167]. It is an adaptive structure that changes its architecture or input information that passes through the network during the training phase [168]. It processes input information, just as the brain does [169]. With the correct inputs, ANN enables detecting faults and predicting the remaining useful life of materials and structures. ANN consists of layers of input nodes or neurones, one or more hidden neurones, and output layers of neurones. The hidden neurones are between the input and output neurones [170]. The two classes of ANN are feedforward network and feedback network [168]. The advantages of the ANN technique are that it offers a processing speed and can process multiple inputs [171]. In fact, ANN can also be used to segment radiographic images of damage in composite laminates for evaluation [172]

El Kadi and Al-Assaf [173] used the strain energy as the input to a modular neural network (MNN) to determine the fatigue life of a composite material. They used the MNN model to reduce pattern interference that could result from various inputs, including maximum stress, stress ratio, and fibre orientation. Fatigue tests of 2 million cycles were conducted on unidirectional fibre reinforced composite laminates using a servo-hydraulic testing machine. A 10% reduction in the elastic modulus for the specimens with 0° orientation was defined as a failure [173]. They compared the result from the MNN model, using the strain energy as input, and the result from ANN, with maximum stress, applied orientation angle, and stress ratio as inputs. The results indicated that strain energy can be used as a valid sole input parameter to the neural network to predict fatigue failure in unidirectional composite materials.

Yam *et al.* [174] integrated vibration responses, wavelet transforms and ANN models. This was done through numerical simulations and experimental analysis. In their study, a piezoelectric patch actuator and sensors were used to excite and acquire the structural

responses. The wavelet energy spectrum of the decomposed structural vibration responses was used to acquire the features of damage in the structure and an ANN was used to classify and detect damage. The results confirmed the suitability of ANN for detection, location, and classification of damage in composite structures. In addition, they could establish mapping relationships between the location and severity of damage and the damage feature of the structure.

Sahin and Shenoi [169] utilised global (changes in natural frequencies) and local (curvature mode shapes) vibration-based inputs for ANNs to identify and predict the criticality of damage in FRPs laminates. They obtained the dynamic characteristics of an undamaged and damaged cantilever composite beam for the first three natural modes using FEA. In their work, the damage was initiated at six different locations along the length of the beam. To train the ANNs for the analysis, a different mix of input data from the first three natural modes of the beam was introduced [169]. They used a variety of stiffness reductions at the different locations along the composite beam to generate 126 damage scenarios. The results obtained indicated that there is a correlation between the chosen features that are used as input data and the correct identification of damage.

Watkins *et al.* [171] used ANNs to outline damages caused by impacts on the composite plate. The type of damage and its severity were linked to the strain signals emitted from the impact on the composite plate. They observed that the impacts that caused damage had a higher peak strain and a more orderly strain profile than that of non-damaging impacts.

Just-Agosto *et al.* [175] combined vibration and thermal signals to detect and characterise damage in a sandwich composite material using ANN. They studied the response to various damages in the structure using the transient temperature response [176] and mode shape curvature (MSC) [177] methods. A numerical analysis was conducted with finite element and finite volume methods. The data collected from the numerical simulations were used to train the neural network. The results they got indicated that the combination of vibration and thermal signatures with the neural network were effective in detecting damage, identifying the type, its location and severity [175].

A vibration-based method with ANN was recently used to establish the fibre volume fraction in GFRP [178]. The fibre volume fraction has a direct effect on the mechanical properties of a composite material. Therefore, this could be used for quality control purposes, for example. In this study, experimental protocols were developed to acquire the pattern of vibration. They also developed an autoregressive model to classify the fibre volume fractions and a pole-tracking algorithm to establish the positions of the autoregressive pole. According to [178], the higher the fibre volume fraction, the higher the stiffness and the strength of a composite material. However, when the fibre volume fraction exceeds a certain amount, it may actually reduce the ultimate strength of the composite laminate [178]. The proposed method by Farhana *et al.* [178] is only suitable for unidirectional GFRP.

Jiang *et al.* [179] used the composition of the composite material and testing conditions as inputs and mechanical properties (compressive modulus, tensile strength, compressive strength, flexural strength, specific wear rate and frictional coefficient) as output parameters of the ANN. The result showed that the ANN could predict the output parameters based on the input parameters accurately, the reason why the proposed technique is offered as a possible approach for SHM. However, the effectiveness of the ANN depends largely on the robustness of the experimental database for the network training [179]. The larger the database, the more accurate its damage predictability. Unfortunately, it is not always easy (or even possible) to get such a large set of data in real-time.

Finally, a comprehensive summary of various damage identification technique and their applications are presented in Table 2.1. The Table provides an overview of the area of application of different techniques, their advantages and limitations. The information can be used as a quick reference to engineers and scientist involved in SHM.

Table 2.1 Summary of the damage techniques.

Techniques	Advantages	Limitations	Ranges of Application	Rytter's Scale	Types of damage detected in composites
Vibration-based techniques	Easy to implement; Cost-effective; High sensitivity to damage.	Non-unique solutions; Errors in measurements; Environmental factors.	Aerospace industries; Automobile industries; Inspection of civil infrastructure.	Stage I, II, III, and IV	Delamination; Cracks.
Transmissibility	Simple to implement; Sensitive to local changes in structures; Uses only the output response; Does not need the operational forces be white noise; Can be a swept sine, coloured noise, or impact.	Difficult to apply without supervision.	Civil engineering; Marine industries (determination of Ship mechanical noise); Automobile industries (applied to data from a real vehicle); Health monitoring in composite structures.	Stage I, II, and III	Delamination; Debonding.
Damping	Sensitive to small cracks; Sensitive to variations in structural stiffness.	Numerous definitions; Errors involved in finding the values of damping; Difficult to model analytically.	Civil engineering; Aeronautic industries; Automobile industries; Health monitoring in composite structures.	Stage I, II, III, and IV	Cracks; Delamination; Debonding; Fibre fracture; Kink bands; Micro-buckling.

Table 2.1 Summary of the damage techniques (continued).

Techniques	Advantages	Limitations	Ranges of Application	Rytter's Scale	Types of damage detected in composites
Lamb Waves	Travels over long distances in structure without deviating; Monitor large area from a single point of application; Cost-effective; Can detect internal damages in thin material; High flexibility; Safe, and no harmful radiation; Can inspect parts; Suitable for remote inspection.	Dispersive nature complicates its application; Multiple waveforms in single frequency affect its application; Cannot detect small damages (e.g. localised pitting); Requires skilled personnel for interpretation; No existing standards to work with.	Aerospace industries; Automotive industries; Audio and acoustics data storage; Production testing; Structural testing; Scientific and medical; Ultrasonic; Pipeline inspection; Bridge cable inspection; Rail defect detection; Gas cylinder inspection; Health monitoring in composite structures.	Stage I and II	Cracks; Delamination; Matrix cracking; Broken fibre; Impacts; Adhesive defects on stiffness; Porosity.
Acoustic Emission	Can detect several types damages caused by fatigue loading; High sensitivity; Permanent installation of sensor for process control; Fast results and global monitoring using multiple sensors; Used for leak detection and location; Suitable for proof testing; In-process weld monitoring; Online monitoring; Less intrusive; Remote scanning; Real-time evaluation.	Cannot characterise damage; Difficult to find damage; Requires load application to generate AE event; Requires skilled personnel to correlate data to the specific damage mechanism; Attenuation (the test specimen can attenuate the AE stress wave); A crack that is not propagating cannot be detected.	Civil engineering; Automobile industries; NDT testing; Machining; Aerospace industries; Health monitoring in composite structures.	Stage I, II, and IV	Translaminar cracks; Fibre breakage; Delamination; Fibre matrix debonding; Matrix micro-cracks

Table 2.1 Summary of the damage techniques (continued).

Techniques	Advantages	Limitations	Ranges of Application	Rytter's Scale	Types of damage detected in composites
Ultrasonic Inspection	Easy to interpret; Can detect early stage of damage initiation; Enhanced sensitivity; Cheap, and readily available.	Limited in depth because of attenuation; Low contrast due to high attenuation and scattering in composites; Variations in composite properties affects its performance.	Aerospace industries; Material research; Quality assurance; Bridges; Monitoring of weld; Gas trailer tubes; Health monitoring in composite structures.	Stage I, II and III	Cracks; Delamination; Debonding.
Acousto-Ultrasonic	Assessment of non-critical damages; A good indicator of accumulated damage due to impact damage.	Not useful for the detection of delamination or voids; Mandatory setup and pre-calculations before testing; Surface roughness and texture affect its performance.	Quality control and assessment of damage in composite materials; Automobile industries; Aeronautic industries; SHM in composite structures.	Stage I, II, III, and IV	Translaminar cracks; Debonding.
Vibro-Acoustic	Sensitive to nonlinearities; Sensitive to cracks; Changes in environmental and loading conditions have negligible effect.	Selection of probe and excitation frequencies needs experienced personnel; The position of clamp with respect to the location of transducer affects the result.	Aeronautic industries; Health monitoring in composite structures; Civil structures; Space industry.	Stage I, II, III, and IV	Fatigue cracks; Delamination; Debonding.

Table 2.1 Summary of the damage techniques (continued).

Techniques	Advantages	Limitations	Ranges of Application	Rytter's Scale	Types of damage detected in composites
Instrumentation	Can check the damage initiation and evolution; Cost-effective; High precision and sensitivity; Requires little human effort and a limited number of sensors.	Add excess weight to the structure; Affects the stiffness and strength of the material.	Civil infrastructure; Manufacturing industries; Automobile industries; Aerospace industries; Petroleum industries; Pipelines inspection; Nuclear installations; Tunnels; SHM in composite structures.	Stage I, II, III, and IV	Cracks; Delamination; Debonding; Matrix fracture; Surface roughness.
Eddy Currents	Convenient to apply; No contact needed.	Only effective in electro-conductive graphite fibre composites; The sensitivity of the search coil decreases as the lift-off and tilting of the probe increases.	Health monitoring in composite structures.	Stage I, II, III, and IV	Cracks; Delamination; Porosity.
Electrical Resistance Measurement	Sensitive to small damages; Cost-effective; Suitable for both on-site and off-site monitoring of FRP structures.	Its sensitivity depends on the fibre volume and the location of the electrodes.	Civil engineering; Health monitoring in composite structures.	Stage I and II	Fibre fracture; Fibre pullout; Delamination; Debonding; Cracks.

Table 2.1 Summary of the damage techniques (continued).

Techniques	Advantages	Limitations	Ranges of Application	Rytter's Scale	Types of damage detected in composites
Infrared Thermography	Enables remote sensing; Rapid coverage of large area; Relatively easy to use; Can Figure out the exact location of damage; Offers a visual picture of health of a structure; Non-contact.	Generates varying thermal properties in different orientations due to anisotropy; Requires sensitive and expensive instrumentation; Difficult to detect damage that are not close to the surface of the structure.	Research and development; Medicine; Predictive maintenance; Inspection of civil structures; Process optimisation; Observation and investigation; Quality control; Roof surveys; NDT testing; SHM in composite structures.	State I and II	Translaminar cracks in GFRP composites; Foreign inclusions; Impact damage; Voids and cracks in CFRP laminates; Delamination; Accumulation of water in composite sandwich panels; Debonding; Fatigue.
Nonlinear Elastic Wave Spectroscopy	Determination of the thickness of thin test specimen; Detection of damage initiation in both metals and composites; Detection of accumulated damage; Characterisation of structure related properties.	Several effects such as dislocations, micro-cracks lead to various kinds of nonlinearity; Difficult to define reference samples for scattered damage; Amplitude determines the nonlinear effect.	Health monitoring in composite structures; Aerospace structures.	Stage I, II, III, and IV	Porosity; Matrix properties; Delamination; Cracks; Debonding; Fracture; Thermal damage; Corrosion.

Table 2.1 Summary of the damage techniques (continued).

Techniques	Advantages	Limitations	Ranges of Application	Rytter's Scale	Types of damage detected in composites
Artificial Neural Networks	Can mimic a structure (adaptive learning); High processing speed and can process multiple inputs; Can be used to segment radiographic images of damage in composite laminates; Real-time operation; Handle noisy data.	Skilled personnel required; Large database needed for more accurate damage prediction – but it is difficult to get large data in real-time; Complex solutions consume a lot of time.	Civil structures; Character recognition; Stock market prediction; Medicine; Security (features of fingerprints and fingerprint recognition system); Robotics; Environmental science, Chemical technology, science, and nanotechnology; SHM in composite structures.	Stage I, II, III, and IV	Fatigue; Fibre fracture

The classification of damage detection methods was first done by Rytter [19].

2.5 Prognosis

Prognosis is the last level among the four steps of classification of damage detection techniques presented by Rytter [19]. It is the prediction of the remaining life cycle of a system when a fault is already present, which is of high importance to several industries. Prognosis saves resources, cuts unplanned breakdown of facilities, and gives a window for maintenance activities or replacement of equipment. Hence, this area of damage detection has recently received considerable attention from researchers.

Surace and Worden [180] proposed an approach to damage prognosis that takes into consideration the consequences of uncertainties. It is based on integrating the damage progression laws within the framework of interval arithmetic. In interval arithmetic, each quantity is represented as an interval of possibilities ranging between upper and lower boundary values. They considered two case studies for the approach: the first case study considers an isotropic finite plate that is under harmonic uniaxial loading. A central mode I through-crack damage was introduced. They assumed the Paris-Erdogan law for the damage propagation model. The second case study considers internal delamination growth in composite plates that is under cyclic compression. In their work, the crack/delamination length was considered as the interval quantity and the remaining life of the crisp is defined in terms of the point when the upper boundary on the length exceeds a specified threshold. Then, the lower boundary becomes the safe-life of the structure. According to the authors, the number of cycles can also be considered as an interval quantity and the safe-life of the structure can be decided in terms of the lower boundary on the lifetime when the length of the crisp crack/delamination exceeds the specified point.

Furthermore, Peng *et al.* [181] proposed a prognosis framework for real-time composite fatigue life prediction. The method of the prognosis combines sensor measurements, bayesian inference, and a mechanical stiffness degradation model for the prediction of real-time fatigue life. They used an open-hole test specimen dataset to prove and validate the proposed method. The authors finally used a prognostic metric to evaluate the predictions of the proposed model. Among several conclusions drawn from their results, the remaining life of the test specimen is small when the stiffness is below 0.75 of the stiffness of the undamaged specimen.

2.6 Concluding Remarks

An updated review of the failure mechanisms in composite structures and non-destructive SHM testing techniques were presented. Despite the excellent mechanical properties of composite materials, they are susceptible to impact damage that can result in unexpected and catastrophic failures. Hence, early damage detection and localisation in composite materials are of utmost importance in order to avert downtime and human risks.

Although several methods for damage detection and localisation have been developed, they all have their own advantages, limitations and scope of application. Also, a challenge is related to damage size, which makes it difficult to detect until a certain minimum dimension is attained. However, the quantification of damage and the prediction of the structure's lifetime (prognosis) still are the most complex areas.

Most techniques are based on a comparison between undamaged and damaged states of the materials. A deviation from the data of the undamaged material indicates the presence of damage. Therefore, the health status of the undamaged material must first be established and used as a reference.

Currently, the use of embedded sensors in composite materials is trending: composites are becoming smart materials. This technique enables the material to act as a self-sensor by detecting and localising damage in real time. However, the integrated sensors add weight to the structure and change its mechanical properties. Furthermore, these materials must be manufactured with the sensors beforehand. Therefore, for composite structures that do not have embedded sensors, other SHM frameworks must be chosen, depending on many different factors that were illustrated throughout this paper.

Many of the techniques are based on changes in the structural dynamic response, which includes changes in the modal properties (natural frequencies, damping modal factors and mode shapes). For composite materials, damping appears to be a suitable damage sensitive feature. This is because there is a correlation between damping and the energy dissipated on the composite material during vibration. It is noteworthy to mention that the natural frequencies can also provide information about the presence of damage, as this is usually related to a reduction in stiffness, but it is the combination of different

parameters what usually makes a more robust method. The assessment of nonlinearities, especially due to delamination, has also shown to be a promising technique to detect damage.

Nevertheless, experimental uncertainties still are the greatest hindrance to most methods, reason why no method truly is false-negative or false-positive free. This can happen when factors such as an increase in temperature, changes in mass due to the installation of sensors and stiffness variations introduce more differences than damage itself. Uncertainty is the one primary limitation of structural damage detection and characterisation.

Based on the numerous papers reviewed, researchers have been more focused on flat composite plates reinforced with synthetic fibres. There are relatively fewer works on more complex structural geometries, hybrid reinforced composites and natural fibre reinforced composites. It would be interesting to assess how the available techniques would perform with more complex designs.

“A good scientist is a person with original ideas. A good engineer is a person who makes a design that works with as few ideas as possible. There are no prima donnas in engineering.”

— Freeman Dyson

3 The Failure Mechanisms of Composite Materials

3.1 Introduction

Due to the high strength to weight and stiffness-to-weight ratios of CFRP composites, these materials have been widely applied in the aerospace, civil, marine, transport, and oil industries. However, their complex damage [182] and failure morphologies such as intralaminar and interlaminar failures [86] constitute a hindrance on their application. Typical failure mechanisms that will be discussed in this section include matrix cracking, fibre fracture, debonding, fibre pullout, delamination, micro-buckling, and kink bands.

3.2 Types of Failure Mechanisms

3.2.1 Matrix Cracking

Matrix cracking is the first type of damage that occurs in composite laminates [183]. This is characterised by cracks that develop between two or more layers that are parallel to the fibres in the ply and extend through the thickness of the ply [184]. According to [68,185–187], matrix cracking in carbon fibre/epoxy (CF/EP) laminates occurs across the whole cross-sectional area of the perpendicular plies. This may or may not trigger other failure modes, depending on the stresses generated due to temperature variations, quasi-static loads or impacts. Figure 3.1 shows matrix cracks developed through the cross-section of a glass fibre reinforced plastic (GFRP) laminate along the reinforced direction [188]. From figure 3.1, the cracks in the matrix are at an angle of 45 degrees, following the orientation of the fibres.

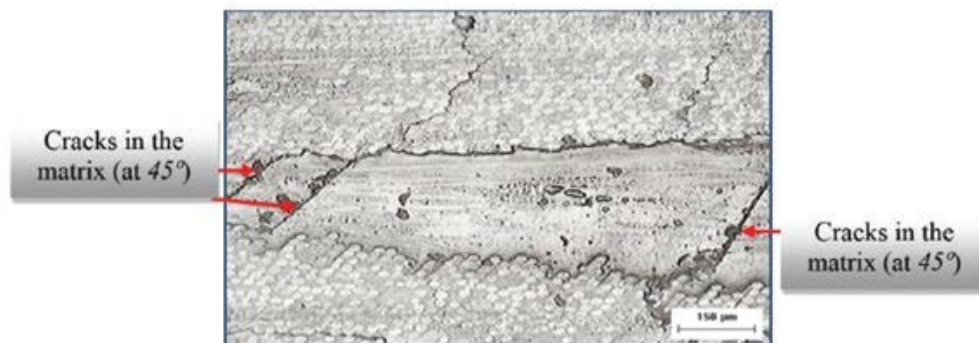


Figure 3.1 Matrix cracks in the GFRP in the reinforced direction [188].

Matrix cracking alone does not usually constitute a problem to structural integrity. However, since it is the forerunner of other (more serious) failure modes in composite laminates, it has deserved much attention from researchers. For example, extensive research has been conducted on matrix cracking and its impact on the performance of composites [187,189–191].

3.2.2 Fibre Fracture

Fibre fracture in a composite structure due to dynamic loading, reduces both the stiffness (Young's modulus) and the strength of the composite [192–194]. For example, the impact of the fibre fracture on the stiffness of the composite laminate was studied in [195]. It was observed that the initiation of the fracture mechanism in the composite has more effect on the buckling load than the reduction of its stiffness. It was also found that fibre fractures have little effect on the stiffness of the composite when compared to its effects on the strength of the material. Therefore, the load carrying capacity of a laminate should be investigated as soon as the fracture is observed.

Davidson and Waas [196] presented a novel method to study the fracture of fibre reinforced composites. Their study focused on the mode I fracture (opening) of CF and glass fibre unidirectional composites under quasi-static loading. They found that crack progression shows smooth and discontinuous responses. A simple algorithm based on the critical fracture internal stress or strain, and a critical material specific crack velocity was used to validate the experimental results.

Bedsole *et al.*[197] introduced carbon nanotubes into the interlaminar zone of unidirectional CFRP composite in order to enhance the properties of interlaminar and intralaminar fracture under dynamic and quasi-static loading conditions. They studied the dynamic interlaminar crack initiation and propagation in a fibre reinforced composite material under dynamic loading using a digital image correlation. Although their results indicated that carbon nanotubes improved the fracture toughness of the material when under dynamic and quasi-static loading conditions, they did not improve the critical stress intensity factor.

Vaughan and McCarthy [198] presented a micromechanics damage model to study the impact of intra-ply properties on the transverse shear deformation of a CF/EP

composite. They observed that the thermal residual stress has a high influence on the initial damage location in the microstructure but has less influence on the overall shear response. It was also found that due to the thermal residual stresses, the transverse fracture surface contracted slightly under the combination of transverse normal and shear loading.

3.2.3 Debonding

Debonding normally occurs at areas with high interfacial stress concentration, [199] which are related to the presence of cracks. See figure 3.2 for CFRP debonding. When subjected to an impact load, a large part of the fibre may be pulled off when adhesion fails.

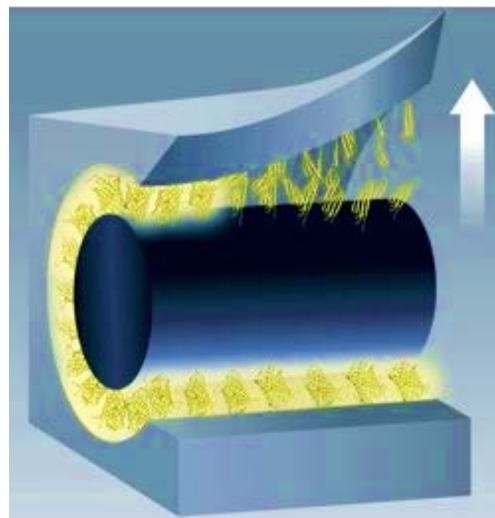


Figure 3.2 Fibre matrix debonding [200].

Several factors such as differential thermal stress, crack, ageing structure [201,202], low-velocity impact, environment and poor design method could be responsible for such a phenomenon to occur.

Although debonding is not the primary cause of failure in composite materials, it compromises the strength at its location and the surrounding fibres, which may result in a breakdown when overloaded [203].

3.2.4 Delamination

Delamination in fibre composites is mainly caused by impacts from foreign objects. It is one of the most vital failure mode in composite materials because of the strength of the composite laminates is inversely proportional to delamination [204]. That is, as the rate of delamination increases, the cohesion between the plies of the composite reduces. Hence, it is necessary to understand if delamination has initiated.

A penalty-based perspective was proposed by [205] to detecting delamination in composite laminates. Schön [206] developed a model to determine the fatigue delamination growth rate in a composite laminate. The model needs to experimentally determine the critical static energy release rates, delamination growth rate at which the critical energy release rate for quasi-static loading is reached, the delamination growth rate, and the threshold value of energy release rate of the delamination crack during a fatigue cycle. Also, [207] evaluated crack initiation and propagation, which influence the delamination process under mode I and II fatigue loading in the composite material. It was concluded that the accumulation of resin and the manufacturing procedure of the composite laminate have a high impact on the fatigue curves of delaminated specimens.

3.2.5 Fibre Pullout

Weak bonding within the laminates is the major cause of fibre pullout. Pochiraju *et al.* [208] studied the stresses caused by fibre pullout when the fibre matrix experienced frictional sliding and underwent compressive thermal residual stresses. They applied asymptotic analysis and Muskhelishvili-Kolosov theory to solve the stress within the area where the fibre was pulled out. A fibre pullout test is therefore required to determine the thermal mechanical properties (stiffness and strength) of the interfaces in a CFRP [209]. Two methods are used to conduct fibre pullout tests, namely single pullout test and multiple pullout tests.

Although a single fibre pullout test is easier to apply, it is not suitable for fibres with small diameters [210]. The multiple fibre pullout test method uses a large portion of fibres, and it gives the comparable results to the single fibre pullout test. Yue and Padmanabhan [210] used the multiple fibre pullout test technique to determine the possibility of increasing the interfacial strength of kevlar fibre/epoxy composites. In

addition, Jia *et al.*[211] proposed a numerical method to probe the fibre pullout in a carbon nanotube (CNT)–hybridised CF. The result shows that the additional bonding of the CNT matrix interface can increase the specific pullout energy and the interfacial shear strength of the hybrid fibre.

3.2.6 Micro-buckling

Fibre micro-buckling reduces the compressive strength of CFRPs [212–214]. It affects the mechanical properties and matrix of the composite laminates (figure 3.3). The local failure and matrix crack occurs due to micro-buckling [215]. Several researchers have conducted an experiment on the cause and effect of micro-buckling in composites. Berbinau *et al.*[216] examined the shear strains that developed in the matrix as a result of fibre micro-buckling. It was confirmed that fibre failure starts on the compression side of a composite, where the maximum fibre curvature occurs.

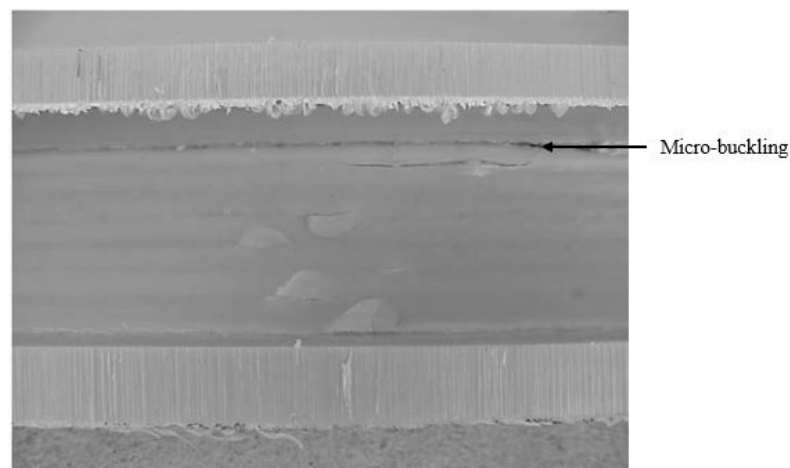


Figure 3.3 Fibre micro-buckling [215].

Mohammadabadi *et al.*[217] studied the thermal buckling of micro-composite laminates and the impact of shear deformation in the composite laminate. In addition, Huang *et al.*[7] proposed the use of finite element analysis (FEA) to study micro-buckling in a laminated composite plate.

3.2.7 Kink Bands

A kink band is a deformation that has a pronounced twist of the fibres with a deviated orientation from the original orientation on the composite laminate. It occurs due to fibre dislocation or plastic micro-buckling in the composite laminate [218], which is

caused by compressive force (See figure 3.4). Kink bands reduce the compressive strength of a composite laminate. When formed, it expands continuously at a constant stress level known as propagation stress [219]. Budiansky *et al.*[220] examined the transverse and band broadening kink propagation based on nonlinear couple stress theory of composite kinking in one dimension. Recently, Svensson *et al.*[221] developed a model to estimate the cohesive law related to kink band evolution in a unidirectional composite laminate.

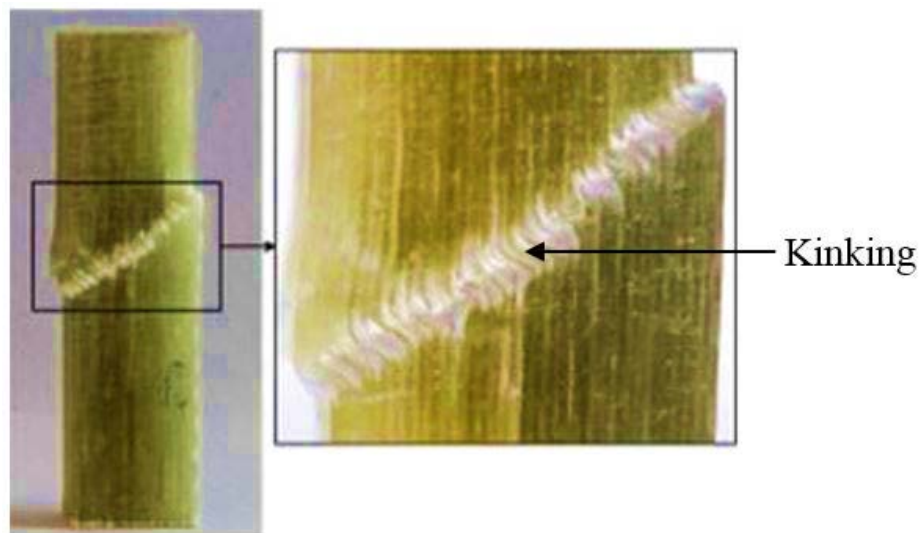


Figure 3.4 Kink band [222].

Despite the immense studies conducted by several researchers to ascertain how compressive failures occur, it has not been easy to estimate the compressive failure in a unidirectional composite. An increase in compressive load introduces fibre damage in the composite. Kink bands could be triggered by the transverse movement of fibres that are close to broken fibres due to shear failures at various frail defects [223]. The initiation of kink bands on a composite laminate drastically reduces its strength and causes it to fail. This was analysed experimentally and through analytical models by Bažant *et al.*[224]. It was confirmed that the size of the kink band has a noticeable effect on its propagation. Vogler and Kyriakides [225] experimentally analysed APC-2/AS4 thermoplastic composites and observed that the quasi-static propagation of kink bands occur at a stress point as high as 40% of the toughness of the undamaged material.

Gonzalez-Chi *et al.*[226] measured the distribution of axial stress around a kink band on a fibre installed in a thermoplastic model composite using Raman spectroscopy

technique. They found out that the maximum interfacial stress was close to the kink band where the bond between the fibre laminate is still intact. Hsu *et al.*[227] simulated the steady state broadening of kink bands with a micromechanical model as examined by Vogler and Kyriakides [219]. The model could forecast the propagation stress remarkably. Likewise, Pimenta *et al.*[228] developed a micromechanical model for the formation of kink bands in a unidirectional fibre reinforced composite. This study followed the one from Pimenta *et al.*[229]. The model could forecast the width of the kink band, the deviation and primary stress fields in fibres and matrix at various phases of the formation of the kink band, the longitudinal compressive toughness of the composite, and the direction of the fibres when the failure was initiated in the fibre.

Furthermore, Pimenta *et al.*[229] investigated the inception and the propagation of kink bands using numerical models and experimental examination. The results show that the formation of kink bands is related to the weakening of the matrix, whereby the fibres around the compressive area fail before any other location. The rate at which kink band releases energy for a unit load decreases initially but increases at a certain length of propagation [230].

3.3 Concluding Remarks

Some primary failure mechanisms in composite structure have been extensively discussed. The aim is to highlight the common failures expected in this research work. The first failure to occur in a composite material is matrix cracking between layers that are parallel to the fibres in the ply. Through this failure mode, other failure modes may occur, for example fibre fracture, etc. The dynamic loading on composite materials could result to possible fibre fracture. Which could impact the stiffness and strength of the structure. This suggest that the load carrying capacity of such structure would be compromised when fibre fracture occurs.

The high interfacial stress concentration in a composite material result to debonding, which also compromise the strength of the material within the vicinity of its occurrence. Also, the compressive strengths can be compromised by fibre micro-buckling and kink bands failure modes. In addition, the presence of foreign object in a composite material could result to delamination. This failure mode is very critical because it is inversely

proportional to the strength of the composite material. Hence, it is important to monitor its occurrence in a composite structure to avert an unforeseen disaster.

“Research ... is nothing but a state of mind - a friendly, welcoming attitude toward change; going out to look for a change instead of waiting for it to come. Research, for practical men, is an effort to do things better.... The research state of mind can apply to anything-personal affairs or any kind...”

— Charles F. Kettering

4 Representation of the Receptance in the Elliptical Plane

4.1 Relevance of the Representation of the Receptance in the Elliptical Plane

The modal parameters of a structure offer information about its behaviour towards any mechanical disturbances (for instance vibration) and damage. This chapter is focused on the following:

- The estimation of the modal damping from the FRF when represented in the Elliptical Plane
- The estimation of the modal constant from the FRF when represented in the Elliptical Plane
- To compare the modal identification Elliptical Plane based method with existing method
- To find the damping factor
- To compare the uncertainty in the estimation of the damping factor from the FRF
- To compare the uncertainty in the determination of the damping factor with other existing methods
- To answer the question, can the ellipse area changes be related to damage?

It is pertinent to note that the area and shape of the ellipse depends on the modal constants, which are local properties, while damping is a global property [5].

4.2 Introduction

Since the early 70s, many researchers have addressed the challenges associated with the procedures of modal identification [24]. All the available modal identification methods have different amount of sophistication and need the utilisation of software that may be expensive to procure.

The Operational Modal Analysis (OMA) has gained more attention than the traditional Experimental Modal Analysis (EMA) in the past few years. For instance, some of the past improvements in OMA identification techniques are presented in [231–234]. In

terms of EMA, later publications are more focused on engineering applications or dealing with uncertainty in existing techniques, as can be found in [58,235,236]. OMA deals with Operational Deflection Shapes (ODS) and many often make use of output-only measurements, this means that excitation loads are not known. EMA utilizes the input forces and output responses to estimate modal parameters and mode shapes. In the past three decades, several modal identification algorithms have been developed [237]. However, even though some improvements have been seen in terms of EMA modal identification techniques [58,236,237], in recent years, some interesting results has been achieved.

If the aim is to determine the global modal characteristics, it is possible to use simple procedures that give quick estimates of the required information. Recently, the issue of identification of the modal damping factors has been presented in [57,238] from a different point of view. In that novel method, the dissipated energy per cycle of vibration was the starting point instead of the governing Equations of the dynamic motion as is the norm. The proposed approach is based on a special plot of the receptance, whereby the sine of the phase angle and the amplitude are the vertical and horizontal axis respectively (similar to the Nyquist plot of the receptance).

As is illustrated in this work, this plot has unique properties, one of which is that the data points around a resonant frequency depict a loop that is shaped like the half of an ellipse. Also, it is illustrated that the major and minor axis of the ellipse are related to the modal constants, which can be determined using numerical extrapolation techniques. The importance of modal constants cannot be overlooked, because they provide information about the mode shapes (local modal characteristics) which, in the general case of non-proportional damping, are complex quantities [24]. The modal identification methods seek to extract from experimental data the modal parameters that characterise the dynamic behaviour of a structure [239]. Therefore, a modal model is derived through the determination of the values (for each mode of vibration) of the natural frequency (not investigated in this work), damping ratio (examined in [57,238]) and complex modal constant (investigated in this work). Once the modal model is known, it can be utilized in diverse areas of structural dynamics, i.e. structural modification, coupling techniques (including mass cancellation), finite element

updating, transmissibility and structural health monitoring, etc. [20,21,24,38,44,240,241].

This work shows the development of a new proposed procedure for the determination of the modal constants and demonstrates its application using both numerical and experimental examples. The proposed technique highlights a useful representation of the modal properties.

4.3 Theoretical Development

This section lays the foundation for the theory of modal response of structures.

4.3.1 Definitions

The general Equation of motion for a Single Degree of Freedom (SDOF) viscous system (see Figure 4.1) is given by:

$$m\ddot{x} + c\dot{x} + kx = Fe^{i\omega t} \quad (22)$$

where m represents the mass, c represents the viscous damping coefficient, k represents the stiffness, F represents the amplitude of the oscillatory force, t represents the time variable and $i = \sqrt{-1}$ represents the imaginary number.

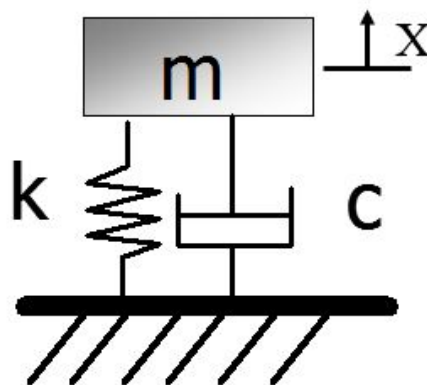


Figure 4.1 Mass-Spring-damper system.

When the system is excited by an harmonic force at a frequency ω , it can be shown [24,242,243] that for each vibration cycle the system dissipates – through its viscous damper – an amount of energy that is directly proportional to the damping coefficient, the excitation frequency and the square of the response amplitude X :

$$W_{diss} = \int_0^T f \dot{x} h t = \pi c \omega X^2 \quad (23)$$

where $T = 2\pi/\omega$ is the time period of oscillation. However, experimental evidence from tests performed on a large variety of materials show that the damping due to internal friction (material hysteresis) is nearly independent of the forcing frequency but still proportional to the square of the response amplitude [242], i. e.:

$$W_{diss} \propto CX^2 \quad (24)$$

where C is a constant. Therefore, from Equations (23) and (24) the equivalent damping coefficient is:

$$c = \frac{C}{\pi\omega} = \frac{h}{\omega} \quad (25)$$

where h is the hysteretic damping coefficient. Under such conditions, Equation (22) can be re-written as:

$$m\ddot{x} + \frac{h}{\omega}\dot{x} + kx = Fe^{i\omega t} \quad (26)$$

If the stiffness is a complex quantity, i.e., defined as the sum of the stiffness itself (k , is the real part) and the damping coefficient (h , is the imaginary part):

$$k^* = k + ih = k(1 + i\eta) \quad (27)$$

where,

$$\eta = h/k \quad (28)$$

and knowing that $\dot{x} = i\omega x$ for harmonic motion, Equation (26) may be re-written as:

$$m\ddot{x} + k(1 + i\eta)x = Fe^{i\omega t} \quad (29)$$

Based on Equation (29) it is concluded that the dissipated energy per cycle of vibration is independent of the forcing frequency.

4.3.2 Determination of the Hysteretic Damping

The experimental measurement of the hysteretic damping factor can be conducted by means of cyclic force-displacement tests in the elastic domain [244]. It can be shown that the energy dissipated per cycle of oscillation is given by the ellipse area of the

force-displacement plot during a complete cycle. Rearrangement of Equations (23), (25) and (28) result in:

$$W_{diss} = \pi h X^2 = \pi \eta k X^2 \quad (30)$$

This area, the integral of the force along the displacement, conforms to the non-conservative work done per cycle. That is to say, in a plot of force vs displacement at a particular frequency, damping can be regarded as a means that initiates a lag between force and displacement and appears as an elongated ellipse [15,242]. Moreover, from [243], it can be demonstrated that the dissipated energy can be written alternatively as:

$$W_{diss} = \pi F X |\sin(\theta)| \quad (31)$$

where θ is the phase angle between the force and the displacement response. From Equations (30) and (31) a relationship between the hysteretic damping coefficient, the displacement, the force, and the phase angle can be established as:

$$h = \frac{F}{X} |\sin(\theta)| \quad (32)$$

For harmonic motion, the ratio between the force and the displacement is a transfer function usually stated as Dynamic Stiffness [24]. Often, in experimentation, the receptance is measured instead, which is the transpose of the Dynamic Stiffness. For harmonic motion, it is stated as:

$$\alpha(\omega) = \frac{x(\omega)}{f(\omega)} \quad (33)$$

The quantities $x(\omega)$ and $f(\omega)$ are the complex response and complex force with amplitudes $X(\omega)$ and $F(\omega)$ respectively. If $H(\omega)$ represents the amplitude of the receptance, then Equation (32) can be re-written as:

$$|\sin[\theta(\omega)]| = h \cdot H(\omega) \quad (34)$$

The aim of all this development was to state Equation (34). This can be further stated as:

$$|\sin(\theta)| = h \cdot H \quad (35)$$

It can be deduced from Equation (34) that the hysteretic damping coefficient h can be determined from the measurement of the amplitude and phase of the receptance. Once the stiffness is known, Equation (28) allows determining the hysteretic damping factor η . The estimation of the damping factor and the generalisation to MDOF systems is discussed in detail in [57,238].

If Equation (34) is plotted in a plane composed by the vertical axis $y \equiv \sin(\theta)$ and the horizontal axis $x \equiv H$, it should be evident that it look much like the Equation of a straight line with slope h . However, it also has other vital properties, examined in the following sections.

4.3.3 Determination of the Real and Imaginary Parts of the Modal Constant

The receptance of a MDOF system can be shown as [24]:

$$\alpha = \sum_{r=1}^N \frac{\bar{A}_r}{\omega_r^2 - \omega^2 + i|\eta_r|\omega_r^2} \quad (36)$$

where \bar{A}_r is the complex modal constant and ω_r is the angular natural frequency, for mode r , and N is the number of DOFs. If the modes are well-spaced, close to a resonance ω_r , the effect from other mode is negligible when compared to the resonant mode [57,238]. Equation (36) becomes:

$$\alpha_{\omega \rightarrow \omega_r} \cong \frac{\bar{A}_r}{\omega_r^2 - \omega^2 + i|\eta_r|\omega_r^2} \quad (37)$$

which looks like the Equation of an SDOF with a complex modal constant;

$$\bar{A}_r = A_R + iA_I \quad (38)$$

where A_R is the real part of the modal constant and A_I is the imaginary part of the modal constant. The following development is based on this assumption: that mode shapes are well-spaced in the frequency spectrum so that Equation (37) is true at the vicinity of mode r .

Condition 1: $|\omega_r^2 - \omega^2| \gg 0$

Away from the natural frequency, and considering, a lightly damped system, for convenience, where $\eta_r \cong 0$, Equation (37) is simplified to:

$$\alpha_{\omega \ll \omega_r} \cong \frac{A_R + iA_I}{\omega_r^2 - \omega^2} = \frac{A_R}{\omega_r^2 - \omega^2} + i \frac{A_I}{\omega_r^2 - \omega^2} \quad (39)$$

Representing the receptance in the Argand plane (see Figure 4.2),

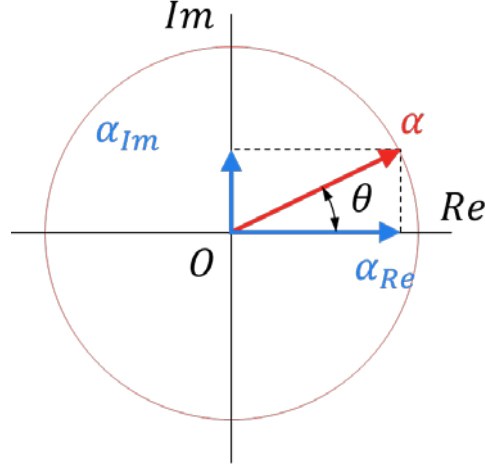


Figure 4.2 The representation of the receptance in the Argand plane.

then the phase $\theta_{\omega \ll \omega_r}$ is related to the imaginary $\alpha_{I \omega \ll \omega_r}$ and real $\alpha_{R \omega \ll \omega_r}$ parts of the receptance by:

$$\tan[\theta_{\omega \ll \omega_r}] = \frac{\alpha_{I \omega \ll \omega_r}}{\alpha_{R \omega \ll \omega_r}} = \frac{\frac{A_I}{\omega_r^2 - \omega^2}}{\frac{A_R}{\omega_r^2 - \omega^2}} = \frac{A_I}{A_R} \quad (40)$$

and

$$\theta_{\omega \ll \omega_r} = \tan^{-1}\left(\frac{A_I}{A_R}\right) \quad (41)$$

Thus, in the $x \equiv H$ vs $y \equiv \sin(\theta)$ plane this becomes:

$$|\sin[\theta_{\omega \ll \omega_r}]| = \sin\left[\tan^{-1}\left(\frac{A_I}{A_R}\right)\right] \quad (42)$$

Condition 2: $|\omega_r^2 - \omega^2| = 0$ at resonance

At the natural frequency, i.e., when $\omega = \omega_r$, Equation (37) reaches its maximum value:

$$\alpha_{\omega=\omega_r} = \frac{A_R + iA_I}{i|\eta_r|\omega_r^2} = \frac{A_I}{|\eta_r|\omega_r^2} - i \frac{A_R}{|\eta_r|\omega_r^2} \quad (43)$$

Hence, the amplitude of the receptance

$$H = |\alpha| = \sqrt{\alpha_{Re}^2 + \alpha_{Im}^2} \quad (44)$$

at the resonance is:

$$H_{\omega=\omega_r} = |\alpha_{\omega=\omega_r}| = \frac{1}{|\eta_r| \omega_r^2} \sqrt{A_I^2 + A_R^2} \quad (45)$$

which, when solved for A_R , becomes:

$$A_R = \sqrt{H_{\omega=\omega_r}^2 |\eta_r^2| \omega_r^4 - A_I^2} \quad (46)$$

Equation (46) allows determining the real part of the modal constant from its complex counterpart, which must be determined in a way. Therefore, if one solves Equation (42) for A_I when considering Equation (46), and after some mathematical procedure, this results in:

$$A_I = \sqrt{\frac{H_{\omega=\omega_r}^2 |\eta_r^2| \omega_r^4}{[\tan |[\sin^{-1}(\theta_{\omega \ll \omega_r})]|]^{-2} + 1}} \quad (47)$$

Equations (46) and (47) allow determining the real and imaginary parts of the modal constant from the plot of the receptance in the $x \equiv H$ vs $y \equiv \sin(\theta)$ plane. The above representation is the elliptical plane modal analysis technique.

4.4 Properties of the Receptance in the ‘Elliptical Plane’

To show the representation of receptance in the ‘elliptical plane’ and how the modal constants are determined, an arbitrary SDOF system having complex modal constant $\bar{A}_r = 1000 + 500i$, 20.4Hz natural frequency and a 1% modal damping factor would be considered. In addition, it is assumed that the receptance was measured experimentally within the frequency range of 0 to 40Hz with an acquisition period of 2s (i.e. a frequency resolution of 0.5Hz). The plots of the amplitude H and phase θ of

the receptance determined in the frequency domain and the ‘elliptical plane’ are shown in figure 4.3 and figure 4.4 respectively.

The approach to determine the modal constants included coding software that does the following:

1. Representation of the receptance in the ‘elliptical plane’;
2. Extrapolation of the data points close to a resonant frequency, with an elliptical function centred at (0, 0) and tangent to an imaginary horizontal line at $y = \pm 1$;
3. Determination of $\theta_{\omega \ll \omega_r}$ from the intersection of the ellipse at the y-axis;
4. Determination of $H_{\omega = \omega_r}$ from the point where the ellipse is tangent to an imaginary vertical line;
5. Determination of the angle the ellipse makes with the horizontal to determine the hysteretic damping coefficient. The hysteretic damping factor is then determined in the same way to what was done in [57,238];
6. Determination of the modal constants from Equations (46) and (47).

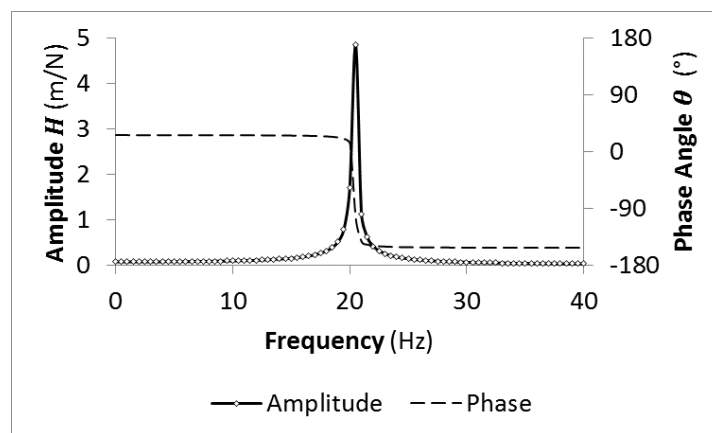


Figure 4.3 Numerical example of the amplitude and phase of a SDOF receptance in the frequency domain.

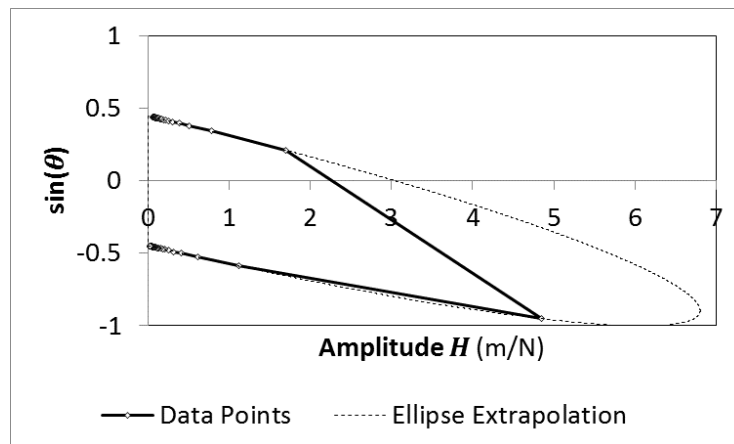


Figure 4.4 Numerical example of the same SDOF receptance represented in figure 4.3 in the ‘elliptical plane’.

The first thing to observe is that when the receptance data points are plotted in the ‘elliptical plane’, it depicts a loop that can be fitted with the half of an ellipse. In such a case, since the data has no noise and it is an SDOF, a suitable relationship between the data and the fit was obtained (figure 4.4). This ellipse has some outstanding properties, namely:

1. The angle of the ellipse depends on the damping coefficient h and the ellipse is centred at $(0, 0)$. This is not surprising, because since Equation (34) is the Equation of a straight line with slope h , as reported earlier in [57,238], and the intercept is at zero.
2. The function is restricted between 1 and -1 since it relies on a sinusoidal trigonometric function. In the illustration presented, where half an ellipse is represented, the elliptical extrapolation is tangent at $y = -1$;
3. Given the fact that the natural frequency (20.4Hz) is not a multiple of the frequency resolution (0.5Hz) in the example presented, the frequency spectrum in Figure 4.3 does not indicate the precise amplitude at the natural frequency (the maximum value as observed from figure 4.3 would be 4.85). The amplitude at the resonance for this given example is determined to be 6.805 from Equation (36) with $N = 1$ (since it is SDOF). Meanwhile, it can be noticed from the example given that the ellipse in Figure 4.4 is tangent at an imaginary vertical line that crosses the x -axis at 6.805, precisely the amplitude at the resonance, $H_{\omega=\omega_r}$. This quantity is required to obtain the modal constants through Equations (46) and (47). The advantage of the ellipse is that it makes it possible

to determine the amplitude at the resonance from experimental data, whereas Equation (36) would not be possible to use as a starting point for most real situations;

4. The value $\theta_{\omega \ll \omega_r}$ needed to determine the imaginary part A_I of the modal constant (Equation 47) can also be determined from the ellipse, since this is when the ellipse crosses the y-axis, i.e. $\theta_{\omega \ll \omega_r} = \sin^{-1}[\sin(\theta_{x=0})]$. This is used to create the ellipse from experimental data.

4.5 Numerical Validation of the “Elliptical Plane” Modal Identification Method

To illustrate the proposed method, a total of ten various cases were simulated. These are listed in table 4.1¹. Cases 1 to 6 all are SDOF: cases 1 and 2 have real modal constants and cases 3 to 6 have complex modal constants with varying signals (as seen in [15] the signal of the modal constants is related to the signal of the slope of the ellipse major axis and the phase angle). Cases 7 and 8 are MDOF (2-DOF) with ‘low’ damping factors (figure 4.5 and figure 4.6) and cases 9 and 10 are MDOF with one ‘highly damped’ mode.

Figure 4.5 and figure 4.6 show the MDOF case 7 in both the frequency domain and ‘elliptical plane’, where the fitting ellipses can be seen clearly. However, the method assumes that the mode shapes are well spaced so that the effect from mode shapes close to the mode shape being identified is negligible. Thus, each mode is determined individually by ‘zooming-in’ in the vicinity of its respective natural frequency. This is shown in figure 4.7, figure 4.8, figure 4.9 and Figure 4.10 where the receptance close to the first and second mode shapes are represented, respectively, in both the frequency domain (amplitude and phase) and the ‘elliptical plane’.

¹ The natural frequencies, modal constants and hysteretic damping factors may not have any physical/real meaning. The aim is to use them for the illustration.

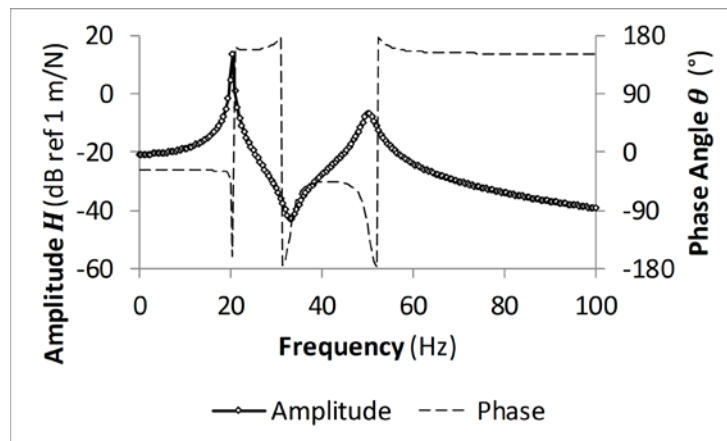


Figure 4.5 Amplitude of the MDOF receptance for numerical case 7 in the frequency domain.

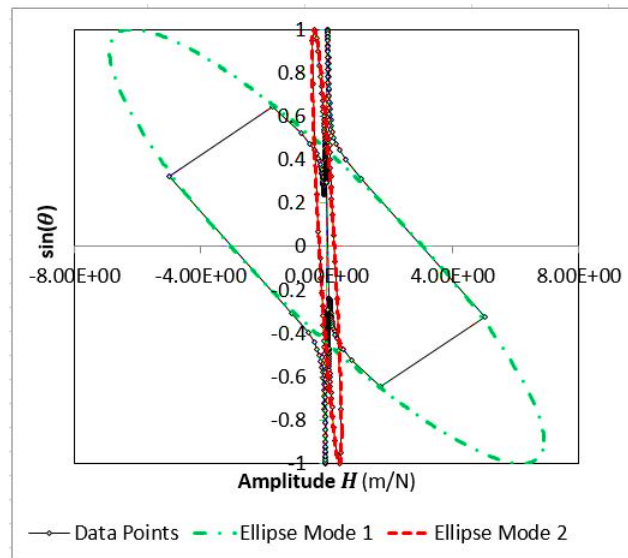


Figure 4.6 MDOF receptance for numerical case 7 (Figure 4.5) represented in the 'Elliptical Plane' with two ellipses fitting the data at the vicinity of the mode shapes (the plot was mirrored for better convenience. Only half of the ellipse is actually visible with the discussed method).

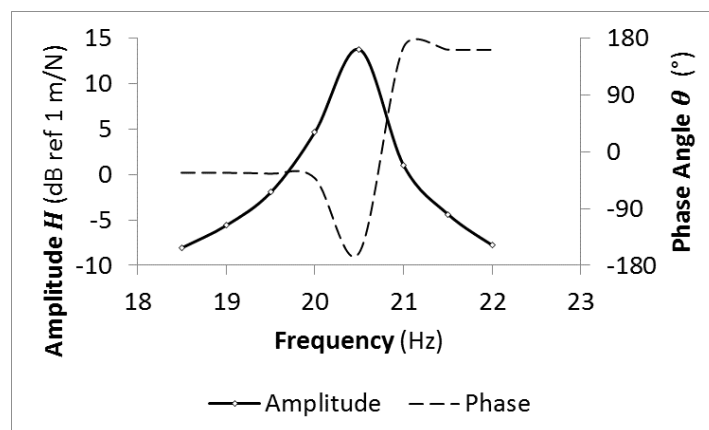


Figure 4.7 Amplitude and phase of the receptance in the frequency domain near the 1st resonance of simulated case 7.

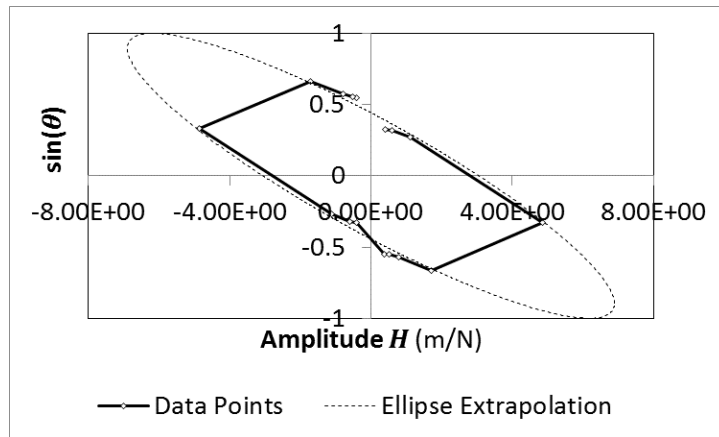


Figure 4.8 Receptance near the 1st resonance of simulated case 7 (represented in the 'Elliptical Plane') with the modal identification fitting ellipse (the plot was mirrored for better convenience).

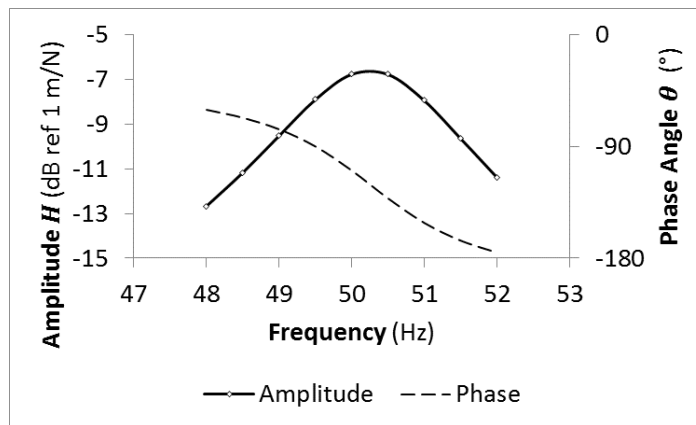


Figure 4.9 Amplitude and phase of the receptance in the frequency domain near the 2nd resonance of simulated case 7.

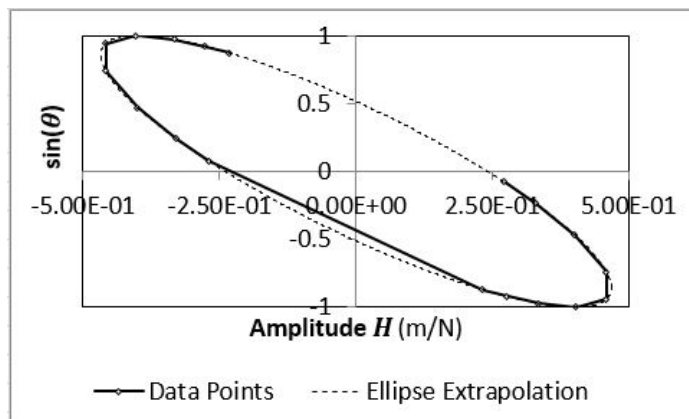


Figure 4.10 Receptance near the 2nd resonance of simulated case 7 (represented in the 'Elliptical Plane') with the modal identification fitting ellipse (the plot was mirrored for better convenience).

The results from the modal identification following the procedure outlined herein are presented in Table 4.1. The percentage difference between the theoretical values (Table 4.1) and the numerical results (Table 4.2) are shown in Table 4.3.

Table 4.1 Numerical models' modal simulated properties.

Case	Mode 1					Mode 2				
	Modal Constant 1		f (Hz)	η (%)	Amp (N/m)	Modal Constant 2		f (Hz)	η (%)	Amp (N/m)
	Real	Imag				Real	Imag			
1	1000	0	20.4	1	6.087	-	-	-	-	-
2	-1000	0	20.4	1	6.087	-	-	-	-	-
3	1000	500	20.4	1	6.805	-	-	-	-	-
4	-1000	-500	20.4	1	6.805	-	-	-	-	-
5	1000	-500	20.4	1	6.805	-	-	-	-	-
6	-1000	500	20.4	1	6.805	-	-	-	-	-
7	1000	-500	20.4	1	6.805	2000	-1200	50.25	5	0.4679
8	1000	-500	20.4	1	6.805	2000	1200	50.25	5	0.4679
9	1000	-500	20.4	1	6.805	2000	-1200	50.25	50	0.04679
10	1000	-500	20.4	50	0.1361	2000	-1200	50.25	5	0.4679

Table 4.2 Results from the modal identification (numerical examples).

Case	Mode 1					Mode 2				
	Modal Constant 1		f (Hz)	η (%)	Amp (N/m)	Modal Constant 2		f (Hz)	η (%)	Amp (N/m)
	Real	Imag				Real	Imag			
1	1041	1.033	20.4	1	6.203	-	-	-	-	-
2	-1000	1.013	"	1	6.087	-	-	-	-	-
3	1000	500	"	1	6.805	-	-	-	-	-
4	-1000	-500	"	1	"	-	-	-	-	-
5	1000	"	"	1	"	-	-	-	-	-
6	-1000	500	"	1	"	-	-	-	-	-
7	1016	-502.1	"	1	6.892	2001	-1198	50.25	5.003	0.4676
8	1000	-500	"	1	6.799	2000	1200	"	5	0.4679
9	993.8	-520.3	"	1.027	6.648	2021	-1201	50.29	49.92	0.04715
10	995.1	-502.1	"	50.16	0.1353	1996	-1208	50.25	4.979	0.4700

Table 4.3 Difference between the theoretical values and the numerical results (all values are expressed in %).

Case	% error mode 1					% error mode 2				
	Modal Constant 1		f (Hz)	η (%)	Amp (N/m)	Modal Constant 2		f (Hz)	η (%)	Amp (N/m)
	Real	Imag				Real	Imag			
1	4.10	-	0.00	0.00	1.91	-	-	-	-	-
2	0.00	-	''	''	0.00	-	-	-	-	-
3	''	0.00	''	''	''	-	-	-	-	-
4	''	''	''	''	''	-	-	-	-	-
5	''	''	''	''	''	-	-	-	-	-
6	''	''	''	''	''	-	-	-	-	-
7	1.60	0.42	''	''	1.28	0.05	-0.17	0.00	0.06	-0.06
8	0.00	0.00	''	''	-0.09	0.00	0.00	''	0.00	0.00
9	-0.62	4.06	''	2.70	-2.31	1.05	0.08	0.08	-0.16	0.77
10	-0.49	0.42	''	0.32	-0.59	-0.20	0.67	0.00	-0.42	0.45

Table 4.3 indicates that there is a correlation between the theoretical models and the results obtained from the modal identification, at least for SDOF systems. Although the results from the MDOF are not that good, but still acceptable. The worst cases were cases 1, 9 and 10. In the ‘ideal’ case 1, where the modal constant is real, the ellipse becomes a straight line, thus the identification process fails due to problems connected to the ellipse curve fitting (i.e., the ellipse has no minor axis). Therefore, a small value had to be added to the imaginary part of the modal constant so that the algorithm yielded significant results. Notwithstanding, in real situations, the modal constants are usually complex quantities; thus, this ‘ideal’ condition may not reflect a real issue. Concerning cases 9 and 10, the slightly higher errors might be linked to the presence of a ‘highly damped’ mode shape. Since the technique was developed for lightly damped systems, this result is not surprising. Although the assumption is that the Elliptical Plane method worked for lightly damped structure, it was still tested under more heavily damped condition to see if the method would still work. It was observed that the method can be used in more heavily damped conditions. Despite the fact that, the maximum error was in the identification of the imaginary part of the first modal constant with only a value of 4.1%.

It is important to note that the modal identification procedure ‘isolated’ the mode shapes as proposed in [15,25], with the purpose of improving the accuracy of the modal parameters’ identification. This approach exists in other modal identification techniques, for example in the BETAlab software [25] that utilises the CRF [245]. In this method, once one mode shape is determined, it is removed from the experimental

curve to annul (or at least minimise) the effect from other mode shapes. This also implies that the modal identification procedure is run at least twice so that each mode is determined with the minimum possible effect from the other mode shapes within the frequency range.

4.6 Experimental Validation of the “Elliptical Plane” Modal Identification Method

4.6.1 Experimentation Setup

The composite plate used in this study is made up of 8 unidirectional layers with a $[0/90]_{2s}$ layup. Each layer is made of an epoxy resin impregnated with CF satin weave Cytec Cycom 934-373KT300. The dimensions of the test plate are, approximately, 360x262x3mm.

Free-free boundary conditions were simulated in the lab. The specimen plate was suspended vertically by 2 nylon strings, which were attached to two 1mm diameter drilled holes positioned at 50mm from the plate’s sides and at 5mm from its top edge. A transfer FRF was measured using a National Instruments DAQ-9234 analogue input data acquisition module on a National Instruments cDAQ-9174 USB chassis. The first channel was assigned to the excitation force (measured with a PCB 208C01 force transducer) and the other one was used to determine the acceleration response using three PCB 352C22 lightweight teardrop accelerometers positioned at the edges of the test plate.

An electromagnetic shaker LDS V201 was used to generate the excitation signal, at a single coordinate, with a copper pushrod 60mm long attached to the force transducer at the other end. A multisine [246] excitation signal ranging from 0 to 200Hz frequency with a 0.25Hz frequency resolution was produced and amplified using an NI 9263 analogue output module and an LDS PA25E power amplifier.

Signal Express 2012 from National Instruments was utilised to process and record the results. The FRFs were recorded under the form of receptance and a rectangular window was used during the signal acquisition. A schematic representation of the

‘zooming-in’ in the vicinity of its respective natural frequency, to eliminate (or reduce) the effect that the neighbouring mode shapes would have on the mode shape being identified. This is shown in Figure 4.14 to Figure 4.21 where the receptances in the vicinity of the four mode shapes are represented in the frequency domain (amplitude and phase) and in the ‘Elliptical Plane’, respectively.

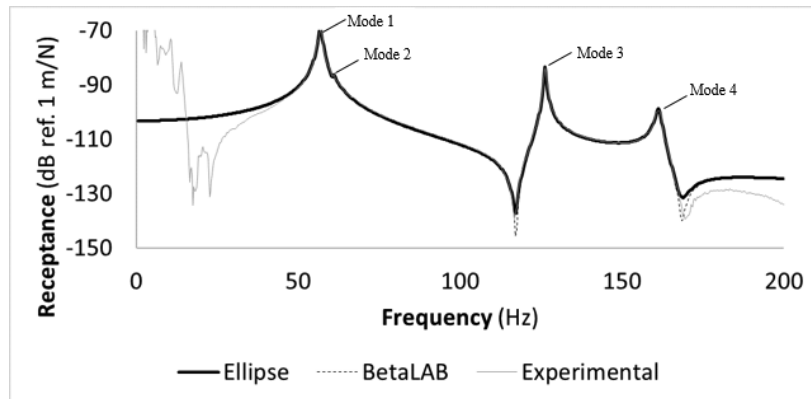


Figure 4.13 Receptance curve in the 0 to 200 Hz frequency range – experimental curve and regenerated identified curves through the Elliptical Plane technique and the software BETAlab.

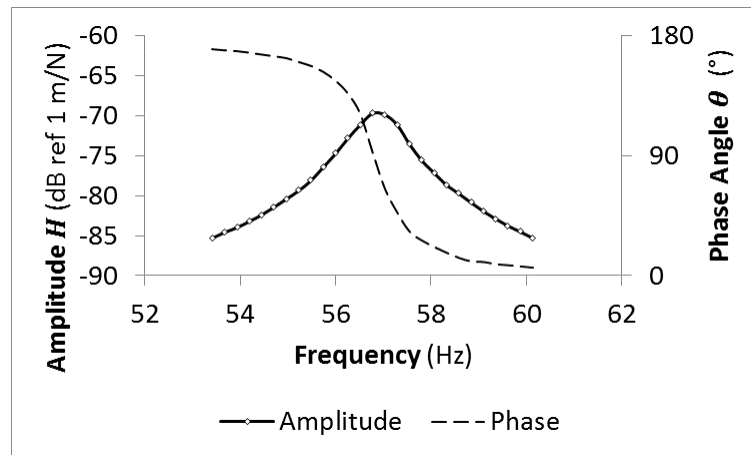


Figure 4.14 Amplitude and phase of the receptance in the frequency domain near the 1st experimental resonance.

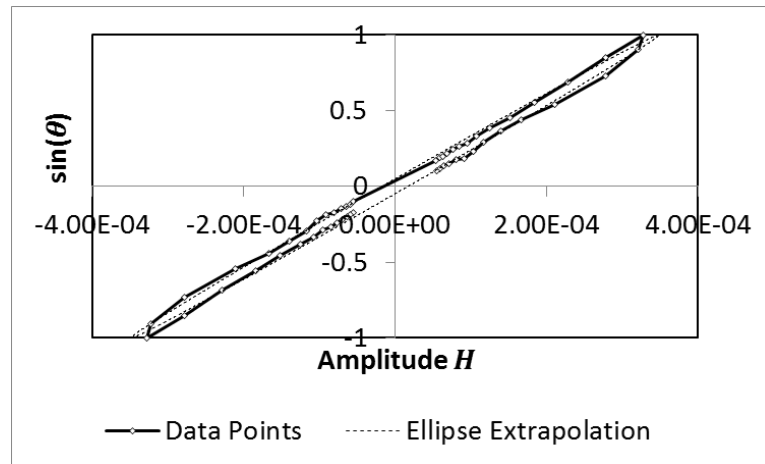


Figure 4.15 Receptance near the 1st experimental resonance (represented in the ‘Elliptical Plane’) with the modal identification fitting ellipse (the plot was mirrored for better convenience).

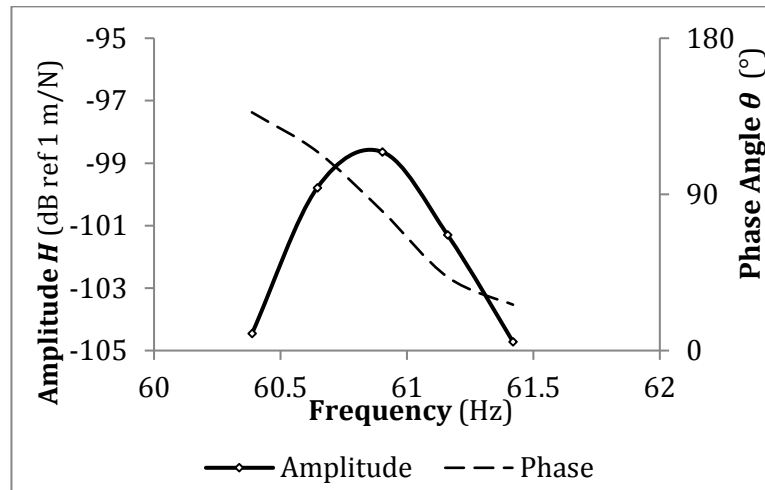


Figure 4.16 Amplitude and phase of the receptance in the frequency domain near the 2nd experimental resonance.

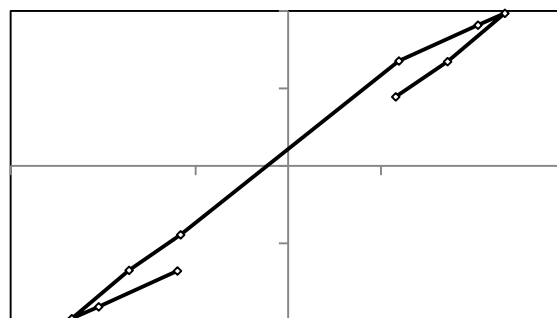


Figure 4.17 Receptance near the 2nd experimental resonance (represented in the ‘Elliptical Plane’) with the modal identification fitting ellipse (the plot was mirrored for better convenience).

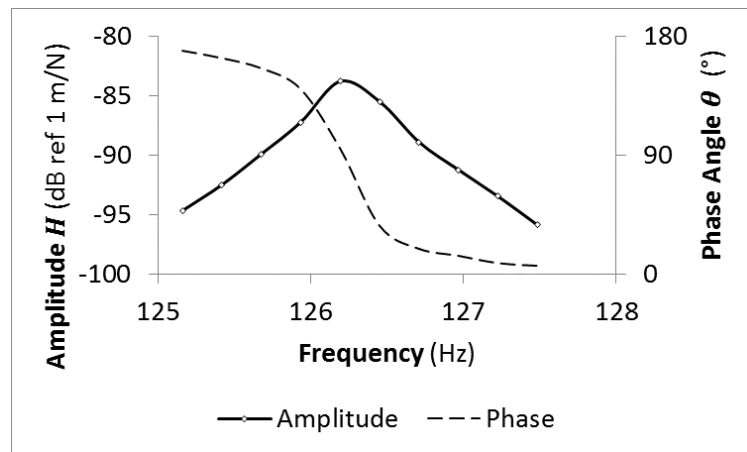


Figure 4.18 Amplitude and phase of the receptance in the frequency domain near the 3rd experimental resonance.

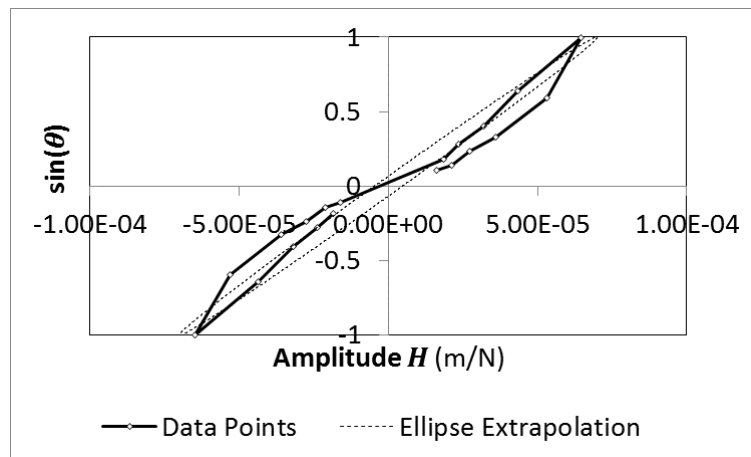


Figure 4.19 Receptance near the 3rd experimental resonance (represented in the 'Elliptical Plane') with the modal identification fitting ellipse (the plot was mirrored for better convenience).

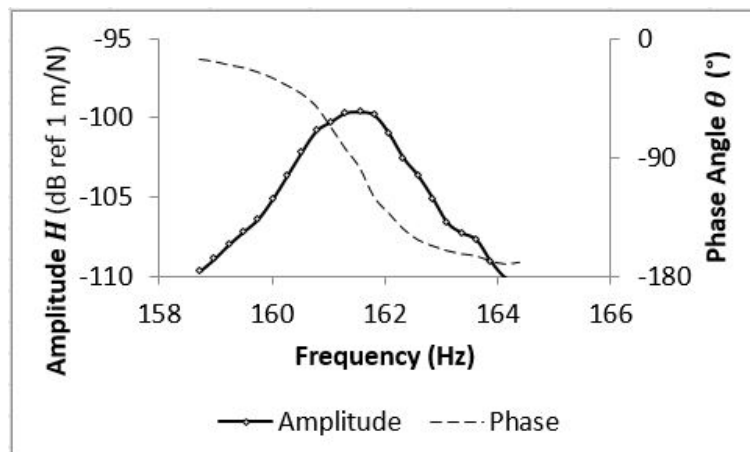


Figure 4.20 Amplitude and phase of the receptance in the frequency domain near the 4th experimental resonance.

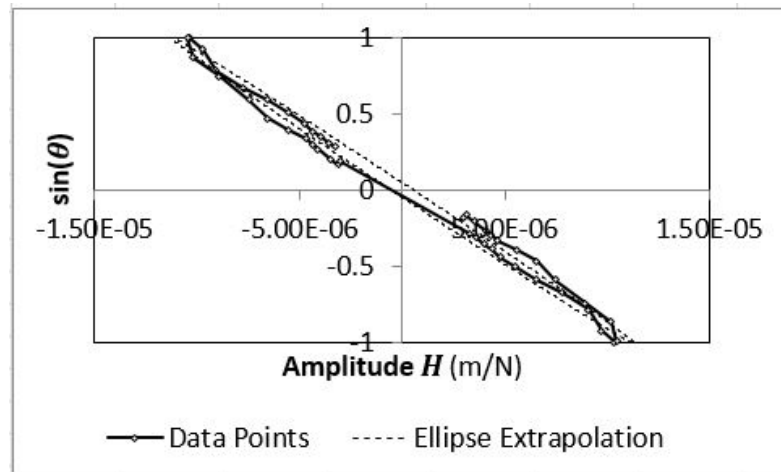


Figure 4.21 Receptance near the 4th experimental resonance (represented in the ‘Elliptical Plane’) with the modal identification fitting ellipse (the plot was mirrored for better convenience).

The percentage difference between the values acquired with the elliptical plane technique (Table 4.4) and BETAlab (Table 4.5) are shown in Table 4.6. It is important to note that, due to noise in the experimental data, the ‘best ellipse fitting’ was determined by a combination of two parameters: a correlation factor (based on a least-squares fit) and the best approximation between the area of the shape formed by the extrapolated ellipse and the data points in the ‘elliptical plane’.

Table 4.4 Results from the Modal identification using the Elliptical Plane technique (experimental examples).

Mode	Identification from Elliptical Plane technique			
	Modal Constants		η (%)	Amp (N/m)
	Real	Imag		
1	-8.243E-01	4.522E-02	1.866	3.470E-04
2	-1.808E-02	3.504E-03	1.051	1.199E-05
3	-2.033E-01	1.171E-02	0.4551	7.118E-05
4	1.155E-01	6.039E-03	0.996	1.121E-05

Table 4.5 Results from the Modal identification using the software BETAlab (experimental examples).

Mode	Identification from BETAlab			
	Modal Constants		η (%)	Amp (N/m)
	Real	Imag		
1	-8.285E-01	4.077E-02	1.876	3.464E-04
2	-1.674E-02	-7.510E-04	0.9793	1.172E-05
3	-1.976E-01	7.004E-03	0.4401	7.143E-05
4	1.148E-01	-8.384E-03	0.9959	1.124E-05

Table 4.6 Difference between the results obtained with the Elliptical Plane technique and the software BETAlab (all values are expressed in %).

Mode	% difference between Ellipse and BETAlab			
	Modal Constants		η (%)	Amp (N/m)
	Real	Imag		
1	0.12	-0.05	-0.35	0.52
2	4.68	-396	5.90	-0.76
3	1.55	92.4	3.89	-2.10
4	0.04	-165	-0.45	0.42

Results from Table 4.6 indicate that, in general, there is good agreement between the Elliptical Plane technique and BETAlab with respect to the real part of the modal constants, the hysteretic damping factor and the amplitude of the receptance. This is also true for the second mode shape (Figure 4.16 and Figure 4.17) which is barely visible in the receptance Figure 4.13. But the same cannot be said of the imaginary part of the modal constants, which vary greatly from one method to the other. This may well be due to the values being two orders of magnitude smaller than their real counterparts, as such, do not affect the regenerated curves² shown in Figure 4.13.

4.6.3 Validation of Experimental Results

Experimental vibration data from a carbon fibre rectangular plate suspended in a free-free simulated setup (see section 4.6.1) was utilised to evaluate the efficiency of the proposed technique better. A comparison was done between the results and the ones obtained using BETAlab, which is a modal identification software developed in [25] that uses the CRF [245]. The reason behind using other method concurrently was to

² Residuals, which are normally included to account for the influence of modes that are not within the measured frequency range, were not determined in this study.

obtain a set of values as a reference point since experimental modal properties are not known in advance for comparison. Thus, the performance of BETAlab was also assessed with the use of numerical cases 7 to 10 outlined in Table 4.1 and available from section 4.5. See the results shown in Table 4.7 and Table 4.8.

Table 4.7 Results from the modal identification using BETAlab (numerical examples).

Case	Mode 1					Mode 2				
	Modal Constant 1		f (Hz)	η (%)	Amp (N/m)	Modal Constant 2		f (Hz)	η (%)	Amp (N/m)
	Real	Imag				Real	Imag			
7	1003	-502.5	20.4	1.001	6.821	1999	-1200	50.25	4.999	0.4679
8	999.8	-499.8	"	0.9995	6.807	2049	1187	"	5.054	0.4700
9	999.0	-505.3	"	0.9980	6.828	1994	-1205	50.27	49.95	0.04675
10	1027.0	-514.0	20.3	51.37	0.137	1999	-1200	50.25	5.001	0.4677

Table 4.8 Difference between the theoretical values and the numerical results from BETAlab (all values are expressed in %).

Case	% error mode 1					% error mode 2				
	Modal Constant 1		f (Hz)	η (%)	Amp (N/m)	Modal Constant 2		f (Hz)	η (%)	Amp (N/m)
	Real	Imag				Real	Imag			
7	0.30	0.50	0.00	0.10	0.24	-0.05	0.00	0.00	-0.02	-0.01
8	-0.02	-0.04	"	-0.05	0.03	2.45	-1.08	"	1.08	0.45
9	-0.10	1.06	"	-0.20	0.34	-0.30	0.42	0.04	-0.10	-0.08
10	2.70	2.80	-0.49	2.74	0.97	-0.05	0.00	0.00	0.02	-0.05

It is important to note that both methods agree quite well with the numerical results. Their performances seem to be same, at least with the numerical results provided. The maximum percentage differences between these results and the theoretical values for the modal constants is 2.80% for BETAlab and 4.06% for method of the Ellipse. However, on average, these differences reduce to 0.74% and 0.61%, respectively. Concerning the modal damping factors, the maximum percentage differences are 2.74% for BETAlab and 2.70% for Ellipse Plane technique, but the average differences are 0.54% and 0.46, respectively. Since the maximum percentage differences are not applicable to the same cases and/or mode shapes, plus the average differences are basically the same and very negligible, it is quite difficult to find a better explanation instead of one that is based on numerical uncertainty/ill-conditioning and human error. It is important to bear in mind that, to a certain extent, both BETAlab and the Elliptical Plane technique depend on the judgment of the user. This also implies that it is hardly

possible to obtain exact results for two modal identifications on the same data points when either of the software is used.

4.7 The Reduction of Uncertainty on the Elliptical Plane Modal Identification Method

The Elliptical Plane method is very effective when the mode shapes are conveniently well-spaced [13,15,57,238]. This assumption is not unusual and has been used in many other modal identification methods [24,247]. However, the determination of the modal properties in the Elliptical Plane is predicated on numerical extrapolation of the ellipse, which implies that both the noise and the frequency resolution play an important role in the results. Classical fitting methods such as clustering or optimisation methods have been addressed using Hough transform [248], Kalman filtering [249], or least squares approach [250–258]. While the clustering approach [248,249] is slow and lack accuracy, optimisation methods [251,255–258] are fast and accurate. Furthermore, the use of varying curve-fitting methods, may slightly give different results or can even fail by rendering straight lines or hyperbolas. In real cases where the available points are not much, there can be a broad range of equally good solutions for same problem.

This section starts by presenting a summary of the modal identification method based on the receptance when represented in the Elliptical Plane. The full development can be found in section 4.3. Different curve-fitting methods are implemented in MATLAB, to improve the performance of the Elliptical Plane modal identification technique. A multiple degree-of-freedom numerical example was used to discuss the results.

4.7.1 Numerical Curve-Fitting Methods

An ellipse as a particular case of conic section can be described [250,251] by the scalar product between the vector of coefficients $\mathbf{c} = \{a, b, c, d, e, f\}^T$ and the vector $\mathbf{v} = \{x^2, xy, y^2, x, y, 1\}^T$ by:

$$F_c(\mathbf{v}) = \mathbf{c} \cdot \mathbf{v} = \{a, b, c, d, e, f\}^T \cdot \{x^2, xy, y^2, x, y, 1\}^T = 0 \quad (48)$$

$$F(x, y) = ax^2 + bxy + cy^2 + dx + ey + f = 0$$

subject to $b^2 < 4ac$. The function $F_c(\mathbf{v}) = F(x, y)$ represents the algebraic distance from a point (x, y) to the conic. The fitting problem [254] can be approached by the use of a least square fitting (LSF) method based on the minimisation of the sum of the squared algebraic distances of the points (x_i, y_i) to the conic:

$$D_1(\mathbf{c}) = \min_c \sum_{k=1}^n F(x_i, y_i)^2 = \min_c \sum_{k=1}^n F_c(\mathbf{v}_i)^2 = \min_c \sum_{k=1}^n (\mathbf{c} \cdot \mathbf{v}_i)^2 \quad (49)$$

with either $a + c = 1$ [252], $a^2 + \frac{1}{2}b + c^2 = 1$ [250], or $\|x - c_1\| + \|x - c_2\| = 2a$ [258] where c_1 and c_2 are the two foci of the ellipse and the norm in this case is determined using a Mahalanobis distance.

An iterative approximation method [250] through a better estimated geometric distance [256] can be expressed:

$$D_2(\mathbf{c}) = \sum_{k=1}^n \frac{F(\mathbf{c} \cdot \mathbf{v}_1)^2}{\|\nabla_x F(\mathbf{c} \cdot \mathbf{v}_1)\|^2} \quad (50)$$

Or by [257]:

$$D_3(\mathbf{c}) \cong \frac{\sum_{i=1}^n F(\mathbf{c} \cdot \mathbf{v}_i)^2}{\sum_{k=1}^n \|\nabla_x F(\mathbf{c} \cdot \mathbf{v}_i)\|^2} \quad (51)$$

The approach in [251,253] replaces the constraint $b^2 < 4ac$ by the equality $b^2 + 1 = 4ac$ and reformulate the fitting problem as:

$$\min_c \|\mathbf{H}\mathbf{c}\|^2 \quad \text{subject to} \quad \mathbf{c}^T \mathbf{D}\mathbf{c} = \mathbf{1} \quad (52)$$

where the matrices \mathbf{H} and \mathbf{D} are expressed as in [253] by:

$$\mathbf{H} = \begin{pmatrix} x_1^2 & x_1 y_1 & y_1^2 & x_1 & y_1 & 1 \\ \vdots & \vdots & \vdots & \vdots & \vdots & \vdots \\ x_k^2 & x_k y_k & y_k^2 & x_k & y_k & 1 \\ \vdots & \vdots & \vdots & \vdots & \vdots & \vdots \\ x_n^2 & x_n y_n & y_n^2 & x_n & y_n & 1 \end{pmatrix} \text{ and } \mathbf{D} = \begin{pmatrix} 0 & 0 & 2 & 0 & 0 & 0 \\ 0 & -1 & 0 & 0 & 0 & 0 \\ 2 & 0 & 0 & 0 & 0 & 0 \\ 0 & 0 & 0 & 0 & 0 & 0 \\ 0 & 0 & 0 & 0 & 0 & 0 \\ 0 & 0 & 0 & 0 & 0 & 0 \end{pmatrix} \quad (53)$$

4.7.2 Numerical Example

A 2-DOF numerical model (a case with the theoretical properties shown in (table 4.1)) is used to test the performance of the improved numerical curve-fitting method. The Elliptical Plane modal identification method procedure assumes that the mode shapes are conveniently well-spaced so that the effect from mode shapes that are close to the mode being identified is very negligible. Therefore, each mode is determined separately by ‘zooming-in’ close to its respective natural frequency. The receptance of this numerical model in the frequency domain is shown in Figure 4.5, where close-ups near the resonant frequencies are shown in Figure 4.7 and Figure 4.9. When represented in the Elliptical Plane with $x \equiv H$ vs $y \equiv \sin(\theta)$ axes, Figure 4.5 takes the form of Figure 4.6, where the shape is elliptical³ close to the resonant frequencies.

Since different methods may lead to distinct best-fitting ellipses or even hyperbolas when “bad/noisy” data is utilised, the most effective method should be used to address the uncertainty in the modal identification. This can be seen in Figure 4.23 where distinct best-fitting ellipses have been obtained for the two sets of data shown in Figure 4.7 and Figure 4.9 from two different fitting methods, such as: the least squares method without any weights [254] presented in Equation (49); and, the computationally efficient (and robust to noise) direct approach [253] shown in Equation (52).

³ In fact, the shape is half-elliptical, as shown in Figure 4.4. The data points in Figure 4.6 were mirrored so that the ‘elliptical nature’ of the representation is better illustrated.

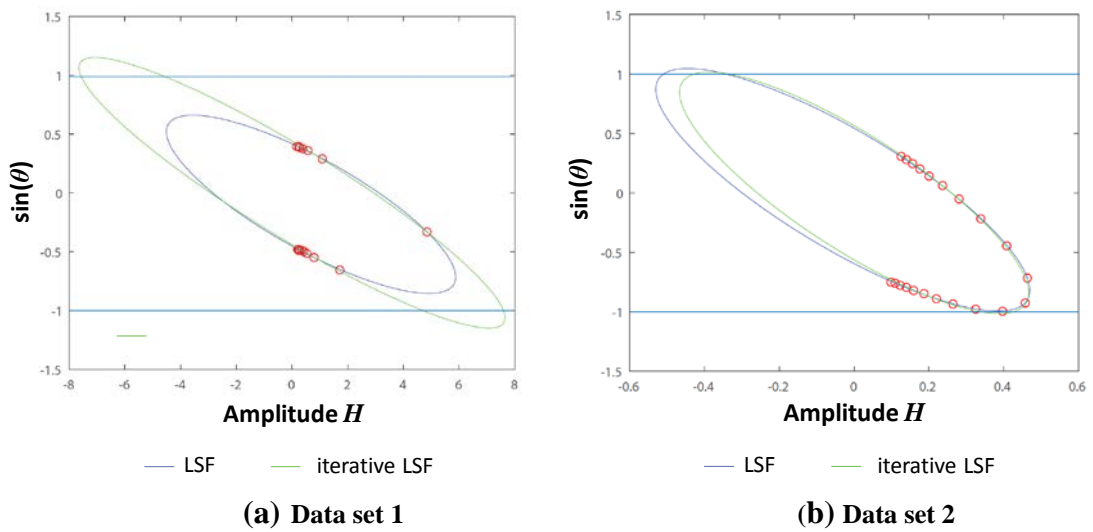


Figure 4.22 Best-fitting ellipses using the LSF method in Equation (49) and the iterative method in Equation (52): (a) data set 1, and (b) data set 2.

Limiting the best fit to the horizontal limits -1 and 1 for the same sets of data shown in Figure 4.22 (due to the properties of the Elliptical Plane discussed in section 4.4), two distinct best-fitting ellipses similar – calculated using a weak Fréchet distance - to one another are obtained. Fréchet distance is a measure of the similarity between curves [259].

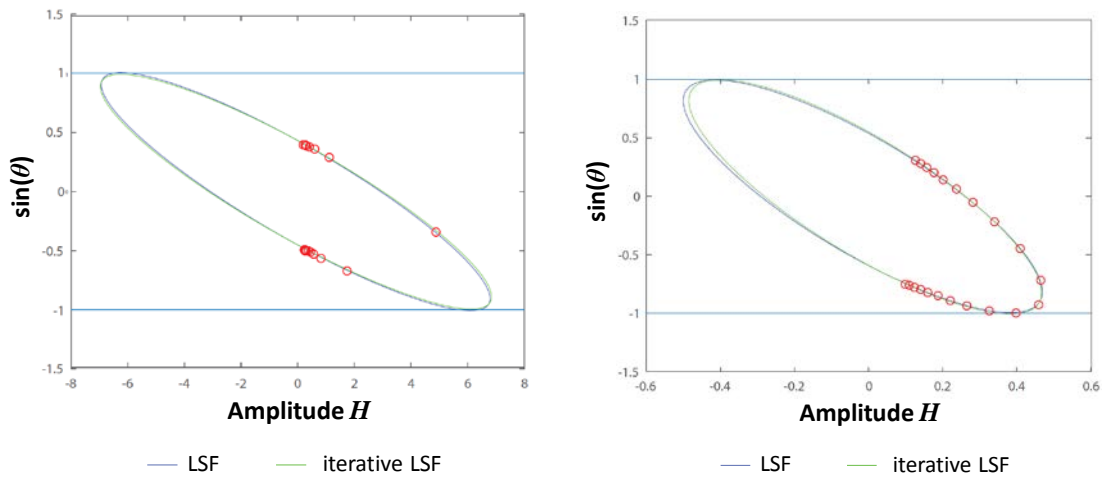


Figure 4.23 Best-fitting ellipses using the LSF method in Equation (49) and the iterative method in Equation (52), after enforcing the limit to be between ± 1 : (a) data set 1, and (b) data set 2.

Generally, different methods such as conic residual or proximity methods produce different ellipses. Moreover, independent of the methods utilised, almost elliptical distribution of the data points produce good and similar fits [251,255], while a more

noisy distribution may produce - depending on the method used - different sets of ellipses or can even fail by rendering straight lines or hyperbolas [251].

In this situation, since data is simulated and has no noise included, both methods rendered quite similar results. The results gotten from both methods were averaged and are presented in Table 4.9. Table 4.9 is the improved results from the optimised curve-fitting being presented compared to Table 4.10 that depends quite significantly on human judgment. The modal identification was performed in the 15–25Hz and 45–55Hz frequency ranges.

Table 4.9 Averaged numerical results from the modal identification in the 15–25Hz and 45–55Hz ranges (values between brackets are the percent error committed).

Mode number	A_R	A_I	η_r (%)	Amplitude
1 (20.4Hz)	994.6 (e=0.5%)	-468.2 (e=6.4%)	0.9769 (e=2.3%)	6.849 (e=0.6%)
2 (50.25Hz)	2322 (e=16.1%)	-1424 (e=18.7%)	6.484 (e=29.7%)	0.4215 (e=9.9%)

In order to understand if the curve fitting methods introduced in this section produced any improvement in the results when compared to what was done in section 4.5, the same data points were identified using the software in section 4.5, which results are shown in Table 4.10.

Table 4.10 Numerical results from the modal identification using the software presented in section 4 in the 15–25 Hz and 45–55 Hz ranges (values between brackets are the percent error committed).

Mode number	A_R	A_I	η_r (%)	Amplitude
1 (20.4Hz)	969.3 (e=3.1%)	-474.8 (e=5.0%)	0.8288 (e=17.1%)	7.926 (e=16.5%)
2 (50.25 Hz)	2584 (e=29.2%)	-1787 (e=48.9%)	6.386 (e=27.7%)	0.4936 (e=5.5%)

Comparison of Table 4.9 and Table 4.10 shows that, For relative lower damping and higher amplitude values (mode 1), errors decreased significantly, from 17.1% to 2.3%,

in the case of damping, and from 16.5% to 0.6%, in the case of the amplitude. For relative higher damping and lower amplitude values (mode 2), errors have deteriorated, but ever so slightly, from 27.7% to 29.7%, in the case of damping, and from 5.5% to 9.9% in the case of the amplitude. However, in this latter case (mode 2) the difference in errors is marginal when compared to the former case (mode 1). Therefore, it can be concluded that, in general, the combination of the two methods introduced in this work generally contributed to the improvement of the results, with a decrease on the average error committed from 19.1% to 10.5%. It is important to mention that modes were not ‘isolated’ (i.e., the regenerated modes were not subtracted from the experimental curves when doing the identification), hence only one modal identification iteration was performed.

4.8 Concluding Remarks

A novel method for the identification of the modal constants from FRFs, based on the dissipated energy per vibration cycle, is presented. It is most suitable for lightly damped systems with conveniently well-spaced mode shapes. It offers a new perspective on the way the receptance may be represented, called the ‘elliptical plane’. This approach brings valuable insights for other researchers in the field. For example, since the elliptical shape of the receptance (close to a resonant frequency) when represented in the ‘elliptical plane’ depends on both local and global modal properties, then it is reasonable to suggest that this representation of the FRF can be utilised in other fields, for instance, SHM.

In previous research [57,238], it was indicated that this method can give a better estimate of the modal damping factors than the method of the inverse. By “isolating” the already identified mode shapes to minimize the amount of effect from the other mode shapes, the results are in agreement with the BETAlab results. However, with regard to the modal constants, namely their imaginary parts, more research is still needed, although the disparities between the results did not seem to noticeably affect the regeneration of the identified curves. Moreover, this may be due to the imaginary parts of the modal constants being one or two orders of magnitude smaller than their real counterparts, thus being more susceptible to uncertainty and error.

The Elliptical Plane method raised questions with regards to the quality of the numerical curve-fitting being utilised. To answer those questions, a combination of the least squares fitting (LSF) employing a Mahalanobis distance and an iterative approximation method was considered. It is shown that there may be multiple solutions for the same problem, especially when the data points are scanty (due to the frequency resolution limitations). However, the method allows identifying a range of values, which implies that we can take the ‘answer in the middle’ (i.e., the average) as the solution to our problem.

Finally, although the method has not been tried on the modal identification of multiple FRF functions, this should not be a real challenge. The issues that are mostly associated with software implementation rather than with the method itself, since the representation of the receptance in the ‘elliptical plane’ greatly depends on local properties. Consistency conditions between the modal constants to satisfy orthogonality properties between the eigenvectors can be applied subsequently, in the same manner to what is done in [245].

“Nothing in life is to be feared; it is only to be understood. Now is the time to understand more so that we may fear less.”

—Marie Curie

5 Experimental Measurements

5.1 Design and Manufacturing of Test Base and Hemispherical Indenter

Figure 5.1 shows the hemispherical indenter and the support base system designed by the author using SolidWorks. Both structures were made of mild carbon steel. The impactor has a 24.50mm diameter hemispherical indenter, a pin slot of 7.85mm diameter and a length of 41.40mm.

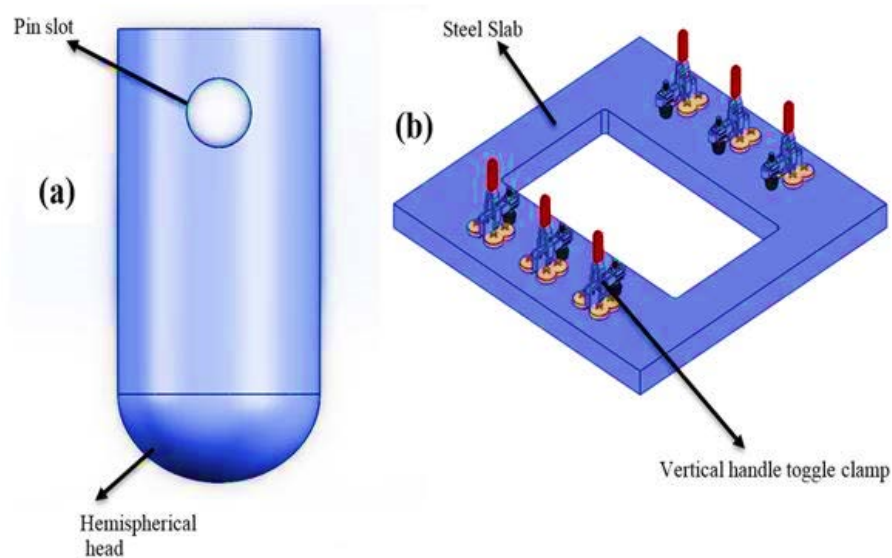


Figure 5.1 (a) Impactor; (b) Test support base.

The area of the support is 350mm^2 , with a hole of $250\text{mm} \times 150\text{mm}$. The six clamps are series 101-A Good Hand vertical handle toggle clamps. Each has a holding capacity of 490.35N and weighs 0.06kg .

5.2 Manufacturing of CFRP Composite Laminates

5.2.1 Stacking Sequence

The stacking sequence provides the rotation angle of fibres with respect to the global axis in degrees and it is enclosed in square bracket notation. It is assumed that the fibre direction is constant in each ply.

The composite laminates considered for this research work were manufactured by hand layup technique by the author in the composite layup laboratory in the University of Hertfordshire. This step entails the laying of prepregs at required angles. The orientation of the fibre and the layup sequence enhance the performance of composite structures. CFRP specimens with seven distinct types of orientations were made (see Table 5.1). Each layer is an epoxy resin impregnated CF.

Table 5.1 Types of specimens and designations.

Qty.	Designation	Material	Stacking sequence	Laminate Type	Dimensions (mm)	Aspect ratio (a/b)
3	Plate A1 – A3	FibreDUX 6268C-HTA (12K)	$[90/\pm 45/0]_S$	Quasi-Isotropic	310x240x2	1.29
2	Plate B1 – B2	„	$[90/0/\pm 45]_S$	„	„	„
4	Plate C1 – C4	„	$[90/0]_{2S}$	Cross-ply (Orthotropic)	„	„
1	Plate D1	„	$[90_2/0_3]_S$	„	312x240x2.4	„
1	Plate D2	Toray T700 (24K)	„	„	342x241x3.1	1.42
1	Plate E1	FibreDUX 6268C-HTA (12K)	$[90_3/0_3]_S$	„	300x241x3	1.24
1	Plate E2	Toray T700 (24K)	„	„	333x240x4	1.39
1	Plate F1	Hexcel® G803 3K 5H	$[0/\pm 45/90]_S$	Quasi-Isotropic	392x242x2	1.62
1	Plate G1	Toray T700 (24K)	$[90_3/0_3/90_3]$	Cross-ply (Orthotropic)	338x241x3	1.40

The dimension of specimens is chosen so that the existence of double modes in vibration that could affect modal analysis is avoided for the convenience of assessing the developed damage identification method.

5.2.2 Manufacturing Process

All the specimens were manufactured in an autoclave at BioMEMS and Microengineering laboratory, and the Autoclave in the Mechanical engineering laboratory at the University of Hertfordshire with prepreg Carbon Fibre (CF). See Figure 5.2 to Figure 5.5.



Figure 5.2 Left: Prepreg cutting process; Right: Pressuring process.

When the roll of prepreg was removed from the freezer, it was allowed to thaw for a minimum of 5 hours; to attain room temperature before the polythene bag is removed. It is important to fully thaw prepreg to avoid condensation on the surface of the material. Any amount of moisture within a curing laminate will impact on the appearance and quality of the manufactured laminate. The remaining materials were resealed and returned to the freezer to avoid moisture entering it. After thawing the prepreg fully, the desired ply orientations were cut out from the roll of prepregs by hand, as shown in Figure 5.2. During the lay-up process, the lay-up was de-bulked regularly with a wooden roller to remove any trapped air between plies, to ensure the prepreg takes the desired shape. The layup was pressurised at 90kPa overnight.

5.2.3 The Curing Process

A cure cycle was applied for autoclave curing of the prepreg laminates, as recommended by the manufacturer; it is preceded by the vacuum bagging process. The bagging procedure is shown in Figure 5.3. To reduce the risk of bag failure, a VAC-PAK HS6262 (Nylon 66) bagging film was used. This bagging film can withstand high temperatures and pressures during curing. In order to prevent sticking to the aluminium plate (used as forming tool) and the breather after curing, the prepreg laminate was sandwiched between two release films. An inner yellow sealant tape strip was positioned 10mm from the edge of the laminate.

Analysis of the Response of Modal Parameters to Damage in CFRP Laminates using a Novel Modal Identification Method

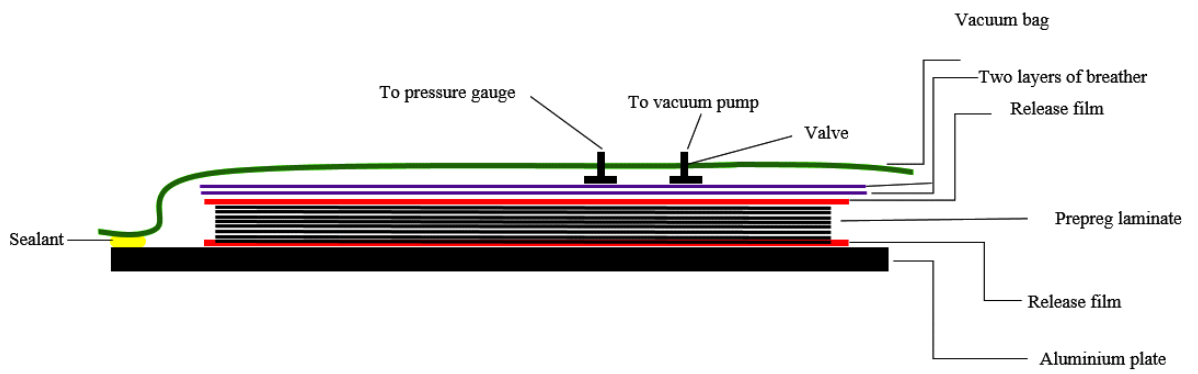


Figure 5.3 Vacuum bagging.

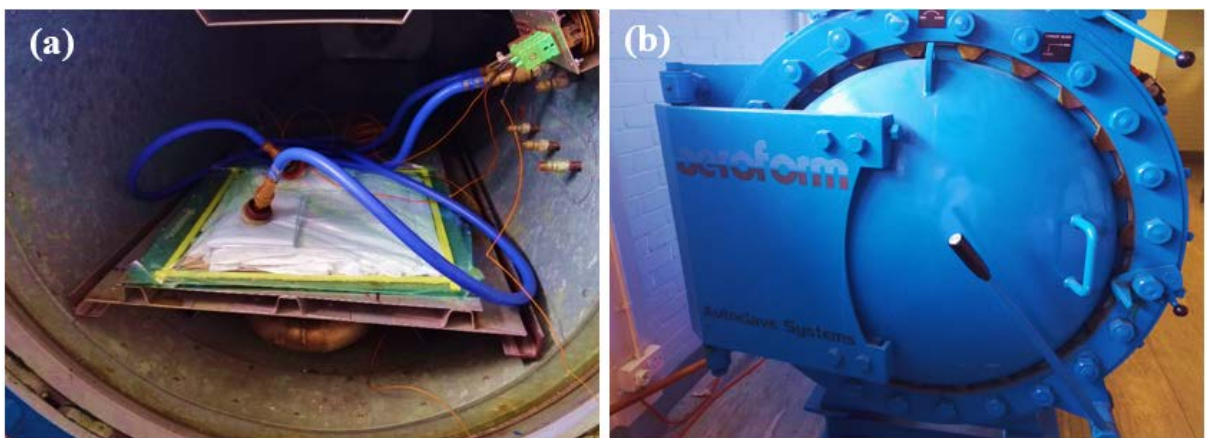


Figure 5.4 Autoclave: (a) when open; (b) when closed.

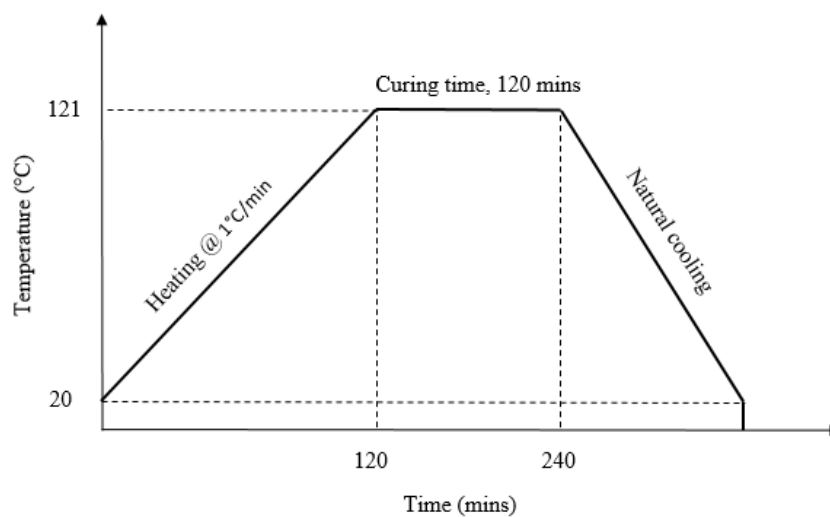


Figure 5.5 Curing cycle.



Figure 5.6 Manufactured samples.

The vacuum bag was secured around the laminate with the sealant tape, while both the pressure gauge and the vacuum pipes were connected to the vacuum bagging through valves. The cure cycle used for this work is shown in Figure 5.5. In order to obtain a good surface quality, even temperature across the laminate, small temperature differences between the components, tool and the source of heat, the start-up heat was 20°C and heat up rate was at 1°C/min until it reached 121°C. The laminate (see Figure 5.6) was cured at 106 kPa for 2 hours and then cooled naturally.

5.3 Generalities on the Experimental Setup

This section is written using as an example specimen F1. The same procedure is used in the other test specimen in Table 5.1. An experimental test is conducted on a quasi-isotropic CFRP specimen. The quasi-isotropic specimen is made from a $[0/45/-45/90]_S$ layup with a dimension of $392\text{mm} \times 242\text{mm} \times 2\text{mm}$. Each of the layers is a woven prepreg formed by Hexcel® G803 3K 5H satin CF impregnated in HexPly® 200 phenolique matrix (200/40%/G803). The specimen was suspended vertically under a free-free simulated configuration with 2 strings of nylon, which were attached to 1mm diameter at 50mm apart from the edge of the test plate and 5mm from its top edge. An electrodynamic shaker (LDS V406 M4-CE) with stinger 60mm long connected to a force transducer, is used to start a single point excitation signal within the range of 0 to 800Hz with a 0.25Hz resolution that was generated and amplified using an NI 9263 analogue output module and an LDS PA25E power amplifier. See Figure 4.12.

The responses were measured at three specific locations using three lightweight PCB teardrop accelerometer, type 352A24, that weighs 0.8 g each, at the corner of the specimen to acquire the FRFs. Figure 5.7 shows the experimental setup.

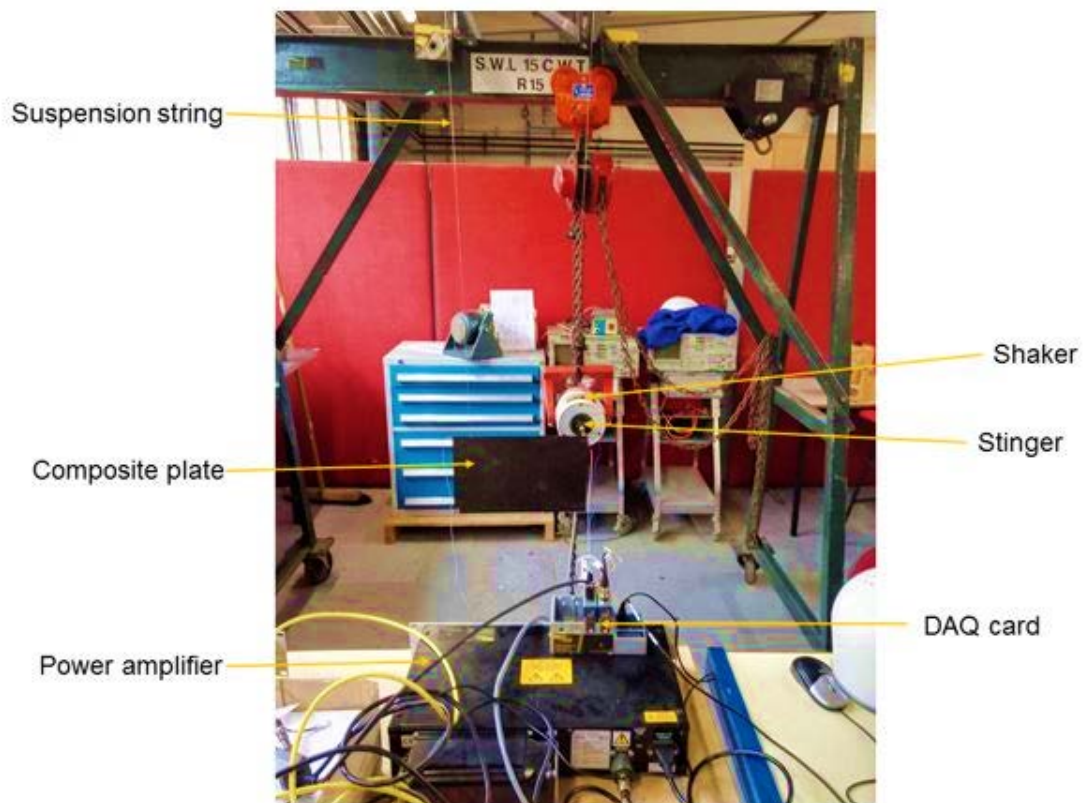


Figure 5.7 The undamaged specimen experimental setup.

This specimen is undamaged. The mechanical shaker is connected to a power amplifier (LDS PA25E), which is connected to a 4-channel differential data acquisition unit. A transfer FRF was determined by employing a National Instrument (NI) DAQ-9234 analogue input data acquisition module on an NI cDAQ-9174 USB chassis. The first channel was assigned to the excitation force. The excitation force was determined with a force transducer, labelled PCB 208C01. Then the other channels were assigned to PCB 352C22 lightweight teardrop accelerometers to measure the acceleration response. The signals from the accelerometers go directly into the data acquisition (DAQ) unit (NI cDAQ-9174). The experiment was repeated, including the setup.



Figure 5.8 Receptance curve and phase plot of an undamaged quasi-isotropic composite laminate as seen in LabVIEW.

A graphical programmable software known as LabVIEW was used to develop BETAlab software used in this work. Signal Express 2012 from NI was used to process and record the test vibration results. The FRFs were recorded in the form of receptance. Examples of receptance curves and phase plots of an FRF are shown in Figure 5.8.

The BETAlab software was built by [25] under LabVIEW 7.1 environment from NI and it is used for modal identification. For more information on BETAlab, refer to [25]. The software is based on the method of the inverse [247] and Characteristic Response Function (CRF) developed by [260]. The CRF presents the receptance for an SDOF system. It accounts for the characteristics of the structure (global properties of the system) and does not depend on its local properties (measurement coordinates) [25]. According to [25], the algorithm extracts the modal parameters from experimental FRF data considering the receptance as:

$$\alpha_{jk}(\omega) = \bar{R}_{jk}(\omega) + \sum_{r=m_1}^{m_2} \frac{r\bar{A}_{jk}}{\omega_r^2 - \omega^2 + i\eta_r\omega_r^2} \quad (54)$$

$$\bar{R}_{jk}(\omega) \cong -\frac{1}{\omega^2 \bar{M}_{jk}^R} + \frac{1}{\bar{K}_{jk}^R} \quad (55)$$

where α is the receptance, \bar{R} is a complex residual, ω is the angular frequency, ω_r is the natural angular frequency, η is the hysterical damping factor, r used to define mode number, \bar{M}^R represents the mass residual and \bar{K}^R is the stiffness residual, m_1 is the lower frequency in the range and m_2 is the upper frequency in the range.

5.4 Experimental Results from BETAlab

5.4.1 Introduction of Damage into Test Specimens

The quasi-static tests were carried out on a Tinius Olsen machine, as shown in Figure 5.9. The machine can bear a maximum of 25kN, and a minimum testing speed of 0.001mm/min. It has a strain gauge-based load cell that measures force with an accuracy of +/-0.2% of applied force across load cell force range. The machine has a built-in force transducer that allows the determination of the reaction force and the crosshead displacement is same as the indenter movement (displacement) because they are all fixed together. Tinius Olsen's Horizon software plots the force versus displacement graph automatically.

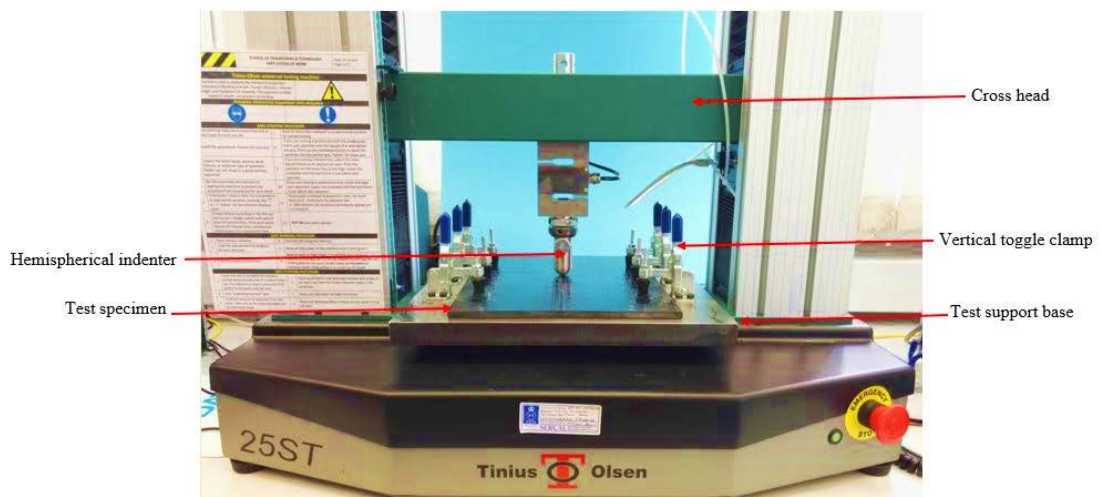


Figure 5.9 Static testing.

To perform the Quasi-Static Testing (QST), two opposing ends of the CFRP plate were clamped with six toggles (three at each side) clamps to prevent slippage. To monitor

the occurrence of slippage during impact, a video recording was done and no slippage was recorded. The testing speed was set to 2mm/min which is good enough to record the force-displacement data. In order to avoid slippage, a prototype test was initially conducted and the support were carefully watched with a video to satisfaction within the testing process.

The energy absorbed by the specimen after loading and unloading is the area under the force/displacement curve as shown from Figure 5.10 to Figure 5.15. The Trapezoidal Rule is used to determine the area under the curve (Figure 5.10) and the absorbed energy by some of the samples are listed in Table 5.2, by approximating the region under the graph of the $f(x)$ function as a trapezoid. Hence, the area is the integral of the product of the force applied and the displacement:

$$U = \int_a^b f(x)dx \approx \frac{b-a}{2n} [f(x_0) + 2f(x_1) + \dots + 2f(x_{n-1}) + f(x_n)] \quad (56)$$

$$U_{absorbed} = U_{loading} - U_{unloading} \quad (57)$$

Where U is the energy, a is the lower limit of integration, b is the upper limit of integration, n is the number of trapezoids, F and x stand for the force exerted on the specimen and its displacement respectively.

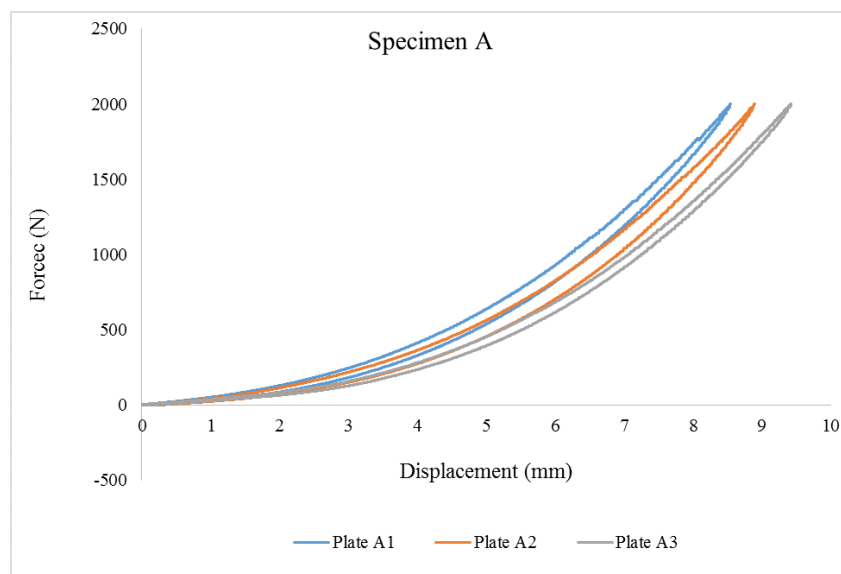


Figure 5.10 Work done by the impactor obtained from the static tests of specimen A.

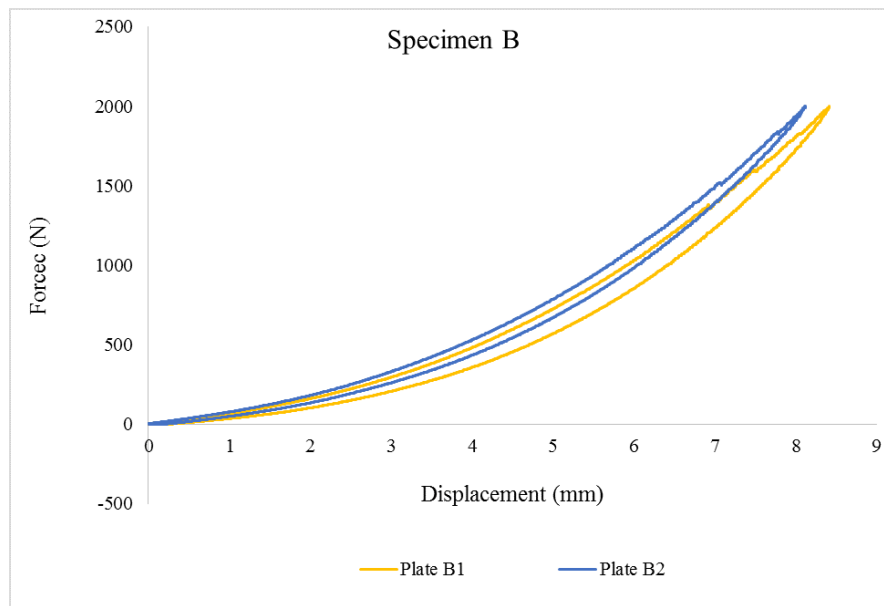


Figure 5.11 Work done by the impactor obtained from the static tests of specimen B.

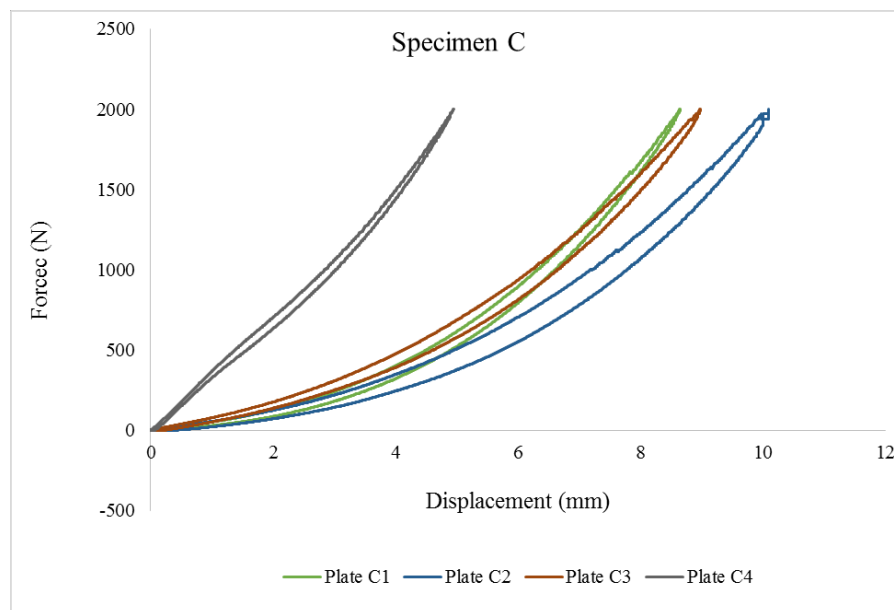


Figure 5.12 Work done by the impactor obtained from the static tests of specimen C.

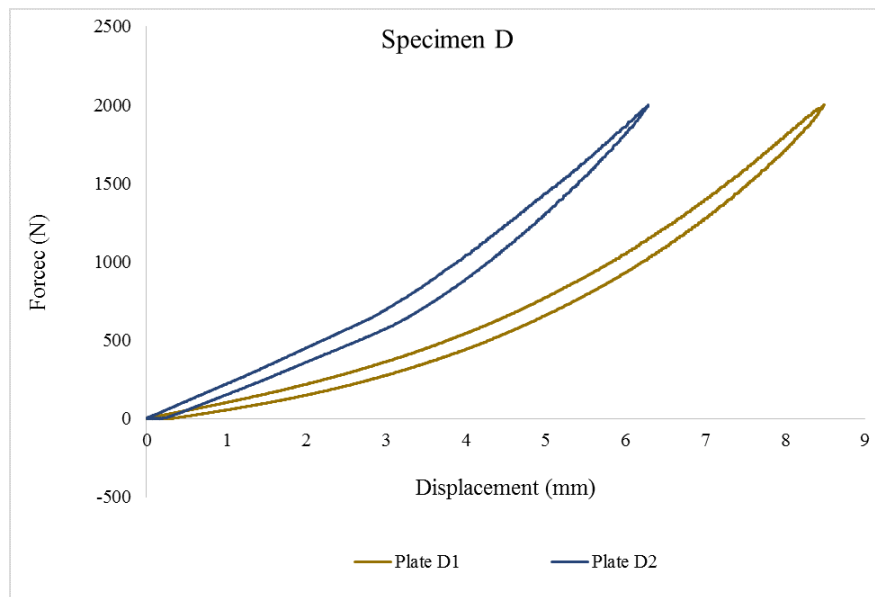


Figure 5.13 Work done by the impactor obtained from the static tests of specimen D.

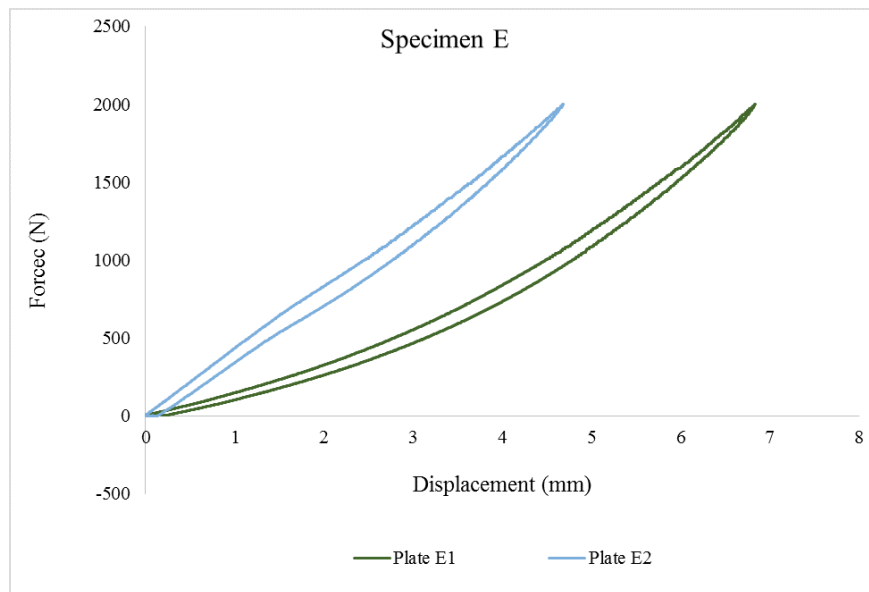


Figure 5.14 Work done by the impactor obtained from the static tests of specimen E.

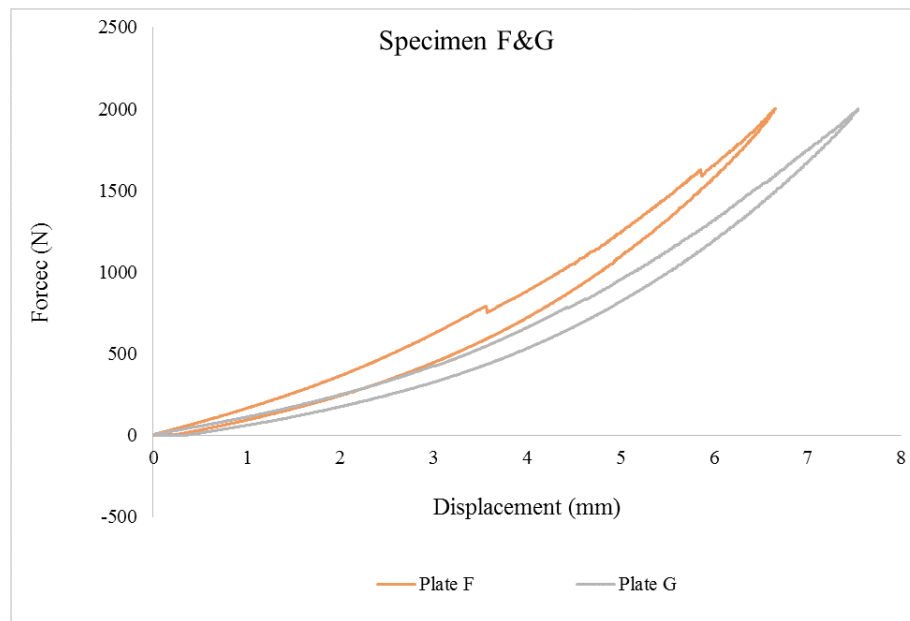


Figure 5.15 Work done by the impactor obtained from the static tests of specimen F and G.

Damage in composite materials usually starts from the propagation of a crack. This type of damage is known as matrix cracking [183]. As the amount of energy absorbed by the plates increases, the velocity of the crack increases until debonding happens. Although we cannot tell for sure which type of damage is present in the laminate, it can be certainly be told that damage is occurring. This is visible from the discontinuities in the Force vs displacement plots (Figure 5.10 to Figure 5.15). Since the development of cracks and microcracks does not affect as much the stiffness of the laminate as debonding does, it is likely that these discontinuities correspond to debonding. The debonding was more pronounced in plates B1, B2, C4, E2, F and G. In fact, in plate F, after first debonding at 756N, the second debonding occurred at 1550N before the continuous crack progression. It was observed that the crack progression was smooth and discontinuous across all the specimens. This results is in tandem with the study conducted by [196]. The debonding is due to mismatch in bending stiffness, which is related to the mismatch in the Poisson ratio.

Table 5.2 Energy absorbed by test specimens.

Test specimen	Amount of Energy Absorbed (J)					
	Healthy - Damage 1	Damage 1 - Damage 2	Damage 2 - Damage 3	Healthy - Damage 2	Healthy - Damage 3	Damage 1 - Damage 3
A1	5.524	12.640	16.581	18.164	34.745	29.221
A2	5.110	12.691	13.499	17.801	31.3	26.19
B1	5.796	5.832	14.675	11.628	26.303	20.507
B2	5.657	8.817	12.520	14.474	26.994	21.337
C1	5.110	12.606	16.641	17.716	34.357	29.247
C2	6.86	11.786	17.61	18.646	36.256	29.396
D1	6.222	9.755	12.528	15.978	28.505	22.283
E1	5.307	8.928	10.385	14.235	24.62	19.313

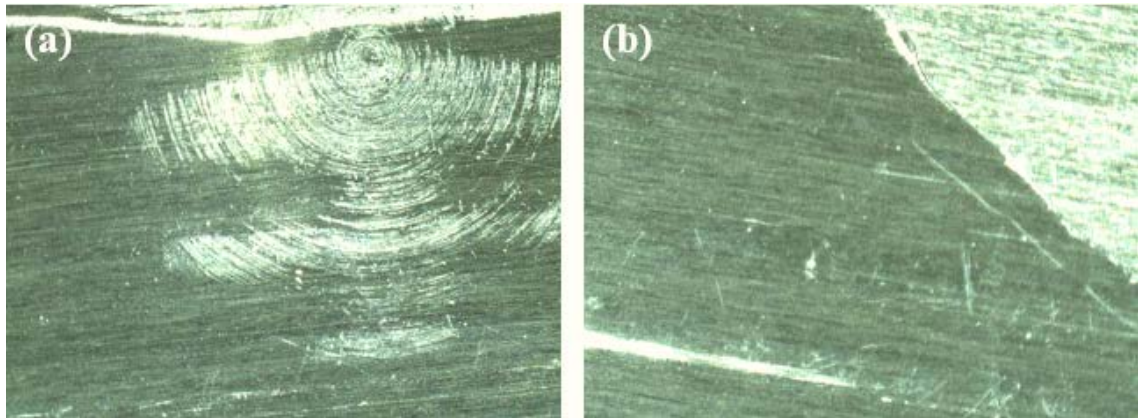


Figure 5.16 A microscopic photograph: (a) impact surface, (b) damaged surface.

The amount of energy absorbed by the specimen is determined by subtracting the area under the unloading curve from the dissipated energy. Figure 5.16 shows the microscopic view of the impact and damaged surface of one of the samples.

5.4.2 Deviation of Frequency and Damping with Damage Progression

The dynamic properties of the healthy and damaged specimens were identified using BETAlab software [261]. The software utilises the characteristic response function (CRF) [245,261]. It is expected that a reduction in the stiffness of the materials would result in the reduction of their natural frequencies. Making an analogy for clarity purposes, the natural frequency of a Single Degree of Freedom (SDOF) mass-lumped system, is given:

$$\omega_n = \sqrt{\frac{k}{m}} \quad (58)$$

where, ω_n , k , and m represent the natural frequency, stiffness, and the mass of the SDOF system respectively. If BVID damage will not produce a change in mass and only in the stiffness, then it is reasonable to assume that the natural frequencies will decrease. This is the underlying assumption in most SHM and damage detection methods. Likewise, some works are based on the fact that the modal damping factors change. However, this mechanism has not yet been totally understood, as evidence does not always show that damping necessarily increases with damage as hinted by other authors [262].

1. Plates A₁ [90/±45/0]_s

Interestingly, the introduction of damage compromised the integrity of the laminates, and reduces its stiffness. This is evident in all the modes, except mode 1, 9 and 10 (Refer to Figure 5.17). That is the reduction in the modal frequencies from modes 2 to 8. This might be because of environmental factors, test equipment, etc., which are inherent to any experiment of this type and that are difficult to control, hence introducing uncertainty that can be of the order of greatness of the changes introduced by damage [57]. However, the 2.2% increase in the modal frequency at mode 1 is relatively negligible. There is a possibility that the high level of increase of the modal frequency at modes 9 and 10 is because the crack has yet progressed to those areas.

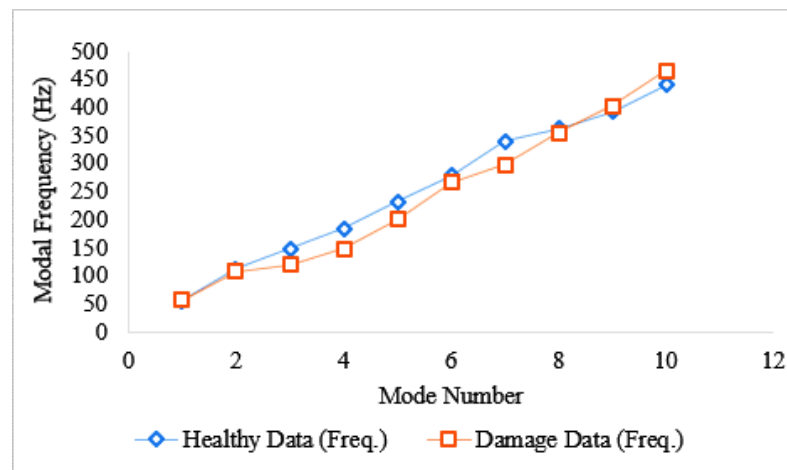


Figure 5.17 Changes in the modal frequency for plate A1.

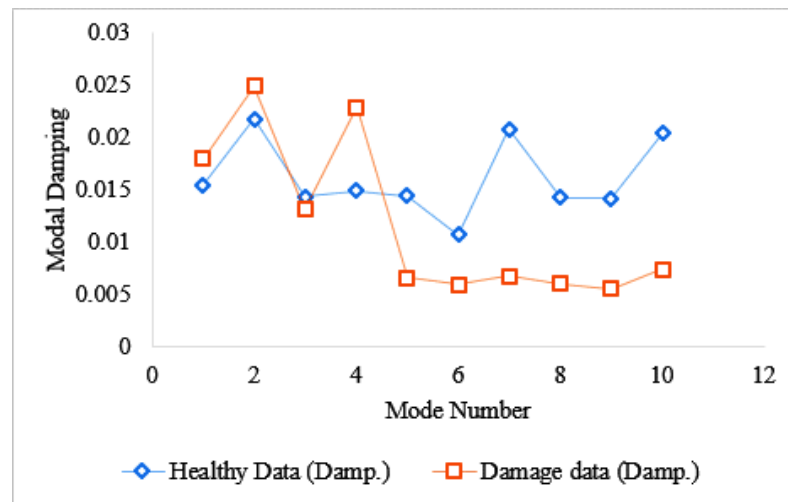


Figure 5.18 Changes in the modal damping for plate A1.

Similarly, in Figure 5.18, it was observed that as the frequencies reduce from modes 2 to mode 8, the modal damping reduces except at modes 2 and 4. At mode 1, both frequency and damping are on the increase as damage is introduced. However, at mode 2 as the frequency reduces, the damping increases. It is interesting to observe that at mode 4 where the highest level of reduction in the modal frequency was recorded, the modal damping has the highest increase. Although this behaviour has yet been thoroughly understood, it provides a sign of hope for the applicability of modal damping in damage identification. There is a significant increase in the modal frequencies and a decrease in the modal damping at both mode 9 and 10.

Also, the significant reduction in the modal frequency occurred from mode 2 to 8. This suggests that those modes are more closely affected by the damage locality. An assumption taken beforehand [261] is that there anti-nodes are at the point of highest concentration of damage. Note that, the reduction level is relative. It is based on the overall reduction rate across all the modes considered in a sample.

2. Plates A₂ [90/±45/0]_s

Figure 5.19 shows the reduction in modal frequencies at modes 2 and from modes 5 to 10, and an increase in the frequencies at modes 1, 3 and 4. This suggests the presence of damage at mode 2, and from 5 to 10 in the test sample. Again, the modal frequency at first mode increases despite the introduction of damage in the laminate.

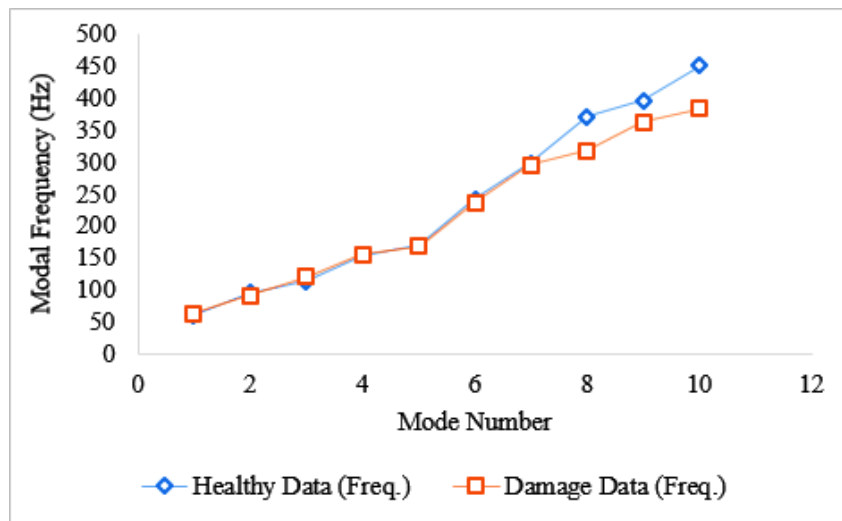


Figure 5.19 Changes in the modal frequency for plate A2.

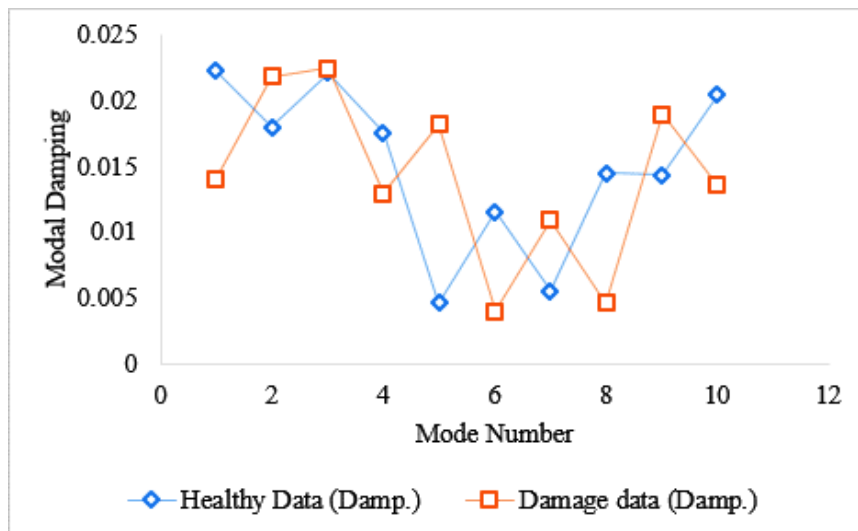


Figure 5.20 Changes in the modal damping for plate A2.

In Figure 5.20, there is a reduction in the modal damping at modes 1, 4, 6, 8, and 10; and an increase at modes 2, 3, 5, 7 and 9. The overall changes can be better understood from the graphical plots shown in Figure 5.19 and Figure 5.20. In addition, the highest increase in modal damping occurred at mode 5, where the lowest reduction of modal frequency occurred. With the highest reduction in the modal frequency at mode 10, it implies that the damage concentration is at that mode. However, the modes impacted by the damage locality are 2, 6, 7, 8, 9 and 10.

3. Plates A₃ [90/±45/0]_s

In specimen A₃, the damage concentration is at modes 2, and from 5 to 10 (Refer to Figure 5.21). This may be because the highest level of reduction in the modal frequencies occurred at those modes. However, the damage is spread across all the modes, except, and again, mode 1.

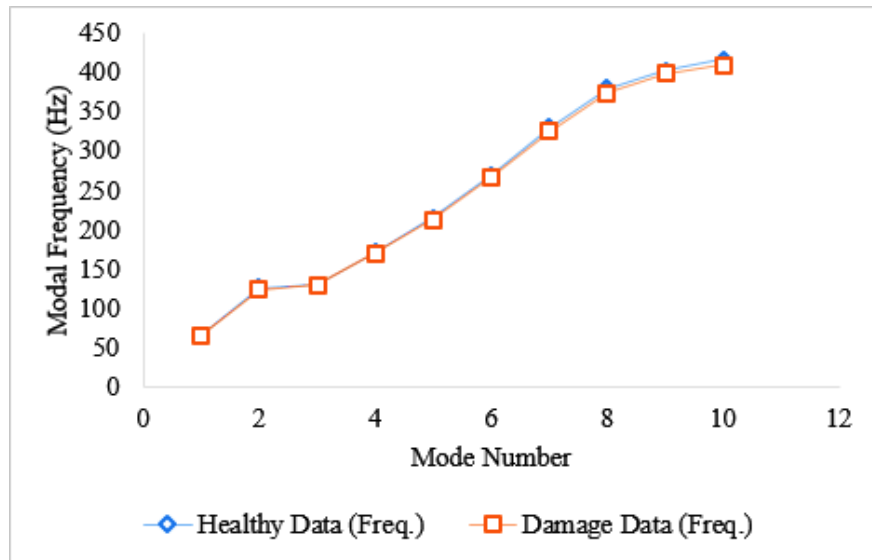


Figure 5.21 Changes in the modal frequency for plate A3.

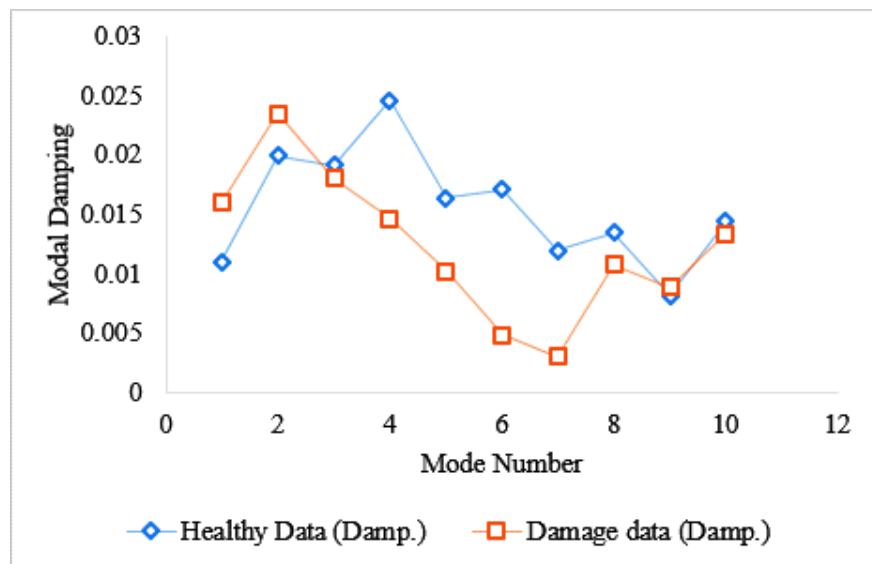


Figure 5.22 Changes in the modal damping for plate A3.

From modes 3 to 8, and 10, both parameters are decreasing as damage is introduced to the specimen (see Figure 5.22). Conversely, there is an increase in both modal

parameters at mode 1. Then at modes 2 and 9, as the modal frequency reduces, the modal damping increases.

It is observed that the change in modal frequency is larger in plate A1 and smaller in plate A3. While, the change in modal damping is smaller in plate A1 and larger in plate A2. Although plate A2 and A1 absorbed the highest and lowest amount of energy respectively, a possible trend between the amount of damage inflicted by the indenter and the changes in the modal frequency and damping is yet visible. The possible damages initiated in the samples are debonding and matrix cracking.

4. Plate B₁ [90/0/±45]_s

The results obtained after the introduction of damage in specimen B1 is as shown in Figure 5.23 and Figure 5.24. The results indicate that as the frequency decreases, the modal damping increases at modes 3, 7 and 9. However, modes 1 and 2 indicate an increase in the modal frequencies and a decrease in the modal damping factors. There is a reduction in both parameters at modes 4 to 6, 8 and 10.

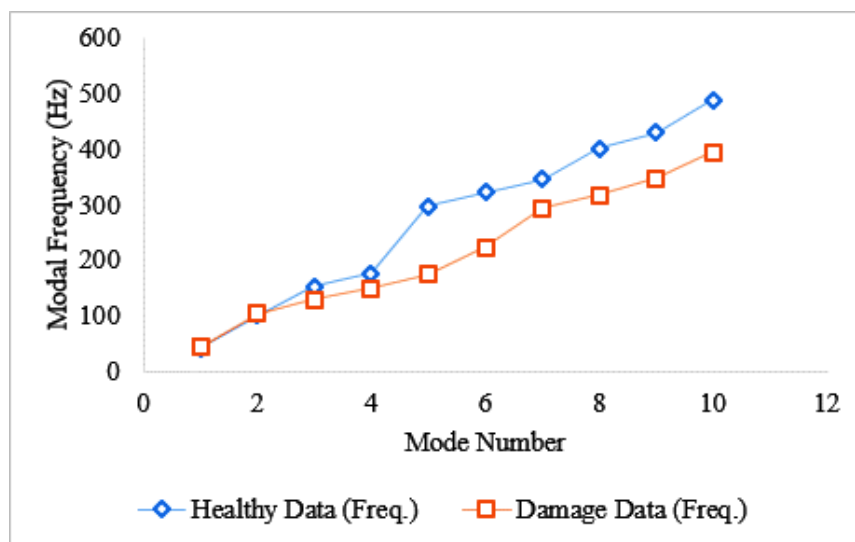


Figure 5.23 Changes in the modal frequency for plate B1.

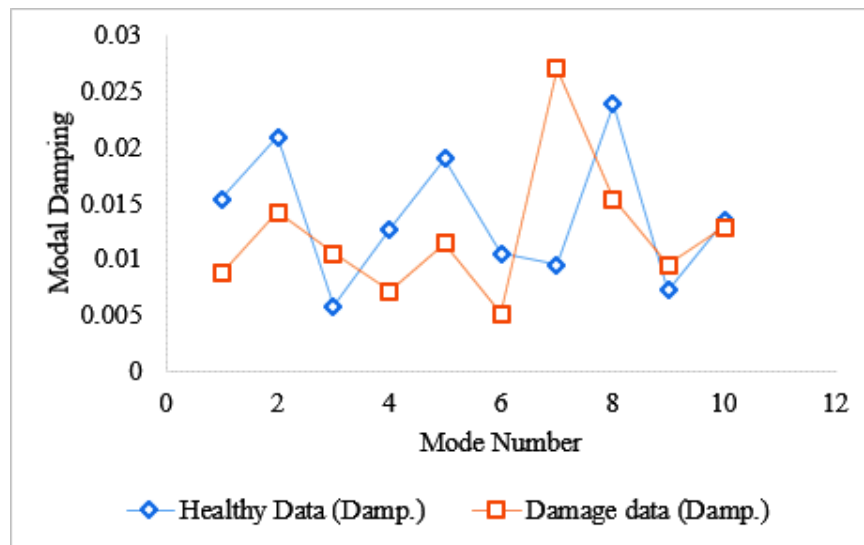


Figure 5.24 Changes in the modal damping for plate B1.

Obviously, the damage locality affects modes 3 to 10, as shown by the very noticeable reduction in the modal frequencies at those modes (see Figure 5.23). However, the impact is more felt from modes 5 to 10. Figure 5.24, shows the behaviour of the modal damping due to damage introduction in the laminates. There is a reduction in the modal damping at modes 1, 2, 4, 5, 6, 8 and 10; and an increase at modes 3, 7 and 9. The highest increase of the damping occurred at mode 7.

5. Plate B₂ [90/0/±45]_S

The response of the modal frequencies to damage in specimen B2 is illustrated in Figure 5.25. It is shown that there is a drop in the modal frequencies at modes 4, 6 to 8; with an increase at the other modes. It is evident that the location where damage was introduced was at mode 6 that has the highest reduction level.

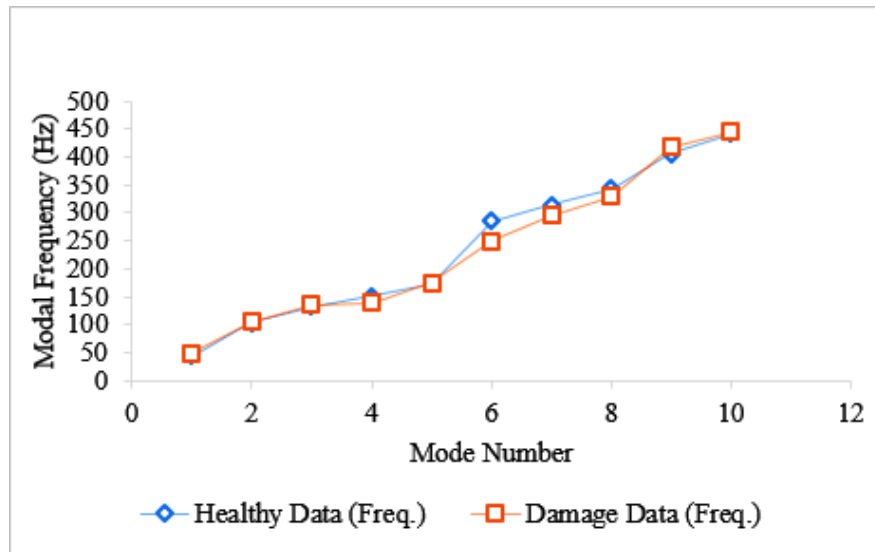


Figure 5.25 Changes in the modal frequency for plate B2.

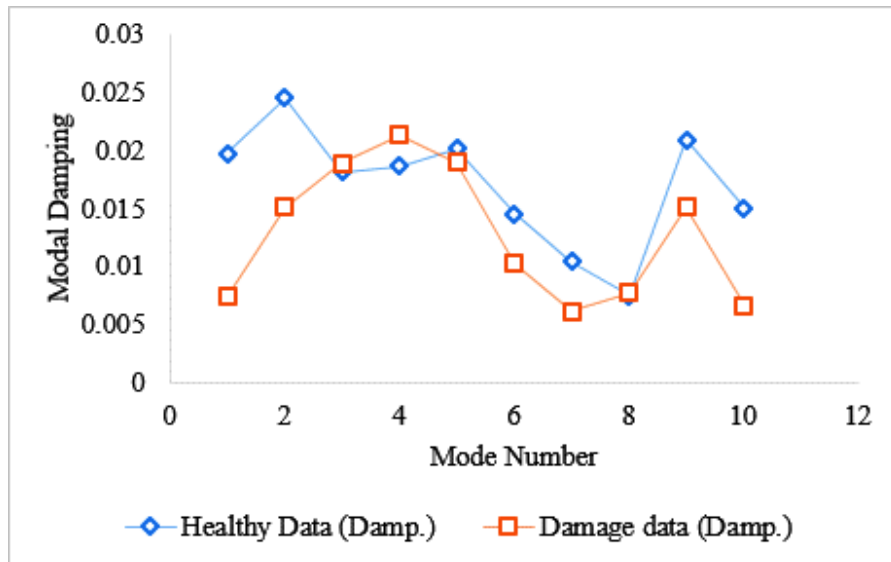


Figure 5.26 Changes in the modal damping for plate B2.

The cracks progressed to the neighbouring modes, that is, modes 4, 7 and 8. It is expected that as the impact damage level increases, the behaviour of the modal frequency will alter due to the increased displacement of the microstructures of the laminates.

In Figure 5.26, with the exception of modes 3, 4 and 8, all other modes show a reduction in the modal damping after the damage was introduced. The reasons behind this behaviour of the modal damping are yet clear. However, the level of the impact damage will be increased to monitor the further response from the modal parameters.

6. Plate B₃ [90/0/±45]₅

Specimen B3 shows an interesting result (refer to Figure 5.27). There is a reduction in the modal frequencies at modes 2, 3, 8, 9 and 10. This is an indication of the presence of damage in the laminates at those locations. Although the damage locality is within those five modes, its concentration is at modes 8, 9 and 10 that has the highest level of reduction in the modal frequencies. Conversely, at modes 1, 4, 5, 6 and 7 the modal frequencies increase as the damage was introduced in the laminates.

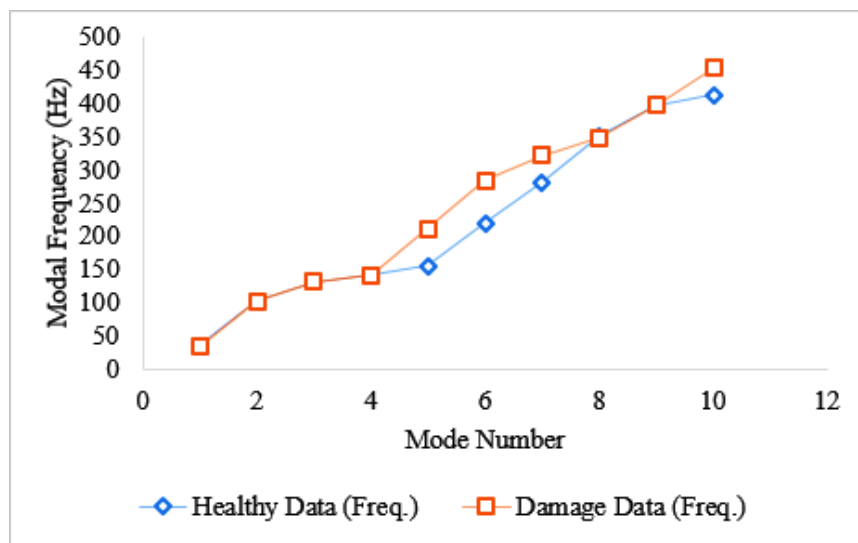


Figure 5.27 Changes in the modal frequency for plate B3.

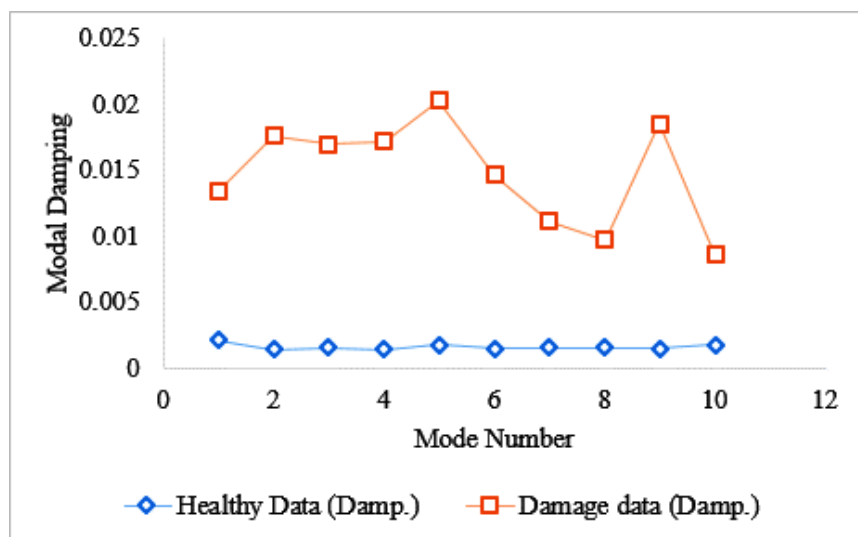


Figure 5.28 Changes in the modal damping for plate B3.

The interesting thing is that there is a noticeable increase in the modal damping factor (see Figure 5.28) at all the modes. Although modal damping hardly provides a clear

indication of the presence of damage in structures [262], this result is proving otherwise. The highest increase in both modal frequencies and modal damping occurred at mode 5.

The results from the three test plates show that, plate B3 has more change in modal frequency than plate B2, and plate B1 recorded the lowest change in modal frequency. It is also observed that the change in modal damping is more in plate B3 and lowest in plate B2. While, the amount of damage introduced in the test plates is higher in plate B2 and lowest in plate B3. Again, there is no clear trend between the amount of damage and the changes in the modal parameters.

7. Plates $C_1 [90/0]_{2S}$

From Figure 5.29, the modal frequencies reduced across all the modes after the damage is introduced, which signals the presence of damage in the laminates. Although all the modes are affected, the damage locality affected modes 2 to 10 significantly. This is true because the level of reduction in the modal frequencies across those modes is higher.

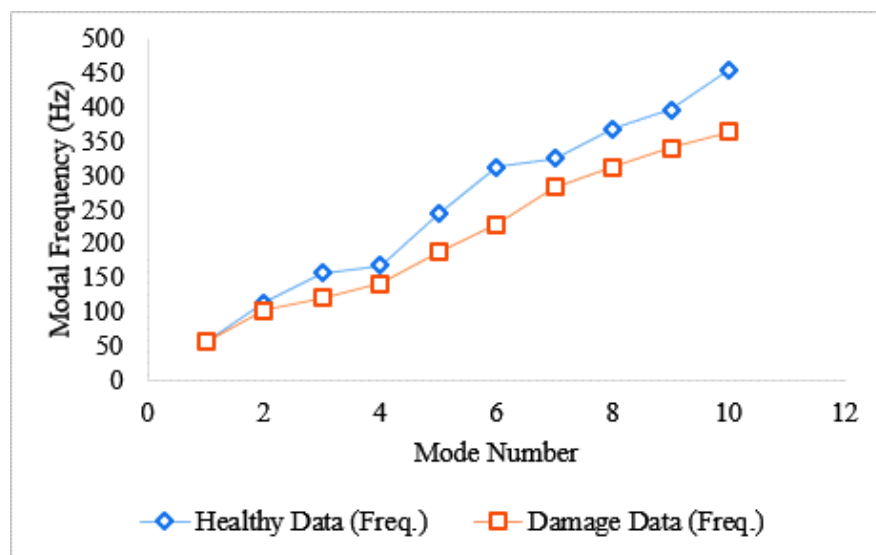


Figure 5.29 Changes in the modal frequency for plate C1.

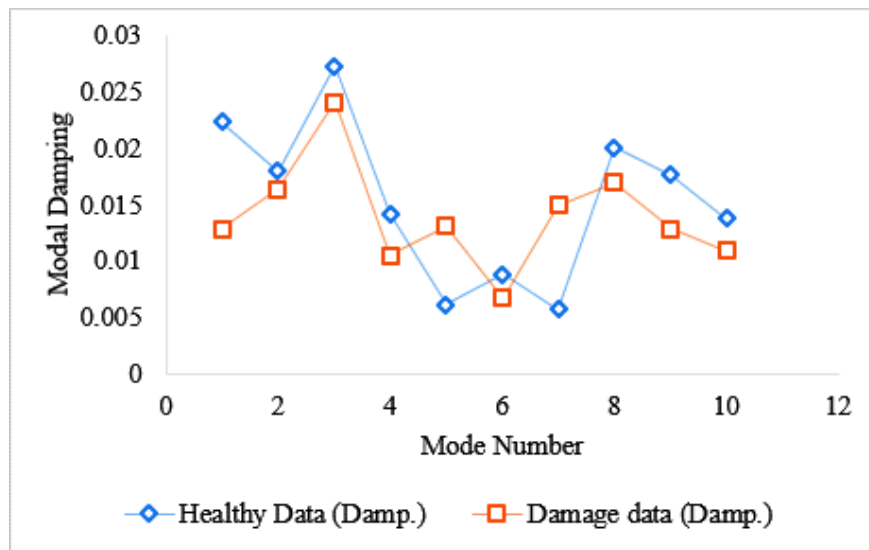


Figure 5.30 Changes in the modal damping for plate C1.

With the highest level of reduction in the modal frequency at mode 10, it suggests that the damage progression started at that mode, before spreading across the other modes. In Figure 5.30, except modes 5 and 7, the modal damping reduced at all other modes. The highest increase in the modal damping occurred at mode 7. Although the modal frequencies decreased at other modes, the level of reduction is relatively insignificant.

8. Plate C₂ [90/0]_{2s}

Figure 5.31 and Figure 5.32, shows the modal frequency and modal damping factor results respectively. The reduction in the modal frequencies at all but modes 3, 5, 6, 7 and 10; indicates the presence of damage in the test specimen. Although the reduction in the modal frequencies at those modes is not well pronounced, it still indicates the location of the damage progression which is at mode 8. Mode 8 records the highest level of reduction in the modal frequencies.

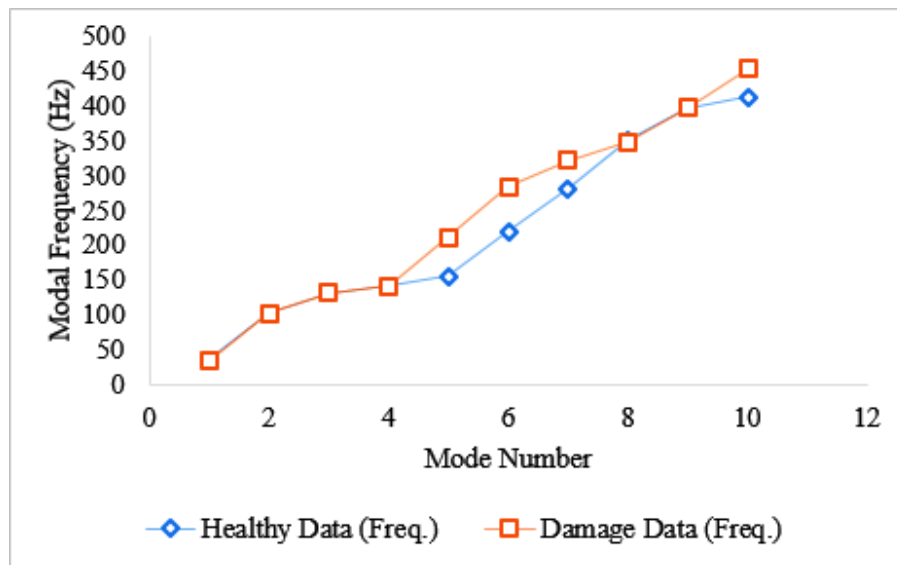


Figure 5.31 Changes in the modal frequency for plate C2.

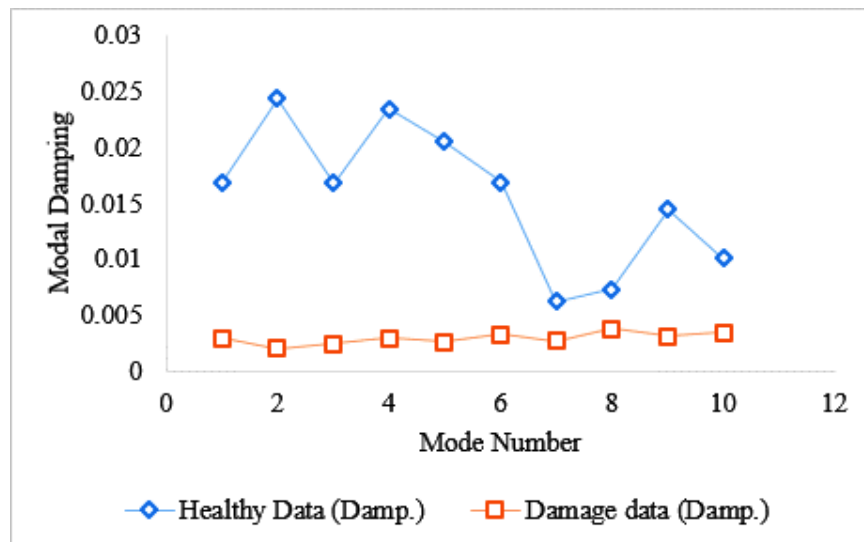


Figure 5.32 Changes in the modal damping for plate C2.

However, as the damage is introduced, the modal damping across all the modes decreased significantly. Again, unlike the modal frequency, the modal damping factor does not provide clear information about the presence of damage in the specimen. Hence, it is difficult to draw a conclusion based on the response of the modal damping to damage in a structure.

9. Plate C₃ [90/0]_{2s}

The presence of damage is indicated by the reduction in the modal frequencies at modes 2 and from modes 5 to 10. Refer to Figure 5.33. This confirms the reduction in the stiffness of the laminates due to the amount of damage introduced through static testing. The direct proportionality between the natural frequency and the stiffness of the material confirms the behaviour of the modal frequency when damage is introduced.

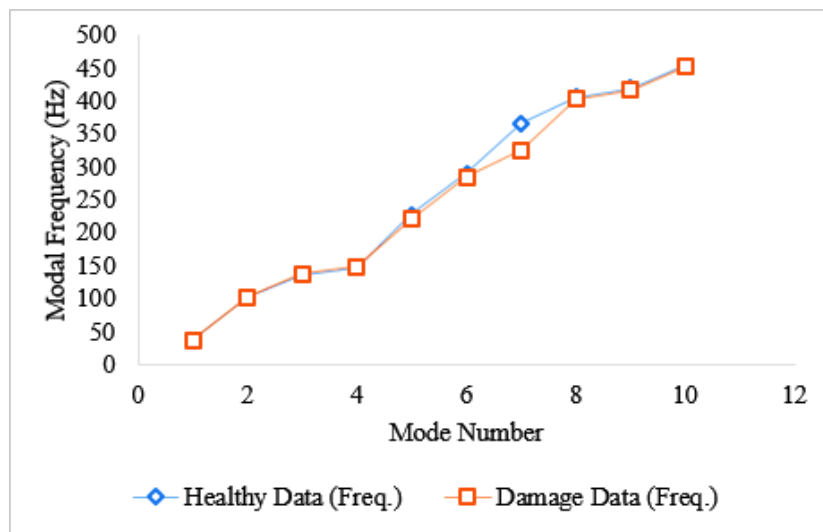


Figure 5.33 Changes in the modal frequency for plate C3.

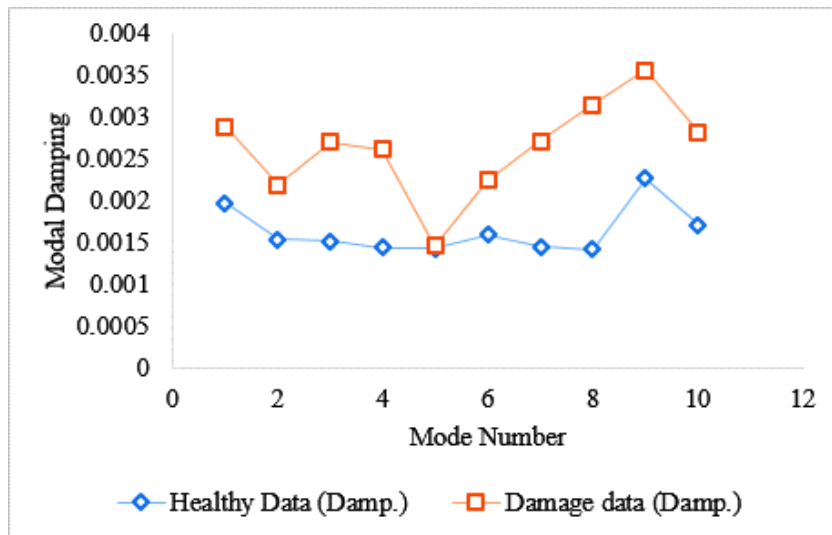


Figure 5.34 Changes in the modal damping for plate C3.

At modes 1, 3 and 4, there is a maximum increase of 0.5% in the modal frequency which is relatively small. The impact of the damage locality is more noticeable at mode 7, signifying the origin of the crack's growth in the laminates, before progressing across

other modes. Furthermore, it is shown in Figure 5.34, that there is an increase in the modal damping factors across all the modes. The increase is between the ranges of 2.7% to 108%, highlighting the uncertainties and difficulty in the identification of damage based on the responses of the modal damping factors.

10. Plate C₄ [90/0]_{2s}

Figure 5.35 shows a very good result, as the modal frequencies at all the modes decreased. This indicates the presence of damage in the specimen. However, the damage is concentrated from modes 8 to 10. This is due to the level of reduction in the modal frequencies at those modes. It indicates the impact level of the damage locality at those modes.

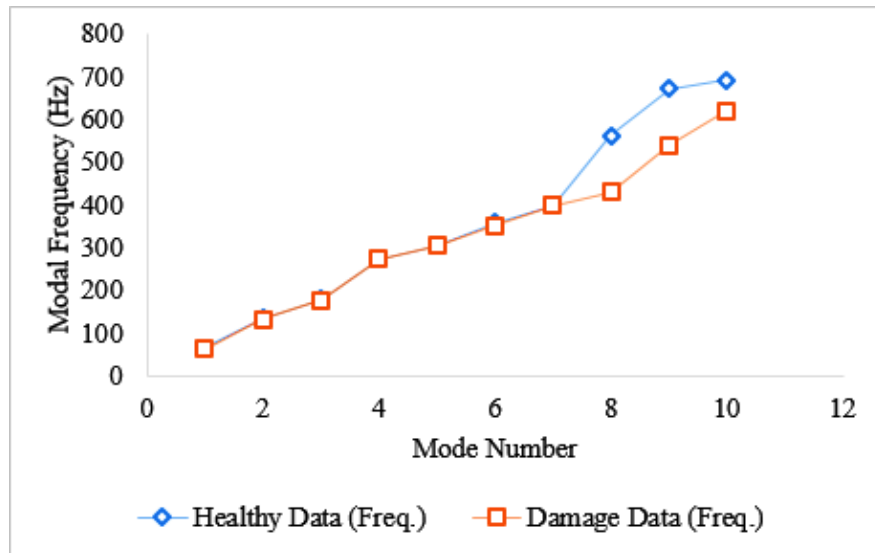


Figure 5.35 Changes in the modal frequency for plate C4.

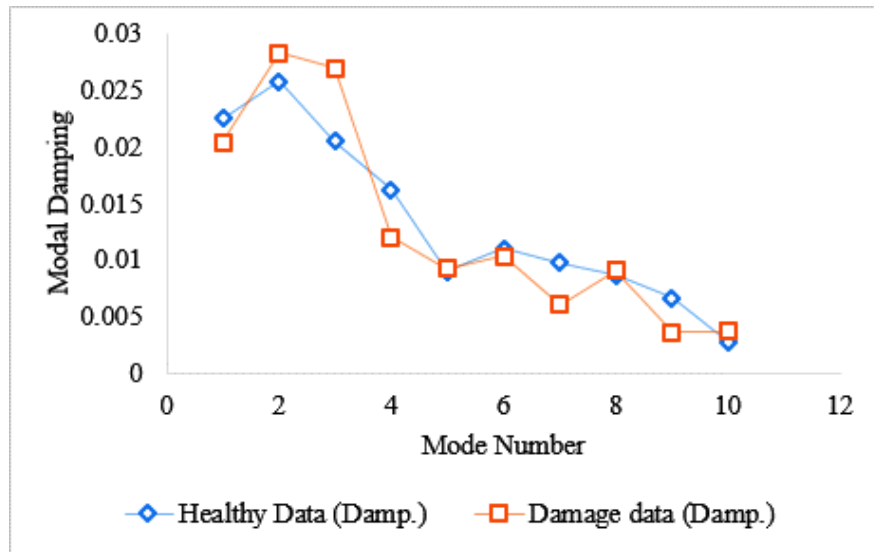


Figure 5.36 Changes in the modal damping for plate C4.

Conversely, the modal damping factors increased by 2.8% to 31.2% at modes 2, 3, 5, 8 and 10 after the damage is introduced. See Figure 5.36. The modal damping factor decreased at modes 1, 4, 6, 7 and 9, so it is again difficult to find a correlation between the modal damping factors and damage.

The results indicate that, there is more change in modal frequency in plate C2 than plate C3 and that of plate C3 is more than both plates C1 and C4. On the contrary, change in modal damping is more in plate C1 than plate C4 and that of plate C4 is more than that of plate C3. Plate C2 has the lowest change in the modal damping. While, the highest amount of damage was inflicted on plate C2, followed by C3, C4 and C1. This indicates that the more the damage in the plate, the more the changes in the modal frequencies. Although there seems to be a trend in these plates, it is difficult to draw a conclusion because the changes in the modal damping is random.

11. Plate D_1 [$90_2/0_3$]_s

There is a reduction in the modal frequencies at all the modes, except from modes 8 to 10, after the introduction of damage in the test specimen. This is a clear indication that there is damage in plate D1 across modes 1 to 7. The decrease in the modal frequencies means that the stiffness of the material has reduced due to damage at those modes.

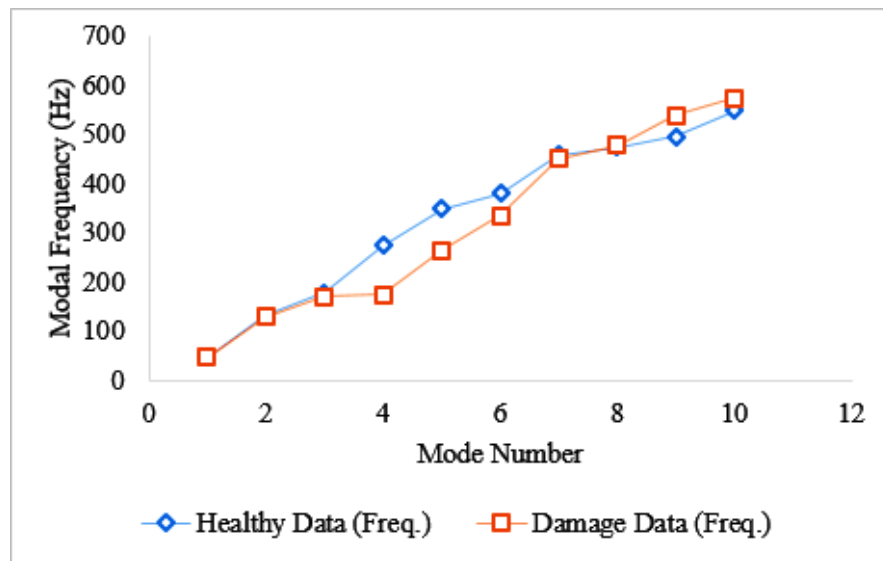


Figure 5.37 Changes in the modal frequency for plate D1.

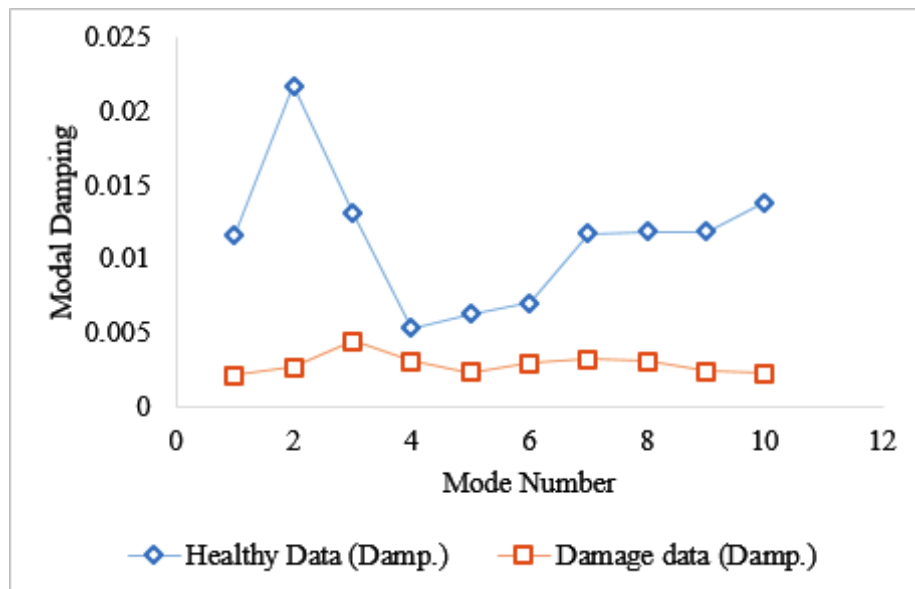


Figure 5.38 Changes in the modal damping for plate D1.

However, the degree of reduction varies at all the modes (see Figure 5.37). The damage concentration is at modes 3 to 7. Those are the modes with significant amount of reduction in the modal frequencies. The amount of reduction is between the ranges of 0.16% to 36.6%. That implies higher level of stiffness reduction within those modes. But the damage locality affected modes 4 to 6 more significantly.

Furthermore, just like the modal frequencies, the modal damping factors decreased at all the modes. This is shown in Figure 5.38. Unlike the modal frequencies, the percentage of reduction of the modal damping is higher. It ranges from 41.91% to

87.52%. Again, except the modal frequency, the modal damping fails to provide a clear information about the presence of damage in the CFRP laminates.

12. Plate D_2 $[90_2/0_3]_S$

A total of 10 modes were considered in specimen D2, as shown in Figure 5.39 and Figure 5.40 for modal frequency and modal damping respectively. In Figure 5.39, the graph shows a reduction in the modal frequencies from mode 4 to 10, and an increase from modes 1 to 3. The level of reduction in the modal frequencies at those modes are all very noticeable. This suggests the impact of the damage locality at those modes. Therefore, confirming the presence of damage in the test specimen. From the graph, it is shown that the damage started at two close modes, 5 and 6. However, the damage is spread across modes 4 to 10, due to the high level of reduction in the modal frequencies at those modes.

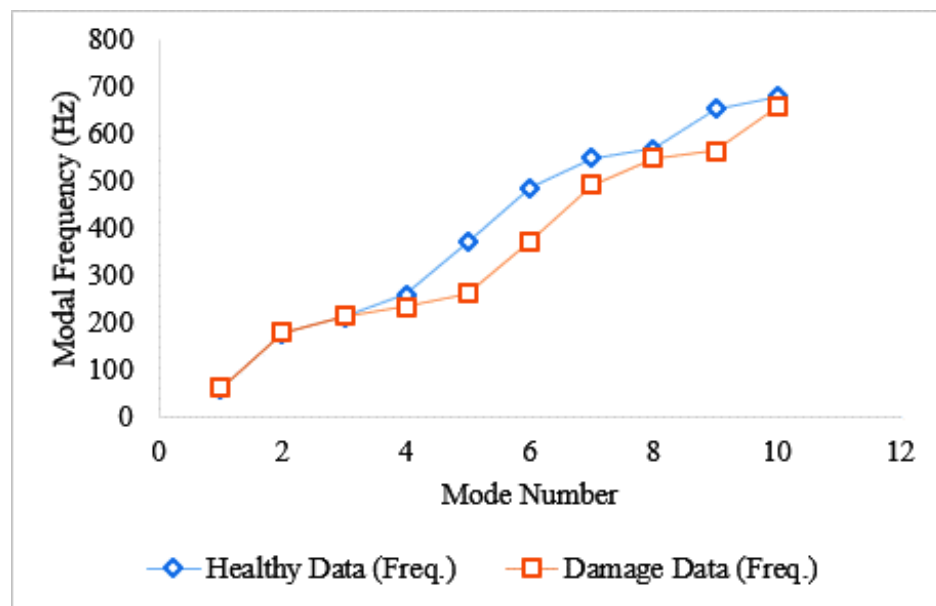


Figure 5.39 Changes in the modal frequency for plate D2.

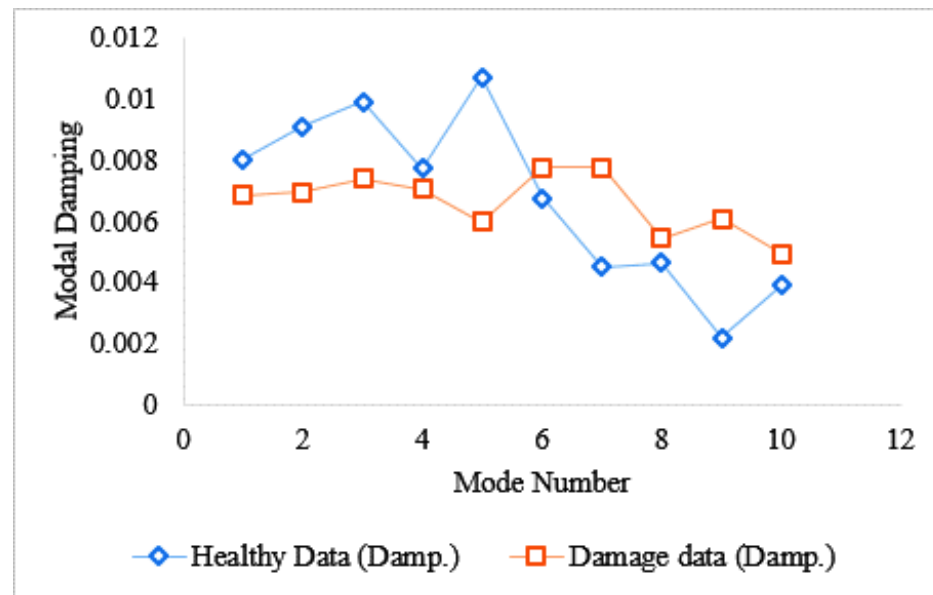


Figure 5.40 Changes in the modal damping for plate D2.

In Figure 5.40, it is shown that the modal damping factor decreased from modes 1 to 5 but increased from modes 6 to 10. As the modal frequencies reduce from modes 1 to 3, the modal damping decreases. On the contrary, as the modal frequencies decrease from modes 6 to 10, the modal damping increases. These 5 modes are within the damage locality based on the response from the modal frequencies. Although it is difficult to draw a conclusion yet, the inverse proportionality between the modal frequency and the modal damping at those modes strongly suggest the impact of the damage locality.

13. Plate $E_1[90_3/0_3]_S$

Figure 5.41, shows a reduction in modal frequency at all the modes, except mode 4 that has a 1% increment. The damage is concentrated around modes 2, 3, 6, 8, 9 and 10. However, modes 6, 8, 9 and 10 show the highest concentrations, which is referred to as the primary damage locations. In other words, the damage locality affected those modes more significantly.

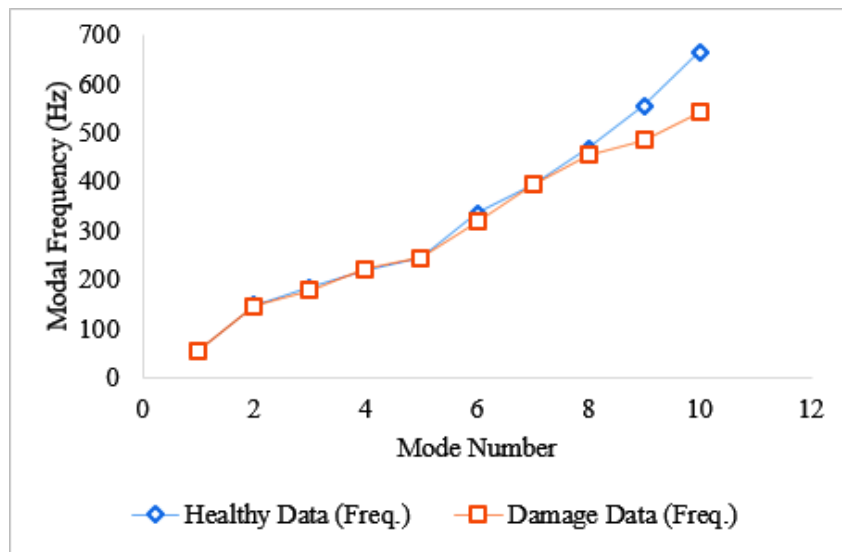


Figure 5.41 Changes in the modal frequency for plate E1.

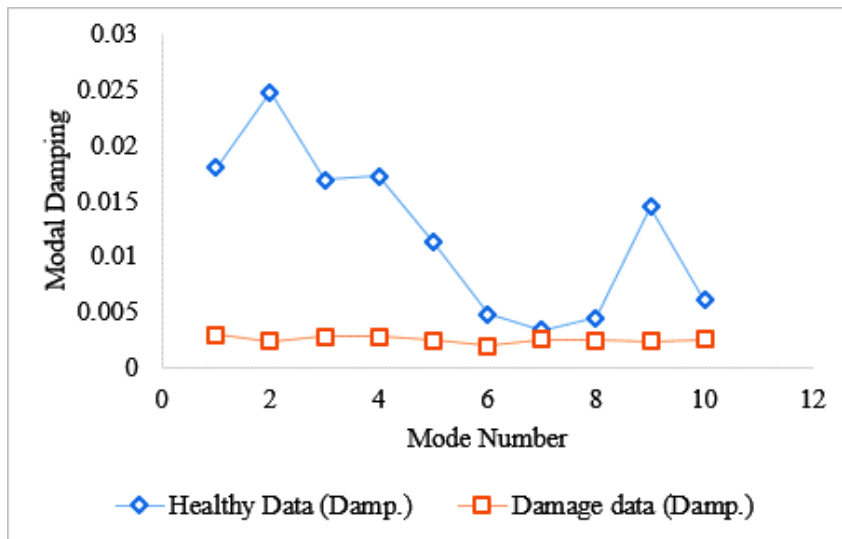


Figure 5.42 Changes in the modal damping for plate E1.

Unlike the modal frequency, the modal damping factor decreased at all the modes as shown in Figure 5.42. The percentage reduction ranges from 26.7% to 90.4%. It is yet unclear the reason behind such a drastic reduction in the modal damping factors. However, the decrease is quite negligible across all the modes.

14. Plate $E_2 [90_3/0_3]_S$

The damage introduced in the specimen compromised its stiffness, which in turn decreased the modal frequencies across the structure. It reduced at all modes but modes 1 and 5. Refer to Figure 5.43. The maximum increment at modes 1 and 5 is about 0.49%, which is negligible. The reduction in the modal frequencies indicates the

presence of damage in the CFRP laminates. Although the damage is present in the specimen, its concentration is localized at certain modes. The modes with the highest levels of reduction in the modal frequency suggest the damage locality.

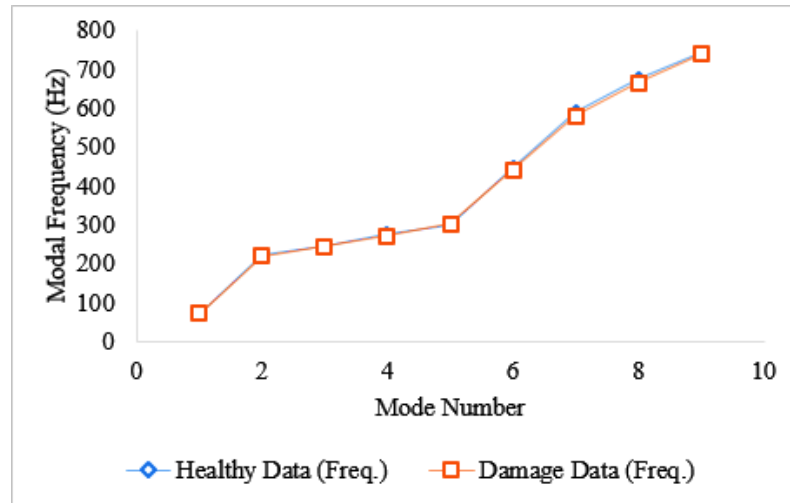


Figure 5.43 Changes in the modal frequency for plate E2.

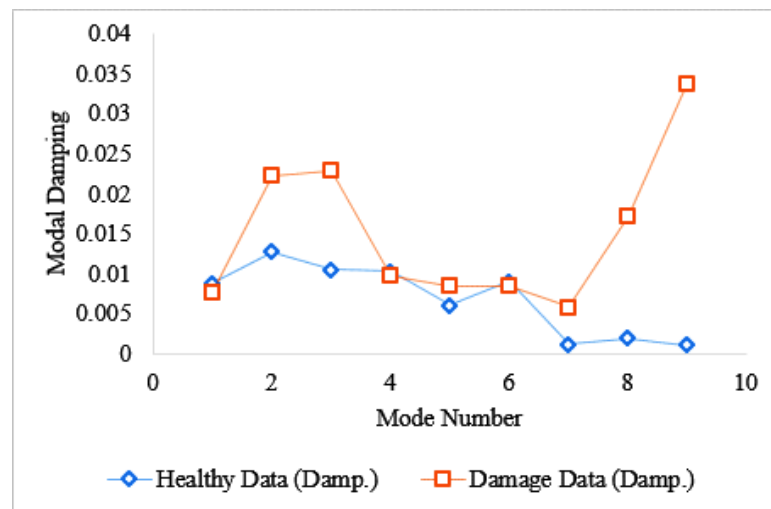


Figure 5.44 Changes in the modal damping for plate E2.

In this test sample, the damage concentrated areas are modes 2, 4, 6, 7 and 9. The variation in the modal damping factors in this sample appears different (see Figure 5.44). Apart from modes 1, 4 and 6; at all other modes, there is an increment in the modal damping factor. This unstable behaviour of damping makes it less helpful as a modal parameter for damage identification in a structure. The modal frequency provides a better indicator in the damage identification process.

There is a trend from Figure 5.37 to Figure 5.44. The more the damage inflicted on the test specimens, the more changes in modal frequencies and the less changes in the modal damping. However, further research is still required to obtain a firmer conclusion.

15. Plate F_1 $[0/\pm 45/90]_S$

Apart from modes 1 and 5, the modal frequencies are reduced at all the modes indicating the presence of damage in the test specimen. This suggests that the stiffness of the laminates has been compromised across nearly all the modes. Because the percentage increase of the modal frequencies at modes 1 and 5 are 1.65% and 0.37% respectively; which are very negligible.

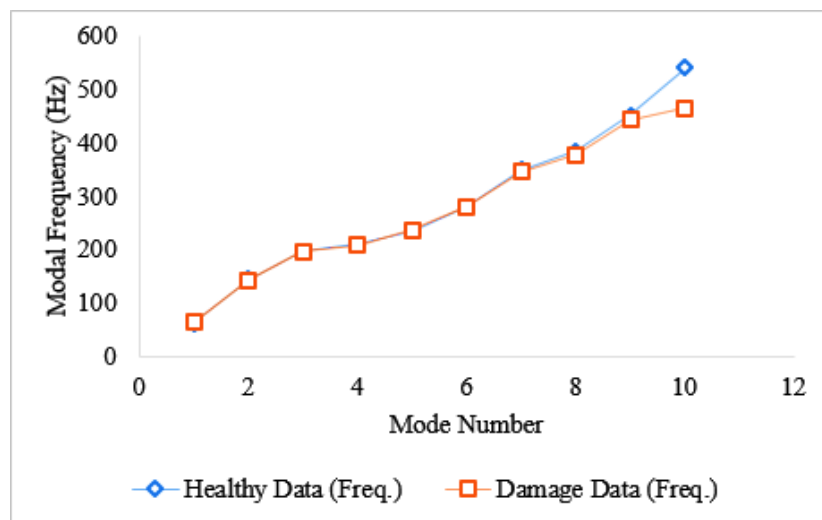


Figure 5.45 Changes in the Modal frequency for plate F_1 .

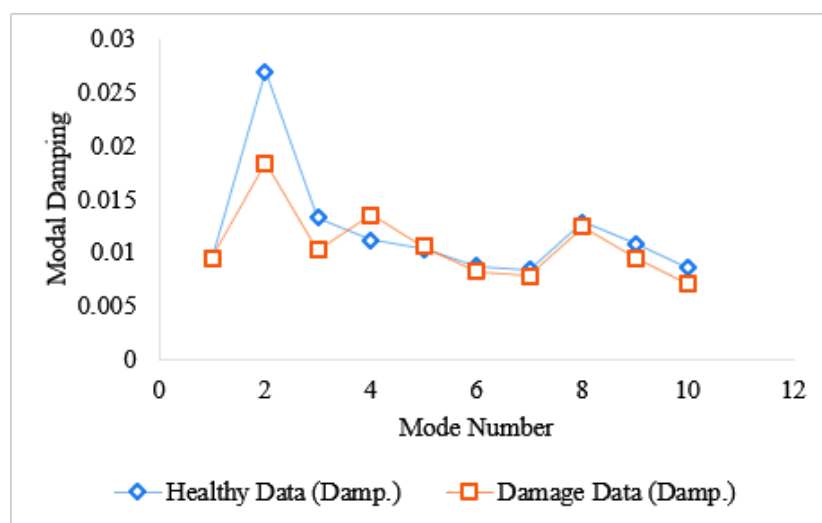


Figure 5.46 Changes in the Modal damping for plate F_1 .

However, the primary location of the damage is from modes 8 to 10; with mode 10 having the highest impact. Refer to Figure 5.45. In Figure 5.46, the result indicates a reduction in the modal damping factors at modes 2, 3, and 6 to 10, while at modes 1, 4 and 5, the modal damping factors increased. Again, it is difficult to draw a conclusion from the behaviour of the modal damping factor.

16. Plate G_1 [$90_3/0_3/90_3$]

As the damage is introduced to the specimen, the deviations in the frequency at modes 1, and from modes 4 to 10 decreased. See Figure 5.47. This suggests that the damage is spread across those modes, but its locality had more impact from modes 4 to 10. Those are the damage concentration areas. The crack growth commenced at mode 6, before propagating to other modes. Obvious, this has compromised the integrity of the test plate due to the reduction in the stiffness of the material.

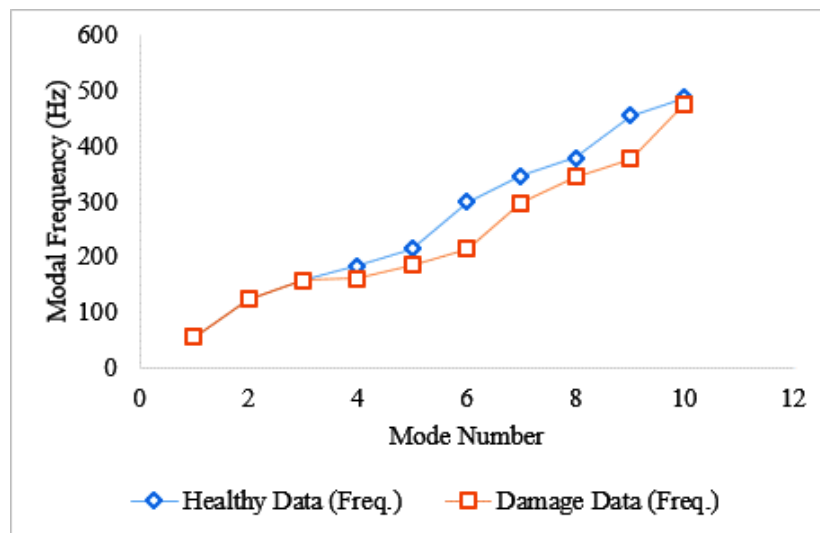


Figure 5.47 Changes in the Modal frequency for plate G_1 .

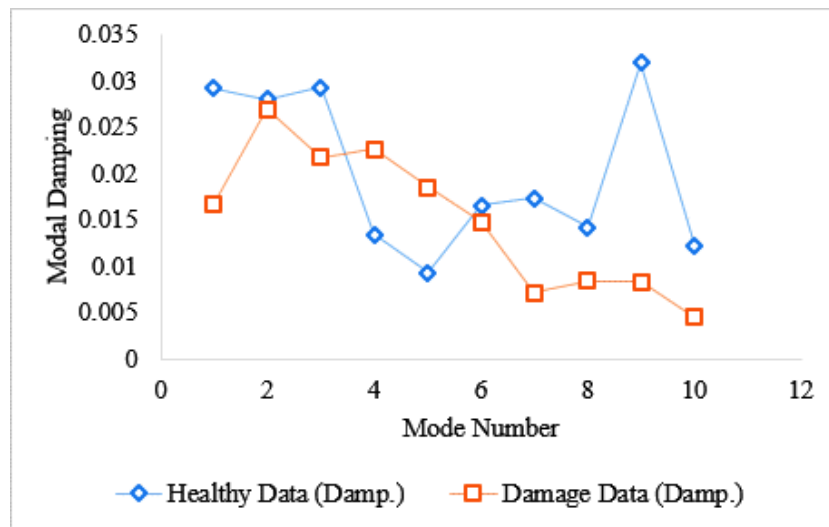


Figure 5.48 Changes in the Modal damping for plate G_1 .

Furthermore, Figure 5.48 shows the behaviour of the modal damping factors after the introduction of damage in the test specimen. The result indicates a reduction in the modal damping at all the modes, except 4 and 5. Again, the amount of reduction in the modal damping across those modes is insignificant.

5.4.3 Preliminary Observations on the Effect of Damage on different Stacking Configurations

This section is focused on how different stacking configurations respond to damage in composite CFRP laminates. The study considered three different stacking sequences, each having two samples making it a total of 6 test plates. The specimens are labelled in alphanumeric style. That is plates A1, A2, B1, B2, C1 and C2, as shown from Figure 5.49 to Figure 5.51. The laminate type of plates A and B is quasi-isotropic, and plate C is a cross-ply (orthotropic). The aim is to understand how the laminate configuration responds to low impact damages in a composite CFRP structure.

After the first test, the modal properties were extracted from the test data using BETAlab software developed by [25]. The software utilises the characteristic response function (CRF) [25,245]. The variation in the modal frequencies and modal damping are shown in Figure 5.49. It was observed that among all the plates, only plate C1 recorded a reduction in the modal frequencies across all the 10 modes. This suggests that it is highly sensitive to damage. In plate A1, the reduction in the modal frequency is from modes 2 to 8; while in plate A2 at mode 2, and from modes 5 to 10 there is a

reduction in the modal frequencies. Plate B1 has a reduction in the modal frequencies from modes 3 to 10, while reduction occurred at mode 4, 6, 7 and 8 in plate B2. The modal frequencies decreased at modes 1, 2, 4, 8 and 9. There is a reduction in the modal frequencies at modes 6 and 7 across all the plates. This implies that the modal stiffness of the plates has been compromised significantly at modes 6 and 7.

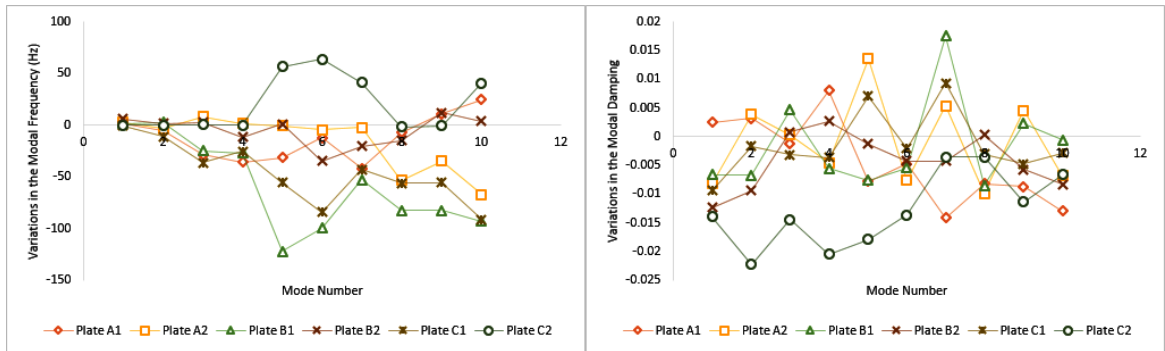


Figure 5.49 Modal parameters response to damage based on stacking configuration (1st test).

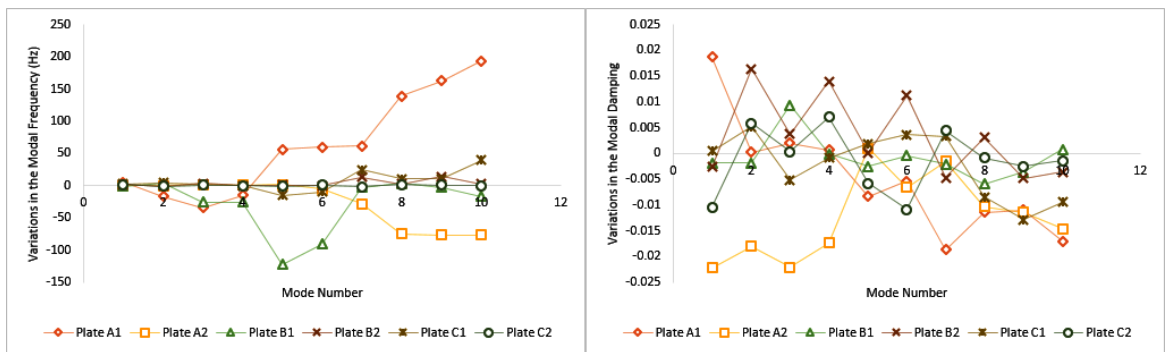


Figure 5.50 Modal parameters response to damage based on stacking configuration (2nd test).

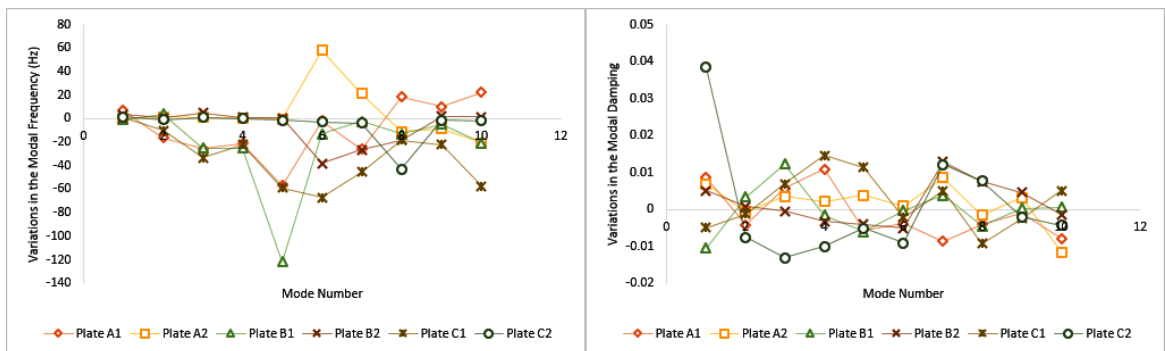


Figure 5.51 Modal parameters response to damage based on stacking sequence (3rd test).

Also, with regards to the modal damping factors, there is a reduction at modes 3, and from modes 5 to 10 in plate A1. However, in plate A2, modes 1, 4, 6, 8 and 10 showed a decrease. Plates B1 and B2 has a decrease in the modal damping at modes 1, 2, 5, 6 and 10. However, plate B1 also recorded a reduction at modes 4 and 8, while plate B2 also had a reduction at modes 7 and 9. Interestingly, plates C1 and C2 has a reduction in the modal damping at modes 1, 2, 3, 4, 6, 8, 9 and 10 in common. Plate C2 also has a reduction at modes 5 and 7.

Furthermore, the second and the third test results are shown in Figure 5.50 and Figure 5.51 respectively. After the second test, there is a reduction in the modal frequencies from modes 2 to 4 in plate A1, while plate A2 recorded a reduction from modes 6 to 10. Except at modes 2 and 8, there is a reduction in the modal frequencies at all modes in plate B1; plate B2 has a reduction only at mode 2. Plate C1 has a reduction at modes 5 and 6, while plate C2 recorded a reduction at modes 2, 5, 7 and 10.

Similarly, after the second test, the modal damping decreased from modes 5 to 10 in plate A1, and plate A2 recorded a reduction across all the modes but mode 5. Plate B1 has a reduction at all the modes except modes 3 and 10, while plate B2 has a reduction at modes 1, 7, 9 and 10. Also, the modal damping reduced at modes 3, 4, 8, 9 and 10 in plates C1. While, plate C2 has a reduction at modes 1, 5, 6, 8, 9 and 10.

Finally, after the last test, the modal frequencies from plate A1 reduced from modes 2 to 7, while plate A2 recorded a reduction at modes 5, 8, 9 and 10. In plate B1, apart from mode 2, all the modes recorded a reduction in the modal frequencies. Then plate B2 has reduction from modes 6 to 8. Coincidentally, plates C1 and C2 has reduction in the modal frequencies at modes 2, and from modes 5 to 10. However, plate C1 also has a reduction at modes 3 and 4.

The modal damping reduced at modes 2 and from modes 5 to 10 in plate A1, while plate A2 recorded a reduction only at modes 2, 8 and 10. Plate B1 has a reduction at modes 1, 4, 5, 6 and 8. On the other hand plate B2 ha a reduction from modes 3 to 6, and at mode10. While, plate C1 has a reduction in the modal damping at modes 1, 2, 6, 8 and 9. All but modes 1, 7 and 8, has a reduction in the modal damping in plate C2. Interestingly, plate B1 recorded the lowest modal frequencies at mode 5 across all the

three tests. This suggest that the damage concentration area in plate B1 is around mode 5.

5.4.4 The Behavioural Pattern of Modal Parameters due to Increased Energy Level

Assuming that BVID damage will not affect the mass, but the stiffness, then it is reasonable to assume that the natural frequencies will decrease if one thinks of a lumped-mass single degree-of-freedom vibration model. This is the underlying assumption in most SHM and damage detection methods. Likewise, some works are based on the fact that the modal damping factors change. However, this mechanism has not yet been totally understood, as evidence does not always show that damping necessarily increases with damage [262], which has been attributed to many reasons, one of which the uncertainty in the identification algorithm used.

This section discussed the impact on the modal parameters due to the increasing energy levels on the specimens. Three different energy levels were introduced into 8 specimens, with the aim of observing the behaviour of the modal parameters within the first 10 modes. Since, damage was introduced three times, then we have six cases (see Table 5.2) to compare in terms of how frequencies and damping evolve.

1. Plates A_{1-2} $[90/\pm 45/0]_S$

The response of the modal frequency and damping to damage in Plate A1 and A2 are shown in Figure 5.52 and Figure 5.53 respectively. In Figure 5.52, after the first increment in the energy absorbed by the test plate, the modal frequencies from modes 2 to 4 were reduced significantly just like as it was in the first test. Similarly, when damage was introduced the third time with an energy level above that of the second test, modes 2 to 7 recorded a drop in the modal frequencies.

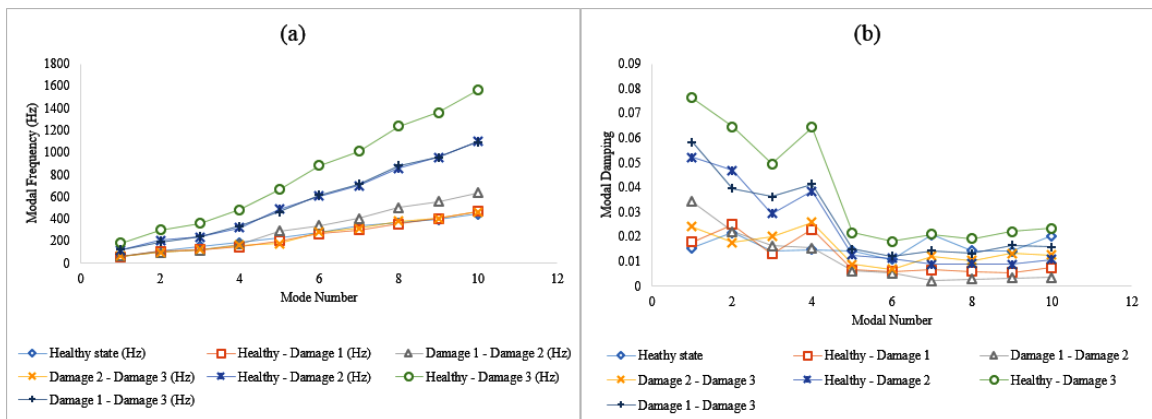


Figure 5.52 Modal parameters response to increased energy level in plate A1: (a) Modal frequency (b) Modal damping.

It is interesting to note that the reduction occurred at the same modes except at mode 8 where reduction occurred only in the first test result. For the fact that the three tests recorded a reduction in the modal frequency from modes 2 to 4, confirms the presence of damage in the test plate. However, despite the increase in the energy level in the test plate, the modal frequencies at modes 1, 9 and 10 are still on the increase even after the three tests. In fact, the percentage increase is higher in the second test from modes 5 to 10.

Furthermore, after the second test, unlike the first test, there is an increase in the modal damping for the first four modes with over 120% increase at mode 1. In all the three test runs as the modal frequencies increases at modes 1, the modal damping increases too. From modes 5 to 10, there is a reduction in the modal damping in all the three test results. Although it is difficult to draw a conclusion from this result due to the unstable behaviour of the modal damping, there is an interesting observation after the second test. It is shown that the level of reduction in modal damping from modes 5 to 10 in test 3 are smaller than that of both test 1 and 2. This implies that as the damaged area increases the modal damping tends to increase as well.

For better understanding of the response of the modal parameters to energy increase, three more cases (from healthy to second damage (18.2J), from healthy to third damage (34.7J), and from second damage to third damage (29.2J)) were considered. In all the three cases, the results indicate an increase in the modal frequency across all the modes. However, the increase is much higher when the energy increases from healthy to third

damage, which has the highest energy. Similarly, the modal damping recorded an increase at all the modes due to the increase in energy to 34.7J. At 18.2J, there is an increase in the frequency at modes 1, 2, 3, 4 and 5. While, at 29.2J, the increase in the modal frequency is from modes 1 to 6, and at mode 9.

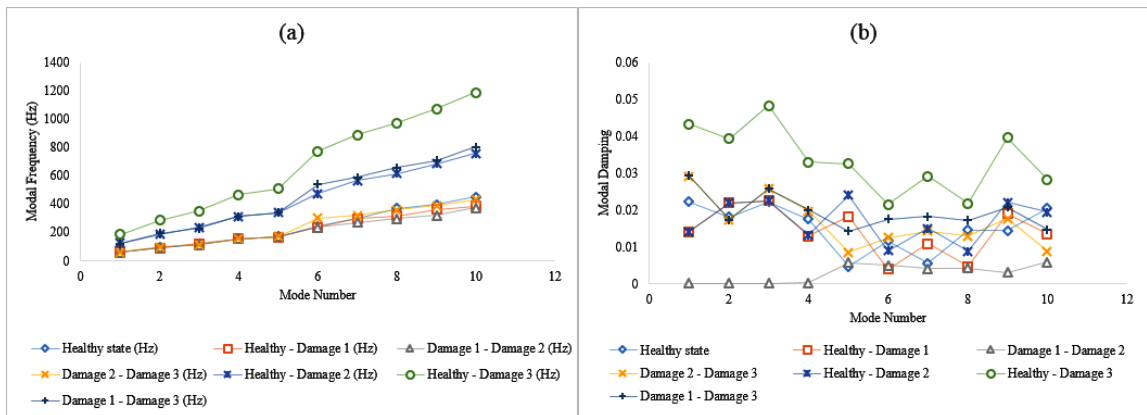


Figure 5.53 Modal parameters response to increased energy level in plate A2: (a) Modal frequency (b) Modal damping.

For plate A2 as illustrated in Figure 5.53, the second test recorded a drop in the modal frequencies from mode 6 to 10. These modes also have a reduction in the modal frequencies in the first test result. After the third test, it was observed that modes 5, 8, 9 and 10 has a reduction in the modal frequencies. These responses from the three test results provide a strong indication of the presence of damage from modes 8 to 10.

Unlike the results from test 1, the modal damping reduced at all, but mode 5 after the second test. It is evident that there is an increase in the modal damping at mode 5 across all the three test results. Also, as the modal frequencies reduces at modes 8 and 10, the modal damping reduces too in all the three test results. Although the modal damping hardly provides a clear information about the presence of damage in a structure, after the third test the number of modes that recorded an increase in the modal damping increased to 7 out of the 10 modes considered. This suggest that if the damage area increases, the modal damping would increase, which is also observed in plate A1.

Also, at the energy level of 17.8J, 31.3J and 26.2J, the modal frequencies across the ten modes were all positive. This suggest that as the energy level increases, the modal frequency increases. However, at 17.8J, the percentage increase at modes 1, 3 and 4 are higher than those at 26.2J. Similarly, at 31.3J, the modal damping increases at all the

modes. Also, there is an increase in the damping at modes 3, 5, 7 and 9 from 17.81J to 31.3J, with the highest percentage increase when the energy level is 31.3J. From the result, it is convenient to say that, the higher the energy level, the higher the percentage increase in the modal frequency and modal damping.

2. Plates $B_{1-2} [90/0/\pm 45]_5$

In Figure 5.54 the behaviour of the modal frequencies from Plate B1 after the tests are shown. Just like the result in test 1, in test 3 the modal frequencies reduced from modes 3 to 10 with mode 1 inclusive. While in the second test, there is a reduction in the modal frequencies at all the modes, except modes 2 and 8.

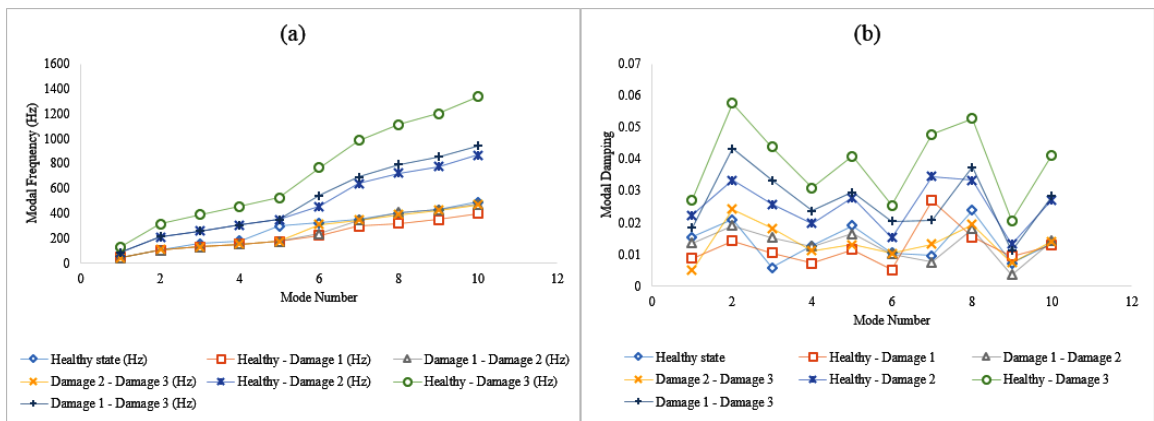


Figure 5.54 Modal parameters response to increased energy level in plate B1: (a) Modal frequency (b) Modal damping.

From the graph of plate B1, it is clearly revealed that the damage concentration is at mode 5 across all the three tests. Of course, this is true because the impact energy was introduced at the same location on the test plate, and the damage progression was evenly spread from modes 3 to 5. Based on the results, it is convenient to assert that there is a correlation between damage and modal frequency. As the damage progresses, the modal frequencies of the laminates decrease at each mode.

Although there is a reduction in the modal damping at some modes after test 1, 2 and 3, there appears to be a shift to the positive side as the damage area increases. After the second test, the gap between the decreased modal damping for the first and second test closes, except at modes 7 and 9. While at mode 3, there is a continuous increase in the modal damping from test 1 to 3. With the increase in the energy level in test 3, there is an increase in the modal damping at modes 2, 3, 7, 9 and 10. With respect to test 1

result, there is a relative increase in the modal damping after test 3; such that even the decreased modal damping at modes 2, 4, 5, 6, 8 and 10 in the first test tends to the positive axis after test 3. These results suggest that as the damage area increases, the modal damping tends to increase.

Similarly, in Figure 5.55 the modal frequency and damping are plotted against the modes to show their response to damage in plate B2. There is a reduction in the modal frequencies from modes 6 to 8 in both test 1 and 3. This suggests the presence of damage around those modes, with the damage concentration at mode 6, being the mode with the highest level of reduction in the modal frequency. However, the modal frequency decreased at mode 4 and 2 in test 1 and 2 respectively. There are 6 modes with increased modal frequencies in the first test, 9 modes in the second test, and 7 modes in the final test.

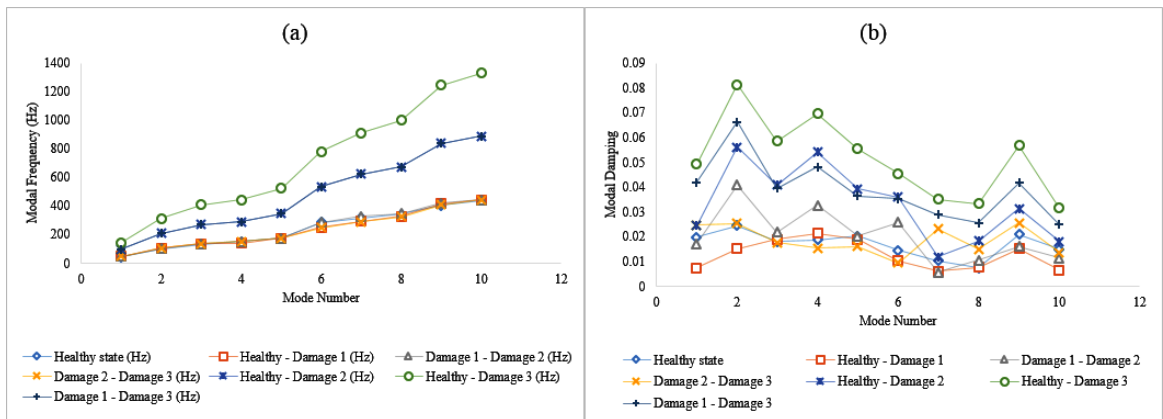


Figure 5.55 Modal parameters response to increased energy level in plate B2: (a) Modal frequency (b) Modal damping.

This suggests that plate B2 has a high tensile strength, hence can withstand possible damage growth to some extent. However, if the amount of stress on the plate keeps increasing, cracks would develop at an exponential rate leading to deformation or otherwise fails. The modal damping response to damage in plate B2 varies as the energy level absorbed increases. There is an increase in the modal damping at modes 2, 3, 4, 5, 6 and 8 after test 2. The increase is higher than that of test 1 at same modes. In fact, after the third test, the modal damping increases as the energy absorbed increases at modes 1, 7, 8 and 9. There is a continuous increase in the modal damping at mode 8 across test 1 to 3.

Although there is a reduction in the modal damping at modes 1, 2, 9 and 10, a closer look at those modes in the plot reveals that as the damage level increases, the percentage difference in the modal damping shifts from the negative axis to the positive axis or closer to it. This behaviour suggests that if the damage area increases, the modal damping will increase as well.

Just like in plate B1, from Figure 5.55, it is shown that, both modal frequency and modal damping are increasing as the energy level increases from 14.5J to 27J, recording the highest increase at 27J. One thing is clear, as the energy level increases, the modal parameters tend to increase.

3. Plates C_{1-2} $C_1 [90/0]_{2s}$

Figure 5.56 shows the plots for both modal frequency and damping for plate C1. Except test 3, the energy was introduced into the plate at the same location during test 1 and 2. This is obvious in the results shown in Figure 5.56. The modal frequencies at all the modes in both test 1 and 3 reduced, except mode 1 in test 3. However, there is a reduction in the modal frequencies at modes 5 and 6 after the second test. Despite the distance between the two points of impact on the plate, all the three test results confirm the presence of damage at modes 5 and 6. This suggests that no matter the location of damage in the laminate, the modal frequency is sensitive enough to detect it.

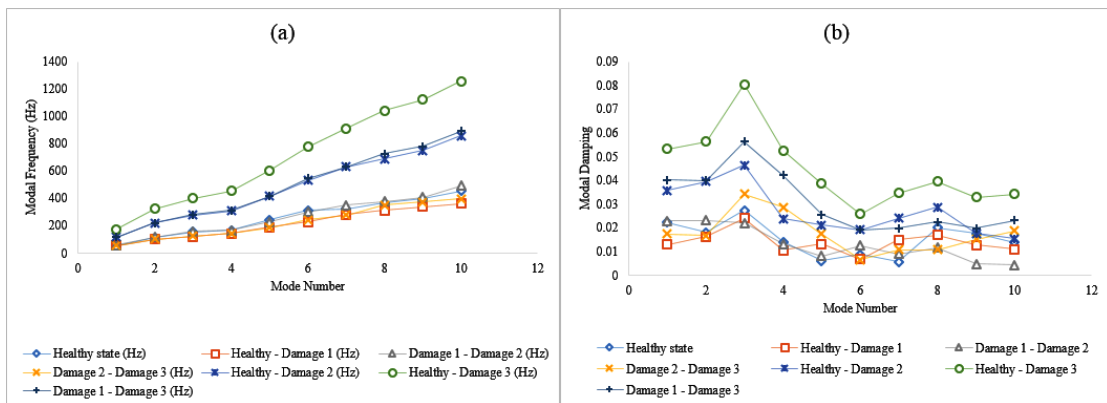


Figure 5.56 Modal parameters response to increased energy level in plate C1: (a) Modal frequency (b) Modal damping.

Furthermore, as regards the modal damping, there is an increase at modes 5 and 7 across the three test results. Also, at mode 4 there is a systematic increase from the negative axis to the positive axis as the energy level increased from test 1 to 3. Although it is

hard to draw a conclusion based on this behaviour, the result shows an element of damage in the plate at modes 4, 5 and 7.

In Figure 5.57, the modal parameters for plate C2 are plotted against the mode number. After test 1, the modal frequency decreased at modes 1, 2, 4, 8 and 9. While, modes 2, 5, 7 and 10 recorded a reduction in the modal frequencies after test 2. Finally, after test 3, the modal frequencies decreased at modes 2 and from 5 to 10.

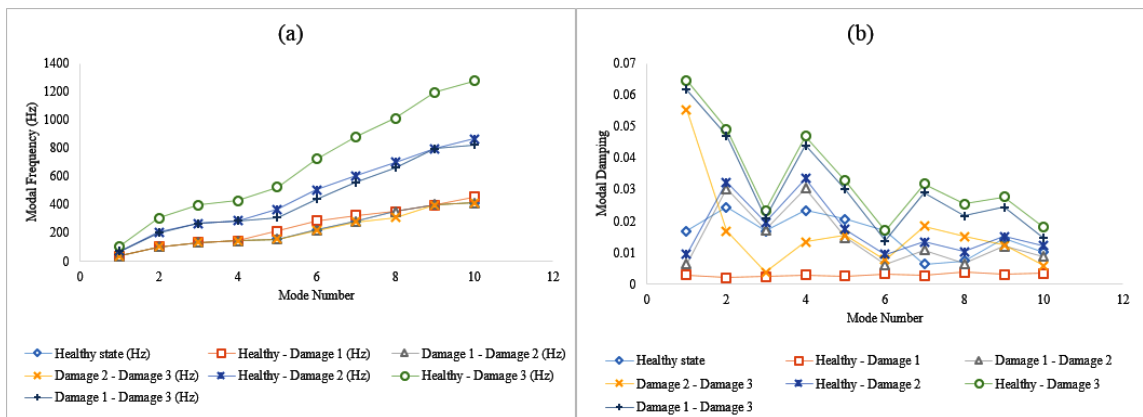


Figure 5.57 Modal parameters response to increased energy level in plate C2: (a) Modal frequency (b) Modal damping.

For the fact that the modal frequency decreased at mode 2 across all the three tests, suggest the presence of damage at that mode. Although the modal damping is reduced across all the modes after test 1, there is an increase at modes 2, 3, 4 and 7 after test 2. When the energy level is increased at test 3, the modal damping increased at modes 1, 7 and 8. On the other hand, as the energy level increases, the negative modal damping (at modes 1, 5, 6 and 9) increases.

The response from the modal parameters in plate C2 is not too different from other plates when the energy increased. With an increased energy from 18.6J to 36.3J, the modal frequencies across the ten modes were increased. There appears to be a direct relationship between energy increase and that of the modal parameters. Because, despite the percentage reduction in the modal damping at modes 1, 5 and 6, they all increased as the energy level increased to 36.3J.

4. Plates $D_1 [90_2/0_3]_S$ and $E_1[90_3/0_3]_S$

The results from plate D1 after test 1 to 3 are shown in Figure 5.58. The result after test 1 indicates a reduction in the modal frequencies from modes 1 to 7; and modes 3 to 10 after test 3. It is interesting to note that the area of damage (from modes 4 to 6) concentration is indicated in test 1 and 3 results. These are the modes with the highest level of reduction in the modal frequencies after the damage is introduced. However, test 2 result does not provide much information, except the reduction in the modal frequency at mode 1.

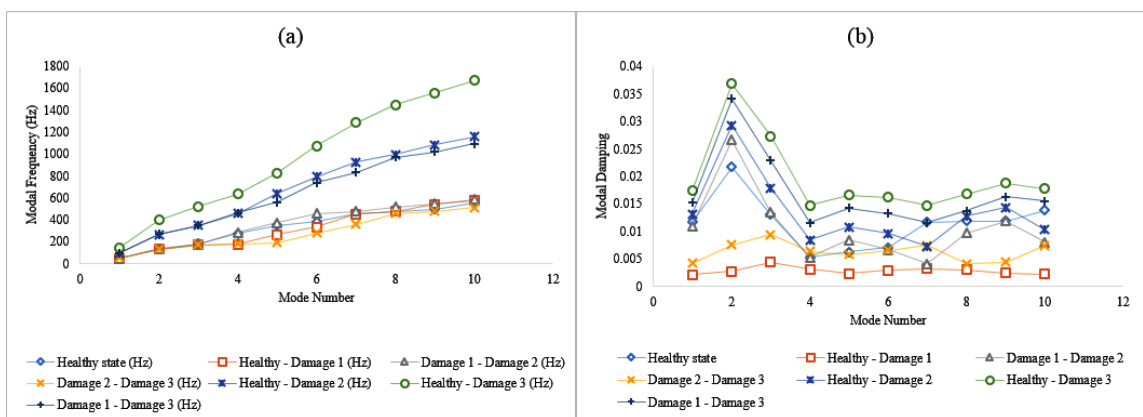


Figure 5.58 Modal parameters response to increased energy level in plate D1: (a) Modal frequency (b) Modal damping.

The modal damping does not provide a clear indication of damage in the test specimen as shown in Figure 5.58. Across all the modes in test 1, the modal damping reduced greatly after the damage introduction. Similarly, in from test 3 result, all but mode 4 recorded a reduction in the modal damping. However, test 2 result shows an increase in the modal damping at modes 2, 3, 5 and 9. Although the negative value is reducing at mode 4 and 7 as the energy level in the test plate increases, the modal damping has yet provided a clear indication of damage in the plate D1.

Figure 5.59 shows the modal parameters from healthy and damaged plate E1. Just like other plates, three different amounts of energies were introduced into the test plate by static testing, and vibration measurement conducted to extract the modal parameters. The modal frequencies reduced at all the modes, but the 4th mode after test 1. From the second test result, it is shown that there is a reduction in the modal frequencies from modes 3 to 10. The two modes with increased modal frequency are less than 1%. This suggests that if the size of the crack increase around those modes, the modal frequencies

would reduce too. Upon the increase of the energy level in test 3, the modal frequencies reduced from modes 1 to 3 and from modes 5 to 10. Based on the results after test 1, 2 and 3, the damage locality is within modes 9 and 10.

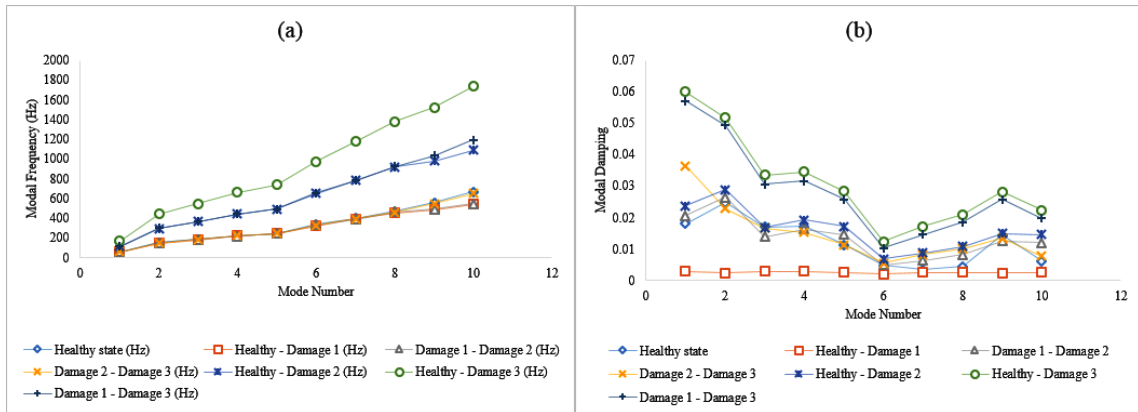


Figure 5.59 Modal parameters response to increased energy level in plate E1: (a) Modal frequency (b) Modal damping.

Although after the first test, the modal damping reduced across all the modes. But there is an increase at modes 1, 2 and from 5 to 8 after the second test is conducted. When the energy is increased further, only modes 1, 6, 7, 8 and 10 recorded an increase in the modal damping. However, with an overall consideration, as the energy level increases from test 1 to 3 (a horizontal consideration), the modal damping increases at modes 1, 3, and from modes 6 to 10. This is true because the negative value decreases and tends to the positive side as the crack size increases.

5.4.5 The Correlation between the Energy Increase and Modal Parameters

This section focused on examining the correlation between the energy increase in the test specimens and their modal parameters (frequency and damping). This was achieved by plotting the energy against the overall variation (i.e., arithmetic average of the modal variations) in both frequency and damping percentages. The plots of the linear trend for the test plates are shown from Figure 5.60 to Figure 5.67.

Analysis of the Response of Modal Parameters to Damage in CFRP Laminates using a Novel Modal Identification Method

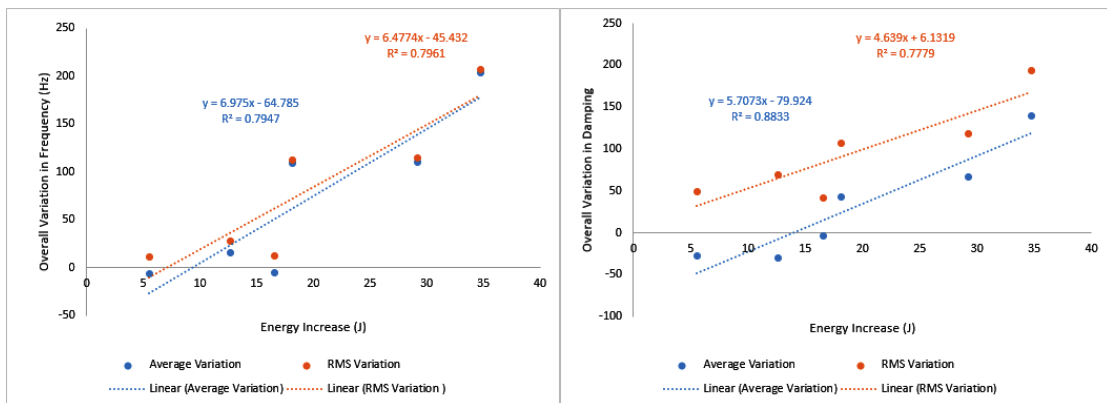


Figure 5.60 Linear trend for identifying the correlation between energy increase and modal parameters from Plate A1: (LHS) modal frequency (RHS) modal damping.

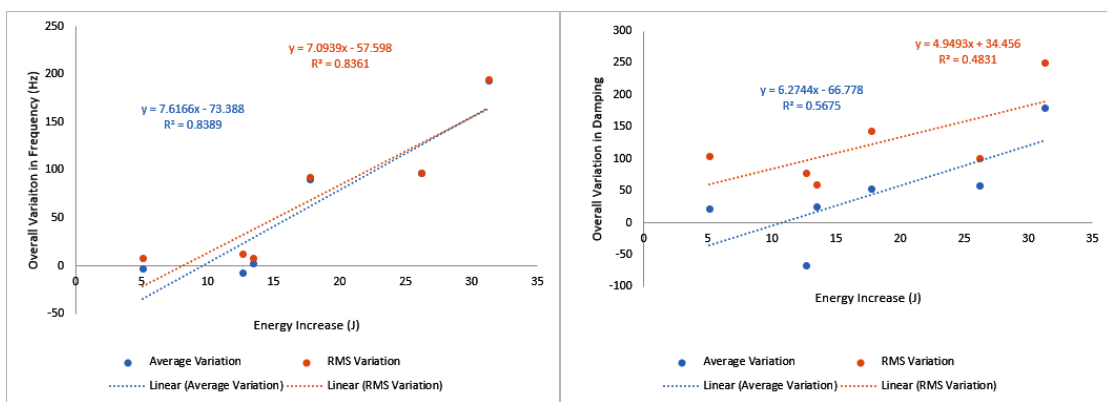


Figure 5.61 Linear trend for identifying the correlation between energy increase and modal parameters from plate A2: (LHS) modal frequency (RHS) modal damping.

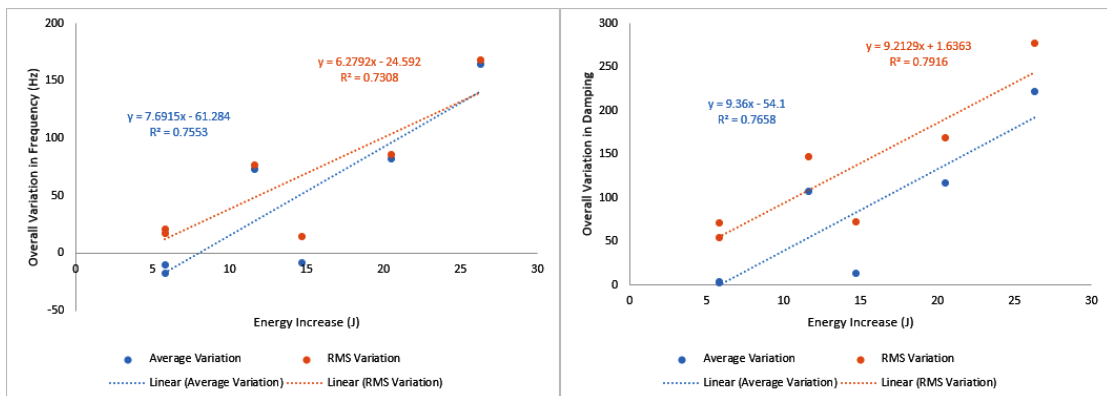


Figure 5.62 Linear trend for identifying the correlation between energy increase and modal parameters from plate B1: (LHS) modal frequency (RHS) modal damping.

Analysis of the Response of Modal Parameters to Damage in CFRP Laminates using a Novel Modal Identification Method

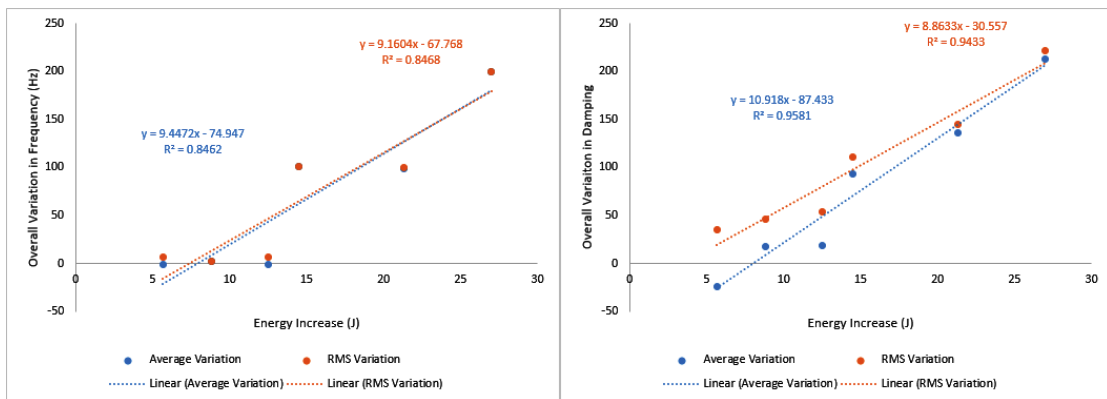


Figure 5.63 Linear trend for identifying the correlation between energy increase and modal parameters from plate B2: (LHS) modal frequency (RHS) modal damping.

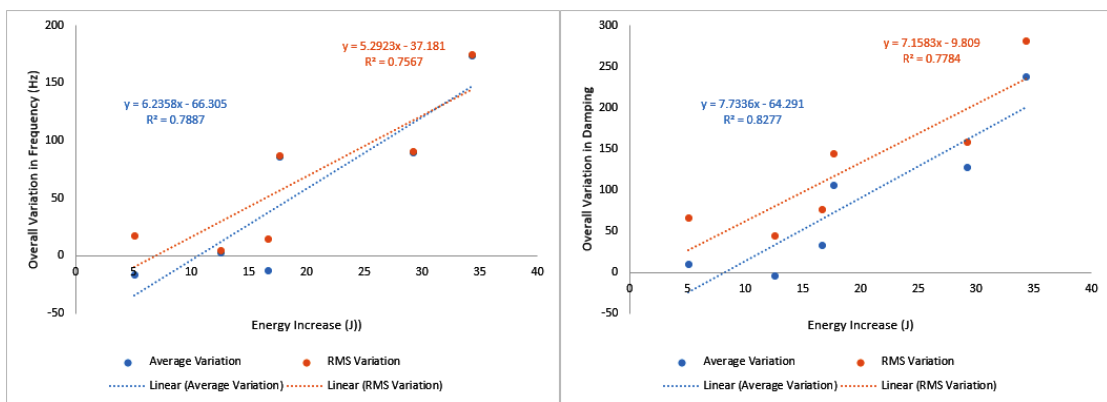


Figure 5.64 Linear trend for identifying the correlation between energy increase and modal parameters from plate C1: (LHS) modal frequency (RHS) modal damping.

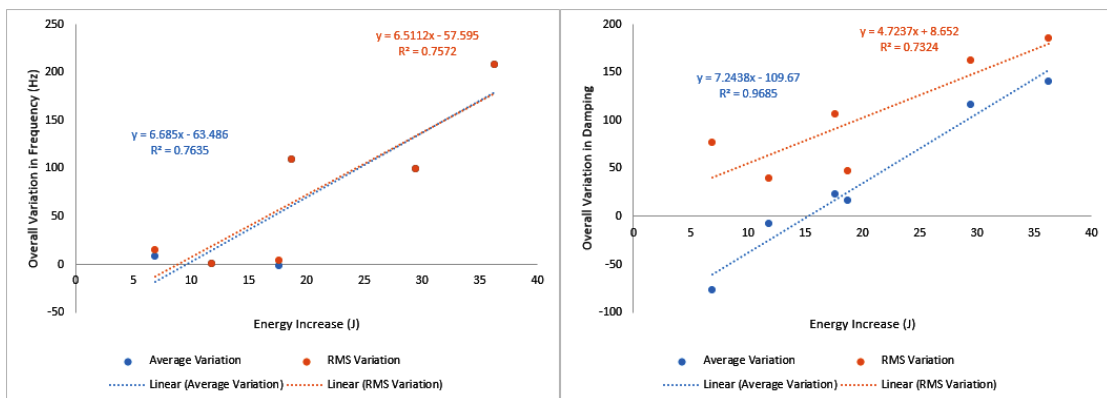


Figure 5.65 Linear trend for identifying the correlation between energy increase and modal parameters from plate C2: (LHS) modal frequency (RHS) modal damping.

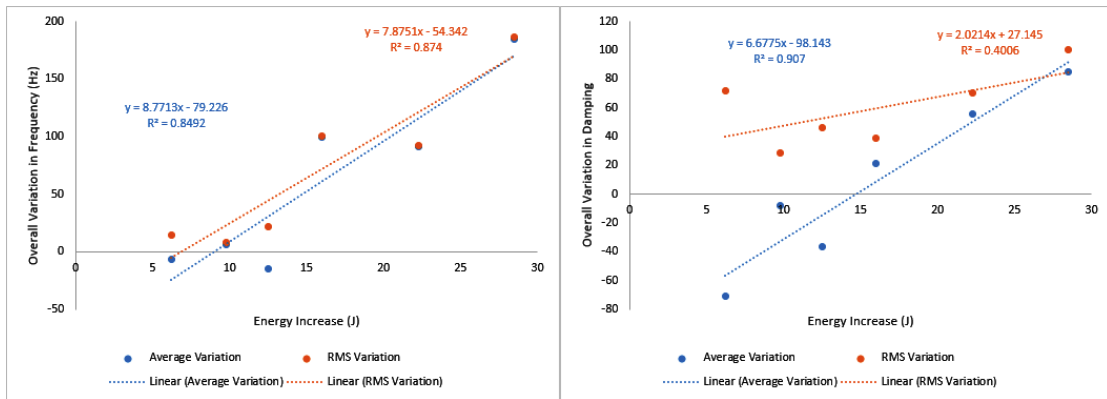


Figure 5.66 Linear trend for identifying the correlation between energy increase and modal parameters from plate D1: (LHS) modal frequency (RHS) modal damping.

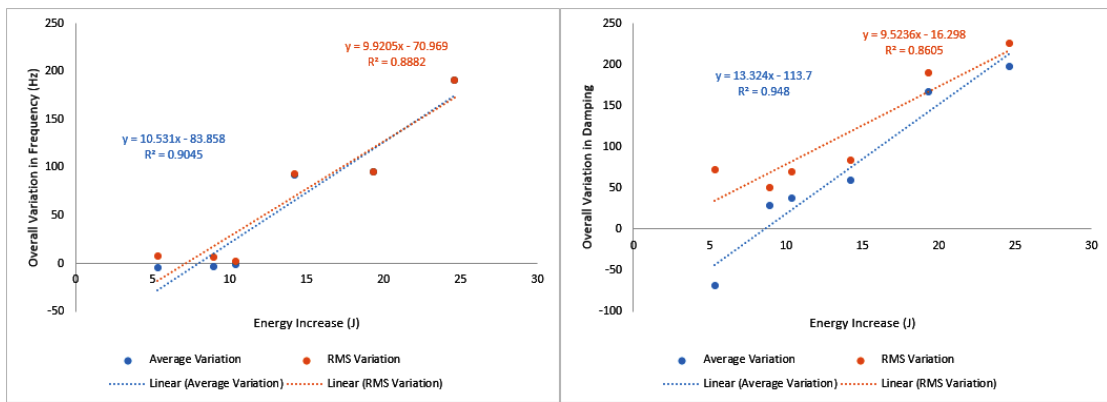


Figure 5.67 Linear trend for identifying the correlation between energy increase and modal parameters from plate E1: (LHS) modal frequency (RHS) modal damping.

From the plots in Figure 5.60 to Figure 5.67, it is observed that as the energy level increases, the percentage change in both parameters increases. Except for plate C2, there seems to be a modal sensitivity to damage threshold where the modal parameters visibly start increasing. This happens from about 15J to 20J and helps understanding much of the discussion in previous sections where the sensitivity of the modal parameters to damage may not always be so clear. Assuming that the relations would be linear, R-squared correlation coefficients were determined, ranging from 0.76 to 0.85 and from 0.58 to 0.97 for the modal frequency and modal damping factors, respectively. This suggests the existence of a correlation between the energy increase and the percentage variation in both modal frequency and damping. However, even if it still shows the greater dispersion on the results from the modal damping factor (due to a larger range), it is supporting the initial assumption that the hysteretic modal damping factors tend to increase with damage in CFRP laminates.

5.5 Experimental Results from the Elliptical Method

5.5.1 Plates A_{1-3} , B_{1-2} , C_{1-3} , D_{1-2} and E_1

The modal parameters provide information about the behaviour towards any mechanical disturbances, for instance, vibration and damage. The aim of this section is to show possible relationships between the changes in the ellipse parameters, such as its area, and damage. The plot of the receptance amplitude, receptance phase and ellipse are shown from Figure 5.68 to Figure 5.75 for plates A1 and B1.

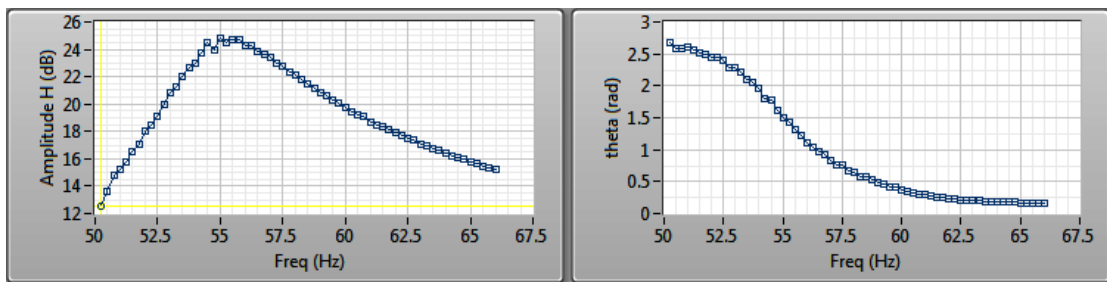


Figure 5.68 Healthy Receptance amplitude and phase for plate A1 at 55Hz.

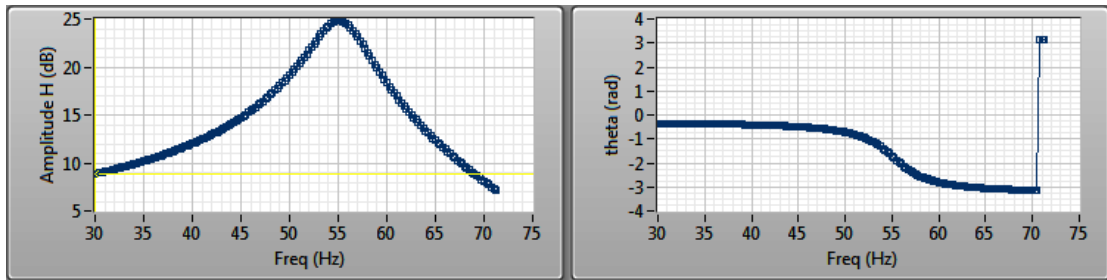


Figure 5.69 Damaged Receptance amplitude and phase for plate A1 at 55Hz.

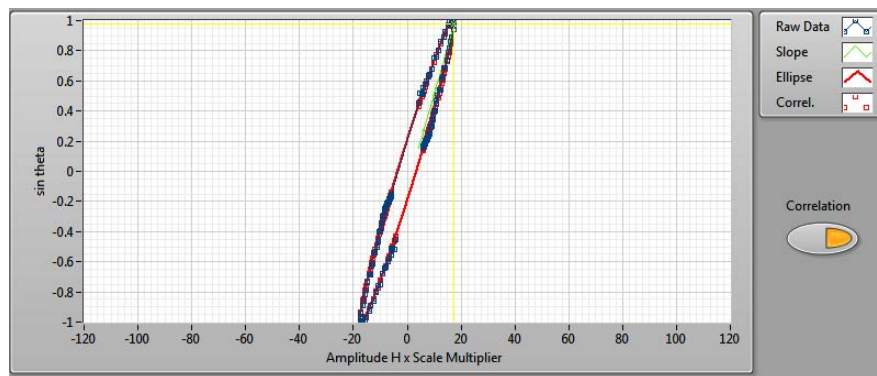


Figure 5.70 Healthy ellipse for plate A1 at 55Hz.

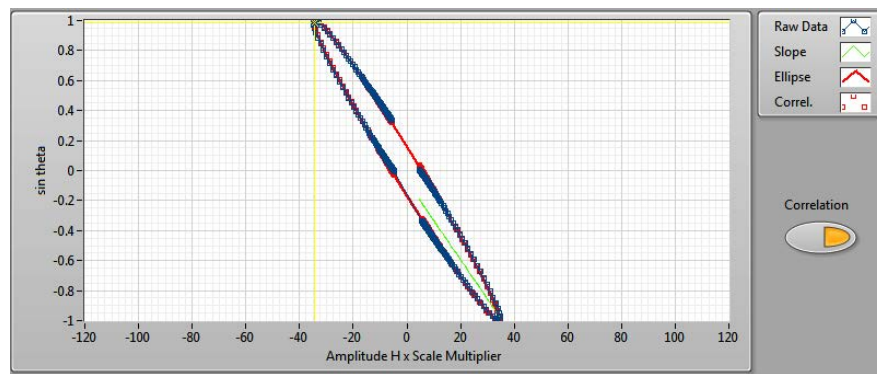


Figure 5.71 Damaged ellipse for plate A1 at 55Hz.

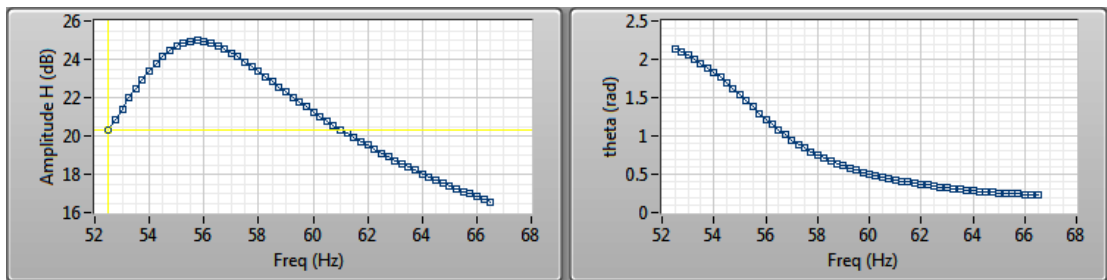


Figure 5.72 Healthy Receptance amplitude and phase for plate B1 at 55Hz.

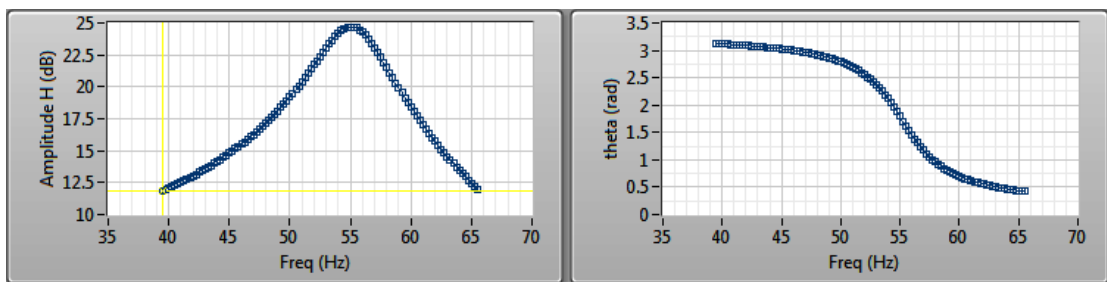


Figure 5.73 Damaged Receptance amplitude and phase for plate B1 at 55Hz.

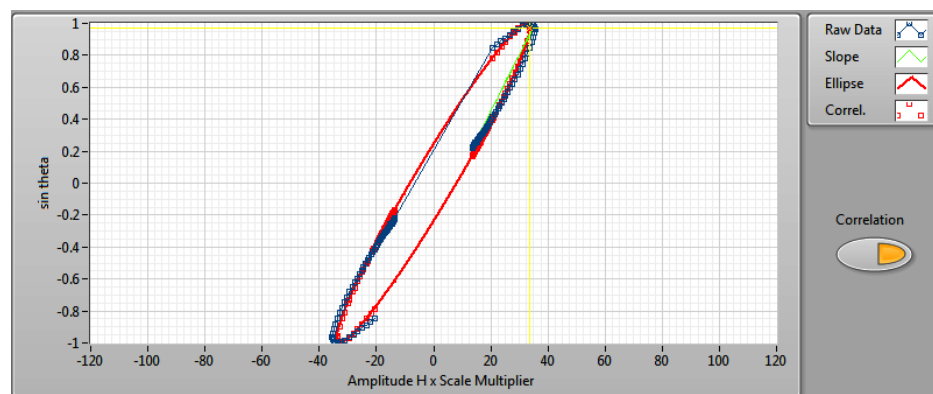


Figure 5.74 Healthy ellipse for plate B1 at 55Hz.

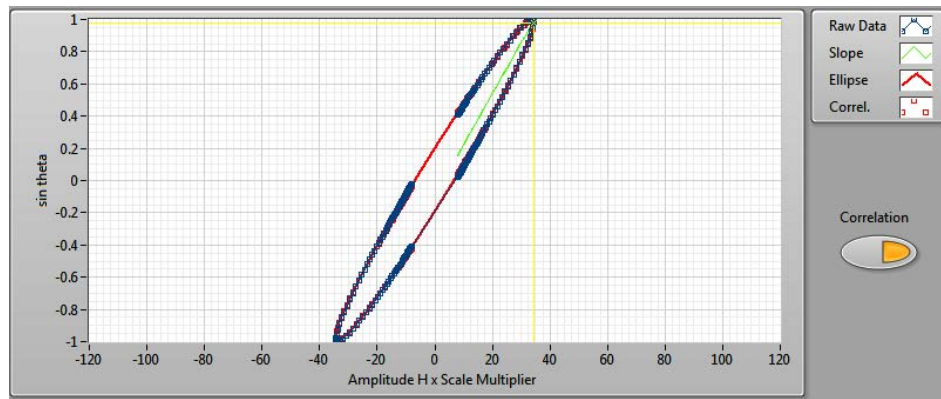


Figure 5.75 Damage ellipse for plate B1 at 55Hz.

The area and shape of the ellipse depend on the modal constants, which are local properties, while modal frequency and damping are global properties. A consistent change in the ellipse area due to damage would suggest a possible correlation. It is evident in Figure 5.76 to Figure 5.78, that there is a wide gap between the area of the ellipse of undamaged and damaged plates. The presence of damage in all the test plates shown from Figure 5.76 to Figure 5.78 caused a drastic reduction in the area of the plate at all the modes. The quantification of the deviation of the elliptical areas is shown in Appendix A.

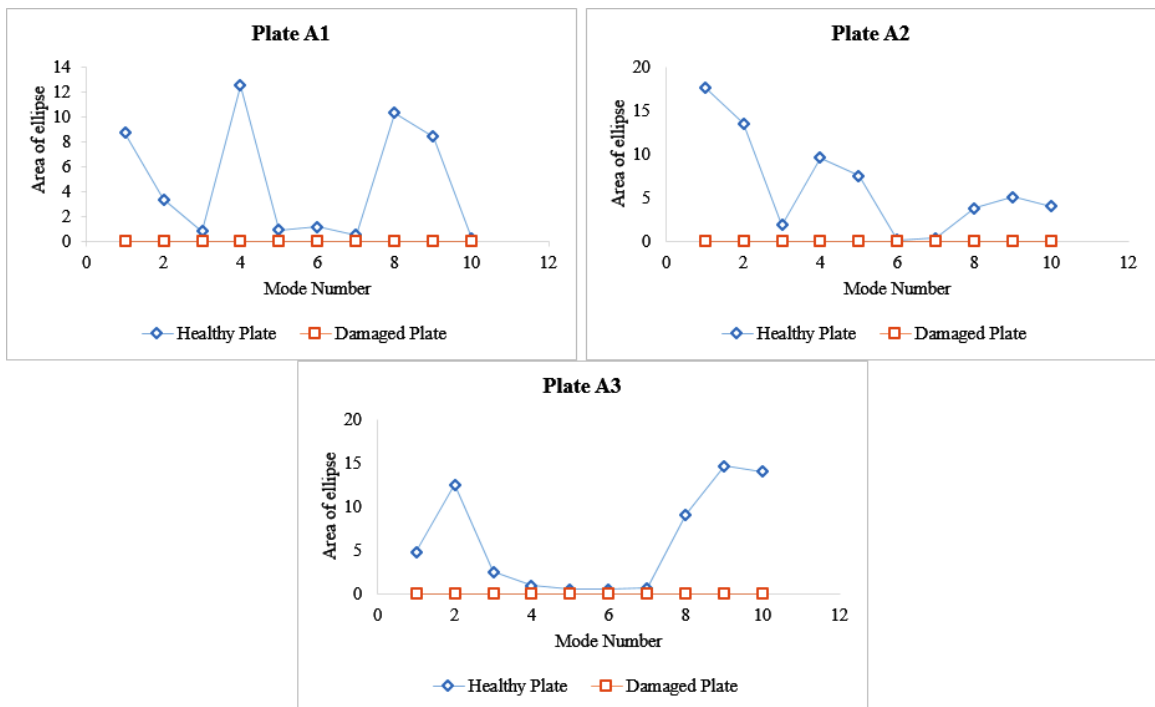


Figure 5.76 Variation in the area of the ellipse for Plates A1, A2 and A3.

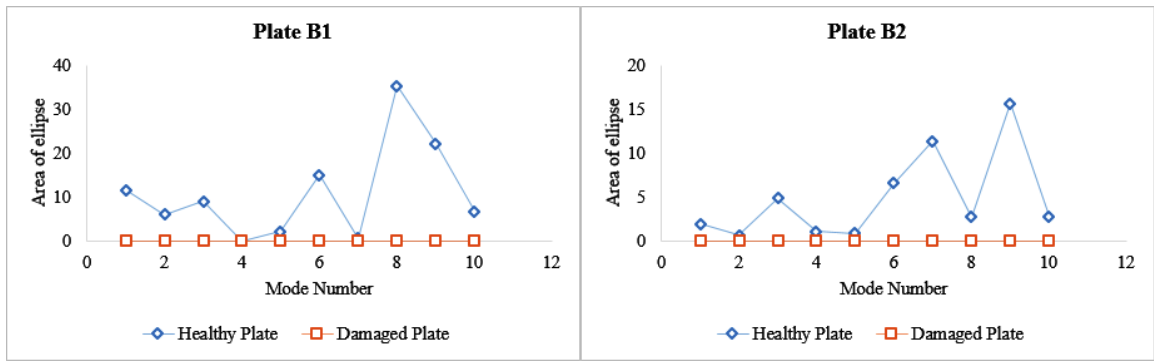


Figure 5.77 Variation in the area of ellipse for Plate B1 and B2.

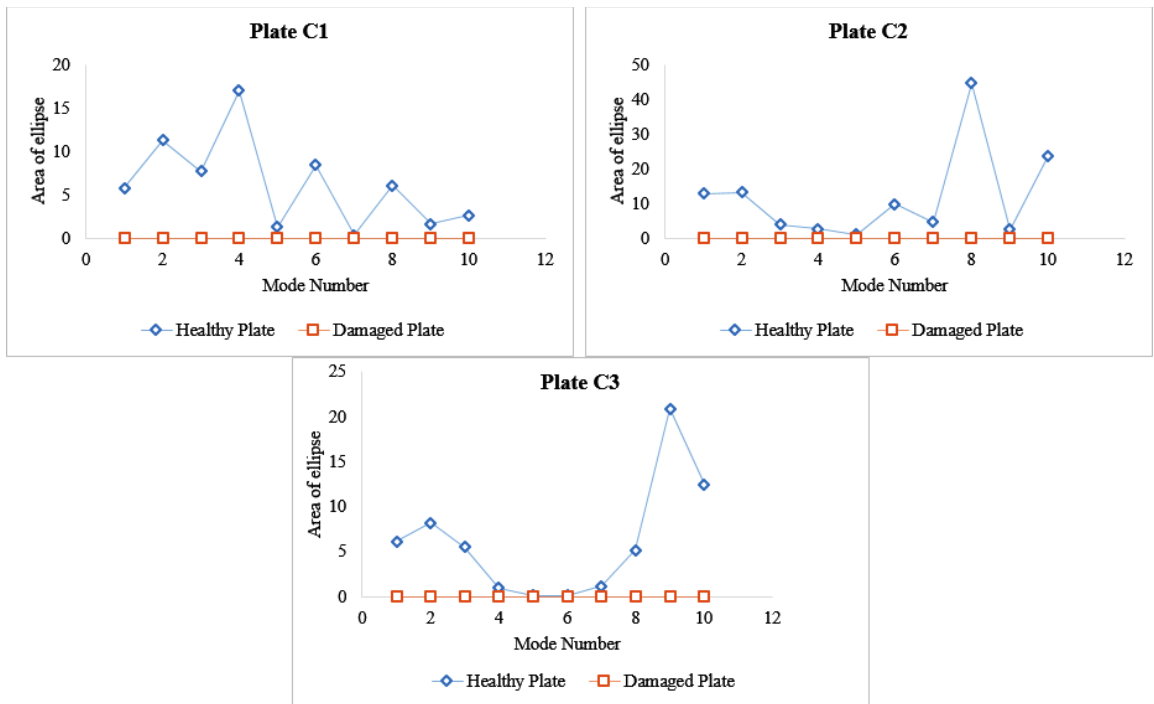


Figure 5.78 Variation in the area of ellipse for Plate C1, C2 and C3.

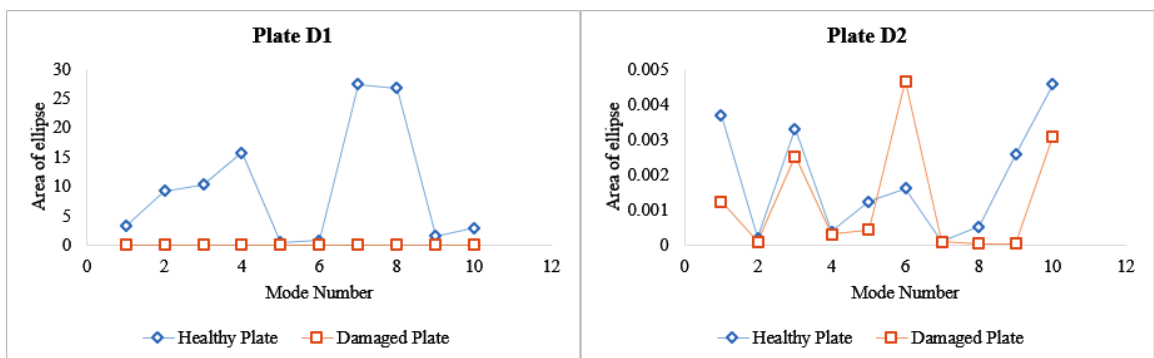


Figure 5.79 Variation in the area of ellipse for Plate D1 and D2.



Figure 5.80 Variation in the area of ellipse for Plate E1.

It is imperative to note that, from Figure 5.76 and Figure 5.78, the level of reduction in the ellipse area when damage was introduced in the test plates are within the same range. Apart from Plate C3 that has a minimum reduction rate of 97% at mode 6, the reduction rate across all the modes in other plates are over 97%. In Figure 5.79 the ellipse area reduced to nearly zero across all modes in plate D1. However, plate D2 recorded a reduction at all the modes, but mode 6. Again, the ellipse area reduced to approximately zero in plate E1 as shown in Figure 5.80.

5.5.2 F_1 and G_1

Figure 5.81 and Figure 5.82 presents the changes in the ellipse area for plates F_1 and G_1 respectively. The result from both plates indicates some disparity between the results from other plates. However, the results are still promising.

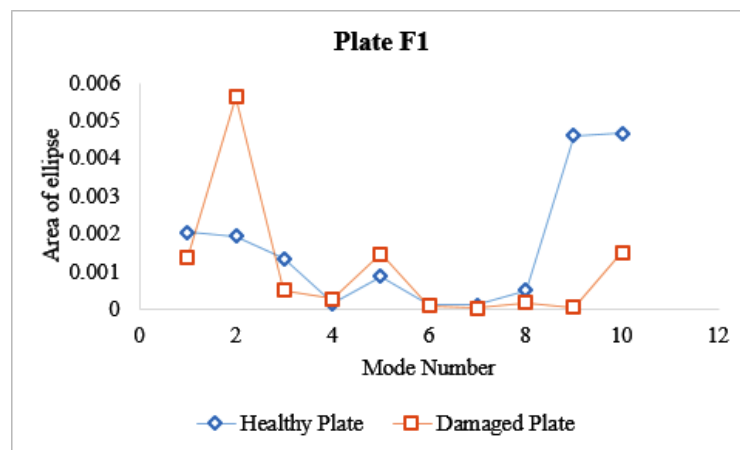


Figure 5.81 Variation in the area of ellipse for plate F1.

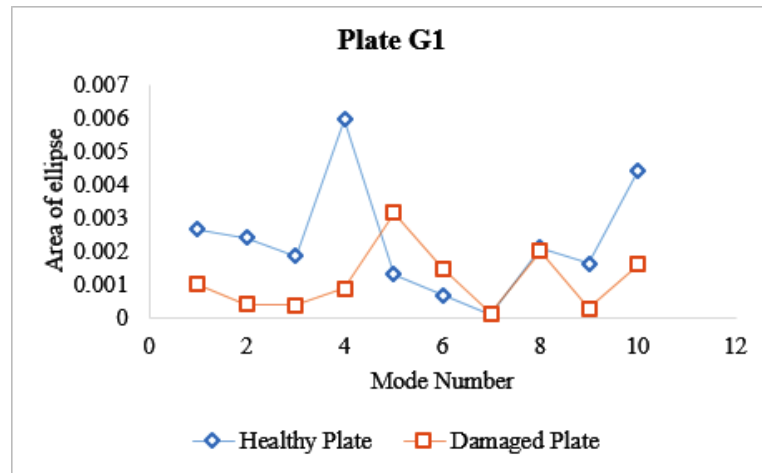


Figure 5.82 Variation in the area of ellipse for Plate G_1

In plate F_1 , as shown in Figure 5.81, except at modes 2, 4 and 5, there is a reduction in the ellipse area after the damage was introduced. As the damage increases, the ellipse area at modes 2, 4 and 5 would reduce. Similarly, in plate G_1 (See Figure 5.82), the ellipse areas reduced at all the modes, but modes 5, 6 and 7. This behaviour indicates the presence of damage in the plate. The overall results from the elliptical method offers an effective method for damage identification in CFRP laminates.

5.6 A Comparison of the Modal Damping between Ellipse Method and BETAlab

This section highlights the behaviour of the damping factor data collected using BETAlab and Elliptical Plane method. Figure 5.83 illustrates the modal damping data from both BETAlab and Ellipse Method as clearly labelled. The objective is to compare the results from both methods.

It is expected that the modal damping factor would increase as damage is introduced into the CFRP laminates [57], but the result from BETAlab in Figure 5.83 indicates that except at modes 1, 2 and 4, there is a reduction at the other modes with the highest reduction at mode 7 and the highest increase at mode 4. The Elliptical Plane method offers a different result. From the ellipse method, there is an increase in the modal damping at modes 1, 2, 3, 6 and 7, with the highest increase at mode 6.

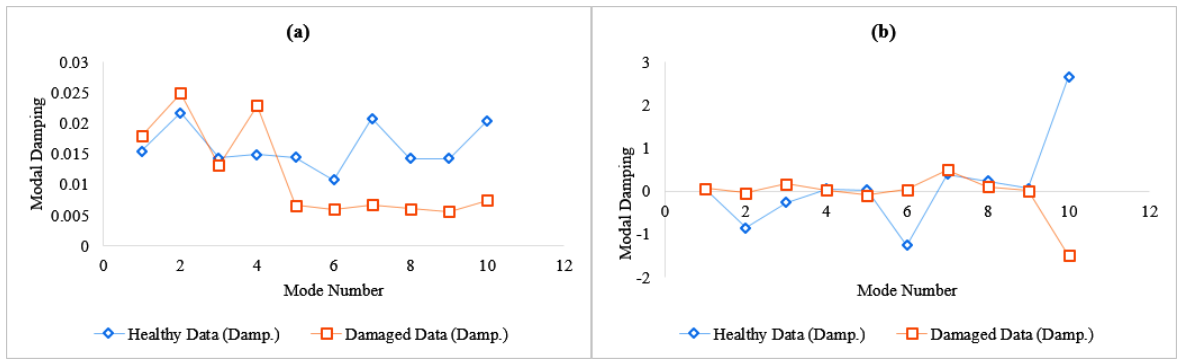


Figure 5.83 Comparison of Plate A1 modal damping from: (a) BETAlab; (b) Ellipse Method.

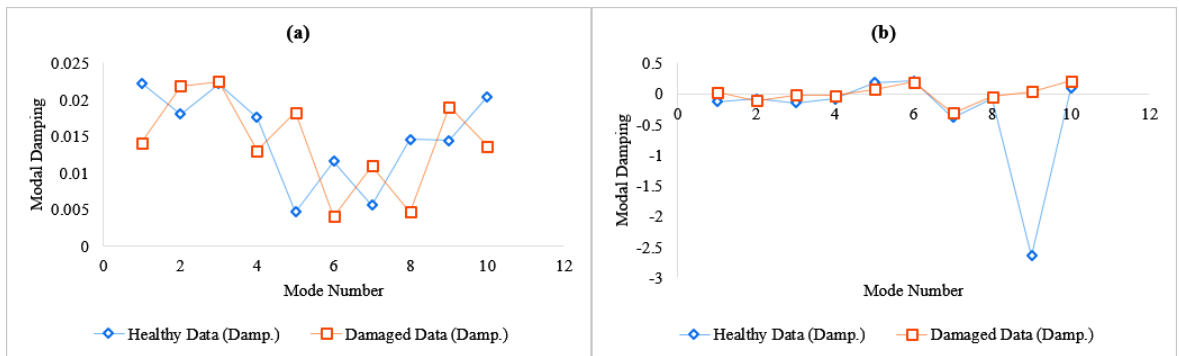


Figure 5.84 Comparison of Plate A2 modal damping from: (a) BETAlab; (b) Ellipse Method.

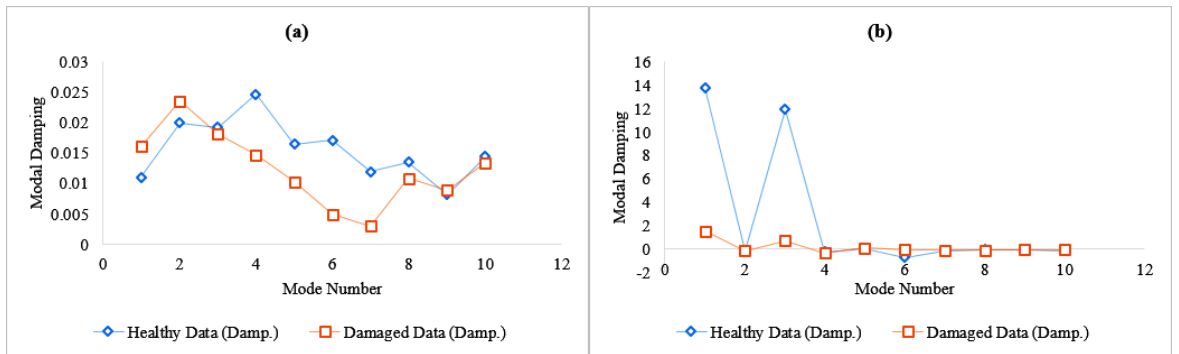


Figure 5.85 Comparison of Plate A3 modal damping from: (a) BETAlab; (b) Ellipse Method.

Similarly, the modal damping from plate A2 is shown in Figure 5.84. From the Figure, it is shown that the data from the BETAlab method recorded an increase in the modal damping at modes 2, 3, 5, 7 and 9, with the highest increase at mode 5. While the ellipse method recorded an increase in the modal damping at modes 1, 3, 4, and from 7 to 10, with the highest increase mode 9.

For plate A3, among the 10 modes from the BETAlab result, only three modes recorded an increase in the modal damping, namely modes 1, 2 and 9 (See Figure 5.85). The

highest increase occurred at mode 1, with a 45% increase. While the result from the ellipse method shows an increase in the modal damping from modes 5 to 7 and at mode 10. Mode 6 has the highest increase in the modal damping.

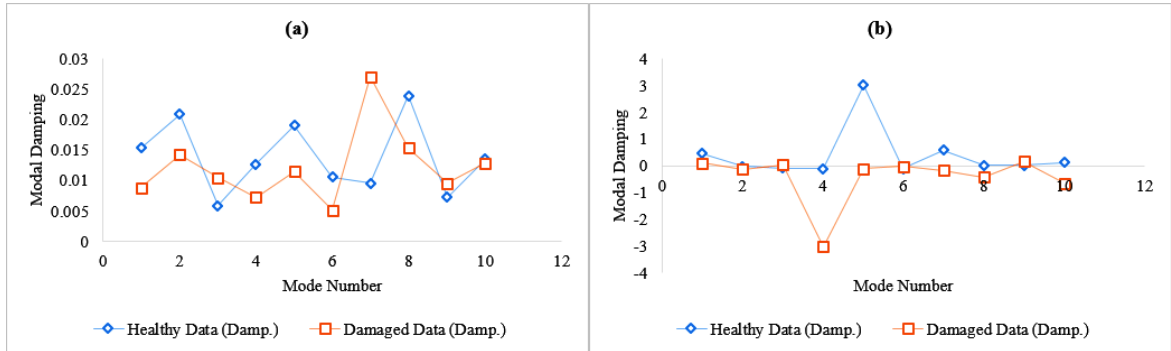


Figure 5.86 Comparison of Plate B1 modal damping from: (a) BETAlab; (b) Ellipse Method.

The results from plates B1 and B2 are shown in Figure 5.86 and Figure 5.87 respectively. From the BETAlab result, the modal damping increased at modes 3, 7 and 9 in plate B1, with the highest increase at mode 7. Similarly, the result from the ellipse method indicated an increase at modes 3, 6 and 9, with the highest increase at mode 9. This results from both methods show a close agreement.

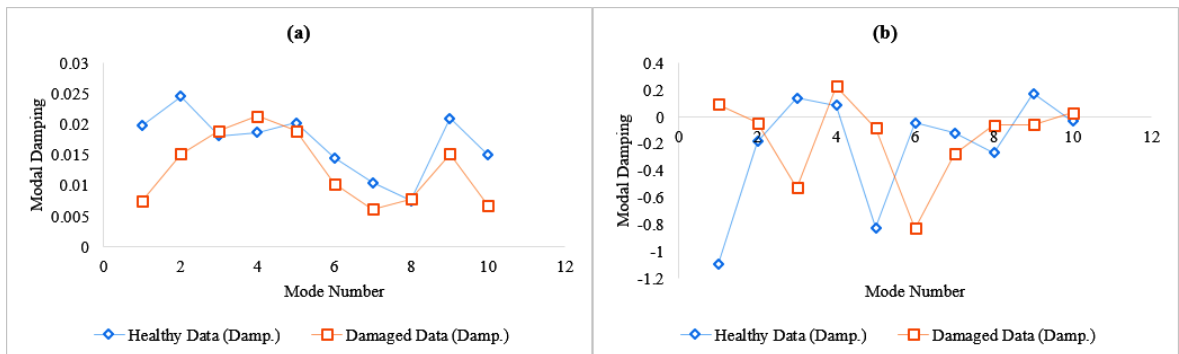


Figure 5.87 Comparison of Plate B2 modal damping from: (a) BETAlab; (b) Ellipse Method.

Furthermore, for plate B2, the modal damping from BETAlab method increased at modes 3, 4 and 8, with the highest increase at mode 4. While the result from the ellipse method recorded an increase in the modal damping at modes 1, 2, 4, 5, 8 and 10. The highest increase occurred at mode 1.

In Figure 5.88 and Figure 5.89 shows the plot of the modal damping extracted from plate C1 and C2 using BETAlab and Ellipse methods respectively. For plate C1, except

for modes 5 and 7, the result from BETAlab indicates a reduction in the modal damping at the other modes. The highest increase in the modal damping occurred at mode 7.

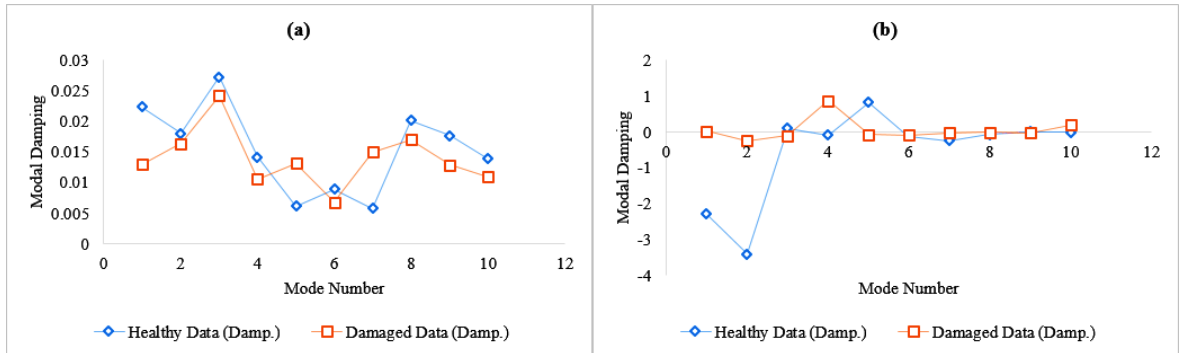


Figure 5.88 Comparison of Plate C1 modal damping from: (a) BETAlab; (b) Ellipse Method.

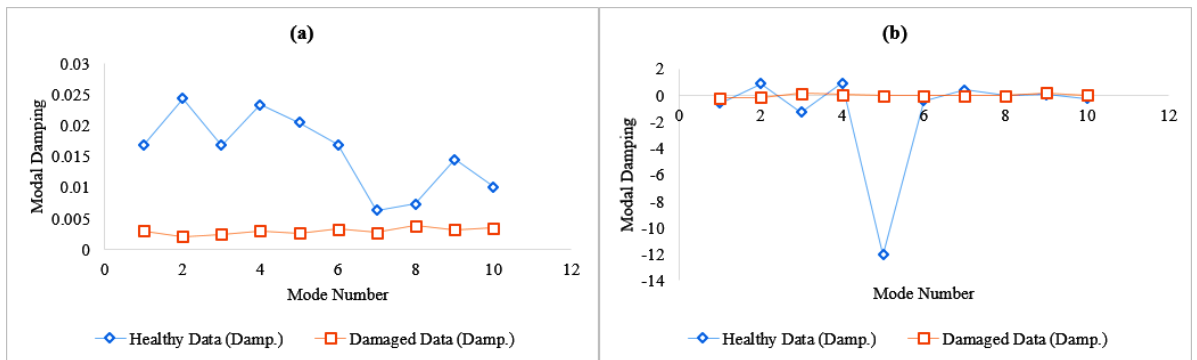


Figure 5.89 Comparison of Plate C2 modal damping from: (a) BETAlab; (b) Ellipse Method.

While the result from the ellipse method shows an increase in the modal damping at modes 1, 2, 4, 6, 7, 8 and 10. This result suggests that the highest increase in the modal damping is at mode 2. However, the BETAlab result from plate C2 shows that at all the 10 modes, there is a reduction in modal damping after the damage was introduced. While, the result from the ellipse method indicates an increase in the modal damping at modes 1, 3, 5, 6, 8, 9 and 10, with the highest increase at mode 5.

Similarly, the BETAlab result shows a reduction in the modal damping at all the modes after the damage was introduced in plate D1 (Figure 5.90). On the contrary, all but modes 2 and 7 had a decrease in the modal damping from the ellipse method. Mode 10 has the highest increase in the modal damping.

The plots for plate D2 are shown in Figure 5.91. The result from the BETAlab method indicates that the modal damping increased from modes 6 to 10, with the highest

increase at mode 9. While the result from the ellipse method shows an increase in the modal damping at modes 1, 2, 3, 5, 6, 7 and 9, with the highest increase at mode 3.

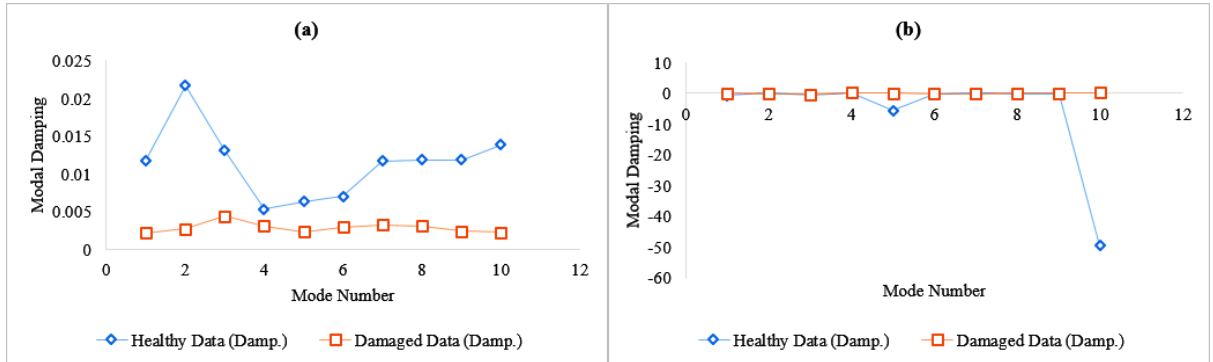


Figure 5.90 Comparison of Plate D1 modal damping from: (a) BETAlab; (b) Ellipse Method.

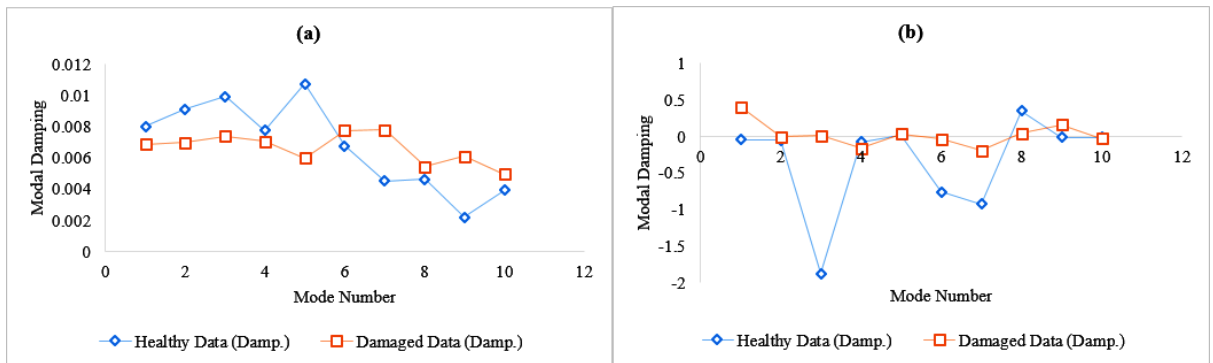


Figure 5.91 Comparison of Plate D2 modal damping from: (a) BETAlab; (b) Ellipse Method.

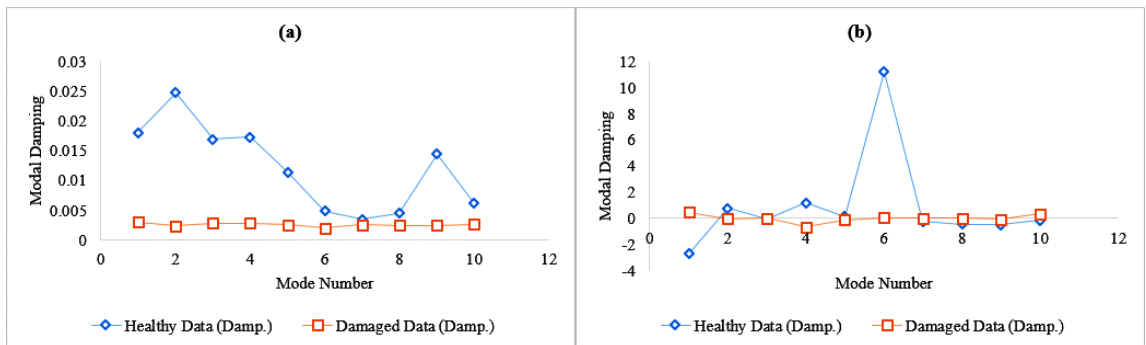


Figure 5.92 Comparison of Plate E1 modal damping from: (a) BETAlab; (b) Ellipse Method.

The results from plate E1 extract using BETAlab and the Ellipse method are shown in Figure 5.92. From the BETAlab plot, the modal damping decreased at all the modes, just like in plates C2 and D1. However, the Elliptical Plane method recorded an increase

in the modal damping at modes 1, 3, and from modes 7 to 10, with the highest increase at mode 1.

In plate F1, except at modes 1, 4 and 5, the result from the BETAlab method shows a reduction in the modal damping at the other modes (See Figure 5.93). Mode 4 has the highest increase in the modal damping. While the Elliptical Plane method shows that, there is an increase in the modal damping at modes 1, 3, 7 and 8, with the highest increase at mode 8.

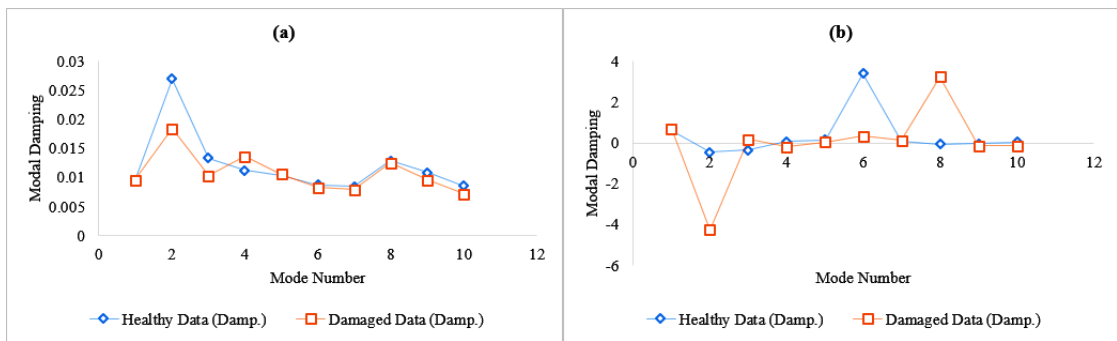


Figure 5.93 Comparison of Plate F1 modal damping from: (a) BETAlab; (b) Ellipse Method.

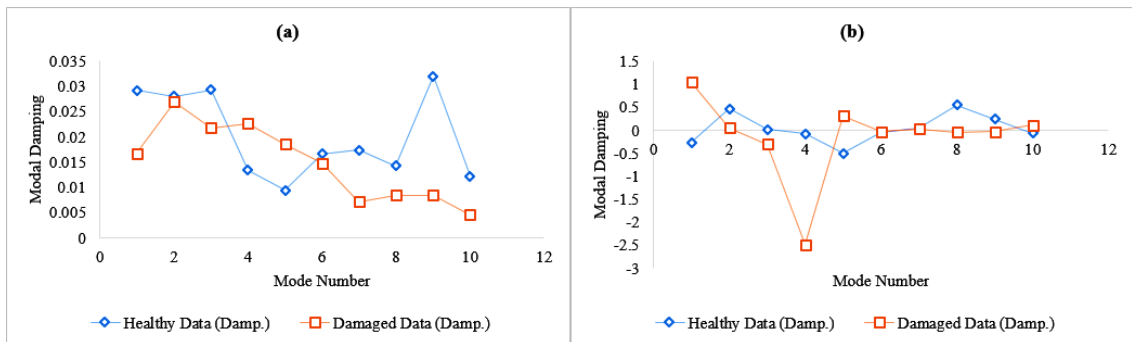


Figure 5.94 Comparison of Plate G1 modal damping from: (a) BETAlab; (b) Ellipse Method.

In Figure 5.94, the modal damping data extracted from plate G1 using BETAlab and Elliptical Plane method are shown. It is evident that among the 10 modes extracted using BETAlab, only modes 4 and 5 has an increase in the modal damping, with the highest increase at mode 4. The rest are all negatives, which implies a reduction. But the result from the Ellipse method shows that the modal damping increased at modes 1, 5, 6 and 10; with the highest increase at mode 1.

Suffice it to say that, the modal damping from the ellipse method has recorded more decrease than the modal damping from the BETAlab method across all the test plates considered. This suggests that the behaviour of the modal damping from the ellipse method could be used for the monitoring of the health of a structure and as such will present a promising future in the area of damage identification in CFRP structures.

5.7 Concluding Remarks

The modal frequency and damping of the test plates with different stacking configurations were figured out and the impact of damage on the variability of the modal properties were analysed. Results indicate that modal frequency is more sensitive to damage in all the specimens, despite the stacking sequence, and that, as damage progresses, frequencies reduce across all modes. As expected from earlier works [6,51], results show changes due to the level of damage induced in the samples. However, it is not always true that the modal parameters will change in a certain direction, as this may depend on the location of damage (e.g., modal constants are local properties), on the stacking sequence of the laminate [263] or a combination of other factors (including experimental uncertainty, appearance of concurrent damage types, etc.) [6].

Although it was not possible to find a correlation between the stacking sequence and how the modal parameters change with damage, it was observed that there is a strong linear correlation between the energy level and the global modal parameters. For instance, as the energy level increases, the percentage changes in both the modal frequency and damping increases, especially from a threshold energy level determined to be between 15J and 20J for the analysed cases.

Finally, the ellipse modal identification software developed within this research project was used to analyse a total of 12 test plates. Except in Plate F_1 and G_1 , the reduction in the ellipse area is across all the modes (i.e. 100% rate of observation). However, its rate of observation in plate F_1 and G_1 is 73%, which still is a good indicator. Although both methods provide a positive result for damage identification, the ellipse modal identification method appears to be more effective. The suitability is based on the clarity of the results. The results from the ellipse modal identification method are more obvious when compared to the BETAlab results.

“No research is ever quite complete. It is the glory of a good bit of work that it opens the way for something still better, and this repeatedly leads to its own eclipse.”

— Mervin Gordon

6 Conclusion and Future Work

6.1 Conclusions

The presence of damage in a CFRP composites impact on its local and global properties. The modal frequency and damping are the global properties, while the modal constants are the local properties. Two different software was used to extract the modal properties from the vibration data, namely: BETAlab and Ellipse Method. Over the years, attention has mainly been focused on the behaviour of the global properties due to damage in the CFRP composites, with less interest in the local properties. This work not only studies the response of the global properties to low impact damage but also considered the possible suitability of the local properties in damage identification in CFRP laminates.

The results from the BETAlab software shows that the modal frequency is more sensitive to damage than the modal damping. As expected from earlier works, results show changes due to the level of damage induced in the samples. As damage progresses in the laminates, the modal frequencies reduce across all modes, thereby suggesting the presence of damage. However, when small energies are introduced, the increase in certain modal frequencies was usually negligible in comparison with the decrease in other frequencies. This apparent inconsistency between the initial hypothesis and the observations for small energies is mainly attributed to experimental error and noise. The modes with the highest amount of reduction in the modal frequencies signify the damage concentration locality. The reduction in the modal frequencies means that the mechanical properties of the CFRP have been compromised. Yet, the modal damping does not provide clear and stable behaviour as regards damage identification in the structure. This made it difficult to detect damage based on the modal damping of the laminates. Although the modal damping is not a good damage indicator, a comparison between the data from BETAlab and the ellipse method indicates that the modal damping from the ellipse method is more sensitive to damage in the laminates.

One important finding was that as the energy level increases, the percentage changes in both the modal frequency and damping increases. The linear Equations reveal that there is a correlation between the increase in energy and the percentage variation in modal

frequency and damping, especially from a threshold energy level determined to be between 15J and 20J for the analysed cases.

Regarding the stacking sequence of the laminates, there does not seem to be any correlation between how the modal parameters change with damage and the stacking sequence of the laminate. Although the initial hypothesis was different, this makes sense. Firstly, the modal damping factors and natural frequencies are global properties (as opposed to local properties, i.e., they are the same at every location of the structure). Secondly, the mechanics of composite materials can be described from global properties of stiffness and mass approximating the laminate to a material with homogeneous microstructure (take, for example, the rule of mixtures) [25].

Finally, a novel method for damage identification from FRF, based on the representation of the receptance on the Elliptical Plane was developed. The Ellipse plane method shows promise for damage detection using the ellipse area. It was observed that as the damage in the CFRP laminates increases the area of the ellipse reduces. Therefore, since the area and shape of the ellipse depend on the modal constants (local modal properties), it implies that there might be a correlation between the damage and the modal constants of the CFRP laminates. However, this would require further experimentation to determine if there is a mathematical correlation (if any) between damage and the shape of the ellipse, for example, by taking into account that damage in CFRPs have complex morphologies that may affect how the modal constants are affected from the presence of damage.

6.2 Future work

Although this research already contributed to the advancement in knowledge in the field of damage detection in composite materials, through the presentation of a novel modal identification method that has important properties that can be used as damage features, it would be interesting to further expand on this research, namely by focusing on the following areas:

- Solving the challenge relating to the unpredictable behaviour of modal damping.
- Determining the correlation between damage and the modal constants.

- Assessing the modal response of complex structural geometries, hybrid reinforced composites and natural fibre reinforced composites.
- It would be important to understand what is determining the modal sensitivity to damage threshold observed in this work. Although this was not assessed in this work (it would require a C-Scan analysis), it would be interesting to understand if this critical value is related with the CFRP failure modes, i.e. when a delamination takes place. If that is the case, then modal parameters could be used as a swift indicator not only to detect and locate damage in a CFRP as done in other works (i.e. [5]), but also to quantifying the severity of damage in the structure at a given instant and helping determining its remaining useful life (prognosis).
- Although the orthotropic laminates indicates more sensitivity to damage than the isotropic laminates, it is difficult to draw a conclusion on the test conducted. The behaviour of the global properties due to damage, should be studied further to ascertain any possible correlation.
- Various curve-fitting techniques yield varying results, to improve accuracy, it is important to determine confidence intervals instead of single point solutions. This is necessary for accurate modal identification, especially when results are used in other applications, such as SHM where data is noisy.

References

- [1] de Medeiros R, Vandepitte D, Tita V. Structural health monitoring for impact damaged composite: a new methodology based on a combination of techniques. *Struct Heal Monit* 2017;147592171668844.
- [2] Abbas M, Shafiee M. Structural health monitoring (SHM) and determination of surface defects in large metallic structures using ultrasonic guided waves. *Sensors (Switzerland)* 2018;18.
- [3] Kessler SS, Spearing SM, Soutis C. Damage detection in composite materials using Lamb wave methods. *Smart Mater Struct* 2002;11:269–78.
- [4] Ye Lin, Ye Lu, Zhongqing Su GM. Functionalized composite structures for new generation airframes: A review. *Compos Sci Technol* 2005;65:1436–46.
- [5] Montalvão D, Ribeiro AMR, Duarte-Silva JAB. Experimental Assessment of a Modal-Based Multi-Parameter Method for Locating Damage in Composite Laminates. *Exp Mech* 2011;51:1473–88.
- [6] Montalvão D, Karanatsis D, Ribeiro AM, Arina J, Baxter R. An experimental study on the evolution of modal damping with damage in carbon fiber laminates. *J Compos Mater* 2014;49:2403–13.
- [7] Huang, L., Sheikh, A. H., Ng, C. T., Griffith MC. An efficient finite element model for buckling analysis of grid stiffened Laminated composite plates. *Compos Struct* 2015;122:41–50.
- [8] Varga M, Vretenar V, Kotlar M, Skakalova V, Kromka A. Fabrication of free-standing pure carbon-based composite material with the combination of sp²-sp³ hybridizations. *Appl Surf Sci* 2014;308:211–5.
- [9] Notta-Cuvier D, Lauro F, Bennani B, Balieu R. Damage of short-fibre reinforced materials with anisotropy induced by complex fibres orientations. *Mech Mater* 2014;68:193–206.
- [10] Shyr T-W, Pan Y-H. Impact resistance and damage characteristics of composite laminates. *Compos Struct* 2003;62:193–203.
- [11] Zhang J, Zhang X. Simulating low-velocity impact induced delamination in composites by a quasi-static load model with surface-based cohesive contact. *Compos Struct* 2015;125:51–7.
- [12] Amafabia DM, Montalvão D, David-West O, Haritos G. A review of structural

- health monitoring techniques as applied to composite structures. *SDHM Struct Durab Heal Monit* 2017;11:91–147.
- [13] Montalvão D, Amafabia DM. An alternative representation of the receptance: The ‘elliptical plane’ and its modal properties. *Mech Syst Signal Process* 2018;103:236–49.
- [14] Montalvão D, Dupac M, Amafabia DM, David-West O, Haritos G. On reducing uncertainty on the Elliptical Plane modal identification method. *MATEC Web Conf* 2018;211:06001.
- [15] Montalvão D, Amafabia DM, Silva JM. And yet another method for the identification of modal constants in experimental modal analysis. *Proc. 7th Int. Oper. Modal Anal. Conf. (IOMAC’17)*, May 10-12, Ingolstadt, Ger. 2017., 2017.
- [16] Amafabia, Daerefa-a Mitsheal David-West O, Montalvão D, George H. Damage detection in CFRP Composite Plates based on evolving Modal Parameters. *BSSM’17 12th Int. Conf. Adv. Exp. Mech.*, University of Sheffield, Sheffield, UK.: 2017, p. 29th – 31st August 2017.
- [17] Amafabia DM, Diogo M, David-West O, Haritos G. Modal Parameters Response to Increased Energy Absorption in CFRP Laminates. *ECS’19 1st Eng. Comput. Sci. Res. Conf.*, University of Hertfordshire, UK.: 2019, p. 17th April 2019.
- [18] Maia NMM, Almeida RAB, Urgueira AP V, Sampaio RPC. Damage detection and quantification using transmissibility. *Mech Syst Signal Process* 2011;25:2475–83.
- [19] Rytter A. *Vibrational Based Inspection of Civil Engineering Structures*. Aalborg University, Denmark, 1993.
- [20] Montalvao D, Maia NMM, Ribeiro AMR. A Review of Vibration Based Structural Health Monitoring with Special Emphasis on Composite Materials. *Shock Vib Dig* 2006;38:295–324.
- [21] Sohn H, Farrar CR, Hemez F, Czarnecki J. A Review of Structural Health Monitoring Literature 1996 – 2001. *Third World Conf Struct Control* 2002:1–7.
- [22] Farrar CR, Doebling SW, Nix DA, Royal THE. Vibration--based structural damage identification. *Philos Trans R Soc London Ser A Math Phys Eng Sci* 2001;359:131–49.

- [23] Tjirkallis A, Kyprianou A. Damage detection under varying environmental and operational conditions using Wavelet Transform Modulus Maxima decay lines similarity. *Mech Syst Signal Process* 2016;66–67:282–97.
- [24] Maia NMM, Silva JMM. *Theoretical and Experimental Modal Analysis*. Taunton: Research Studies Press and John Wiley and Sons, Somerset; 1997.
- [25] Montalvão D. A modal-based contribution to damage location in laminated composites plates. PhD thesis, Instituto Superior Técnico, Universidade de Lisboa, Portugal, 2010.
- [26] Ooijevaar TH, Loendersloot R, Warnet LL, de Boer A, Akkerman R. Vibration based structural health monitoring of a composite T-beam. *Compos Struct* 2010;92:2007–15.
- [27] Kessler SS, Spearing SM, Atalla MJ, Cesnik CE, Soutis C. Damage detection in composite materials using frequency response methods. *Compos Part B Eng* 2002;33:87–95.
- [28] Kim HY. Vibration-Based Damage Identification Using Reconstructed FRFs in Composite Structures. *J Sound Vib* 2003;259:1131–46.
- [29] Manoach E, Samborski S, Mitura A, Warminski J. Vibration based damage detection in composite beams under temperature variations using Poincaré maps. *Int J Mech Sci* 2012;62:120–32.
- [30] Herman AP, Orifici AC, Mouritz AP. Vibration modal analysis of defects in composite T-stiffened panels. *Compos Struct* 2013;104:34–42.
- [31] Sung D, Kim C, Hong C. Monitoring of impact damages in composite laminates using wavelet transform. *Compos Part B Eng* 2002;33:35–43.
- [32] Pérez MA, Gil L, Oller S. Impact damage identification in composite laminates using vibration testing. *Compos Struct* 2014;108:267–76.
- [33] Wang Z-X, Qiao P, Xu J. Vibration analysis of laminated composite plates with damage using the perturbation method. *Compos Part B Eng* 2015;72:160–74.
- [34] Devriendt C, Presezniak F, De Sitter G, Vanbrabant K, De Troyer T, Vanlanduit S, et al. Structural health monitoring in changing operational conditions using transmissibility measurements. *Shock Vib* 2010;17:651–75.
- [35] Mao Z, Todd M. A model for quantifying uncertainty in the estimation of noise-contaminated measurements of transmissibility. *Mech Syst Signal Process* 2012;28:470–81.

- [36] Zhou YL, Perera R, Sevillano E. Damage Identification from Power Spectrum Density Transmissibility. Proc 6th Eur Work Struct Heal Monit 2012:1–7.
- [37] Ribeiro A, Maia N, Silva J. Experimental evaluation of the transmissibility matrix. SPIE Proc Ser 1999:1126–9.
- [38] Ribeiro AMR, Silva JMM, Maia NMM. On the generalisation of the transmissibility concept. Mech Syst Signal Process 2000;14:29–35.
- [39] Ribeiro AMR, Maia NMM, Silva JMM. Response prediction from a reduced set of known responses using the transmissibility. Proc Int Modal Anal Conf - IMAC 2000;1:425–7.
- [40] Yi X, Zhu D, Wang Y, Guo J, Lee K-M. Transmissibility-function-based structural damage detection with tetherless mobile sensors. Proc 5th Int Conf Bridg Maintenance, Saf Manag 2010:328–35.
- [41] Lang ZQ, Park G, Farrar CR, Todd MD, Mao Z, Zhao L, et al. Transmissibility of non-linear output frequency response functions with application in detection and location of damage in MDOF structural systems. Int J Non Linear Mech 2011;46:841–53.
- [42] Lang ZQ, Billings SA. Energy transfer properties of non-linear systems in the frequency domain. Int J Control 2005;78:345–62.
- [43] Devriendt C, Guillaume P. The use of transmissibility measurements in output-only modal analysis. Mech Syst Signal Process 2007;21:2689–96.
- [44] Devriendt C, Guillaume P. Identification of modal parameters from transmissibility measurements. J Sound Vib 2008;314:343–56.
- [45] Sampaio, R.P.C., Maia, N., Ribeiro, A.M.R. and Silva J. Transmissibility techniques for damage detection. Proc Int Modal Anal Conf 2001;2:1524–7.
- [46] Maia NMM, Ribeiro AMR, Fontul M, Montalvão D, Sampaio RPC. Using the Detection and Relative Damage Quantification Indicator (DRQ) with Transmissibility. Key Eng Mater 2007;347:455–60.
- [47] Li XZ, Peng ZK, Dong XJ, Zhang WM, Meng G. A New Transmissibility Based Indicator of Local Variation in Structure and Its Application for Damage Detection 2015;2015.
- [48] Zhang L, Lang Z, Yang W. Transmissibility Damage Indicator for Wind Turbine Blade Condition Monitoring. Autom. Comput. (ICAC), 2015 21st Int. Conf. on., IEEE; 2015, p. 1–4.

- [49] Keye, S., Rose, M. and Sachau D. Localizing delamination damages in aircraft panels from modal damping parameters. Proc 19th Int Modal Anal Conf (IMAC XIX), Kissimmee 2001:412–7.
- [50] Shahdin A, Mezeix L, Bouvet C, Morlier J, Gourinat Y. Monitoring the effects of impact damages on modal parameters in carbon fiber entangled sandwich beams. Eng Struct 2009;31:2833–41.
- [51] Montalvão D, Ribeiro AMR, Duarte-Silva J. A method for the localization of damage in a CFRP plate using damping. Mech Syst Signal Process 2009;23:1846–54.
- [52] Rilo, N. F., Ferreira, L. M. S. and Leal RACP. Low-velocity impact analysis of glass/epoxy plates. Proc. 5th Int. Conf. Mech. Mater. Des., 2006.
- [53] Sutherland LS, Guedes Soares C. The use of quasi-static testing to obtain the low-velocity impact damage resistance of marine GRP laminates. Compos Part B Eng 2012;43:1459–67.
- [54] Herb V, Couégnat G ME. Damage assessment of thin SiC/SiC composite plates subjected to quasi-static indentation loading. Compos Part A Appl Sci Manuf 2010;41:1677–85.
- [55] Othman A, Abdullah S, Ariffin AK, Mohamed NAN. Investigating the quasi-static axial crushing behavior of polymeric foam-filled composite pultrusion square tubes. Mater Des 2014;63:446–59.
- [56] Zhang J, Zhao L, Li M, Chen Y. Compressive fatigue behavior of low velocity impacted and quasi-static indented CFRP laminates. Compos Struct 2015;133:1009–15.
- [57] Montalvão D, Silva JMM. An alternative method to the identification of the modal damping factor based on the dissipated energy. Mech Syst Signal Process 2015;54:108–23.
- [58] Gonilha; J.A., Correia; J.R., F.A. B, E. C, Cunha; Á. Modal identification of a GFRP-concrete hybrid footbridge prototype: Experimental tests and analytical and numerical simulations. Compos Struct 2013;106:724–33.
- [59] Kiral Z, İçten BM, Kiral BG. Effect of impact failure on the damping characteristics of beam-like composite structures. Compos Part B Eng 2012;43:3053–60.
- [60] Su Z, Ye L, Lu Y. Guided Lamb waves for identification of damage in composite

- structures: A review. *J Sound Vib* 2006;295:753–80.
- [61] Lee K Il, Yoon SW. Propagation of time-reversed Lamb waves in acrylic cylindrical tubes as cortical-bone-mimicking phantoms. *Appl Acoust* 2016;112:10–3.
- [62] Lamb H. On waves in an elastic plate. In: The Royal Society, editor. *Proc. R. Soc. London A Math. Phys. Eng. Sci.*, vol. 93, 1917, p. 114–28.
- [63] Su Z, Ye L. Identification of damage using Lamb waves: from fundamentals to applications. vol. 48. Springer Science & Business Media; 2009.
- [64] Cawley P, Alleyne D. The use of Lamb waves for the long range inspection of large structures. *Ultrasonics* 1996;34:287–90.
- [65] Diamanti K, Soutis C, Hodgkinson JM. Lamb waves for the non-destructive inspection of monolithic and sandwich composite beams. *Compos Part A Appl Sci Manuf* 2005;36:189–95.
- [66] Yang C, Ye L, Su Z, Bannister M. Some aspects of numerical simulation for Lamb wave propagation in composite laminates. *Compos Struct* 2006;75:267–75.
- [67] Ng CT, Veidt M. A Lamb-wave-based technique for damage detection in composite laminates. *Smart Mater Struct* 2009;18:074006.
- [68] Hu N, Liu Y, Li Y, Peng X, Yan B. Optimal Excitation Frequency of Lamb Waves for Delamination Detection in CFRP Laminates. *J Compos Mater* 2010;44:1643–63.
- [69] Ning Hu, Shimomukai T, Fukunaga H, Zhongqing Su. Damage Identification of Metallic Structures Using A0 Mode of Lamb Waves. *Struct Heal Monit* 2008;7:271–85.
- [70] Okabe Y, Fujibayashi K, Shimazaki M, Soejima H, Ogisu T. Delamination detection in composite laminates using dispersion change based on mode conversion of Lamb waves. *Smart Mater Struct* 2010;19:115013.
- [71] Manson G, Worden K, Monnier T, Guy P, Pierce SG, Culshaw B. Some experimental observations on the detection of composite damage using lamb waves. *Strain* 2011;47:254–68.
- [72] Mustapha S, Ye L, Wang D, Lu Y. Assessment of debonding in sandwich CF/EP composite beams using A0 Lamb wave at low frequency. *Compos Struct* 2011;93:483–91.

- [73] Ooijselaar TH, Rogge MD, Loendersloot R, Warnet LL, Akkerman R, Tinga T. Nonlinear dynamic behavior of an impact damaged composite skin-stiffener structure. *J Sound Vib* 2015;353:243–58.
- [74] Zhao X, Royer RL, Owens SE, Rose JL. Ultrasonic Lamb wave tomography in structural health monitoring. *Smart Mater Struct* 2011;20:105002.
- [75] Ben BS, Ben BA, Vikram KA, Yang SH. Damage identification in composite materials using ultrasonic based Lamb wave method. *Measurement* 2013;46:904–12.
- [76] Ramadas C, Padiyar J, Balasubramaniam K, Joshi M, Krishnamurthy C V. Lamb wave based ultrasonic imaging of interface delamination in a composite T-joint. *NDT E Int* 2011;44:523–30.
- [77] Rathod VT, Roy Mahapatra D. Ultrasonic Lamb wave based monitoring of corrosion type of damage in plate using a circular array of piezoelectric transducers. *NDT E Int* 2011;44:628–36.
- [78] Carboni M, Gianneo A, Giglio M. A Lamb waves based statistical approach to structural health monitoring of carbon fibre reinforced polymer composites. *Ultrasonics* 2015;60:51–64.
- [79] Keulen CJ, Yildiz M, Suleman A. Damage Detection of Composite Plates by Lamb Wave Ultrasonic Tomography with a Sparse Hexagonal Network Using Damage Progression Trends. *Shock Vib* 2014;2014:1–8.
- [80] Mustapha S, Ye L, Dong X, Alamdari MM. Evaluation of barely visible indentation damage (BVID) in CF/EP sandwich composites using guided wave signals. *Mech Syst Signal Process* 2016;76:497–517.
- [81] Mba D, Rao RB. Development of Acoustic Emission Technology for Condition Monitoring and Diagnosis of Rotating Machines: Bearings, Pumps, Gearboxes, Engines, and Rotating Structures. *Shock Vib Dig* 2006;38:3–16.
- [82] Yun H Do, Choi WC, Seo SY. Acoustic emission activities and damage evaluation of reinforced concrete beams strengthened with CFRP sheets. *NDT E Int* 2010;43:615–28.
- [83] Carpinteri A, Lacidogna G, Accornero F, Mpalaskas A., Matikas TE, Aggelis DG. Influence of damage in the acoustic emission parameters. *Cem Concr Compos* 2013;44:9–16.
- [84] Selman E, Ghiami A, Alver N. Study of fracture evolution in FRP-strengthened

- reinforced concrete beam under cyclic load by acoustic emission technique: An integrated mechanical-acoustic energy approach. *Constr Build Mater* 2015;95:832–41.
- [85] Mechraoui SE, Laksimi A, Benmedakhene S. Reliability of damage mechanism localisation by acoustic emission on glass/epoxy composite material plate. *Compos Struct* 2012;94:1483–94.
- [86] Liu PF, Chu JK, Liu YL, Zheng JY. A study on the failure mechanisms of carbon fiber/epoxy composite laminates using acoustic emission. *Mater Des* 2012;37:228–35.
- [87] Noorsuhada MN. An overview on fatigue damage assessment of reinforced concrete structures with the aid of acoustic emission technique. *Constr Build Mater* 2016;112:424–39.
- [88] Aggelis DG, Barkoula NM, Matikas TE, Paipetis AS. Acoustic structural health monitoring of composite materials : Damage identification and evaluation in cross ply laminates using acoustic emission and ultrasonics. *Compos Sci Technol* 2012;72:1127–33.
- [89] Huang W, Zhang W, Li F. Acoustic emission source location using a distributed feedback fiber laser rosette. *Sensors (Basel)* 2013;13:14041–54.
- [90] Blom J, Wastiels J, Aggelis DG. Application of acoustic emission on the characterization of fracture in textile reinforced cement laminates. *Sci World J* 2014;2014.
- [91] Bobrov A, Stepanova L. Studying the parameters of acoustic emission signals during inspection of cast parts of a freight car truck. *Russ J Nondestruct Test* 2013;49:722–7.
- [92] Hamdi SE, Le Duff A, Simon L, Plantier G, Sourice A, Feuilloy M. Acoustic emission pattern recognition approach based on Hilbert-Huang transform for structural health monitoring in polymer-composite materials. *Appl Acoust* 2013;74:746–57.
- [93] Blom J, El Kadi M, Wastiels J, Aggelis DG. Bending fracture of textile reinforced cement laminates monitored by acoustic emission: Influence of aspect ratio. *Constr Build Mater* 2014;70:370–8.
- [94] Bravo A, Toubal L, Koffi D, Erchiqui F. Damage Characterization of Bio and Green Polyethylene–Birch Composites under Creep and Cyclic Testing with

- Multivariable Acoustic Emissions. *Materials* (Basel) 2015;8:7322–41.
- [95] Fotouhi M, Suwarta P, Jalalvand M, Czel G, Wisnom MR. Detection of fibre fracture and ply fragmentation in thin-ply UD carbon/glass hybrid laminates using acoustic emission. *Compos Part A Appl Sci Manuf* 2016;86:66–76.
- [96] Akil HM, De Rosa IM, Santulli C, Sarasini F. Flexural behaviour of pultruded jute/glass and kenaf/glass hybrid composites monitored using acoustic emission. *Mater Sci Eng A* 2010;527:2942–50.
- [97] Baran I, Tutum CC, Nielsen MW, Hattel JH. Process induced residual stresses and distortions in pultrusion. *Compos Part B Eng* 2013;51:148–61.
- [98] Carlone P, Baran I, Hattel JH, Palazzo GS. Computational approaches for modeling the multiphysics in pultrusion process. *Adv Mech Eng* 2013;2013:301875.
- [99] Novo PJ, Silva JF, Nunes JP, Marques AT. Pultrusion of fibre reinforced thermoplastic pre-impregnated materials. *Compos Part B Eng* 2016;89:328–39.
- [100] Aymerich F, Staszewski WJ. Impact damage detection in composite laminates using nonlinear acoustics. *Compos Part A Appl Sci Manuf* 2010;41:1084–92.
- [101] Potel C, Chotard T, de Belleval J-F, Benzeggagh M. Characterization of composite materials by ultrasonic methods: modelization and application to impact damage. *Compos Part B Eng* 1998;29:159–69.
- [102] Ng SC, Ismail N, Ali A, Sahari B, Yusof JM, Chu BW. Non-destructive Inspection of Multi-layered Composite Using Ultrasonic Signal Processing. *IOP Conf. Ser. Mater. Sci. Eng.*, vol. 17, IOP Publishing; 2011, p. 012045.
- [103] Steiner K V, Eduljee RF, Huang X, Gillespie Jr JW. Ultrasonic NDE techniques for the evaluation of matrix cracking in composite laminates. *Compos Sci Technol* 1995;53:193–8.
- [104] Aymerich F, Meili S. Ultrasonic evaluation of matrix damage in impacted composite laminates. *Compos Part B Eng* 2000;31:1–6.
- [105] Kinra VK, Ganpatye AS, Maslov K. Ultrasonic Ply-by-Ply Detection of Matrix Cracks in Laminated Composites. *J Nondestruct Eval* 2006;25:37–49.
- [106] Hosur MV, Murthy CRL, Ramamurthy TS, Shet A. Estimation of impact-induced damage in CFRP laminates through ultrasonic imaging. *NDT E Int* 1998;31:359–74.
- [107] Hasiotis T, Badogiannis E, Tsouvalis NG. Application of ultrasonic C-scan

- techniques for tracing defects in laminated composite materials. *Stroj Vestnik/Journal Mech Eng* 2011;57:192–203.
- [108] Sharma A, Sharma S, Sharma S, Mukherjee A. Ultrasonic guided waves for monitoring corrosion of FRP wrapped concrete structures. *Constr Build Mater* 2015;96:690–702.
- [109] Vary A. Acousto-ultrasonic characterization of fiber reinforced composites 1981.
- [110] Vary A, Bowles K. Use of an ultrasonic-acoustic technique for nondestructive evaluation of fiber composite strength. *Nasa Tech Memo* 1978.
- [111] Gyekenyesi AL, Morscher GN, Cosgriff LM. In situ monitoring of damage in SiC/SiC composites using acousto-ultrasonics. *Compos Part B Eng* 2006;37:47–53.
- [112] Loutas TH, Kostopoulos V. Health monitoring of carbon/carbon, woven reinforced composites: Damage assessment by using advanced signal processing techniques. Part II: Acousto-ultrasonics monitoring of damage development. *Compos Sci Technol* 2009;69:273–83.
- [113] Barbezat M, Brunner a. J, Huber C, Flueler P. Integrated Active Fiber Composite Elements: Characterization for Acoustic Emission and Acousto-ultrasonics. *J Intell Mater Syst Struct* 2007;18:515–25.
- [114] Loutas TH, Kostopoulos V. Health monitoring of carbon/carbon, woven reinforced composites. Damage assessment by using advanced signal processing techniques. Part I: Acoustic emission monitoring and damage mechanisms evolution. *Compos Sci Technol* 2009;69:265–72.
- [115] Chrysochoidis NA, Barouni AK, Saravanos DA. Delamination detection in composites using wave modulation spectroscopy with a novel active nonlinear acousto-ultrasonic piezoelectric sensor. *J Intell Mater Syst Struct* 2011;22:2193–206.
- [116] Loutas T., Vavouliotis A, Karapappas P, Kostopoulos V. Fatigue damage monitoring in carbon fiber reinforced polymers using the acousto-ultrasonics technique. *Polym Compos* 2010;31:1409–17.
- [117] Torres-Arredondo MA, Tibaduiza DA, McGugan M, Toftegaard H, Borum KK, Mujica LE, et al. Multivariate data-driven modelling and pattern recognition for damage detection and identification for acoustic emission and acousto-

- ultrasonics. *Smart Mater Struct* 2013;22:105023.
- [118] Zhou C, Hong M, Su Z, Wang Q, Cheng L. Evaluation of fatigue cracks using nonlinearities of acousto-ultrasonic waves acquired by an active sensor network. *Smart Mater Struct* 2013;22:015018.
- [119] Yoder NC, Adams DE. Vibro-Acoustic Modulation Utilizing a Swept Probing Signal for Robust Crack Detection. *Struct Heal Monit* 2010;9:257–67.
- [120] Aymerich F, Staszewski WJ. Experimental Study of Impact-Damage Detection in Composite Laminates using a Cross-Modulation Vibro-Acoustic Technique. *Struct Heal Monit* 2010;9:541–53.
- [121] Kim S, Adams DE, Sohn H, Rodriguez-Rivera G, Myrent N, Bond R, et al. Crack detection technique for operating wind turbine blades using Vibro-Acoustic Modulation. *Struct Heal Monit* 2014;13:660–70.
- [122] Dutta D, Sohn H, Harries K a., Rizzo P. A Nonlinear Acoustic Technique for Crack Detection in Metallic Structures. *Struct Heal Monit* 2009;8:251–62.
- [123] Ryles M, Ngau FH, Mcdonald I, Staszewski WJ. Comparative study of nonlinear acoustic and Lamb wave techniques for fatigue crack detection in metallic structures. *Fatigue Fract Eng Mater Struct* 2008;31:674–83.
- [124] Klepka A, Pieczonka L, Staszewski WJ, Aymerich F. Impact damage detection in laminated composites by non-linear vibro-acoustic wave modulations. *Compos Part B Eng* 2014;65:99–108.
- [125] Klepka A, Staszewski WJ, di Maio D, Scarpa F. Impact damage detection in composite chiral sandwich panels using nonlinear vibro-acoustic modulations. *Smart Mater Struct* 2013;22:084011.
- [126] Sarigül AS, Karagözlü E. Vibro-acoustic analysis of composite plates. *J Phys Conf Ser* 2014;490:012212.
- [127] Pieczonka L, Ukowski P, Klepka A, Staszewski WJ, Uhl T, Aymerich F. Impact damage detection in light composite sandwich panels using piezo-based nonlinear vibro-acoustic modulations. *Smart Mater Struct* 2014;23:105021.
- [128] Masmoudi S, El Mahi A, Turki S. Fatigue behaviour and structural health monitoring by acoustic emission of E-glass/epoxy laminates with piezoelectric implant. *Appl Acoust* 2016;108:50–8.
- [129] Alexopoulos N., Bartholome C, Poulin P, Marioli-Riga Z. Structural health monitoring of glass fiber reinforced composites using embedded carbon

- nanotube (ENT) fibres. *Compos Sci Technol* 2010;70:260–71.
- [130] Ghezzi F, Starr AF, Smith DR. Integration of networks of sensors and electronics for structural health monitoring of composite materials. *Adv Civ Eng* 2010;2010.
- [131] Ksouri S, Matmat M, Boukabache H, Escriba C, Fourniols J. Damage detection in composite laminates aeronautics structures through accelerometers network. *Adv Mater Sci* 2011;11:37–43.
- [132] Giurgiutiu V, Santoni-Bottai G. Structural Health Monitoring of Composite Structures with Piezoelectric-Wafer Active Sensors. *AIAA J* 2011;49:565–81.
- [133] Nauman S, Cristian I, Koncar V. Simultaneous Application of Fibrous Piezoresistive Sensors for Compression and Traction Detection in Glass Laminate Composites. *Sensors* 2011;11:9478–98.
- [134] Dziendzikowski M, Dragan K, Kurnyta A, Kornas Ł, Latoszek A, Zabłocka M, et al. An approach to structural health monitoring of composite structures based on embedded PZT transducers. *Fatigue Aircr Struct* 2014;1:113–8.
- [135] Luo S, Liu T. Graphite Nanoplatelet Enabled Embeddable Fiber Sensor for in Situ Curing Monitoring and Structural Health Monitoring of Polymeric Composites. *ACS Appl Mater Interfaces* 2014;6:9314–20.
- [136] Cenek S, Mudit R, Radek H. Structural Health Monitoring of Composite Structures using embedded PZT Sensors in Space Application. 2nd Eur. Conf. Progn. Heal. Manag. Soc., 2014.
- [137] Lang W, Boll D, Schotzko T. Function Scale Integration – Embedding Sensors in Materials for Structural Health Monitoring. 6th Eur Work Struct Heal Monit 2012:1–8.
- [138] Salas M, Focke O, Herrmann A., Lang W. Wireless Power Transmission for SHM of Fibre reinforced composite materials. *Sensors Journal, IEEE* 2014;14:2171–6.
- [139] Lu S, Jiang M, Sui Q, Sai Y, Jia L. Damage identification system of CFRP using fiber Bragg grating sensors. *Compos Struct* 2015;125:400–6.
- [140] Kinet D, Mégret P, Goossen K., Qiu L, Heider D, Caucheteur C. Fiber Bragg Grating Sensors toward Structural Health Monitoring in Composite Materials: Challenges and Solutions. *Sensors* 2014;14:7394–419.
- [141] Zuluaga-Ramírez P, Frövel M, Belenguer T, Salazar F. Non contact inspection

- of the fatigue damage state of carbon fiber reinforced polymer by optical surface roughness measurements. *NDT E Int* 2015;70:22–8.
- [142] Zuluaga-Ramírez P, Arconada Á, Frövel M, Belenguer T, Salazar F. Optical sensing of the fatigue damage state of CFRP under realistic aeronautical load sequences. *Sensors* 2015;15:5710–21.
- [143] Yin W, Withers PJ, Sharma U, Peyton AJ. Noncontact Characterization of Carbon-Fibre-Reinforced Plastics Using Multifrequency Eddy Current Sensors. *Instrum Meas Technol Conf Proceedings, 2007 IMTC 2007 IEEE 2009*;58:738–43.
- [144] Khandetskii VS, Martynovich LY. Eddy-Current Nondestructive Detection of Delaminations Near Edges of Composite Materials. *Russ J Nondestruct Test* 2001;37:207–13.
- [145] Bonavolontà C, Valentino M, Pepe GP, Bonavolontà, C., Valentino, M. and Pepe G. Characterization of the damage process in GLARE 2 using an eddy current technique based on HTS-SQUID magnetometer. *Supercond Sci Technol* 2007;20:51–6.
- [146] Bonavolontà C, Valentino M, Marrocco N, Pepe GP. Eddy current technique based on-SQUID and GMR sensors for non-destructive evaluation of fiber/metal laminates. *IEEE Trans Appl Supercond* 2009;19:808–11.
- [147] Mizukami K, Mizutani Y, Todoroki A, Suzuki Y. Detection of delamination in thermoplastic CFRP welded zones using induction heating assisted eddy current testing. *NDT E Int* 2015;74:106–11.
- [148] Suzuki Y, Todoroki A, Mizutani Y, Matsuzaki R. Impact Damage Detection in CFRP Using Statistical Analysis of Resistance-Temperature Characteristics. *J Solid Mech Mater Eng* 2011;5:33–43.
- [149] Kupke M, Schulte K, Schüler R. Non-destructive testing of FRP by d.c. and a.c. electrical methods. *Compos Sci Technol* 2001;61:837–47.
- [150] Abry JC, Choi YK, Chateauinois A, Dalloz B, Giraud G, Salvia M. In-situ monitoring of damage in CFRP laminates by means of AC and DC measurements. *Compos Sci Technol* 2001;61:855–64.
- [151] Wen J, Xia Z, Choy F. Damage detection of carbon fiber reinforced polymer composites via electrical resistance measurement. *Compos Part B Eng* 2011;42:77–86.

- [152] De Baere I, Van Paepegem W, Degrieck J. Electrical resistance measurement for in situ monitoring of fatigue of carbon fabric composites. *Int J Fatigue* 2010;32:197–207.
- [153] Abry JC, Bochart S, Chateauminois A, Salvia M, Giraud G. In situ detection of damage in CFRP laminates by electrical resistance measurements. *Compos Sci Technol* 1999;59:925–35.
- [154] Wang S, Chung DDL, Chung JH. Impact damage of carbon fiber polymer-matrix composites, studied by electrical resistance measurement. *Compos Part A Appl Sci Manuf* 2005;36:1707–15.
- [155] Viets C, Kaysser S, Schulte K. Damage mapping of GFRP via electrical resistance measurements using nanocomposite epoxy matrix systems. *Compos Part B Eng* 2014;65:80–8.
- [156] Kwon DJ, Wang ZJ, Choi JY, Shin PS, Devries KL, Park JM. Damage sensing and fracture detection of CNT paste using electrical resistance measurements. *Compos Part B Eng* 2016;90:386–91.
- [157] Mayr G, Plank B, Sekelja J, Hendorfer G. Active thermography as a quantitative method for non-destructive evaluation of porous carbon fiber reinforced polymers. *NDT E Int* 2011;44:537–43.
- [158] Meola C, Toscano C. Flash thermography to evaluate porosity in carbon fiber reinforced polymer (CFRPs). *Materials (Basel)* 2014;7:1483–501.
- [159] Meola C, Carlomagno GM. Impact damage in GFRP: New insights with infrared thermography. *Compos Part A Appl Sci Manuf* 2010;41:1839–47.
- [160] Tashan J, Al-mahaidi R. Investigation of the parameters that influence the accuracy of bond defect detection in CFRP bonded specimens using IR thermography. *Compos Struct* 2012;94:519–31.
- [161] Montanini R, Freni F. Non-destructive evaluation of thick glass fiber-reinforced composites by means of optically excited lock-in thermography. *Compos Part A Appl Sci Manuf* 2012;43:2075–82.
- [162] Maier A, Schmidt R, Oswald-Tranta B, Schledjewski R. Non-destructive thermography analysis of impact damage on large-scale CFRP automotive parts. *Materials (Basel)* 2014;7:413–29.
- [163] Van Den Abeele, K.A. Johnson PA, Sutin A. Nonlinear elastic wave spectroscopy (NEWS) techniques to discern material damage, part I: nonlinear

- wave modulation spectroscopy (NWMS). *Res Nondestruct Eval* 2000;12:17–30.
- [164] Meo M, Zumpano G. Nonlinear elastic wave spectroscopy identification of impact damage on a sandwich plate. *Compos Struct* 2005;71:469–74.
- [165] Zumpano G, Meo M. Damage detection in an aircraft foam sandwich panel using nonlinear elastic wave spectroscopy. *Comput Struct* 2008;86:483–90.
- [166] Zumpano G, Meo M. Damage localization using transient non-linear elastic wave spectroscopy on composite structures. *Int J Non Linear Mech* 2008;43:217–30.
- [167] El Kadi H, Al-Assaf Y. Prediction of the fatigue life of unidirectional glass fibre/epoxy composite laminate using different neural network paradigms. *Compos Struct* 2002;55:239–46.
- [168] Sheela KG, Deepa SN. Review on methods to fix number of hidden neurons in neural networks. *Math Probl Eng* 2013;2013.
- [169] Sahin, M. and Sheno, R.A. Vibration-based damage identification in beam-like composite laminates by using artificial neural networks. *Proc Inst Mech Eng Part C J Mech Eng Sci* 2003;217:661–76.
- [170] El Kadi H. Modeling the mechanical behavior of fiber-reinforced polymeric composite materials using artificial neural networks—A review. *Compos Struct* 2006;73:1–23.
- [171] Watkins S., Akhavan F, Dua R, Chandrashekhara K, Wunsch DC. Impact-induced damage characterization of composite plates using neural networks. *Smart Mater Struct* 2007;16:515–24.
- [172] De Albuquerque VHC, Tavares JMR, Durao LM. Evaluation of Delamination Damage on Composite Plates using an Artificial Neural Network for the Radiographic Image Analysis. *J Compos Mater* 2010;44:1139–59.
- [173] El Kadi H, Al-Assaf Y. Energy-based fatigue life prediction of fiberglass/epoxy composites using modular neural networks. *Compos Struct* 2002;57:85–9.
- [174] Yam LH, Yan YJ, Jiang JS. Vibration-based damage detection for composite structures using wavelet transform and neural network identification. *Compos Struct* 2003;60:403–12.
- [175] Just-Agosto F, Serrano D, Shafiq B, Cecchini A. Neural network based nondestructive evaluation of sandwich composites. *Compos Part B Eng* 2008;39:217–25.
- [176] Shilbayeh, N. and Iskandarani, M.Z. Application of new feature extraction

- technique to PVT images of composite structures. *Inf Technol J* 2004;3:332–6.
- [177] Doebling, S.W., Farrar, C.R., Prime, M.B. and Shevitz DW. *Damage Identification and Health Monitoring of Structural and Mechanical Systems from Changes in Their Vibration Characteristics: A Literature Review*. (No. LA--13070-MS). Los Alamos Natl. Lab., NM (United States): 1996, p. 1–136.
- [178] Farhana, N.I.E., Majid MA, Paulraj MP, Ahmadhilmi E, Fakhzan MN, Gibson A. A novel vibration based non-destructive testing for predicting glass fibre/matrix volume fraction in composites using a neural network model. *Compos Struct* 2016;144:96–107.
- [179] Jiang Z, Zhang Z, Friedrich F. Prediction on wear properties of polymer composites with artificial neural networks. *Compos Sci Technol* 2007;67:168–76.
- [180] Surace C, Worden K. Extended Analysis of a Damage Prognosis Approach Based on Interval Arithmetic. *Strain* 2011;47:544–54.
- [181] Peng T, Liu Y, Saxena A, Goebel K. In-situ fatigue life prognosis for composite laminates based on stiffness degradation. *Compos Struct* 2015;132:155–65.
- [182] Schwab M, Todt M, Wolfahrt M, Pettermann HE. Failure mechanism based modelling of impact on fabric reinforced composite laminates based on shell elements. *Compos Sci Technol* 2016;128:131–7.
- [183] Nairn JA, Hu S. Micromechanics of damage: a case study of matrix microcracking. *Damage Mech Compos Mater* 1994:187–243.
- [184] Nairn JA. *Matrix Microcracking in Composites*. *Polym. Matrix Compos.*, vol. 2, Elsevier Science; 2000, p. 1–34.
- [185] Tong J, Guild FJ, Ogin SL, Smith PA. On matrix crack growth in quasi-isotropic laminates-I. Experimental investigation. *Compos Sci Technol* 1997;57:1527–35.
- [186] Jen M., Lee C. Strength and life in thermoplastic composite laminates under static and fatigue loads. Part I: Experimental. *Int J Fatigue* 1998;20:605–15.
- [187] Gayathri P, Umesh K, Ganguli R. Effect of matrix cracking and material uncertainty on composite plates. *Reliab Eng Syst Saf* 2010;95:716–28.
- [188] Tinô SR., Aquino EMF. Fracture Characteristics and Anisotropy in Notched Glass Fiber Reinforced Plastics. *Mater Res* 2014;17:1610–9.
- [189] Henaff-Gardin C, Lafarie-Frenot M., Gamby D. Doubly periodic matrix cracking in composite laminates Part 2: Thermal biaxial loading. *Compos Struct*

- 1996;36:131–40.
- [190] Nairn JA. NASA Contractor Report 4479. Salt Lake City, Utah: 1992.
- [191] Park C., McManus H. Thermally induced damage in composite laminates: predictive methodology and experimental investigation. *Compos Sci Technol* 1996;56:1209–19.
- [192] Ou Y, Zhu D, Zhang H, Huang L, Yao Y, Li G, et al. Mechanical characterization of the tensile properties of glass fiber and its reinforced polymer (GFRP) composite under varying strain rates and temperatures. *Polymers (Basel)* 2016;8:196.
- [193] Bai Y, Keller T, Vallée T. Modeling of stiffness of FRP composites under elevated and high temperatures. *Compos Sci Technol* 2008;68:3099–106.
- [194] Reis JML, Coelho JLV, Monteiro AH, Da Costa Mattos HS. Tensile behavior of glass/epoxy laminates at varying strain rates and temperatures. *Compos Part B Eng* 2012;43:2041–6.
- [195] Craven R, Pindoria S, Olsson R. Finite element study of compressively loaded fibres fractured during impact. *Compos Sci Technol* 2009;69:586–93.
- [196] Davidson P, Waas A. Non-smooth mode I fracture of fibre-reinforced composites: an experimental, numerical and analytical study. *Philosophical Transactions of the Royal Society of London A. Math Phys Eng Sci* 2012;370:1942–65.
- [197] Bedsole RW, Bogert PB, Tippur H V. An experimental investigation of interlaminar and intralaminar dynamic fracture of CFRPs: Effect of matrix modification using carbon nanotubes. *Compos Struct* 2015;132:1043–55.
- [198] Vaughan T., McCarthy C. A micromechanical study on the effect of intra-ply properties on transverse shear fracture in fibre reinforced composites. Part A. *Appl Sci Manuf* 2011;42:1217–28.
- [199] Neto P, Alfaiate J, Vinagre J. Assessment of the dependence of CFRP-concrete behaviour on the width of the bonded materials. *Compos Part B Eng* 2016;91:448–57.
- [200] Lörcher S, Winkler T, Makyla K, Ouellet-Plamondon, C. Burgert I, Bruns N. Mechanical unfolding of a fluorescent protein enables self-reporting of damage in carbon-fibre-reinforced composites. *J Mater Chem A* 2014;2:6231–7.
- [201] Swamy R., Mukhopadhyaya P. Debonding of carbon-fibre-reinforced polymer

- plate from concrete beams. *Proc Inst Civ Eng Struct Build* 1999;134:301–17.
- [202] Dhieb, H., Buijnsters, J.G., Elleuch, K. and Celis J. Effect of relative humidity and full immersion in water on friction, wear and debonding of unidirectional carbon fibre reinforced epoxy under reciprocating sliding. *Compos Part B Eng* 2016;88:240–52.
- [203] Gamstedt E. Effects of debonding and fiber strength distribution on fatigue-damage propagation in carbon fiber-reinforced epoxy. *J Appl Polym Sci* 2000;95:716–28.
- [204] Latifi, M., Van der Meer, F. P., and Sluys LJ. A level set model for simulating fatigue-driven delamination in composites. *Int J Fatigue* 2015;80:434–42.
- [205] Barbieri, E., and Meo M. A meshfree penalty-based approach to delamination in composites. *Compos Sci Technol* 2009;69:2169–77.
- [206] Schön J. A model of fatigue delamination in composites. *Compos Sci Technol* 2000;60:553–8.
- [207] Argüelles, A., Viña, J., Canteli, A. F., and Bonhomme J. Fatigue delamination, initiation, and growth, under mode I and II of fracture in a carbon-fiber epoxy composite. *Polym Compos* 2010;31:700–6.
- [208] Pochiraju, K. V., Lau, A. C. W. and Wang ASD. Analysis of fiber pull out or push-in with frictional sliding at the fiber-matrix interface. *Compos Eng* 1995;5:611–31.
- [209] Chandra, N., and Ghonem H. Interfacial mechanics of push-out tests: theory and experiments. *Appl Sci Manuf* 2001;32:575–84.
- [210] Yue, C. Y., and Padmanabhan K. Interfacial studies on surface modified Kevlar fibre/epoxy matrix composites. *Compos Part B Eng* 1999;30:205–17.
- [211] Jia, Y., Chen, Z., and Yan W. A numerical study on carbon nanotube–hybridized carbon fibre pullout. *Compos Sci Technol* 2014;91:38–44.
- [212] Harich, J., Lapusta, Y., and Wagner W. 3D FE-modeling of surface and anisotropy effects during micro-buckling in fiber composites. *Compos Struct* 2009;89:551–5.
- [213] Lee, J., and Soutis C. A study on the compressive strength of thick carbon fibre–epoxy laminates. *Compos Sci Technol* 2007;67:2015–26.
- [214] Vinet, A., and Gamby D. Prediction of long-term mechanical behaviour of fibre composites from the observation of micro-buckling appearing during creep

- compression tests. *Compos Sci Technol* 2008;68:526–36.
- [215] Zheng, Z., and Engblom JJ. Fiber micro-buckling of continuous glass-fiber reinforced hollow-cored recycled plastic extrusions under long-term flexural loads. *Compos Struct* 2002;56:157–64.
- [216] Berbinau P, Soutis C, Guz IA. Compressive failure of 0° unidirectional carbon-fibre-reinforced plastic (CFRP) laminates by fibre microbuckling. *Compos Sci Technol* 1999;59:1451–5.
- [217] Mohammadabadi, M., Daneshmehr, A. R., and Homayounfard M. Size-dependent thermal buckling analysis of micro composite laminated beams using modified couple stress theory. *Int J Eng Sci* 2015;92:47–62.
- [218] Wind, J. L., Steffensen, S., and Jensen HM. Comparison of a composite model and an individually fiber and matrix discretized model for kink band formation. *Int J Non Linear Mech* 2014;67:319–25.
- [219] Vogler TJ, Kyriakides S. On the axial propagation of kink bands in fiber composites : Part i experiments. *Int J Solids Struct* 1999;36:557–74.
- [220] Budiansky, B., Fleck, N. A., and Amazigo JC. On kink-band propagation in fiber composites. *J Mech Phys Solids* 1998;46:1637–53.
- [221] Svensson, D., Alfredsson, K. S., Stigh, U., and Jansson NE. Measurement of cohesive law for kink-band formation in unidirectional composite. *Eng Fract Mech* 2016;151:1–10.
- [222] Sun W, Vassilopoulos AP, Keller T. Experimental investigation of kink initiation and kink band formation in unidirectional glass fiber-reinforced polymer specimens. *Compos Struct* 2015;130:9–17.
- [223] Bai, J., and Phoenix SL. Compressive failure model for fiber composites by kink band initiation from obliquely aligned, shear-dislocated fiber breaks. *Int J Solids Struct* 2005;42:2089–128.
- [224] Bazant ZP, Kim J-JH, Daniel IM, Becq-Giraudon E, Zi G. Size Effect on Compression Strength of Fiber Composites Failing by Kink Band Propagation. *Int J Fract* 1999;95:103–41.
- [225] Vogler, T. J., and Kyriakides S. Initiation and axial propagation of kink bands in fiber composites. *Acta Mater* 1997;45:2443–54.
- [226] Gonzalez-Chi, P. I., Flores-Johnson, E. A., Carrillo-Baeza, J. G., and Young RJ. Micromechanical analysis of the kink-band performance at the interface of a

- thermoplastic composite under tensile deformation. *Polym Compos* 2010;31:1817–21.
- [227] Hsu S-Y, Vogler TJ, Kyriakides S. On the axial propagation of kink bands in fiber composites : Part II analysis. *Int J Solids Struct* 1999;36:575–95.
- [228] Pimenta, S., Gutkin, R., Pinho, S. T., and Robinson P. A micromechanical model for kink-band formation: Part II—Analytical modelling. *Compos Sci Technol* 2009;69:956–64.
- [229] Pimenta, S., Gutkin, R., Pinho, S. T., and Robinson P. A micromechanical model for kink-band formation: Part I — Experimental study and numerical modelling. *Compos Sci Technol* 2009;69:948–55.
- [230] Zi, G., and Bažant ZP. Eigenvalue method for computing size effect of cohesive cracks with residual stress, with application to kink-bands in composites. *Int J Eng Sci* 2003;41:1519–34.
- [231] Le T-P, Paultre P. Modal identification based on the time–frequency domain decomposition of unknown-input dynamic tests. *Int J Mech Sci* 2013;71:41–50.
- [232] Cheng L, Zheng D. The identification of a dam’s modal parameters under random support excitation based on the Hankel matrix joint approximate diagonalization technique. *Mech Syst Signal Process* 2014;42:42–57.
- [233] Mellinger P, Döhler M, Mevel L. Variance estimation of modal parameters from output-only and input/output subspace-based system identification. *J Sound Vib* 2016;379:1–27.
- [234] Feng D, Feng MQ. Identification of structural stiffness and excitation forces in time domain using noncontact vision-based displacement measurement. *J Sound Vib* 2017;406:15–28.
- [235] Zapico-Valle JL, García-Diéguez M, Alonso-Cambor R. Nonlinear modal identification of a steel frame. *Eng Struct* 2013;56:246–59.
- [236] Khoshnoud, F., Khoshnoud, F. and Esat II. Modal description of vibratory behaviour of structures using fuzzy membership functions. *J Multi-Body Dyn* 2004;218:173–81.
- [237] Zhang L, Brincker R, Andersen P. An Overview of Operational Modal Analysis: Major Development and Issues. *Proc. 1st Int. Oper. Modal Anal. Conf. IOMAC, Copenhagen, Denmark: 2005, p. April 26-27.*
- [238] Montalvão D, Silva JMM. A contribution to the modal identification of the

- damping factor based on the dissipated energy. Proc. 9th Int. Conf. Struct. Dyn. (EURODYN 2014), vol. 54, Porto, Portugal: 2014, p. 2571–7.
- [239] J. Silva, N. Maia, A. Ribeiro. Modal Constants Consistency: Application of a New Method for Solving Overdetermined Non-linear Equations. Proc. 12th Int. Modal Anal. Conf. (XII IMAC), Honolulu, Hawaii.: 1994.
- [240] Allemang RJ. The modal assurance criterion - Twenty years of use and abuse. *Sound Vib* 2003;37:14–21.
- [241] Silva JMM, Maia NMM, Ribeiro AMR. Cancellation of Mass-Loading Effects of Transducers and Evaluation of Unmeasured Frequency Response Functions. *J Sound Vib* 2000;236:761–79.
- [242] Lazan BJ. Damping of materials and members in structural mechanics. Pergamon Press Ltd, Oxford, England; 1968.
- [243] L. Meirovitch. Elements of Vibration Analysis. McGraw-Hill, International Edition; 1986.
- [244] Montalvão D, Cláudio RALD, Ribeiro AMR, Duarte-Silva J. Experimental measurement of the complex Young's modulus on a CFRP laminate considering the constant hysteretic damping model. *Compos Struct* 2013;97:91–8.
- [245] Silva JMM, Maia NMM, Ribeiro AMR. Structural Dynamic Identification with Modal Constant Consistency using the Characteristic Response Function (CRF). *Mach Vibrat* 1996;5:83–8.
- [246] Guillaume P, Verboven P, Vanlanduit S PE. Multisine Excitations- New Developments and Applications in Modal Analysis. Proc 19th Int Modal Anal Conf (IMAC XIX) 2001;2:1543–9.
- [247] Ewins DJ. Modal testing: theory and practice. Letchworth: Research Studies Press; 1984.
- [248] Wu, Wen-Yen and M-JJW. Elliptical object detection by using its geometric properties. *Pattern Recognit* 1993;26:1499–509.
- [249] Porrill J. Fitting ellipses and predicting confidence envelopes using a bias corrected Kalman filter. *Image Vis Comput* 1990;8:37–41.
- [250] Bookstein FL. Fitting conic sections to scattered data. *Comput Graph Image Process* 1979;9:56–71.
- [251] Fitzgibbon A, Pilu M, Fisher RB. Direct least square fitting of ellipses. *IEEE Trans Pattern Anal Mach Intell* 1999;21:476–80.

- [252] Gander, Walter, Gene H. Golub and RS. Least-squares fitting of circles and ellipses. *BIT Numer Math* 1994;34:558–78.
- [253] Hal R, Flusser J. Numerically stable direct least squares fitting of ellipses. *Proc 6th Int Conf Cent Eur Comput Graph Vis* 1998;98:125–32.
- [254] Haralick, Robert M. and LG. *Computer and robot vision*. Addison-wesley; 1992.
- [255] Kanatani K, Rangarajan P. Hyper least squares fitting of circles and ellipses. *Comput Stat Data Anal* 2011;55:2197–208.
- [256] Sampson PD. Fitting conic sections to “very scattered” data: An iterative refinement of the Bookstein algorithm. *Comput Graph Image Process* 1982;18:97–108.
- [257] Taubin G. Estimation of planar curves, surfaces, and nonplanar space curves defined by implicit equations with applications to edge and range image segmentation. *IEEE Trans Pattern Anal Mach Intell* 1991;11:15–38.
- [258] Yu J, Kulkarni SR, Poor HV. Robust ellipse and spheroid fitting. *Pattern Recognit Lett* 2012;33:492–9.
- [259] Har-Peled S, Raichel B. The fréchet distance revisited and extended. *ACM Trans Algorithms* 2014;10:1–22.
- [260] Maia, N. M. M., Silva, J. M. M. and Ribeiro AMR. A New Concept in Modal Analysis: The Characteristic Response Function. *Int J Anal Exp Modal Anal* 1994;9:191–202.
- [261] Montalvão D. A modal-based contribution to damage location in laminated composites Plates. PhD thesis, Instituto Superior Técnico, Universidade de Lisboa, Portugal., 2010.
- [262] Montalvão D, Dimitris K, Ribeiro AM, Arina J, Baxter R. An experimental study on the evolution of modal damping with damage in carbon fiber laminates. *J Compos Mater* 2014;49:2403–13.
- [263] Mlyniec A, Korta J, Kudelski R, Uhl T. The influence of the laminate thickness, stacking sequence and thermal aging on the static and dynamic behavior of carbon/epoxy composites. *Compos Struct* 2014;118:208–16.

Appendix A: Deviation in the Elliptical Areas

A.1 Area of Ellipse for Plates A_1 and A_2

Note: minus sign (-) means a reduction; positive sign (+) means an increase.

Mode	Area of Ellipse							
	Test specimen A_1				Test specimen A_2			
	Healthy Plate	Damage Plate	Variation	% Variation	Healthy Plate	Damage Plate	Variation	% Variation
1	8.709302	0.000643	-8.70866	-99.9926	17.61227	0.005273	-17.607	-99.9701
2	3.343537	0.000787	-3.34275	-99.9765	13.48396	0.003887	-13.4801	-99.9712
3	0.824029	0.000764	-0.82327	-99.9073	1.877685	0.00087	-1.87682	-99.9537
4	12.48928	0.001589	-12.4877	-99.9873	9.596134	0.000617	-9.59552	-99.9936
5	0.940124	0.000845	-0.93928	-99.9101	7.540367	0.00041	-7.53996	-99.9946
6	1.147677	0.000786	-1.14689	-99.9315	0.172932	0.000222	-0.17271	-99.8716
7	0.52639	0.00069	-0.5257	-99.8689	0.399016	3.75E-05	-0.39898	-99.9906
8	10.3068	0.000963	-10.3058	-99.9907	3.799313	0.000928	-3.79839	-99.9756
9	8.370118	0.005736	-8.36438	-99.9315	5.096328	0.000757	-5.09557	-99.9851
10	0.241192	0.000233	-0.24096	-99.9034	4.003486	0.000839	-4.00265	-99.979

A.2 Area of Ellipse for Plates A_3 and B_1

Mode	Area of Ellipse							
	Test specimen A_3				Test specimen B_1			
	Healthy Plate	Damage Plate	Variation	% Variation	Healthy Plate	Damage Plate	Variation	% Variation
1	4.799755	0.001117	-4.79864	-99.9767	11.52533	0.001567	-11.5238	-99.9864
2	12.49834	0.00183	-12.4965	-99.9854	6.059295	0.001684	-6.05761	-99.9722
3	2.515284	0.002162	-2.51312	-99.914	9.022893	0.002385	-9.02051	-99.9736
4	0.968251	0.000409	-0.96784	-99.9578	0.090267	0.000555	-0.08971	-99.3852
5	0.500629	0.00048	-0.50015	-99.9041	2.147829	0.000862	-2.14697	-99.9599
6	0.494068	0.000592	-0.49348	-99.8802	14.95537	0.000161	-14.9552	-99.9989
7	0.702029	0.000593	-0.70144	-99.9155	0.554138	0.00037	-0.55377	-99.9332
8	9.092416	0.000709	-9.09171	-99.9922	35.20457	0.001567	-35.203	-99.9955
9	14.6093	0.002596	-14.6067	-99.9822	22.0891	0.003456	-22.0856	-99.9844
10	13.99917	0.002889	-13.9963	-99.9794	6.752323	0.00021	-6.75211	-99.9969

A.3 Area of Ellipse for Plates B_2 and C_1

Mode	Area of Ellipse							
	Test specimen B_2				Test specimen C_1			
	Healthy Plate	Damage Plate	Variation	% Variation	Healthy Plate	Damage Plate	Variation	% Variation
1	1.982004	0.001549	-1.98046	-99.9218	5.76972	0.00137	-5.76835	-99.9763
2	0.63888	0.000311	-0.63857	-99.9513	11.26318	0.001161	-11.262	-99.9897
3	4.89225	0.001761	-4.89049	-99.964	7.689135	0.000661	-7.68847	-99.9914
4	1.116083	0.000165	-1.11592	-99.9852	16.97017	0.000139	-16.97	-99.9992
5	0.8722	0.00055	-0.87165	-99.9369	1.330381	0.000245	-1.33014	-99.9816
6	6.566766	9.22E-05	-6.56667	-99.9986	8.404855	0.001878	-8.40298	-99.9777
7	11.32776	6.40E-06	-11.3278	-99.9999	0.373818	0.000381	-0.37344	-99.8981
8	2.743788	0.000592	-2.7432	-99.9784	6.0516	0.000802	-6.0508	-99.9867
9	15.60175	0.001627	-15.6001	-99.9896	1.631485	5.30E-05	-1.63143	-99.9968
10	2.771246	0.002153	-2.76909	-99.9223	2.694372	6.61E-05	-2.69431	-99.9975

A.4 Area of Ellipse for Plates C_2 and C_3

Mode	Area of Ellipse							
	<i>Test specimen C_2</i>				<i>Test specimen C_3</i>			
	Healthy Plate	Damage Plate	Variation	% Variation	Healthy Plate	Damage Plate	Variation	% Variation
1	12.86663	0.005078	-12.8615	-99.9605	6.136082	0.002856	-6.13323	-99.9535
2	13.3148	0.000811	-13.314	-99.9939	8.187981	0.001275	-8.18671	-99.9844
3	4.020365	0.000204	-4.02016	-99.9949	5.496891	0.00031	-5.49658	-99.9944
4	2.67598	0.000206	-2.67577	-99.9923	0.928851	0.001186	-0.92767	-99.8723
5	1.17794	0.000124	-1.17782	-99.9895	0.113056	0.001803	-0.11125	-98.4052
6	9.806815	0.000437	-9.80638	-99.9955	0.14154	0.003676	-0.13786	-97.4029
7	4.787165	0.002289	-4.78488	-99.9522	1.154289	0.000842	-1.15345	-99.9271
8	44.65337	0.005564	-44.6478	-99.9875	5.123136	0.003888	-5.11925	-99.9241
9	2.51124	0.004483	-2.50676	-99.8215	20.88607	0.002236	-20.8838	-99.9893
10	23.7682	0.000715	-23.7675	-99.997	12.43974	0.000471	-12.4393	-99.9962

A.5 Area of Ellipse for Plates D_1 and E_1

Mode	Area of Ellipse							
	<i>Test specimen D_1</i>				<i>Test specimen E_1</i>			
	Healthy Plate	Damage Plate	Variation	% Variation	Healthy Plate	Damage Plate	Variation	% Variation
1	3.215641	0.003274	-3.21237	-99.8982	5.638476	8.37E-05	-5.63839	-99.9985
2	9.209759	0.000519	-9.20924	-99.9944	57.23235	0.003324	-57.229	-99.9942
3	10.30306	0.002717	-10.3003	-99.9736	41.8361	0.000373	-41.8357	-99.9991
4	15.7832	0.001423	-15.7818	-99.991	25.98873	0.001069	-25.9877	-99.9959
5	0.46349	0.005762	-0.45773	-98.7568	18.06366	0.000263	-18.0634	-99.9985
6	0.781995	0.004098	-0.7779	-99.476	13.04952	0.001165	-13.0484	-99.9911
7	27.3888	7.77E-05	-27.3887	-99.9997	19.07945	0.001707	-19.0777	-99.9911
8	26.78143	0.000402	-26.781	-99.9985	41.02973	0.002586	-41.0271	-99.9937
9	1.505118	0.000909	-1.50421	-99.9396	7.12828	0.001667	-7.12661	-99.9766
10	2.925371	0.007786	-2.91759	-99.7338	17.13578	0.000333	-17.1354	-99.9981

A.6 Area of Ellipse for Plates F_1 and G_1

Mode	Area of Ellipse							
	<i>Test specimen F_1</i>				<i>Test specimen G_1</i>			
	Healthy Plate	Damage Plate	Variation	% Variation	Healthy Plate	Damage Plate	Variation	% Variation
1	0.002037	0.001384	-0.00065	-32.0569	0.002657	0.001011	-0.00165	-61.9496
2	0.001935	0.005628	0.003693	190.8527	0.002405	0.00042	-0.00199	-82.5364
3	0.001348	0.000509	-0.00084	-62.2404	0.00186	0.000395	-0.00147	-78.7634
4	0.000143	0.000267	0.000124	86.71329	0.00594	0.000884	-0.00506	-85.1178
5	0.000866	0.001455	0.000589	68.01386	0.001317	0.003138	0.001821	138.2688
6	0.000114	8.99E-05	-2.4E-05	-21.1726	0.000694	0.001472	0.000778	112.1037
7	0.000101	3.67E-05	-6.4E-05	-63.691	0.000118	0.000132	0.000014	11.86441
8	0.000497	0.000168	-0.00033	-66.1972	0.002113	0.002007	-0.00011	-5.01656
9	0.004591	4.05E-05	-0.00455	-99.118	0.001621	0.000277	-0.00134	-82.9118
10	0.004658	0.001497	-0.00316	-67.8617	0.004419	0.001615	-0.0028	-63.4533

Appendix B: Variation in the Modal Parameters (BETAlab)

B.1 Variation in the Modal Parameters for Plates A₁

Mode	(Test specimen A ₁)							
	Modal frequency (Hz)				Modal damping			
	Healthy Plate	Damage Plate	Variation	% Variation	Healthy Plate	Damage Plate	Variation	% Variation
1	55.35155	56.56806	1.216511	2.19779	0.015457	0.01794	0.002483	16.06392
2	112.4879	107.1435	-5.34432	-4.75102	0.021732	0.024947	0.003215	14.79385
3	148.7033	119.9519	-28.7514	-19.3347	0.01433	0.013111	-0.001219	-8.50663
4	183.8862	147.8246	-36.0616	-19.6108	0.01488	0.022914	0.008034	53.99194
5	231.9076	200.3637	-31.5439	-13.6019	0.014427	0.006582	-0.007845	-54.3772
6	278.5683	266.3426	-12.2256	-4.38874	0.01069	0.005924	-0.004766	-44.5837
7	338.8619	297.1261	-41.7358	-12.3165	0.020797	0.006702	-0.014095	-67.7742
8	361.767	354.5578	-7.20917	-1.99277	0.014251	0.006032	-0.008219	-57.6731
9	391.5385	402.4564	10.91785	2.788448	0.014209	0.005532	-0.008677	-61.0669
10	440.2174	464.7168	24.49936	5.565286	0.020383	0.007394	-0.012989	-63.7247

B.2 Variation in the Modal Parameters for Plates A₂

Mode	(Test specimen A ₂)							
	Modal frequency (Hz)				Modal damping			
	Healthy Plate	Damage Plate	Variation	% Variation	Healthy Plate	Damage Plate	Variation	% Variation
1	60.47797	63.1528	2.674828	4.422814	0.022279	0.014062	-0.00822	-36.8823
2	95.44299	92.0856	-3.35739	-3.51769	0.018042	0.021883	0.003841	21.28921
3	113.202	121.2158	8.013764	7.079172	0.022169	0.022497	0.000328	1.479544
4	154.7506	156.2391	1.48854	0.961896	0.01759	0.013002	-0.00459	-26.083
5	169.303	168.8725	-0.43053	-0.25429	0.004673	0.018217	0.013544	289.8352
6	242.3501	237.6873	-4.66286	-1.92402	0.011579	0.003995	-0.00758	-65.4979
7	298.7867	296.2557	-2.53098	-0.84708	0.005576	0.010908	0.005332	95.6241
8	371.2236	317.9035	-53.3201	-14.3633	0.014532	0.004635	-0.0099	-68.1049
9	397.0022	362.4285	-34.5737	-8.70868	0.014389	0.018981	0.004592	31.91327
10	451.2582	384.0818	-67.1764	-14.8865	0.020434	0.013612	-0.00682	-33.3855

B.3 Variation in the Modal Parameters for Plates A₃

Mode	(Test specimen A ₃)							
	Modal frequency (Hz)				Modal damping			
	Healthy Plate	Damage Plate	Variation	% Variation	Healthy Plate	Damage Plate	Variation	% Variation
1	65.98118	66.21056	0.229386	0.347654	0.011018	0.016045	0.005027	45.62534
2	126.6291	123.2954	-3.33364	-2.6326	0.019986	0.02355	0.003564	17.83248
3	130.2594	129.5195	-0.73993	-0.56804	0.019196	0.018102	-0.00109	-5.6991
4	171.8864	170.2306	-1.65581	-0.96332	0.024636	0.014689	-0.00995	-40.3759
5	215.0926	212.9556	-2.13702	-0.99354	0.016419	0.010262	-0.00616	-37.4992
6	270.2996	267.5571	-2.74249	-1.01461	0.017105	0.004883	-0.01222	-71.4528
7	329.7224	325.2455	-4.47687	-1.35777	0.011973	0.003014	-0.00896	-74.8267
8	380.3454	373.6717	-6.67365	-1.75463	0.013485	0.010796	-0.00269	-19.9407
9	402.4559	399.1527	-3.30316	-0.82075	0.008182	0.008892	0.00071	8.677585
10	417.4216	409.1861	-8.2355	-1.97295	0.014448	0.013395	-0.00105	-7.28821

B.4 Variation in the Modal Parameters for Plates B_1

Mode	<i>(Test specimen B_1)</i>							
	<i>Modal frequency (Hz)</i>				<i>Modal damping</i>			
	Healthy Plate	Damage Plate	Variation	% Variation	Healthy Plate	Damage Plate	Variation	% Variation
1	43.096489	44.699192	1.602703	3.718871	0.015367	0.008772	-0.0066	-42.9166
2	102.076538	104.558174	2.481636	2.431152	0.020926	0.014254	-0.00667	-31.8838
3	154.112457	129.420776	-24.6917	-16.0219	0.005852	0.010496	0.004644	79.35748
4	177.354156	150.58429	-26.7699	-15.094	0.012675	0.007188	-0.00549	-43.2899
5	297.134033	175.148453	-121.986	-41.0541	0.019017	0.011436	-0.00758	-39.8643
6	323.268036	223.514908	-99.7531	-30.8577	0.010526	0.005117	-0.00541	-51.387
7	347.360046	294.313568	-53.0465	-15.2713	0.009521	0.027041	0.01752	184.0143
8	401.399048	318.691711	-82.7073	-20.6048	0.023911	0.015388	-0.00852	-35.6447
9	430.037903	347.70462	-82.3333	-19.1456	0.007216	0.009491	0.002275	31.52716
10	488.977478	396.097534	-92.8799	-18.9947	0.013488	0.012868	-0.00062	-4.59668

B.5 Variation in the Modal Parameters for Plates B_2

Mode	<i>(Test specimen B_2)</i>							
	<i>Modal frequency (Hz)</i>				<i>Modal damping</i>			
	Healthy Plate	Damage Plate	Variation	% Variation	Healthy Plate	Damage Plate	Variation	% Variation
1	44.101353	49.852097	5.750744	13.03984	0.019776	0.0074	-0.01238	-62.5809
2	103.40023	104.723671	1.323441	1.279921	0.024561	0.015173	-0.00939	-38.2232
3	132.948761	135.874466	2.925705	2.200626	0.018153	0.018915	0.000762	4.197653
4	151.352249	139.797409	-11.5548	-7.6344	0.018709	0.021371	0.002662	14.22845
5	173.423187	174.212784	0.789597	0.455301	0.020217	0.018978	-0.00124	-6.12851
6	284.722107	250.161514	-34.5606	-12.1384	0.014526	0.010289	-0.00424	-29.1684
7	314.987457	294.755035	-20.2324	-6.42325	0.010413	0.006128	-0.00429	-41.1505
8	343.374725	328.657104	-14.7176	-4.28617	0.007509	0.007796	0.000287	3.82208
9	405.577972	417.734192	12.15622	2.997258	0.020929	0.015159	-0.00577	-27.5694
10	440.842346	444.379608	3.537262	0.802387	0.015021	0.006692	-0.00833	-55.449

B.6 Variation in the Modal Parameters for Plates B_3

Mode	<i>(Test specimen B_3)</i>							
	<i>Modal frequency (Hz)</i>				<i>Modal damping</i>			
	Healthy Plate	Damage Plate	Variation	% Variation	Healthy Plate	Damage Plate	Variation	% Variation
1	46.943035	47.921844	0.978809	2.0851	0.00211	0.013423	0.011313	536.1611
2	103.218201	102.863327	-0.35487	-0.34381	0.001429	0.017626	0.016197	1133.45
3	137.472672	137.094788	-0.37788	-0.27488	0.001589	0.016955	0.015366	967.0233
4	154.159866	172.149963	17.9901	11.66977	0.001437	0.017207	0.01577	1097.425
5	173.224319	253.215805	79.99149	46.17798	0.001805	0.02029	0.018485	1024.1
6	280.966858	292.29129	11.32443	4.030522	0.001535	0.014631	0.013096	853.1596
7	310.34021	336.445068	26.10486	8.411691	0.001543	0.011137	0.009594	621.7758
8	399.937439	359.999115	-39.9383	-9.98614	0.001557	0.009768	0.008211	527.3603
9	443.853851	425.275055	-18.5788	-4.18579	0.001518	0.018527	0.017009	1120.487
10	471.96817	448.772919	-23.1953	-4.91458	0.001809	0.008635	0.006826	377.3355

B.7 Variation in the Modal Parameters for Plates C_1

Mode	(Test specimen C_1)							
	Modal frequency (Hz)				Modal damping			
	Healthy Plate	Damage Plate	Variation	% Variation	Healthy Plate	Damage Plate	Variation	% Variation
1	56.899643	56.349133	-0.55051	-0.96751	0.022326	0.012914	-0.00941	-42.1571
2	113.191887	102.071632	-11.1203	-9.82425	0.018019	0.016364	-0.00166	-9.18475
3	156.815903	120.428421	-36.3875	-23.2039	0.027281	0.024167	-0.00311	-11.4145
4	167.998169	142.522903	-25.4753	-15.164	0.014189	0.010515	-0.00367	-25.8933
5	244.054169	188.684723	-55.3694	-22.6874	0.006149	0.013136	0.006987	113.6282
6	312.239258	228.114334	-84.1249	-26.9425	0.008862	0.00676	-0.0021	-23.7193
7	325.314758	282.554077	-42.7607	-13.1444	0.005706	0.014992	0.009286	162.741
8	368.297729	312.256042	-56.0417	-15.2164	0.020111	0.01701	-0.0031	-15.4194
9	396.854004	341.268555	-55.5854	-14.0065	0.017644	0.012872	-0.00477	-27.046
10	455.290619	364.06311	-91.2275	-20.0372	0.013837	0.010963	-0.00287	-20.7704

B.8 Variation in the Modal Parameters for Plates C_2

Mode	(Test specimen C_2)							
	Modal frequency (Hz)				Modal damping			
	Healthy Plate	Damage Plate	Variation	% Variation	Healthy Plate	Damage Plate	Variation	% Variation
1	34.937496	34.756165	-0.18133	-0.51902	0.016855	0.002945	-0.01391	-82.5274
2	102.62207	102.361	-0.26107	-0.2544	0.024351	0.002069	-0.02228	-91.5034
3	131.818893	132.113571	0.294678	0.223548	0.016826	0.002427	-0.0144	-85.5759
4	142.413559	142.385895	-0.02766	-0.01943	0.023416	0.002963	-0.02045	-87.3463
5	156.043533	212.541855	56.49832	36.20677	0.02053	0.002632	-0.0179	-87.1797
6	220.818588	284.249054	63.43047	28.72515	0.016894	0.003283	-0.01361	-80.5671
7	281.563202	322.783813	41.22061	14.63991	0.006277	0.002694	-0.00358	-57.0814
8	351.091034	349.568665	-1.52237	-0.43361	0.007339	0.003828	-0.00351	-47.8403
9	398.406006	397.845917	-0.56009	-0.14058	0.014488	0.003134	-0.01135	-78.3683
10	412.960175	453.298584	40.33841	9.768111	0.010111	0.003461	-0.00665	-65.77

B.9 Variation in the Modal Parameters for Plates C_3

Mode	(Test specimen C_3)							
	Modal frequency (Hz)				Modal damping			
	Healthy Plate	Damage Plate	Variation	% Variation	Healthy Plate	Damage Plate	Variation	% Variation
1	37.205898	37.806858	0.60096	1.615228	0.001971	0.002887	0.000916	46.47387
2	103.149445	102.416794	-0.73265	-0.71028	0.001535	0.002192	0.000657	42.8013
3	137.231262	137.922424	0.691162	0.503648	0.001514	0.002705	0.001191	78.66579
4	148.069672	148.428024	0.358352	0.242016	0.001445	0.002621	0.001176	81.38408
5	227.223938	220.733261	-6.49068	-2.85651	0.001428	0.001467	0.000039	2.731092
6	290.629791	284.797638	-5.83215	-2.00673	0.001596	0.002244	0.000648	40.6015
7	367.32489	325.841003	-41.4839	-11.2935	0.001448	0.002716	0.001268	87.56906
8	406.680847	403.336853	-3.34399	-0.82226	0.001417	0.003152	0.001735	122.4418
9	419.659973	416.832397	-2.82758	-0.67378	0.002264	0.003569	0.001305	57.64134
10	453.164276	452.113464	-1.05081	-0.23188	0.001713	0.002824	0.001111	64.85698

B.10 Variation in the Modal Parameters for Plates C_4

Mode	(Test specimen C_4)							
	Modal frequency (Hz)				Modal damping			
	Healthy Plate	Damage Plate	Variation	% Variation	Healthy Plate	Damage Plate	Variation	% Variation
1	65.33989	64.506012	-0.83388	-1.27622	0.022547	0.020436	-0.00211	-9.36266
2	134.868912	134.072052	-0.79686	-0.59084	0.025773	0.028362	0.002589	10.0454
3	179.509872	178.23996	-1.26991	-0.70743	0.020544	0.026959	0.006415	31.22566
4	275.081024	274.469025	-0.612	-0.22248	0.016274	0.012047	-0.00423	-25.9739
5	306.223083	305.643799	-0.57928	-0.18917	0.009048	0.009299	0.000251	2.774094
6	358.7547	352.132935	-6.62177	-1.84576	0.011057	0.010335	-0.00072	-6.5298
7	400.144562	398.963196	-1.18137	-0.29523	0.009743	0.006106	-0.00364	-37.3294
8	561.927368	430.839203	-131.088	-23.3283	0.008716	0.009124	0.000408	4.681046
9	672.886536	540.097839	-132.789	-19.7342	0.006624	0.003603	-0.00302	-45.6069
10	692.775146	620.009583	-72.7656	-10.5035	0.002842	0.003717	0.000875	30.78818

B.11 Variation in the Modal Parameters for Plates D_1

Mode	(Test specimen D_1)							
	Modal frequency (Hz)				Modal damping			
	Healthy Plate	Damage Plate	Variation	% Variation	Healthy Plate	Damage Plate	Variation	% Variation
1	48.388958	48.313831	-0.07513	-0.15526	0.011694	0.00215	-0.00954	-81.6145
2	131.510391	130.057892	-1.4525	-1.10447	0.021719	0.00271	-0.01901	-87.5224
3	178.770538	170.469406	-8.30113	-4.64346	0.013103	0.004431	-0.00867	-66.1833
4	275.35498	174.536301	-100.819	-36.6141	0.005328	0.003095	-0.00223	-41.9107
5	348.802979	265.54187	-83.2611	-23.8705	0.006322	0.002331	-0.00399	-63.1288
6	381.546753	335.658264	-45.8885	-12.027	0.00703	0.002961	-0.00407	-57.8805
7	458.353027	452.234894	-6.11813	-1.33481	0.011707	0.003222	-0.00849	-72.478
8	474.929749	478.213501	3.283752	0.691418	0.011849	0.003065	-0.00878	-74.1328
9	496.989166	539.915771	42.9266	8.637332	0.01186	0.002409	-0.00945	-79.688
10	548.868286	574.850281	25.982	4.73374	0.013826	0.002263	-0.01156	-83.6323

B.12 Variation in the Modal Parameters for Plates D_2

Mode	(Test specimen D_2)							
	Modal frequency (Hz)				Modal damping			
	Healthy Plate	Damage Plate	Variation	% Variation	Healthy Plate	Damage Plate	Variation	% Variation
1	59.877434	61.753349	1.875915	3.132925	0.008029	0.006872	-0.00116	-14.4103
2	177.326706	179.927094	2.600388	1.466439	0.00913	0.006974	-0.00216	-23.6145
3	211.240265	214.167236	2.926971	1.385612	0.009921	0.007393	-0.00253	-25.4813
4	259.302063	233.941772	-25.3603	-9.78021	0.00775	0.007049	-0.0007	-9.04516
5	370.08313	261.969513	-108.114	-29.2133	0.010733	0.005985	-0.00475	-44.2374
6	486.620331	372.727753	-113.893	-23.4048	0.006754	0.007776	0.001022	15.13177
7	550.662842	492.513641	-58.1492	-10.5599	0.004528	0.007781	0.003253	71.84187
8	568.319641	549.894409	-18.4252	-3.24205	0.004634	0.005442	0.000808	17.43634
9	653.246765	565.821899	-87.4249	-13.3831	0.00218	0.006105	0.003925	180.0459
10	680.201538	658.743225	-21.4583	-3.1547	0.003913	0.004954	0.001041	26.60363

B.13 Variation in the Modal Parameters for Plates E_1

Mode	<i>(Test specimen E_1)</i>							
	<i>Modal frequency (Hz)</i>				<i>Modal damping</i>			
	Healthy Plate	Damage Plate	Variation	% Variation	Healthy Plate	Damage Plate	Variation	% Variation
1	55.480534	55.233414	-0.24712	-0.44542	0.018011	0.002973	-0.01504	-83.4934
2	149.463028	146.015396	-3.44763	-2.30668	0.0248	0.002379	-0.02242	-90.4073
3	184.726898	179.653885	-5.07301	-2.74622	0.016948	0.002829	-0.01412	-83.3078
4	220.414536	222.656799	2.242263	1.017294	0.017253	0.002836	-0.01442	-83.5623
5	246.083603	245.389389	-0.69421	-0.2821	0.011386	0.002479	-0.00891	-78.2276
6	335.941437	320.028839	-15.9126	-4.73672	0.004789	0.001955	-0.00283	-59.1773
7	395.581451	394.9086	-0.67285	-0.17009	0.003428	0.002513	-0.00092	-26.6919
8	469.693848	455.003387	-14.6905	-3.12767	0.004464	0.002466	-0.002	-44.7581
9	555.377869	486.417206	-68.9607	-12.4169	0.014458	0.00242	-0.01204	-83.2619
10	665.871094	542.608521	-123.263	-18.5115	0.006108	0.002576	-0.00353	-57.8258

B.14 Variation in the Modal Parameters for Plates E_2

Mode	<i>(Test specimen E_2)</i>							
	<i>Modal frequency (Hz)</i>				<i>Modal damping</i>			
	Healthy Plate	Damage Plate	Variation	% Variation	Healthy Plate	Damage Plate	Variation	% Variation
1	72.448181	72.711899	0.263718	0.364009	0.00886	0.00775	-0.00111	-12.5282
2	223.153946	220.861298	-2.29265	-1.02738	0.012793	0.022353	0.00956	74.72837
3	245.534195	245.113388	-0.42081	-0.17138	0.010554	0.022982	0.012428	117.7563
4	275.885956	272.298553	-3.5874	-1.30032	0.010308	0.009843	-0.00047	-4.51106
5	301.122803	302.587067	1.464264	0.486268	0.006117	0.008544	0.002427	39.67631
6	447.499176	441.046326	-6.45285	-1.44198	0.009052	0.008575	-0.00048	-5.26955
7	589.654846	580.059814	-9.59503	-1.62723	0.001185	0.005821	0.004636	391.2236
8	675.352417	664.926208	-10.4262	-1.54382	0.001957	0.017268	0.015311	782.371
9	740.969971	740.108948	-0.86102	-0.1162	0.001151	0.033898	0.032747	2845.091

B.15 Variation in the Modal Parameters for Plates F_1

Mode	<i>(Test specimen F_1)</i>							
	<i>Modal frequency (Hz)</i>				<i>Modal damping</i>			
	Healthy Plate	Damage Plate	Variation	% Variation	Healthy Plate	Damage Plate	Variation	% Variation
1	62.954136	63.990578	1.036442	1.646345	0.009429	0.009497	6.8E-05	0.721179
2	145.372482	143.877548	-1.49493	-1.02835	0.026965	0.018418	-0.00855	-31.6966
3	197.753021	197.315826	-0.4372	-0.22108	0.013295	0.01026	-0.00304	-22.8281
4	209.776566	209.207809	-0.56876	-0.27113	0.011205	0.01356	0.002355	21.0174
5	236.578079	237.446243	0.868164	0.366967	0.010372	0.010595	0.000223	2.150019
6	280.275635	280.256622	-0.01901	-0.00678	0.008727	0.008278	-0.00045	-5.14495
7	349.187531	346.321381	-2.86615	-0.82081	0.008464	0.007859	-0.00061	-7.14792
8	384.907318	378.513916	-6.3934	-1.66102	0.012883	0.012471	-0.00041	-3.19801
9	452.145386	443.671844	-8.47354	-1.87407	0.010827	0.009494	-0.00133	-12.3118
10	541.782471	465.332428	-76.45	-14.1108	0.008557	0.007099	-0.00146	-17.0387

B.16 Variation in the Modal Parameters for Plates G_1

Mode	<i>(Test specimen G_1)</i>							
	Modal frequency (Hz)				Modal damping			
	Healthy Plate	Damage Plate	Variation	% Variation	Healthy Plate	Damage Plate	Variation	% Variation
1	56.440022	55.268631	-1.17139	-2.07546	0.029255	0.01677	-0.01249	-42.6765
2	124.252182	124.561043	0.308861	0.248576	0.028071	0.026969	-0.0011	-3.92576
3	158.016495	158.668091	0.651596	0.412359	0.029337	0.02174	-0.0076	-25.8956
4	184.138474	160.716431	-23.422	-12.7198	0.013419	0.022676	0.009257	68.98428
5	215.186844	186.288467	-28.8984	-13.4294	0.009361	0.018565	0.009204	98.32283
6	300.119751	214.562943	-85.5568	-28.5076	0.016622	0.014826	-0.0018	-10.805
7	345.904785	298.377655	-47.5271	-13.7399	0.01736	0.007156	-0.0102	-58.7788
8	379.02359	344.274811	-34.7488	-9.16797	0.014196	0.008457	-0.00574	-40.4269
9	455.085052	378.293396	-76.7917	-16.8741	0.031987	0.008396	-0.02359	-73.7518
10	488.201416	476.063599	-12.1378	-2.48623	0.012229	0.004546	-0.00768	-62.8261

Appendix C: Achievement

